Development and Characterisation of Passive CMOS Sensors for Pixel Detectors in High Radiation Environments

Dissertation
zur
Erlangung des Doktorgrades (Dr. rer. nat.)
der
Mathematisch-Naturwissenschaftlichen Fakultät
der
Rheinischen Friedrich-Wilhelms-Universität Bonn

vorgelegt von
Yannick Manuel Dieter
aus
Waiblingen

Bonn 2022

Angefertigt mit Genehmigung der Mathematisch-Naturwissenschaftlichen Fakultät
der Rheinischen Friedrich-Wilhelms-Universität Bonn

1. Gutachter: Prof. Dr. Jochen Dingfelder
2. Gutachter: Prof. Dr. Klaus Desch

Tag der Promotion: 23.06.2022
Erscheinungsjahr: 2022

Abstract

With the upgrade of the Large Hadron Collider (LHC) to the High-Luminosity LHC (HL-LHC), the instantaneous luminosity increases by a factor of five with respect to its design value from 2027. To keep the detectors at the HL-LHC operational in this harsh radiation environment with unprecedented hit rates and radiation levels, they undergo major upgrades. The ATLAS experiment replaces its current tracking detector by a large-area and all-silicon tracking detector consisting of silicon strip and hybrid pixel detectors (ATLAS ITk detector). This challenging upgrade requires the development of radiation tolerant technologies for both the readout electronics and the sensing part of the detector.

In this thesis, the utilisation of a commercial CMOS process line for the production of sensors for hybrid pixel detectors is investigated. CMOS process lines offer high throughput at comparatively low costs and are thus a cost-effective solution for the production of large-area detectors. Further benefits arise from the availability of several features in the used CMOS technology like many metal layers, poly-silicon layers and MIM-capacitors which can help to enhance the sensor design. These features are mostly not available in conventional sensor productions.

After an intensive R&D-programme over several years, large-area passive CMOS sensors compatible with the future readout chip of the ATLAS ITk pixel detector have been successfully manufactured and characterised for the first time. Within the scope of this work, the radiation tolerance (using protons) of passive CMOS sensors up to a fluence of $1 \times 10^{16}\,\mathrm{n_{eq}/cm^2}$ is demonstrated. Furthermore, the performance of passive CMOS sensors before and after irradiation is studied in detail and compared with the sensor requirements for the future ATLAS ITk pixel detector. Crucial parameters like production yield, breakdown behaviour, electronic noise, hit-detection efficiency and charge collection behaviour are investigated. Passive CMOS sensors are found to meet the requirements for the ATLAS ITk pixel detector. In particular, an (in-time) hit-detection efficiency larger than 99 % is measured after irradiation demonstrating the suitability of passive CMOS sensors for harsh radiation environments.

Contents

1 Introduction

The Standard Model of particle physics (SM) describes in a remarkable way our current understanding of the constituents of the universe, the elementary particles, and the interactions between these particles. Over several decades, this model was tested in great detail and provided many successful predictions. The last remaining building block of the SM, the Higgs boson, was finally discovered in 2012. However, some phenomena cannot be explained by the SM, and thus require an extension (physics beyond the SM). Precision tests of the SM and searches for physics beyond it requires large accelerators that are capable of producing particle collisions with extreme energies (TeV range) at the highest rates. The largest and most powerful accelerator in the world is the Large Hadron Collider (LHC), which, together with its associated experiments, opens up the possibility of searching for new physics at unprecedented energies. One of the large multi-purpose experiments at the LHC is the ATLAS[1] experiment.

To fully exploit the physics potential of the LHC, its luminosity is increased by a factor of five with respect to its design value starting in 2027 (high-luminosity LHC or just HL-LHC). Especially the pixel detectors, which are responsible for the tracking and vertexing of particles and located close to the interaction point, are exposed to extreme radiation and have to copy with high particle densities. To meet the challenging requirements for the detectors at the HL-LHC, new radiation tolerant technologies are necessary which facilitate fast electronic processing of the data. Further, a higher granularity (smaller pixel size) is required to resolve the high-density tracks. Tremendous efforts are made to develop technologies that meet these demanding requirements for both the readout electronics and the sensing part (sensor) of the detectors, so that the ambitious upgrades of the detectors at the HL-LHC can be realised.

Typically, a CMOS process is used to manufacture the readout chip for pixel detectors. Within this study, an approach is investigated in which a commercial CMOS process is utilised not for the production of the readout chip, but for the production of the sensor. CMOS process lines offer high throughput at comparatively low costs and are thus a cost-effective solution for large-area detectors like the ATLAS detector at the HL-LHC. The area covered by the pixel detector of the new ATLAS tracking detector (ITk detector) increases from $2\,\mathrm{m}^2$ to approximately $13\,\mathrm{m}^2$. Additional advantages arise from the fact that poly-silicon layers, MIM-capacitors and several metal layers are available in a CMOS process which help to enhance the sensor design. Such features are typically not available in conventional sensor productions.

[1] **A** **T**oroidal **L**HC **A**pparatu**S**

Within the scope of this work, passive CMOS pixel sensors compatible with the future readout chip of the ATLAS ITk detector are investigated for the use in harsh radiation environments. Several crucial performance parameters are determined as well as studies using a beam telescope in a minimum ionising particle beam are conducted. Their performance before and after irradiation up to the fluences expected in the ATLAS detector is compared with the requirements for sensors of the ATLAS detector. A prototype passive CMOS sensor is investigated to compare different pixel designs and demonstrate radiation tolerance of passive CMOS sensors up to a fluence of $1 \times 10^{16}\,\mathrm{n_{eq}/cm^2}$. In addition, large-area passive CMOS sensors utilising "reticle stitching" are examined to investigate their suitability for harsh radiation environments like the ATLAS experiments.

In Chap. 2 a brief introduction to the LHC and the ATLAS detector is given. The fundamentals of silicon pixel detectors are presented in Chap. 3 including a discussion of the signal formation in pixel detectors and the detection principle of pixel detectors. In addition, the effects of radiation damage on the performance of the sensor are discussed. The chapter is concluded with a description of the future ATLAS pixel detector and the requirements for its sensors. In Chap. 4, the fabrication and design of the passive CMOS sensors investigated within this thesis are presented. Chap. 5 discusses the track reconstruction and efficiency calculation implemented within the *beam telescope analysis* software. The application of a Kalman Filter for track reconstruction of minimum ionising particles and for the alignment of detectors is described. The characterisation of passive CMOS sensors before and after irradiation is presented in Chap. 6. In the first part of this chapter, the measurement techniques and the calibration of the detectors are presented. Subsequently, the performance of passive CMOS pixel sensors before and after irradiation is investigated including the determination of the (in-time) hit-detection efficiency and charge collection behaviour using a minimum ionising particle beam. Other performance parameters like leakage current, electronic noise and detector capacitance are studied as well. A summary of the research conducted as part of this thesis is found in Chap. 7.

2 The ATLAS experiment at the LHC

The ATLAS experiment aims to precisely study the Standard Model of particle physics (SM) and searches for physics phenomena beyond the SM. It is located at the Large Hadron Collider (LHC) which provides a rich physics potential with its high-energy proton-proton collisions at extreme rates. With the help of the ATLAS detector, the Higgs boson was discovered and the SM was completed. Future research of the ATLAS experiment targets precision measurements of the Higgs boson and searches for new particles and phenomena beyond the SM.

In this chapter, the LHC and its future high-luminosity upgrade are introduced. Further, an overview of the current ATLAS detector with focus on its innermost subsystem is given. Finally, the upcoming upgrade of the ATLAS detector is briefly discussed.

2.1 The Large Hadron Collider

The Large Hadron Collider (LHC) [EB08] is the largest and most powerful particle accelerator in the world. It is located inside a tunnel 100 m under ground at CERN (Conseil Européen pour la Recherche Nucléaire) at the French-Swiss border, close to Geneva (Fig. 2.1). Inside the accelerator, which has a circumference of approximately 27 km, two proton beams with an energy of 6.5 TeV (centre-of-mass energy of $\sqrt{s} = 13\,\text{TeV}$) collide at four interaction points, where the four main experiments of the LHC, the ATLAS [Aad+08], CMS [Cha+08], LHCb [Alv+08] and ALICE [Aam+08] experiment, are located. The oppositely circulating proton beams are each consisting of 2808 bunches which collide every 25 ns, corresponding to a bunch crossing frequency of 40 MHz. With an average pile-up (collisions per bunch crossing) of approximately 25, this results in 1 billion collisions every second. The proton beams are guided through the beam line via super-conducting dipole magnets [Abe+20]. To accelerate the protons up to an energy of 6.5 TeV, several pre-accelerators, most notably the Proton Synchrotron (PS) and Super Proton Synchrotron (SPS), accelerate the protons before injection into the LHC.

The goal of the LHC is to provide an instrumentation to explore the Standard Model of particle physics and study physics beyond the SM. Future research is focussing on the investigation of the origin of mass and quark-gluon plasma (SM physics) as well as supersymmetry, dark matter and dark energy and baryon-antibaryon asymmetry (physics beyond the SM). One of the most prominent discovery at the LHC so far was the discovery of the SM Higgs boson in 2012 by the ATLAS and CMS experiments [Aad+12; Cha+12], a particle predicted almost 50

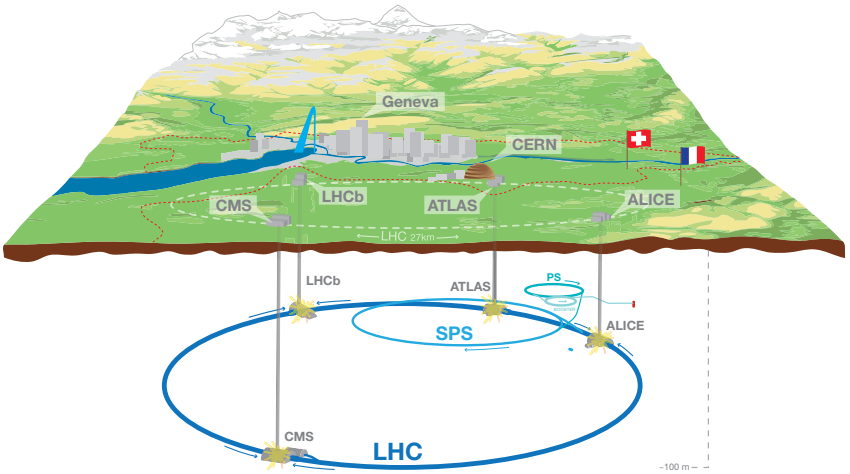

Figure 2.1: Overview of the Large Hadron Collider located at CERN with its four main experiments ATLAS, CMS, LHCb and ALICE. From [Ser14].

years before [EB64].

Typically, the cross section of physics processes at the LHC (e.g. the production of Higgs bosons) is very small[1] so that the number of events available for analysis is limited. A measure for the number of observed events per time $\dot{N}$ of a process with cross section σ is the *instantaneous* luminosity $\mathcal{L}$:

$$\dot{N} = \mathcal{L}\sigma\,. \tag{2.1}$$

The luminosity is a parameter of an accelerator and the aim is to increase the luminosity as much as possible to allow the observation of rare processes. For Gaussian beam profiles with widths σ_x and σ_y, the luminosity is given by [Hin13]

$$\mathcal{L} = \frac{bN_1N_2f}{4\pi\sigma_x\sigma_y}\,F\,, \tag{2.2}$$

where b is the number of bunches of the colliding beams which contain N_1 and N_2 particles and circulate with frequency f. The factor F is a geometrical reduction factor due to the crossing angle of the bunches. The nominal design luminosity (instantaneous) of the LHC is $\mathcal{L} = 10^{34}\,\mathrm{cm}^{-2}\,\mathrm{s}^{-1}$ [Abe+20]. The *integrated* luminosity $\mathcal{L}_{\mathrm{int}} = \int \mathcal{L}\,\mathrm{d}t$ is a measure of the number of observed events N of a process with cross section σ:

$$N = \mathcal{L}_{\mathrm{int}}\sigma\,. \tag{2.3}$$

To reduce the relative statistical uncertainty $\sigma^{\mathrm{rel}}_{\mathrm{stat}}$ which scales inversely with the square-root

[1] The cross section of all Higgs boson production mechanisms at the LHC is $\mathcal{O}(100\,\mathrm{pb})$ [Zyl+20].

of the number of observed events N (follows a Poisson distribution)

$$\sigma_{\text{stat}}^{\text{rel}} \sim \frac{1}{\sqrt{N}}\,, \tag{2.4}$$

the aim is to record as much data as possible. A small statistical uncertainty is crucial to reach a required sensitivity.

The amount of recorded events is given in units of *integrated* luminosity ($1\,\text{fb}^{-1} = 10^{39}\,\text{cm}^{-2}$). Until the end of 2018, the LHC delivered a total integrated luminosity of approximately $190\,\text{fb}^{-1}$. During its operation between 2022 and 2025 (after a shutdown in the period from 2019 to 2022), the LHC aims to increase the total integrated luminosity up to $350\,\text{fb}^{-1}$ [CER20].

2.1.1 The HL-LHC upgrade

It is experimentally confirmed that the instantaneous luminosity of the current LHC is limited to around $2 \times 10^{34}\,\text{cm}^{-2}\,\text{s}^{-1}$ [Abe+20]. The gain of recording more data at this luminosity in terms of a reduction of the statistical uncertainty is not efficient any more as it would require approximately ten more years to halve the statistical error. Therefore, the High-Luminosity LHC (HL-LHC) project [Ros11] was established in 2010 to fully exploit the physics potential of the LHC. With the HL-LHC upgrade it is planned to increase the *instantaneous* luminosity by a factor of five with respect to the design value. Starting from the operation of the HL-LHC in 2027, the target is to collect $3000\,\text{fb}^{-1}$ within 12 years. This is ten times higher than the predicted *integrated* luminosity of the LHC. [CER20; Abe+20].

To achieve such a high luminosity, the accelerator requires major upgrades including 11 - 12 T superconducting magnets, compact superconducting cavities and other cutting-edge technologies [Abe+20]. With the help of these upgrades, the bunches can be focused even more and the overlap of the colliding bunches can be enlarged which increases the luminosity according to Eq. 2.2. The required research and development phase for that started already more then ten years ago, simultaneously to the LHC physics programme. [Abe+20]

In addition to the accelerator upgrade, also the experiments at the LHC have to upgrade and partially replace their detectors. The HL-LHC imposes challenging requirements on the detectors in terms of radiation tolerance (due to increase in *integrated* luminosity) as well as hit and data rate capabilities (due to increase in *instantaneous* luminosity). In addition, detectors with higher granularity are necessary to cope with the increased track density. With the HL-LHC, the average number of collisions per bunch crossing increases from around 25 up to 200 [Abe+20]. Dedicated research and development campaigns have been already carried out and are now moving into pre-production phase such that the upgraded detectors can be installed within the shutdown period from 2026 to 2028. [CER20; Abe+20]

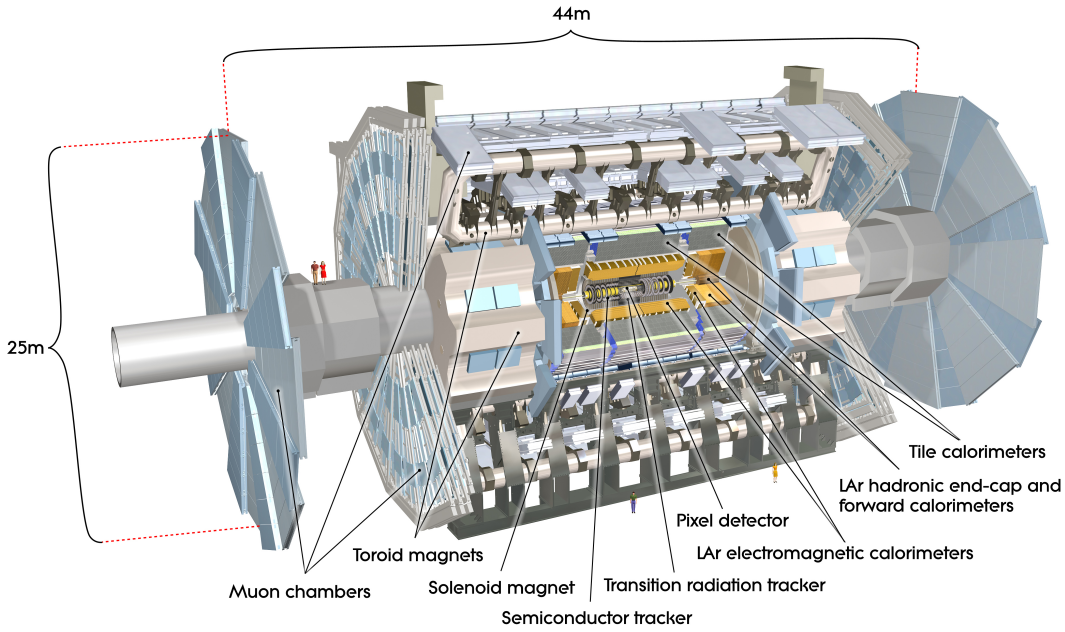

Figure 2.2: Layout of the current ATLAS detector. Different subsystems are labelled. The interaction point is located at the centre of the detector. From [Peq08b].

2.2 The ATLAS detector

The ATLAS detector, alongside the CMS detector, is one of the two general-purpose detectors to probe the symmetric proton-proton collisions at the LHC. It enables tracking and vertexing as well as energy measurements and identification of particles emerging from these collisions with almost full azimuthal angle coverage and large pseudorapidity[2] acceptance. Several subsystems consisting of concentric barrel sections and end-caps are arranged around the interaction point, as illustrated in Fig. 2.2.

Closest to the interaction point, the Inner Detector (ID) is located in a 2 T solenoid magnetic field (parallel to the beam axis). The ID consists of silicon pixel and strip detectors as well as a transition radiation tracker. It facilitates high-precision vertexing, electron identification and measurements of transverse momentum (perpendicular to beam axis) of charged particles. To measure the energy of electromagnetically and hadronically interacting particles, the ID is surrounded by a calorimeter system consisting of a liquid-argon (LAr) electromagnetic and hadronic calorimeter. The outermost subsystem of the ATLAS detector is the muon spectrometer allowing a precise estimation of the direction of muons passing the spectrometer. Further,

[2]The pseudorapidity is defined as $\eta = -\ln(\tan(\theta/2))$, with θ being the polar angle.

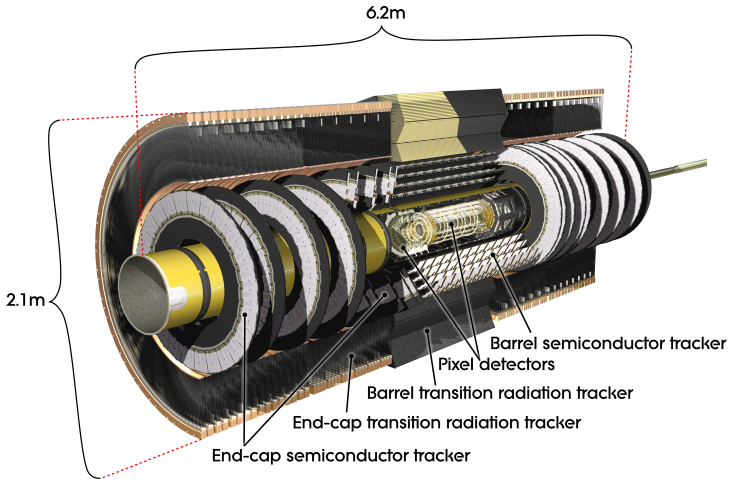

Figure 2.3: Layout of the ATLAS Inner Detector consisting of silicon pixel and strip detectors and a transition radiation detector. Without insertable B-layer (IBL). The interaction point is located at the centre of the detector. From [Peq08a].

several 3.5 T toroid magnets enable the momentum measurement of muons. [Aad+08]

Processing and storage of data from all collisions occurring with 1 GHz (1 billion collisions every second) is impossible. Therefore, the ATLAS detector features a dedicated trigger system [Owe18]. The first level of this trigger system, called LV1 trigger, decides whether to continue processing of the data based on a subset of the detector information. This reduces the data rate to around 100 kHz. The subsequent high-level trigger provides a reduction of the data rate down to 200 Hz. The trigger system is a crucial part of the detector as it requires an overall rejection factor of 5×10^6 while maintaining high efficiency for rare physics processes. [Aad+08]

A comprehensive overview of the ATLAS detector is given in [Aad+08]. In the following, the design of the Inner Detector is briefly presented.

Inner Detector

The Inner Detector (ID) enables a high-precision reconstruction of particle trajectories traversing the sensitive detector area. This allows the determination whether the particle originated from a proton-proton collision (primary vertex) or is the product of a particle decay (secondary vertex). This process is known as "vertexing". A magnetic field bends the particle trajectory and thus enables the estimation of the transverse momentum which is inversely proportional to the curvature of the particle trajectory. From the direction of the curvature, the sign of the particle's charge can be determined. This functionality is realised with different sub-detectors, as shown in Fig. 2.3.

The silicon pixel detector, with an area of $2\,\mathrm{m}^2$, is located closest to the interaction point. The pixel detector consists of four layers and three forward and backward end-caps of hybrid pixel detectors. Hybrid pixel detectors (see Sec. 3.3) are extremely radiation tolerant, and therefore well suited for the usage close to the interaction point where the irradiation levels are highest. The innermost layer ($r = 33\,\mathrm{mm}$) is called insertable B-layer (IBL) [Cap+10] and was installed in 2013. This additional layer was necessary to preserve the tracking performance of the current pixel detector as the already installed layers suffered from radiation damage and high pile-up occupancies due to the progressive increase in luminosity towards the design value. Further, it improves the vertex resolution and secondary vertex finding. [Cap+10; Aad+08]

The Semiconductor Tracker (SCT) surrounds the pixel detector. It consists of four double layers and two end-caps of silicon strip detectors. The lower granularity of strip detectors reduces the complexity of the readout and production costs and thus they are well suited to cover larger areas. In addition, the requirements in terms of hit rate and radiation tolerance in the outer layers are not as stringent as in the layers close to the interaction point. The innermost layer of the SCT is located at a radius of 299 mm. In total, the SCT covers an area of $61\,\mathrm{m}^2$. [Air+99]

The transition radiation tracker (TRT) is the outermost and largest subsystem of the ID covering a radius from $0.5\,\mathrm{m} - 1.1\,\mathrm{m}$. It consists of many thousands of drift tubes filled with a gas mixture. The spaces between the tubes are filled with polymers to produce transition radiation which is used for particle identification. It provides a relatively poor single-hit spatial resolution (compared to the pixel detector), but a larger number of hits per track (more than 30). The TRT enables continuous tracking and facilitates electron identification via transition radiation. [Aab+17]

2.2.1 The ATLAS Phase-II upgrade

To make the ATLAS detector operational at the HL-LHC, it is necessary to upgrade and replace many detector systems. The increase in luminosity imposes challenging requirements on the detectors at the HL-LHC. To be able to cope with the increased hit rate, the subsystems, especially those close to the interaction point, require higher granularity and faster readout. In addition, radiation tolerant technologies are necessary to cope with the extreme radiation levels. Upgrades targeting this are summarised as ATLAS Phase-II upgrades and are supposed to be installed during a shutdown phase in the period from 2026 to 2028.

The main upgrade of the ATLAS detector is the complete replacement of the Inner Detector with an all-silicon tracking detector, called Inner Tracker (ITk). An overview of the ITk detector is given in Sec. 3.4. Further, the electronics of the LAr calorimeter systems are replaced and the muon spectrometers are upgraded to cope with the more stringent requirements of the HL-LHC. A new High-Granularity Timing Detector is installed to improve the pile-up reduction in the forward region [CER18]. The ATLAS trigger system is re-designed and foresees a split LV0/LV1

hardware trigger with a total LV1 trigger acceptance rate of 200 kHz. A detailed summary of these upgrades can be found in [ATL17b; ATL17a; ATL17c; ATL17d].

3 Silicon pixel detectors

Until the 1980s mainly cloud and bubble chambers [Wil27; Gla60] were employed in particle physics and led to the discovery of many new particles, e.g. [And32; Bar+64]. Those were the first detectors that could make the trajectory of ionising particles visible. However, those detectors could not be read out electronically. With the development towards accelerators with higher luminosity, fast readout electronics became necessary, and therefore mainly semiconductor detectors were used in particle physics from the 1980s onwards. Due to the rapid developments in microelectronics, highly segmented semiconductor detectors (e.g. silicon pixel detectors [Ros+06]) with fast data processing capabilities could be manufactured. In addition, silicon pixel detectors became affordable over time, so that they could be used for large-area detectors, e.g. for the detectors at the LHC.

Today, silicon pixel detectors can withstand the highest particle rates and offer high-precision 3D-spatial information of ionising particle trajectories [Wer19; GW18]. They are the technology of choice for high-precision tracking and vertexing in detectors for high-energy physics experiments (like the ATLAS experiment at the LHC). Due to the low density (low Z), cheap production, large abundance and advances in microprocessing and microelectronics of silicon, it is widely utilised as detection material. Pixel detectors are also used outside of high-energy physics experiments, e.g. for X-ray imaging in biomedicine [BCL18] or for the detection of synchrotron light [Göt+09].

This chapter introduces the basic principles and functionality of silicon pixel detectors. In Sec. 3.1, the signal generation by particles interacting with the detector material and their detection principle is explained. Radiation damage in silicon with a focus on bulk damage is discussed in Sec. 3.2. One of the technologies most commonly used for pixel detectors (hybrid pixel detectors) is introduced in Sec. 3.3. Finally, an example of a large-area pixel detector, the silicon pixel detector of the future ATLAS detector, is presented in Sec. 3.4.

3.1 Signal generation and detection

The design of a detector (sensor and readout electronics) is strongly connected to the way the signal is generated in the detector material (e.g. semiconductor). The most important process for signal generation in semiconductor detectors is the energy loss by ionisation. The movement of charge carriers induces a signal which can be further processed by the readout electronics.

For high-rate environments, fast signal processing is essential and requires fast charge collection.

In this section, the interaction of charged particles and photons with matter is discussed (signal generation). Furthermore, the detection principle of semiconductor detectors (pn-junction) is presented. The section concludes with a description of the charge carrier movement in silicon and the resulting signal formation at the readout electrodes. A comprehensive discussion of these topics can be found in [KW20; Spi05; SN06; Zyl+20].

3.1.1 Energy loss of charged particles and photons

Charged particles interact in many single collisions with the atoms of the penetrated medium leading to ionisation and excitation of the atoms [Zyl+20; KW20]. The energy loss W in a single collision is often small ($< 100\,\mathrm{eV}$) [Zyl+20], and fluctuates. The mean energy loss (per length) of relativistic charged heavy[1] particles is described by the "Bethe equation" [Zyl+20]

$$-\left\langle \frac{\mathrm{d}E}{\mathrm{d}x} \right\rangle = K \frac{Z}{A} \frac{z^2}{\beta^2} \left[\frac{1}{2} \ln \left(\frac{2 m_e c^2 \beta^2 \gamma^2 W_{\max}}{I^2} \right) - \beta^2 - \frac{\delta(\beta\gamma)}{2} \right], \tag{3.1}$$

with:

- $K = 4\pi N_A r_e^2 m_e c^2 = 0.307\,\mathrm{MeV\,cm^2\,mol^{-1}}$ [KW20], where r_e is the classical electron radius and m_e the electron mass
- z, β being the charge and velocity of the penetrating particle
- Z, A being the atomic number and atomic mass number of the penetrated medium
- $W_{\max} = \frac{2 m_e c^2 \beta^2 \gamma^2}{1 + 2\gamma m_e/M + (m_e/M)^2}$ being the maximum energy transfer in a single collision
- I being the mean excitation energy of the penetrated medium, $I = 173\,\mathrm{eV}$ in Si [Zyl+20]
- $\delta(\beta\gamma)$ being the density correction factor

Eq. 3.1 is valid for $0.1 \lesssim \beta\gamma \lesssim 1000$ with an error of a few percent [Zyl+20]. Often, the energy loss is called *stopping power* as particles are stopped due to their energy loss in the medium. Typical units of the stopping power are $\mathrm{MeV\,cm^2/g}$ which is independent of the density ρ of the medium.

For low energies, the term $1/\beta^2$ dominates and the mean energy loss decreases with $1/\beta^2$. At $\beta\gamma \approx 3-3.5$ the mean energy loss is minimal. A particle with an energy around this minimum is called *minimum ionising particle* (MIP). Within this thesis, particles with $\beta\gamma > 3.5$ are also considered as MIPs. With increasing energy the logarithmic term starts to dominate and the energy loss increases. The reasons for this are twofold: First, the maximum energy transfer $W_{\max}$ increases with increasing $\beta\gamma$. Second, the transverse electric field (perpendicular

[1] Particles with a mass larger than the electron mass are considered as "heavy".

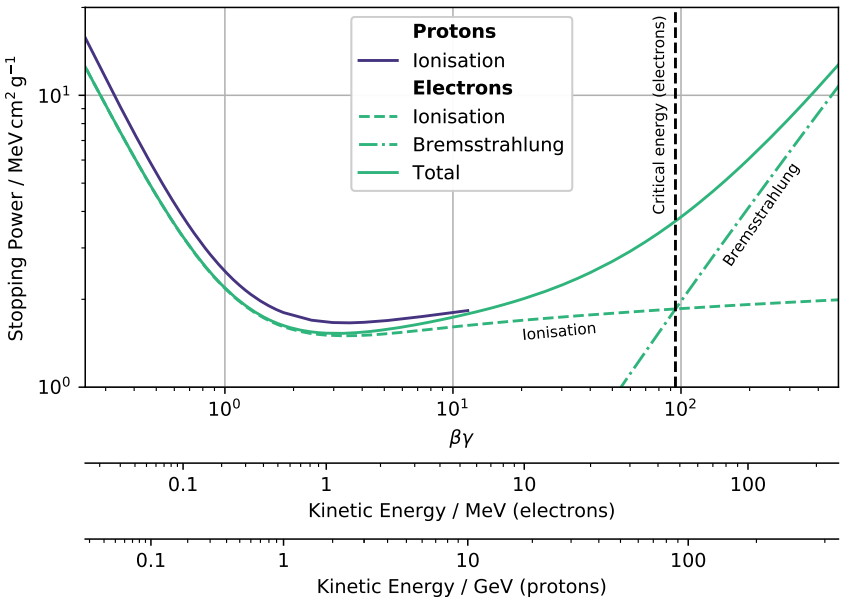

Figure 3.1: Mean energy loss of protons and electrons in silicon as a function of $\beta\gamma$. The different contributions to the energy loss of electrons are indicated. The critical energy for which the energy loss by bremsstrahlung and ionisation is the same is illustrated by the black dashed line. For protons only the dominating energy loss by ionisation is shown. The axes on the bottom show the kinetic energies for protons and electrons, respectively. Values were derived from the programs ESTAR and PSTAR [Ber+05].

to particle direction) of the particle becomes larger with increasing energy due to relativistic effects, and is responsible for the explicit $\beta^2\gamma^2$ dependence of the logarithmic term in Eq. 3.1. However, the particle polarises the medium which leads to a decrease of the logarithmic rise at high energies. This effect is described by the density-effect correction term $\delta(\beta\gamma)$ and is parametrised for different energy regions [SBS84]:

$$\delta(\beta\gamma) = \begin{cases} 2\zeta \ln 10 + C_D & \text{for} \quad \zeta \geq \zeta_1 \,, \\ 2\zeta \ln 10 + C_D + a(\zeta_1 - \zeta)^k & \text{for} \quad \zeta_0 \leq \zeta < \zeta_1 \,, \\ \delta_0 10^{2(\zeta - \zeta_0)} & \text{for} \quad \zeta < \zeta_0 \,, \end{cases} \tag{3.2}$$

with $C_D = 2\ln(\hbar\omega_p/I) - 1 = -4.4351$ [SBS84] for silicon and $\zeta = \log(\beta\gamma)$.

The energy loss of electrons by ionisation differs from that of heavy charged particles due to their kinematics ($m_e \ll M_{\text{nucleus}}$), spin and indistinguishability (electron-electron collisions). A comprehensive discussion of collision loss of electrons can be found in [SB82]. The mean energy loss for protons (only ionisation) and electrons in silicon is shown in Fig. 3.1. Values

are obtained from the programs ESTAR and PSTAR [Ber+05]. Besides ionisation, charged particles also lose energy by bremsstrahlung [KW20] which describes the emission of a photon via interaction of the charged particle with the Coulomb field of the nucleus. The energy loss via bremsstrahlung is proportional to E/m^2 [Jac98], whereas the energy loss by ionisation is logarithmically proportional to the energy (see Eq. 3.1). Therefore, bremsstrahlung is largely suppressed for heavy charged particles. In contrast to that, even at relatively low energies (a few tens of MeV) [Zyl+20], electrons mainly lose energy via bremsstrahlung, as visible in Fig. 3.1. For $\beta\gamma \gtrsim 100$, the energy loss of electrons is dominated by bremsstrahlung. A detailed discussion of bremsstrahlung is found in [KW20].

The point at which the energy loss by ionisation and bremsstrahlung is the same is defined as the *critical energy* E_c [Zyl+20], as illustrated in Fig. 3.1 (black dashed line). The critical energy of electrons and muons in silicon is [Zyl+20]

$$E_c(\text{muons}) = 582\,\text{GeV} \tag{3.3}$$

$$E_c(\text{electrons}) = 40.19\,\text{MeV}\,. \tag{3.4}$$

The characteristic distance traversed by high-energy electrons in matter is called *radiation length* X_0. It is the mean distance over which an electron loses all but $1/e$ ($\approx 37\,\%$) of its total energy by bremsstrahlung [Zyl+20]. The thickness x of a particle detector is often expressed as a fraction of the radiation length, since interactions of particles with matter (e.g. multiple scattering, see Sec. 3.1.2) affecting the detector performance depend on the radiation length. The fraction x/X_0 is called *material budget*. The radiation length in silicon is $X_0^{\text{Si}} = 21.82\,\text{g/cm}^2$ corresponding to a distance of 9.370 cm using a density $\rho_{\text{Si}} = 2.329\,\text{g/cm}^3$ of silicon [Zyl+20].

For large energy transfers $W \gg I$, so-called *high-energy knock-on electrons* (δ-electrons) are produced from collisions with the shell electrons [KW20]. The distribution of the emission angle of δ-electrons has a maximum at $\theta = 90°$ corresponding to a small kinetic energy of the δ-electron ($\mathcal{O}$(keV)) [KW20]. According to Eq. 3.1, this is in the $1/\beta^2$ regime leading to a high ionisation-density path. If the broad ionisation path cannot be resolved, δ-electrons can deteriorate the spatial resolution. Further, energetic δ-electrons can leave (thin) detector layers without contributing to the *deposited energy* in a detector. In addition, photons from bremsstrahlung can escape the detector volume due to their small absorption probability (see Sec. 3.1.1) in thin detectors and consequently also do not contribute to the deposited energy in a detector. It is therefore useful to restrict the maximum energy transfer to $W_{\text{cut}} < W_{\text{max}}$. The *restricted energy loss* which only considers energy transfers up to W_{cut} is expressed as [Zyl+20]

$$-\left.\frac{\mathrm{d}E}{\mathrm{d}x}\right|_{W<W_{\text{cut}}} = K\frac{Z}{A}\frac{z^2}{\beta^2}\left[\frac{1}{2}\ln\left(\frac{2m_e c^2\beta^2\gamma^2 W_{\text{cut}}}{I^2}\right) - \frac{\beta^2}{2}\left(1+\frac{W_{\text{cut}}}{W_{\text{max}}}\right) - \frac{\delta(\beta\gamma)}{2}\right]. \tag{3.5}$$

The restricted energy loss approaches a constant ("Fermi plateau") for high $\beta\gamma$ [Zyl+20].

For the reasons explained above, mainly ionisation contributes to the deposited energy in (thin) silicon detectors. Therefore, MIPs represent a "worst-case scenario" (minimal signal) and are used for the characterisation of silicon pixel detectors presented in Chapter 6.

Fluctuations in energy loss

The total energy loss over a distance fluctuates as the number of collisions (Poissonian distributed) and the energy transfer in a single collision fluctuate. Single (but rare) high-energy transfers (δ-electrons) lead to an asymmetric shape of the total energy loss fluctuations. The mean of this distribution is given by the "Bethe equation" (Eq. 3.1). Often, detectors cannot measure the complete tail of the energy loss distribution due to particles escaping the sensitive volume (see above) which strongly influences the measured mean energy loss. A more useful parameter to characterise the energy loss is the most probable value which is independent of the long tail of the energy loss distribution. The energy loss distribution is described by a Landau-Vavilov distribution [Vav57; Lan44] for detectors with moderate thickness[2] [Zyl+20]. The most probable value for a detector with a thickness x is given by [Bic88]

$$\Delta_p = \xi \left[\ln \left(\frac{2 m_e c^2 \beta^2 \gamma^2}{I} \right) + \ln \frac{\xi}{I} + j - \beta^2 - \delta(\beta\gamma) \right] , \tag{3.6}$$

with $j = 0.2$ [Zyl+20] and

$$\xi = \frac{1}{2} K \frac{Z}{A} \rho \frac{z^2}{\beta^2} x \, . \tag{3.7}$$

The most probable value Δ_p / x per thickness depends logarithmically on the detector thickness, whereas the mean energy loss is independent of the detector thickness. For thin detectors, the Landau distribution fails to describe the energy loss fluctuations, since the distributions are significantly wider than the Landau width $w = 4\xi$ [Bic88]. Nevertheless, Eq. 3.6 is still valid for thin detectors. For thick detectors, the energy loss distribution is less asymmetric but never approaches a Gaussian function [Zyl+20]. From a simulation using GEANT4 [Ago+03] a most probable energy loss of approximately 270 eV/µm is extracted for MIPs in a 100 µm thin silicon detector.

An example of a Landau distribution calculated using the Python package *pylandau* [Poh] can be seen in Fig. 3.2. The most probable value is the point at which the Landau function reaches its maximum. The mean value is significantly larger than the most probable value due to the asymmetric shape of the Landau distribution.

Often, a convolution of a Gaussian and a Landau function (Langau) is used to describe the measured energy deposition of MIPs in silicon pixel detectors as presented in Chapter 6. This convolution describes sufficiently well the measured spectra. The most probable value is used to estimate the amount of collected charge in silicon pixel detectors.

[2] Moderate thicknesses means $\kappa = \frac{\xi}{W_{\max}} \lesssim 0.05 - 0.1$ with ξ defined by Eq. 3.7.

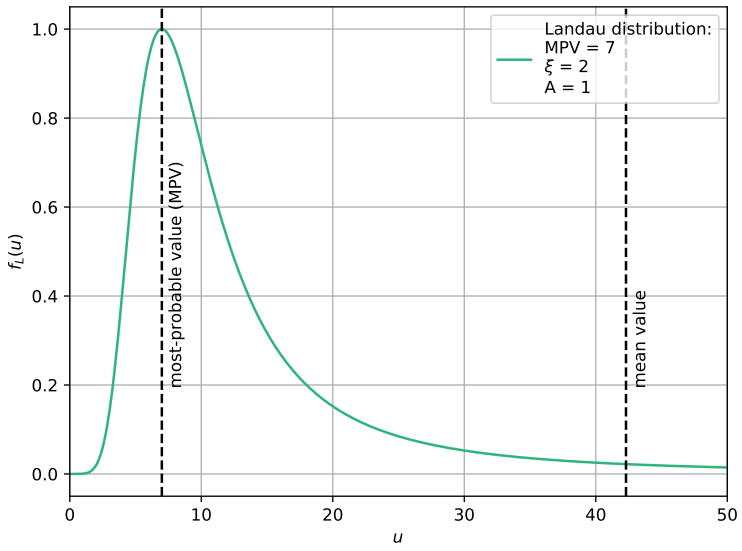

Figure 3.2: Example of a Landau distribution calculated using *pylandau* [Poh]. The most probable and mean values are indicated. The mean (numerically calculated) is significantly larger than the most probable value due to the asymmetric shape of the Landau distribution.

Energy loss of photons

The energy loss of photons differs significantly from that of charged particles. For charged particles, the energy loss in matter leads to a finite, well defined range corresponding to the radiation length X_0. In contrast to that, for photons an absorption probability exists which is described by the Lambert-Beer law [KW20]

$$I(x) = I_0 e^{-\mu x} \,. \tag{3.8}$$

The intensity $I(x)$ of a photon beam with initial intensity I_0 decreases exponentially with the penetration depth x. The coefficient μ is called *absorption coefficient* and the reciprocal [KW20]

$$\lambda = \frac{1}{\mu} = \frac{1}{n\sigma} \tag{3.9}$$

is called the *absorption length* or mean free path with $n = \rho\frac{N_A}{A}$ being the target density and σ the total cross section. The absorption coefficient for photons in silicon as a function of the photon energy is depicted in Fig. 3.3. The contributions of the different processes relevant[3] for particle detectors are shown. A comprehensive discussion of interactions of photons with matter can be found in [KW20]. In the following, the relevant photon interaction processes are

[3] Relevant processes refers to processes with detectable energy transfer.

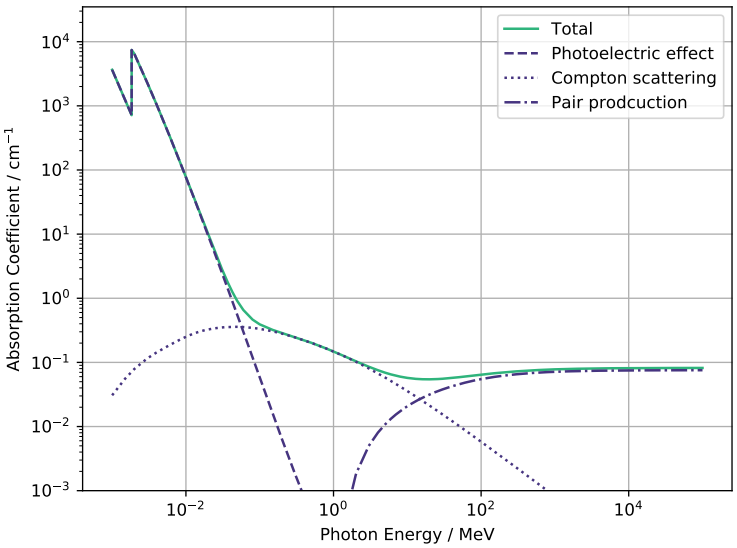

Figure 3.3: Absorption coefficient for photons in silicon as a function of photon energy. Different contributions to the total absorption coefficient are indicated. Values from [Ber+10].

briefly summarised [KW20]:

- **Photoelectric effect**: Photons interacting via the photoelectric effect transfer their complete energy to an atom (fully absorbed) resulting in an emission of an electron (ionisation of atom), in case the photon energy exceeds the binding energy of the electron. The kinetic energy of the emitted electron is the energy of the photon subtracted by the binding energy of the shell electron. The photoelectric effect is the dominant process in the keV regime. The cross section of the photoelectric effect decreases rapidly with increasing photon energy and strongly increases with increasing Z of the traversed medium (at fixed photon energy). Jumps in the cross section are created when the photon energy exceeds the binding energy of an inner shell (absorption edges). The created vacancy by the photoelectric effect inside a shell of an atom can be filled by an electron from an outer shell. This leads to the emission of a photon[4] (X-ray fluorescence) with discrete energy corresponding to the difference of the two energy levels (X-ray transition). Every element has different energy levels resulting in characteristic X-ray fluorescence of each element. The observed X-ray fluorescence peaks are called *characteristic lines*. As the energy of these sharply defined characteristic lines is known, X-ray fluorescence with different elements is used for the calibration of pixel detectors as presented in Sec. 6.3.2. The absorption length for photons interacting via the photoelectric effect in silicon is shown in Fig. 3.4.

[4] Instead of the emission of a photon, an electron (Auger-electron) can be emitted which is, however, suppressed for high-Z materials.

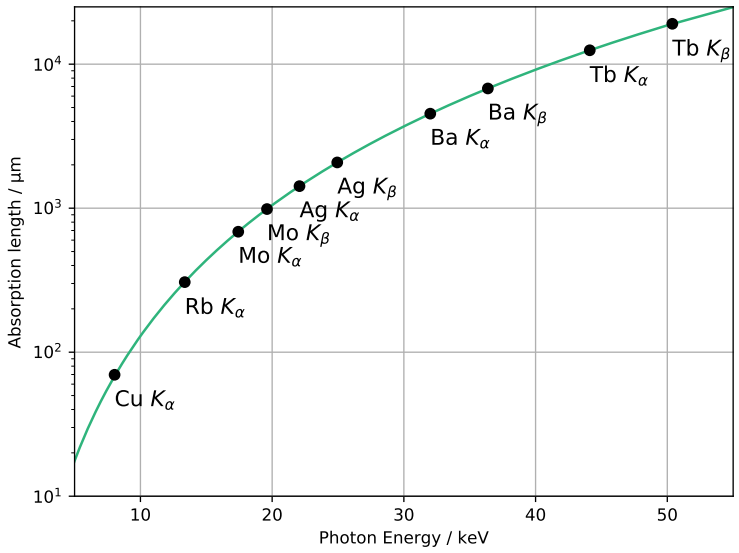

Figure 3.4: Absorption length for photons interacting via the photoelectric effect in silicon as a function of the photon energy. Elements used for detector calibration are indicated. Values from [Ber+10].

The various elements used for detector calibration are indicated. The energy deposition of low energy photons takes place close to the surface of the sensor. The absorption of photons, and therefore their detection, is suppressed towards higher photon energies.

- **Compton scattering**: Compton scattering describes the scattering of a photon off an electron[5] which is thereby kicked out of the atom. This elastic scattering transfers the kinetic energy $T = E_\gamma - E'_\gamma$ (recoil energy) to the electron. The energy E'_γ of the scattered photon is given by [KW20]

$$E'_\gamma = \frac{E_\gamma}{1 + \frac{E_\gamma}{m_e c^2}\,(1 - \cos\theta_\gamma)}\,, \tag{3.10}$$

with E_γ being the initial energy (before scattering) of the photon and θ_γ the angle between the direction of the incoming photon and the scattered photon. The recoil energy of the electron is maximal for $\theta = 180°$ leading to the so-called *Compton edge*. Since the scattered photon is not necessarily absorbed in the detector layer, the Compton spectrum is continuous which is known as the *Compton continuum*. Compton scattering is the dominant process for photon energies around 1 MeV.

- **Pair production**: Pair production is the conversion of a photon to an electron-positron

[5] The electron is considered to be "quasi-free", i.e. the photon energy is much larger than the binding energy.

pair in the Coulomb field of a nucleus. Due to energy conservation the energy of the photon has to be larger than twice the electron mass (plus the recoil energy transferred to the nucleus). The cross section for pair production in the high-energy approximation is given by [KW20]

$$\sigma_{\text{pair}} \approx \frac{7}{9}\frac{1}{X_0}\frac{A}{N_A \rho}\,. \tag{3.11}$$

Characteristic is the dependence on the radiation length X_0. Pair production is the dominant process for photon energies larger than 10 MeV.

3.1.2 Multiple Coulomb scattering

Besides the energy loss of charged particles when penetrating a medium, charged particles scatter multiple times randomly (stochastic process) in the Coulomb field of the nuclei. This results in a statistical distribution of the total scattering angle after traversing a given distance. The effect is known as *multiple scattering* and is described by the Rutherford cross section [KW20]

$$\left.\frac{\mathrm{d}\sigma}{\mathrm{d}\Omega}\right|_{\text{Rutherford}} = \left(\frac{zZ\alpha\hbar}{\beta p}\right)^2 \frac{1}{4\sin^4\frac{\theta}{2}}\,, \tag{3.12}$$

with θ being the scattering angle, z, β, p the charge, velocity and momentum of the scattered particle and Z the charge of the nucleus. The distribution of the scattering angle is described by a Molière distribution [Mol47]. For most applications the number of scatterings in the traversed medium is large enough and the scattering angles are small ($\mathcal{O}$(mrad)) such that the distribution can be approximated with a Gaussian distribution due to the central limit theorem. However, the Gaussian distribution deviates from the Molière distribution especially at the tails towards large, but rare, scattering angles for which the probability is higher in case of the exact Molière distribution. Displacements due to multiple scattering are neglected in thin detectors. In the approximation of Gaussian distributed scattering angles, the distribution can be parametrised using the standard deviation given by [LD91]

$$\theta_{\text{MS}} = \frac{13.6}{\beta c p} z \sqrt{\frac{x}{X_0}} \left[1 + 0.038 \ln\left(\frac{x}{X_0}\right)\right]\,, \tag{3.13}$$

with z, β, p being the charge, velocity and momentum (in MeV) of the scattered particle, x the traversed material thickness and X_0 the radiation length. Characteristic is the dependence on the material budget x/X_0 and the particle momentum p. To achieve high spatial resolution, the influence of multiple scattering should be minimised (small θ_{MS}). Therefore, silicon tracking detectors are as thin as possible and contributions of materials with small radiation length (high Z and ρ) are avoided inside the detector. To minimise the effect of multiple scattering for the characterisation of pixel detectors presented in Chapter 6 high energy (large p) particle beams are used.

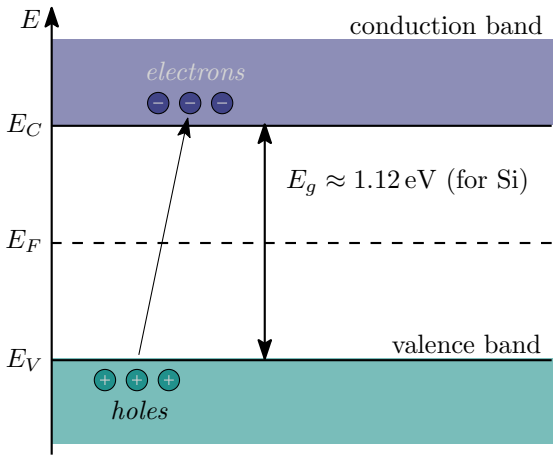

Figure 3.5: Simplified energy-band structure of an intrinsic (un-doped) semiconductor (Si as an example). Thermal excitation can overcome the energy gap separating the valence and conduction band. As a result, electrons are lifted up into the conduction band and holes remain in the valence band. The Fermi energy level E_F lies (approximately) in the middle of the energy gap. Based on [SN06].

The parametrisation shown in Eq. 3.13 is used to describe multiple scattering in detector layers for track reconstruction. In Sec. 5.1 the application of a Kalman Filter for track reconstruction using pixel detectors is presented. Since multiple scattering is a *Markov process* [Frü+00], i.e. the future of a state only depends on its actual state and not on the previous ones [Jaz13], multiple scattering in each detector layer can be described independently. This property is utilised within the track reconstruction using a Kalman Filter.

3.1.3 Charge carriers in silicon

Silicon is a semiconductor and its atoms are arranged in a "diamond" lattice structure [KW20]. The energy levels of individual atoms are energetically so dense ($\mathcal{O}$(meV)) that they can be combined in so-called *energy bands*. The two highest not fully occupied energy bands are called *valence band* and *conduction band*. These two bands are separated by a *bandgap* which forms a region of "forbidden" energy states. The energy band structure of silicon is depicted in Fig. 3.5. Thermal excitation or external energy transfer (e.g. by ionisation of charged particles) can overcome the bandgap and an electron is lifted into the conduction band, whereas a hole remains in the valence band. Freely moving negative charge carriers (electrons) in the conduction band and freely moving positive charge carriers (holes[6]) in the valence band contribute to conductivity in a semiconductor. In silicon, the energy gap is $E_g = 1.12\,\text{eV}$ [KW20] at room temperature. A slight dependence of the energy gap with temperature is observed [AFW96]. The generation of

[6]Holes are not considered as "real" particles, but as positive charge carriers with an effective mass.

electron-hole pairs (e/h-pairs) in silicon requires additional momentum transfer to the lattice (indirect bandgap) [SN06].

As only not fully occupied energy bands contribute to conductivity, the conduction properties of semiconductors strongly depend on the charge carrier density in the energy bands and it is sufficient to consider only the valence and conduction band. The number of electrons, i.e. occupied levels in the conduction band, is given by the density of (allowed) states $N(E)$ multiplied with the occupation probability $f(E)$ integrated over the energies of the conduction band [SN06]

$$n = \int_{E_C}^{\infty} N(E) f(E)\,\mathrm{d}E\,. \tag{3.14}$$

The electrons (in the conduction band) and holes (in the valence band) are spin-1/2 particles, and therefore follow the Fermi-Dirac statistics given by [SN06]

$$f(E) = \frac{1}{1+\exp\left(\frac{E-E_F}{k_B T}\right)}\,, \tag{3.15}$$

with E_F being the Fermi energy, T the temperature and k_B the Boltzmann constant. At the Fermi energy the occupation probability is 50 % [SN06]. The Fermi energy generally lies close to the middle of the bandgap for intrinsic (un-doped semiconductors), as shown in Fig. 3.5. Using $n = p = n_i$ (mass-action law) valid in thermal equilibrium[7] the evaluation of Eq. 3.14 yields the intrinsic charge carrier density [SN06]

$$n_i = \sqrt{N_C N_V}\exp\left(-\frac{E_g}{2k_B T}\right) \approx 1.01\times 10^{10}\,\mathrm{cm}^{-3} \qquad (\text{for Si at } 300\,\mathrm{K})\,. \tag{3.16}$$

N_C and N_V are the effective densities of states in the conduction and valence band, respectively. Remarkable is the exponential temperature dependence[8] of the charge carrier density (Eq. 3.16) changing the conductivity of semiconductors strongly with temperature. The conductivity in semiconductors with both electrons and holes as charge carriers (intrinsic semiconductor) in given by [SN06]

$$\sigma_i = \frac{1}{\rho_i} = q\left(\mu_e n + \mu_h p\right) = q n_i\left(\mu_e + \mu_h\right)\,, \tag{3.17}$$

with ρ_i being the intrinsic resistivity of the semiconductor and μ_e and μ_h the mobilities of electrons and holes in the semiconductor (see Sec. 3.1.5). At absolute zero ($T = 0\,\mathrm{K}$) a semiconductor is non-conductive.

Charged particles penetrating a semiconductor create e/h-pairs due to energy loss by ionisa-

[7] In thermal equilibrium the excitation of electrons into the conduction band is balanced by recombination of electrons in the conduction band with holes in the valence band resulting in equal amount of charge carriers $n = p = n_i$.

[8] N_C and N_V also show a temperature dependence ($\sim T^{3/2}$) which is however negligible with respect to the exponential temperature dependence shown in Eq. 3.16.

tion. In silicon, the average energy to create an e/h-pair is [Sch+00]

$$w_i = 3.65\,\text{eV}\,. \tag{3.18}$$

Assuming a detector with thickness $d = 150\,\mu\text{m}$ and surface $A = 1\,\text{cm}^2$ results in

$$N_{\text{ionisation}} = \frac{\mathrm{d}E/\mathrm{d}x|_{\text{MPV}} \cdot d}{w_i} \approx 1.1 \times 10^4\,\text{e/h} - \text{pairs}\,, \tag{3.19}$$

with $\mathrm{d}E/\mathrm{d}x|_{\text{MPV}} \approx 270\,\text{eV}/\mu\text{m}$ (Sec. 3.1.1). The number of intrinsic charge carriers in silicon is

$$N_{\text{intrinsic}} = n_i \cdot d \cdot A \approx 1.5 \times 10^8\,\text{e/h} - \text{pairs}\,. \tag{3.20}$$

That is four orders of magnitude larger than the number of charge carriers created by ionising particles rendering intrinsic silicon unsuitable for particle detection (at room temperature). To utilise silicon for particle detection (at room temperature) it is necessary to remove the intrinsic charge carriers such that the charge carrier generation by ionising particles dominates. This is achieved by doping the semiconductor allowing the formation of a pn-junction that can be used for particle detection. The pn-junction is discussed in the following section.

3.1.4 The pn-junction as a particle detector

An important property of semiconductors is that their conductivity can be changed by intentional introduction of impurity atoms. This process is termed *doping* of semiconductors. Tetravalent semiconductors like silicon can be doped by pentavalent elements (P, As, Sb), so-called *donors*, creating an excess of electrons as charge carriers. This type of semiconductor is called *n-doped* semiconductor. Doping with trivalent elements (B, Al, Ga), so-called *acceptors*, creates an excess of holes as charge carriers. This type of semiconductor is called *p-doped* semiconductor. Doping changes the energy-band structure of a semiconductor. In n-doped semiconductors an additional donor level (E_D) is introduced which lies just below the conduction band. Conversely, in p-doped semiconductors an additional acceptor level (E_A) is introduced which lies just above the valence band. The differences between the introduced energy levels and the valence or conduction band are a few $10^{-2}\,\text{eV}$ [KW20]. Due to the small distance of the energy levels the atoms in the p- and n-doped semiconductor are (almost) fully ionised at room temperature. Using Eq. 3.17 the resistivity of doped semiconductors with doping concentrations N_A (of acceptors) and N_D (of donors) is then given by

$$\rho_{\text{p-doped}} = \frac{1}{q \cdot \mu_h \cdot p}\,, \tag{3.21}$$

$$\rho_{\text{n-doped}} = \frac{1}{q \cdot \mu_e \cdot n}\,, \tag{3.22}$$

with $p = N_A - N_D \approx N_A$ being the hole concentration in p-doped materials ($N_A \gg n_i \gg N_D$) and $n = N_D - N_A \approx N_D$ being the electron concentration in n-doped materials ($N_D \gg n_i \gg N_A$), also referred to as *majority* charge carrier concentrations. The *minority* charge carrier concentrations $n_p \approx \frac{n_i^2}{N_A}$ (electron concentration in p-doped material) and $p_n \approx \frac{n_i^2}{N_D}$ (hole concentration in n-doped material) are much smaller.

If a p-doped and an n-doped semiconductor are brought into contact, a so-called *pn-junction* is formed. The pn-junction is the basic principle for particle detection with semiconductors. Silicon is the most widely used material for particle detectors. A simplified view of a pn-junction with the assumption of an abrupt junction is illustrated in Fig. 3.6. In the p-doped part holes are the majority charge carriers, whereas in the n-doped part electrons are the majority charge carriers. The strong gradient in charge carrier density leads to a diffusion current I_{diff} causing a diffusion of holes from the p-doped part towards the n-doped part and vice versa for electrons. At the boundary, the charge carriers recombine and a zone free of charge carriers is created, called *depletion zone*. The atoms in the depletion zone remain ionised which causes a negative space-charge region in the p-doped part and a positive space-charge region in the n-doped part. The opposite space-charge leads to an electrical field causing a drift current I_{drift} opposite to the diffusion current and consequently an equilibrium state is reached (without external electrical field). The resulting *build-in voltage* is $V_{bi} \approx 0.6\,\text{V}$ [KW20] in silicon.

The space-charge density in thermal equilibrium is [KW20]

$$\rho(x) = \begin{cases} -eN_A & \text{for} \quad -x_p < x < 0\,, \\ eN_D & \text{for} \quad 0 < x < x_n\,, \end{cases} \tag{3.23}$$

with N_D and N_A being the doping concentration of the p-doped and n-doped part. Typically, one part of the junction has a much larger doping concentration than the other part (here: $N_D \gg N_A$). Due to the (overall) charge-neutrality of the semiconductor [KW20]

$$x_p N_A = x_n N_D \tag{3.24}$$

holds, and therefore the depletion zone extends further into the more weakly doped part (here p-doped part). Using Maxwell's equation the electrical field is

$$E(x) = \begin{cases} \frac{-eN_A}{\epsilon\epsilon_0}(x + x_p) & \text{for} \quad -x_p < x < 0\,, \\ \frac{eN_D}{\epsilon\epsilon_0}(x - x_n) & \text{for} \quad 0 < x < x_n\,. \end{cases} \tag{3.25}$$

The electrical field drops to zero at x_n and x_p, respectively, since the space-charge is zero outside

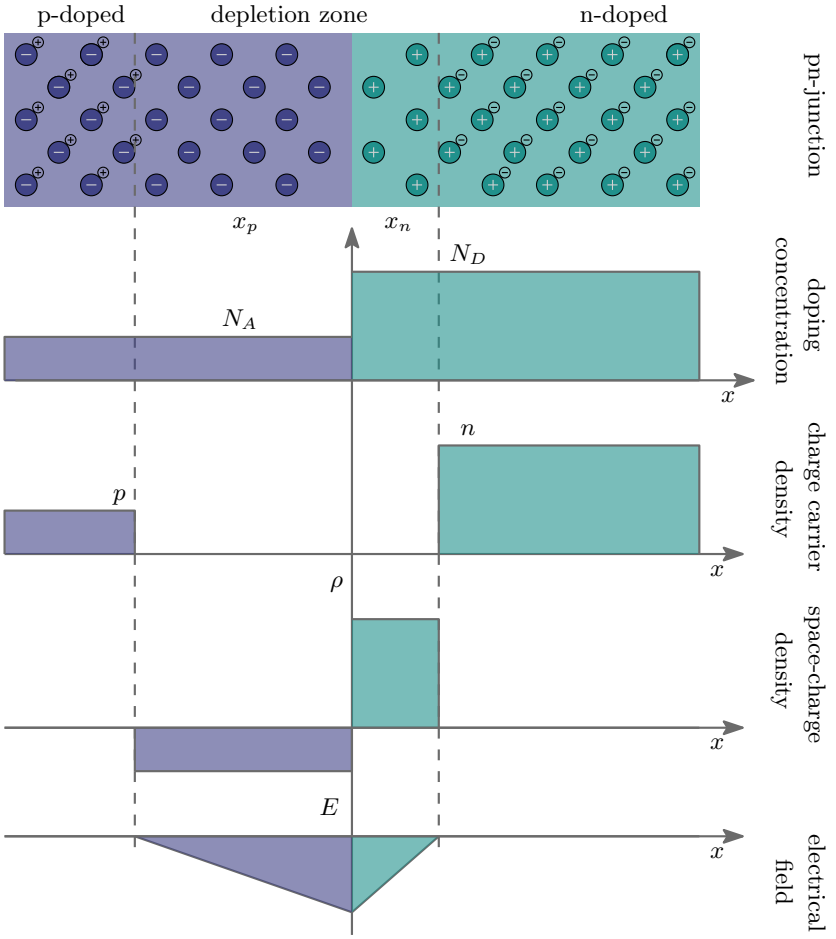

Figure 3.6: Simplified view of a pn-junction with doping concentrations N_A and N_D. The p-doped part is coloured in blue and the n-doped part is coloured in green. At the boundary of the pn-junction a depletion zone is formed. Charge carrier density, space-charge density and electrical field are depicted. Adapted from [KW20].

the depletion zone. The depths x_n and x_p are given by

$$x_n = \sqrt{\frac{2\epsilon\epsilon_0}{e} V_{bi} \frac{N_A}{N_D\,(N_D + N_A)}}\,, \tag{3.26}$$

$$x_p = \sqrt{\frac{2\epsilon\epsilon_0}{e} V_{bi} \frac{N_D}{N_A\,(N_D + N_A)}}\,. \tag{3.27}$$

As mentioned above, the doping concentrations N_A and N_D differ by many orders of magnitude. To realise an n-in-p sensor, the n-doped part as the *charge collecting electrode* is strongly doped ($N_D > 1 \times 10^{18}/\mathrm{cm}^3$) and the p-doped part as the *bulk* is weakly doped ($N_A \approx 1 \times 10^{12}/\mathrm{cm}^3$). In this way, a good ohmic contact between the readout electrode and the readout electronics (connected with metal layers) is achieved, whereas a high-resistivity (a few $\mathrm{k}\Omega\,\mathrm{cm}$) bulk, into which the depletion zone grows, is formed (see Eq. 3.21). Finally, the width of the depletion zone as a function of the *effective doping concentration* $N_{\mathrm{eff}} = N_D - N_A$ (doping concentration of the bulk) is given by

$$d = x_n + x_p \approx x_p \approx \sqrt{\frac{2\epsilon\epsilon_0}{eN_{\mathrm{eff}}} V_{bi}}\,. \tag{3.28}$$

Using $V_{bi} \approx 0.6\,\mathrm{V}$ and typical bulk doping concentrations of $N_{\mathrm{eff}} \approx 1 \times 10^{12}/\mathrm{cm}^3$ the depletion zone is a few µm wide. Since the collected charge (deposited energy) is proportional to the width of the depletion zone, the charge signal due to the build-in potential is not large enough for particle detection. To extend the depletion zone up to typical detector thicknesses of $100\,\mu\mathrm{m} - 200\,\mu\mathrm{m}$ an external voltage is required. Applying the voltage in reverse direction (negative potential at p-doped part and positive potential at n-doped part) the width d of the depletion zone grows according to

$$d \approx \sqrt{\frac{2\epsilon\epsilon_0}{eN_{\mathrm{eff}}} \left(V_{bi} + V_{\mathrm{bias}}\right)}\,, \tag{3.29}$$

with V_{bias} being the reversely applied external voltage called *bias voltage*. Expressing the width of the depletion zone as a function of the bulk resistivity ρ_{bulk} yields ($V_{\mathrm{bias}} \gg V_{bi}$)

$$d\,[\mu\mathrm{m}] \approx 0.3\sqrt{V_{\mathrm{bias}}\,[\mathrm{V}] \cdot \rho_{\mathrm{bulk}}\,[\Omega\,\mathrm{cm}]}\,, \tag{3.30}$$

for p-typed bulks. With typical bulk resistivities of $\rho_{\mathrm{bulk}} \approx 7\,\mathrm{k}\Omega\,\mathrm{cm}$ a bias voltage of $V_{\mathrm{bias}} < 35\,\mathrm{V}$ is required to deplete a 150 µm thin detector. The voltage for which the depletion zone extends over the entire detector thickness d_{det} is called *full depletion voltage* and is proportional to the effective doping concentration

$$V_{\mathrm{dep}} = \frac{e \cdot d_{\mathrm{det}}^2}{2\epsilon\epsilon_0} \cdot N_{\mathrm{eff}}\,. \tag{3.31}$$

Usually, silicon detectors are operated *over-depleted*, i.e. $V_{\mathrm{bias}} > V_{\mathrm{dep}}$ to increase the electrical

field which decreases charge collection times (see Sec. 3.1.6). Eq. 3.30 is used to study the charge collection behaviour of silicon pixel sensors, as presented in Sec. 6.7.6.

Due to the charge carrier free zone the pn-junction can be viewed as a parallel plate capacitor filled with a dielectric ϵ and with capacitance [KW20]

$$C_{\text{plate}} = \frac{\epsilon\epsilon_0}{d} A \,, \tag{3.32}$$

with thickness d and area A. Since the width of the depletion zone depends on the applied voltage (see Eq. 3.29), the capacitance of a pn-junction per unit area ($A = 1$) is given by

$$C_{\text{pn-junction}}(V) = \begin{cases} \sqrt{\frac{eN_{\text{eff}}\epsilon\epsilon_0}{2V_{\text{bias}}}} & \text{for} \quad V_{\text{bias}} \leq V_{\text{dep}} \,, \\ \frac{\epsilon\epsilon_0}{d_{\text{max}}} & \text{for} \quad V_{\text{bias}} > V_{\text{dep}} \,. \end{cases} \tag{3.33}$$

Before the pn-junction is fully depleted the capacitance decreases with increasing bias voltage and saturates after full depletion. The parallel plate capacitor model can also be applied (with some limitations) to a pixel sensor. From Eq. 3.33, it is visible that the capacitance depends on the geometry of the pixels and the doping concentration. A measurement of the capacitance as a function of the bias voltage (CV-curve) allows for a determination of the depletion voltage, as presented in Sec. 6.7.2.

3.1.5 Movement of charge carriers in silicon

The charge carrier movement in semiconductors is described by the Boltzmann transport equation [KW20]. It is assumed that electrons and holes move freely by introducing "effective masses" for both charge carriers. The movement is composed of a drift (in case of an electrical field) and a diffusion movement.

The acceleration of charge carriers due to the electrical field E is compensated by collisions with the lattice leading to an equilibrium. This is described by the Drude model [Dru00] and yields in the stationary case (time-independent drift velocity)

$$v_D = \mu(E) E \,, \tag{3.34}$$

with v_D being the drift velocity. The mobility $\mu(E)$ of the charge carriers depends on the electrical field. An empirical ansatz yields [CT67]

$$\mu(E) = \frac{\mu_0}{\left[1 + \left(\frac{\mu_0 E}{v_{\text{sat}}}\right)\right]^{1/\beta}} \,, \tag{3.35}$$

with μ_0 being the *low-field mobility*, v_{sat} the saturation drift velocity and β an empirically calculated number (different for electrons and holes). For explicit values see [Ros+06]. The

mobility of electrons in silicon is constant for $E \lesssim 5000\,\mathrm{V/cm}$ [Ros+06], but decreases for higher electrical fields. Typical values for the low-field mobility for electrons and holes in silicon (at room temperature) are [KW20]

$$\mu_e = 1450\,\mathrm{cm^2/(V\,s)}\,, \qquad \mu_h = 500\,\mathrm{cm^2/(V\,s)}\,. \tag{3.36}$$

The mobility of electrons is approximately three times higher than the mobility of holes which are more susceptible to trapping, especially after irradiation (see Sec. 3.2). Due to the dependency of the mobility on the electrical field strength, the drift velocity increases with increasing electrical field strength and saturates at $E \gtrsim 20\,\mathrm{kV/cm}$ [Jac+77] for electrons in silicon. Typical (average) electrical fields for the ATLAS pixel detectors ($d \approx 150\,\mu\mathrm{m}$) are approximately $5\,\mathrm{kV/cm}$ (80 V operational voltage) at the beginning and approximately $40\,\mathrm{kV/cm}$ (600 V operational voltage) at the end of operation[9].

The diffusion of an ensemble of charge carriers (e.g. created by a MIP) is due to the random thermal motion of the charge carriers. This leads to a charge cloud whose spatial distribution is described by a Gaussian function. The lateral extension of the charge cloud is [KW20]

$$\sigma(t) = \sqrt{2Dt}\,, \tag{3.37}$$

where $D = \frac{k_B T}{e}\mu$ (Einstein relation) is the diffusion coefficient and is related to the charge carrier mobility μ. The charge cloud expands with drift time t (and thus with depth $z(t)$) and has typical dimensions of a few µm in silicon (depending on the bias and depletion voltage) [Poh20].

Typically, the readout electrode of a detector is segmented in two dimensions (*pixel* detector) to obtain a 2-dimensional spatial information from the collected charge of each readout electrode. In pixel detectors, multiple pixels can collect a fraction of the charge signal (depending on the size of the charge cloud and hit position of the particle), an effect known as *charge sharing* (see e.g. [Poh20]). If the shared signal exceeds the threshold of the readout channel this leads to clusters of hits (locally associated pixel hits). The number of hit pixels in a cluster is called *cluster size*. Charge sharing is beneficial for the reconstruction of the cluster position [Spa+18].

The average[10] fraction of charge per pixel for ATLAS ITk sensors ($50 \times 50\,\mu\mathrm{m}^2$ pixels with thicknesses of 100 µm and 150 µm, see Sec. 3.4) is larger than 90 % for slightly over-depleted detectors [Poh20]. Charge sharing effects due to diffusion[11] are therefore assumed to be small for bias voltages much larger than the depletion voltage (typical operation before irradiation). The effect of charge sharing when using single-pixel charge spectra for the calibration of pixel detectors is discussed in Sec. 6.3.2. Charge sharing effects at the pixel corners are visualised in Sec. 6.6.4. Charge sharing and the formation of elongated pixel clusters due to large incidence

[9] The larger operational voltage at the end of operation is necessary due to bulk damage caused during operation of the detector (see Sec. 3.2).

[10] Assuming uniform irradiation within the pixel.

[11] Other mechanisms for charge sharing such as large incidence angles of particles or Lorentz angles due to magnetic fields are not considered here.

angles are discussed in Sec. 6.7.7.

3.1.6 Signal formation by moving charge carriers

Ionising particles traversing a depleted pn-junction deposit energy, and thus create e/h-pairs along the flight path. Due to the electrical field (created by the external bias voltage) the charge carriers are separated and drift (diffusion is neglected here) towards the electrodes. Electrons drift towards the n-doped part and holes drift towards the p-doped part (in reverse bias operation). As soon as the charge carriers move, a signal is induced at the electrodes. The signal can be measured as a current signal or as a charge signal if the current signal is integrated via a capacitance (see Sec. 3.3).

According to the Shockley-Ramo theorem [Sho38; Ram39] the induced signal on electrode i (in a multi-electrode system) by a moving charge q can be calculated using the *weighting potential* $\phi_{w,i}$ or the *weighting field* $\vec{E}_{w,i} = -\vec{\nabla}\phi_{w,i}$

$$i_{S,i} = q\vec{E}_{w,i}\,\vec{v}_D\,, \tag{3.38}$$

$$\mathrm{d}Q_i = -q\vec{E}_{w,i}\,\mathrm{d}\vec{r}, \tag{3.39}$$

with $i_{S,i}$ being the induced current signal and $\mathrm{d}Q_i$ the induced charge signal. The weighting potential obeys the Laplace equation and is calculated by setting the potential of electrode i to 1 and that of all others to 0:

$$\Delta\phi_{w,i}(\vec{r}) = 0 \qquad \text{and} \qquad \phi_{w,i}|_{S_i} = 1,\ \phi_{w,i}|_{S_{i\neq j}} = 0\,. \tag{3.40}$$

The weighting field is defined by the geometry of the multi-electrode system and is independent of stationary space-charge (important when considering depleted pixel detectors) [KW20]. Using Eq. 3.34 the drift velocity can be expressed in terms of the mobility $\mu_{e,h}$ and the electrical field $\vec{E}_d$ in the detector, which yields

$$i_{S,i} = q\mu_{e,h}\vec{E}_{w,i}\cdot\vec{E}_d\,. \tag{3.41}$$

Considering a depleted pn-junction with thickness d (corresponding to an unsegmented detector with two electrodes) the electrical field increases linearly (towards the junction) and is superimposed with a constant component in case of a bias voltage V_{bias} [KW20]

$$\vec{E}_d(x) = -\left(\frac{V_{\mathrm{bias}} + V_{\mathrm{dep}}}{d} - \frac{2V_{\mathrm{dep}}}{d^2}x\right)\vec{e}_x\,, \tag{3.42}$$

with the depletion voltage (Eq. 3.31)

$$V_{\mathrm{dep}} \approx \frac{eN_{\mathrm{eff}}}{2\epsilon\epsilon_0}\,d^2\,. \tag{3.43}$$

The weighting field of this geometry is constant and given by [KW20]

$$\vec{E}_{w,i} = -\frac{1}{d}\,\vec{e}_x\,. \tag{3.44}$$

The mobility can be expressed using the characteristic times for the charge carrier movement [KW20]

$$\tau_{e,h} = \frac{d^2}{2\mu_{e,h}V_{\text{dep}}}\,. \tag{3.45}$$

Finally, the induced current at the positive electrode created by an ionising particle producing N equally distributed e/h-pairs along its flight path is given by [KW20]

$$i_S^e(t) = -\frac{eN}{d^2}\frac{1}{\tau_e}\,\mathrm{e}^{-t/\tau_e}\left[\frac{a}{b}\,x_{\text{max}}^e - \frac{1}{2}\,(x_{\text{max}}^e)^2\right] \qquad \text{for } t < T_{\text{max}}^e\,, \tag{3.46}$$

$$i_S^h(t) = \frac{eN}{d^2}\frac{1}{\tau_h}\,\mathrm{e}^{+t/\tau_h}\left[\frac{a}{b}\,\left(d - x_{\text{min}}^h\right) - \frac{1}{2}\left(d^2 - \left(x_{\text{min}}^h\right)^2\right)\right] \qquad \text{for } t < T_{\text{max}}^h\,, \tag{3.47}$$

with

$$x_{\text{max}}^e = \frac{a}{b} + \left(d - \frac{a}{b}\right)\,\mathrm{e}^{+t/\tau_e} \qquad \text{and} \qquad x_{\text{min}}^h = \frac{a}{b}\left(1 - \mathrm{e}^{-t/\tau_h}\right)\,. \tag{3.48}$$

As soon as all charge carriers have arrived at the electrode, i.e. for $t > T_{\text{max}}^e$ or $t > T_{\text{max}}^h$, respectively, the induced signal vanishes (no more moving charge carriers). The maximal drift times to traverse the detector thickness are given by

$$T_{\text{max}}^e = \tau_e \ln\frac{a}{a - bd}\,, \tag{3.49}$$

$$T_{\text{max}}^h = \tau_h \ln\frac{a}{a - bd}\,, \tag{3.50}$$

with the constants

$$a = \frac{V_{\text{bias}} + V_{\text{dep}}}{d}\,, \qquad b = \frac{2V_{\text{dep}}}{d^2}\,. \tag{3.51}$$

Integrating the signal current (Eq. 3.46) over time yields the induced charge at the signal electrode.

Fig. 3.7 illustrates the induced current (top) and charge (bottom) at the positive electrode for a particle creating $N = 10\,000$ e/h-pairs (MIP) in an unsegmented detector with thickness $d = 150\,\mu\text{m}$. On the left side of the figure, the signal is shown for a *slightly* over-depleted ($V_{\text{bias}} = 1.3 \cdot V_{\text{dep}}$) detector, whereas the right side shows the signal for a detector which is *strongly* over-depleted ($V_{\text{bias}} = 3 \cdot V_{\text{dep}}$). The signal component of electrons shows a fast rise due to their higher mobility compared to holes. However, both charge carrier types contribute equally to the total induced charge signal in an unsegmented detector. Further, it is visible that over-depletion, which increases the electrical field, and therefore the drift velocity, is beneficial as it reduces charge collection times. With $V_{\text{bias}} = 3 \cdot V_{\text{dep}}$ the total charge signal saturates after 5 ns, whereas for $V_{\text{bias}} = 1.3 \cdot V_{\text{dep}}$ the charge collection time is larger than 10 ns.

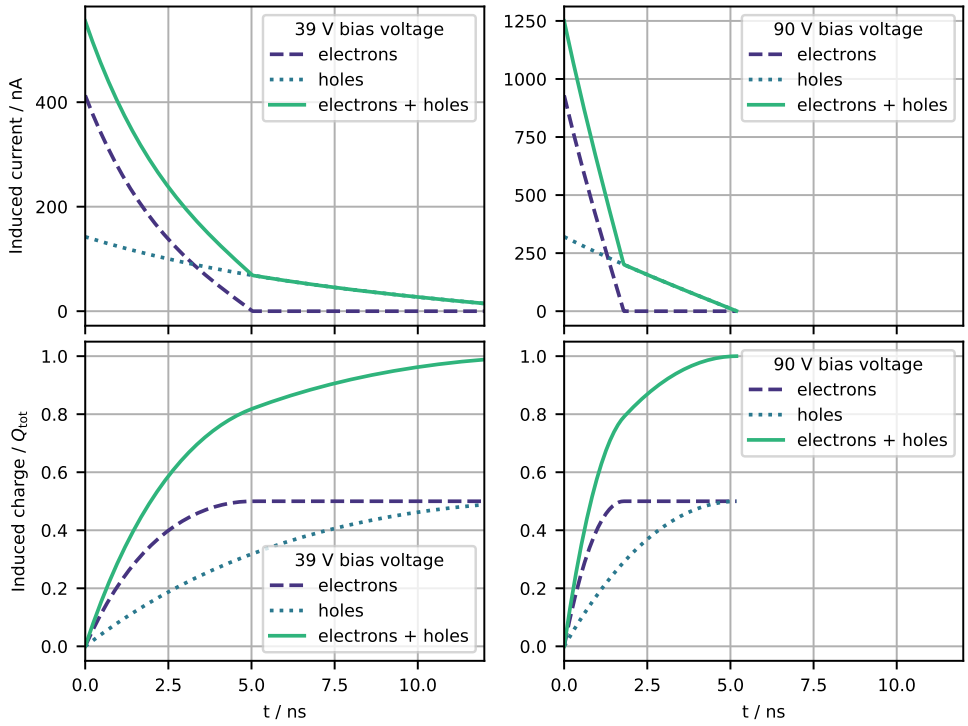

Figure 3.7: Induced current (top) and charge (bottom) at the positive electrode of an unsegmented detector by a perpendicular track of a MIP. Values are calculated according to Eq. 3.46 using $N = 10000$ e/h-pairs, $d = 150\,\mu\text{m}$ and $V_{\text{dep}} = 30\,\text{V}$. Induced charge is normalised to total charge. Left: $V_{\text{bias}} = 1.3 \cdot V_{\text{dep}}$. Right: $V_{\text{bias}} = 3 \cdot V_{\text{dep}}$.

For a position sensitive readout, the readout electrode of a detector is segmented in two dimensions (pixel detector). For segmented electrodes, expressions for the weighting potential and field exist (see e.g. [KW20; RA14]), but often numerical calculations are used to determine the induced signal. With respect to the calculations for unsegmented electrodes, the weighting field is not constant any more in a pixel detector. The weighting field increases rapidly towards the signal electrode [Poh20; KW20], and thus the induced current signal differs significantly from that of an unsegmented detector, see [Spi05]. The slope with which the weighting field increases towards the signal electrode increases with the ratio of the detector thickness d and readout electrode width w (d/w), see e.g. [KW20]. Due to the increasing weighting field towards the signal electrode, the induced charge signal at the signal electrode is dominated by the type of charge carrier arriving at the electrode in a pixel detector. Charges near the signal electrode have therefore a significantly larger contribution to the signal with respect to charge carriers far away from the signal electrode, known as the *small pixel effect* [KW20]. Thus, electrons are preferred as the collected charge carriers for fast and large signals. In addition, a strong electrical field

close to the signal electrode, i.e. a depletion zone growing from the signal electrode, is necessary for a large signal (maximises $\vec{E}_{w,i} \cdot \vec{E}_d$ term in Eq. 3.41). Moreover, fast charge collection helps to reduce charge loss after irradiation which is caused by reduced charge carrier lifetimes (see Sec. 3.2). Consequently, n-in-p pixel sensors which collect electrons and have a depletion zone growing from the readout electrode are used for pixel detectors at the HL-LHC.

3.2 Radiation damage

The extreme radiation at the LHC (mostly pions close to the interaction point [ATL17a]) to which the detectors are exposed causes damage to the detector material with time, known as *radiation damage*. This changes the property of the detector material and has significant impact on the operation of the detectors. The immunity against radiation damage induced effects is called *radiation tolerance*. Radiation damage consists of two basic mechanisms [KW20]:

- **Surface damage**: Originating from *ionising energy loss*, which damages the surface, boundaries and interfaces (Si-SiO_2), and thus mainly affects the performance of the readout chip. Surface damage can be largely suppressed if the device is unpowered during irradiation (transistors are not biased) [Gon+07].

- **Bulk damage**: Predominantly caused by *non-ionising energy loss* (NIEL), i.e. elastic collisions of incoming particles with the lattice leading to displacements of atoms in the lattice and more complex distortions of the lattice (crystal defects). Since these effects lead to damages of the substrate volume (bulk), they mainly affect the properties of the sensor.

Radiation damage is crucial especially for the innermost detector layers which are exposed to extreme particle fluxes.

A measure of bulk damage is the *neutron-equivalent fluence* (see below). After the end of operation of the new ATLAS pixel detector the layers closest to the interaction point are exposed to fluences of approximately $1.3 \times 10^{16}\,\mathrm{n_{eq}/cm^2}$ [ATL17a]. The corresponding surface damage, expressed as *total ionising dose* (TID), in the innermost layers is up to 1000 Mrad [ATL17a]. This requires the design of radiation tolerant sensors and readout electronics, so that the effect of radiation damage is small and the detector is still functional with sufficient performance after irradiation. Enormous effort in the design of radiation tolerant semiconductor devices for high-rate environments was made, see e.g. [Man13]. Generally, it was shown that n-in-p sensors (p-bulk) are more radiation tolerant than sensor with an n-bulk [Cas10b], and are therefore the technology of choice for the new ATLAS pixel detector. Further, it was observed that oxygen-enriched bulk materials are more radiation tolerant (in the case of charged hadron irradiation) [Lin+01]. A comprehensive review of bulk damage in silicon can be found in [Mol18]. A discussion of surface damage is given in [KW20].

The following section discusses radiation damage due to displacements in the crystal lattice (bulk damage) in more detail. After introducing the different types of crystal defects, a quantitatively description of the resulting generation and recombination processes (Shockley-Read-Hall statistics) is given. Finally, the change in the properties of the bulk material is discussed and the consequences for the operation of irradiated sensors are highlighted.

3.2.1 Bulk damage

Particles traversing the detector material mainly lose their energy via ionisation, which is a reversible process, and therefore does not lead to permanent damage of the crystal lattice [KW20]. However, there is also a contribution of *non-ionising energy loss* (NIEL) which is due to elastic (and also inelastic) collisions of incoming particles with lattice atoms. This causes knock-off of atoms (dislocation) leading to point-like defects or cluster defects[12] depending on the transferred energy to the *primary knock-off atom*. The maximal energy transfer by non-relativistic particles (e.g. protons or neutrons) and relativistic particles (electrons) in an elastic collision with the nuclei is [KW20]

$$W_{\text{max}}^{\text{non-rel}} = 4\,\frac{Mm}{(m+M)^2}\,E_{\text{kin}}\,, \tag{3.52}$$

$$W_{\text{max}}^{\text{rel}} = 2\,\frac{E_{\text{kin}}^{e} + 2m_e}{M}\,E_{\text{kin}}^{e}\,, \tag{3.53}$$

with M being the mass of the nuclei (e.g. Si nuclei). The mass and kinetic energy of an incoming non-relativistic particle are m and E_{kin}, respectively, whereas for relativistic particles they are m_e and E_{kin}^{e}. In silicon, the minimal energy required to dislocate a single atom of the lattice is approximately 25 eV, whereas approximately 5 keV are required to produce cluster defects [Van+80]. From Eq. 3.52 it is comprehensible that bulk damage is particle type and energy dependent. An overview of defect formation of various types of hadron irradiations is given in [Huh02]. Low-energy protons (MeV range) cause many homogeneously distributed point-like defects and only few cluster defects. In contrast, high-energy protons (GeV range) and 1 MeV neutrons create localised cluster defects and fewer vacancies.

The various types of crystal defects due to displacement of atoms are summarised in Fig. 3.8. The simplest defects are vacancies, i.e. unoccupied sites of the crystal lattice, or interstitials, i.e. occupation of "in-between" sites of the lattice by atoms. It is also possible that more complex distortions of the lattice are formed like di-vacancies or even triple-vacancies. These defects can build combinations with impurity atoms like oxygen (O) or carbon (C). All of these crystal defects change the properties of a semiconductor by the introduction of new energy levels.

[12] If the primary knock-off atom has sufficient energy it can knock-off other atoms until it comes to rest leading to cluster defects with dimensions of 10 nm × 200 nm, see e.g. [KW20].

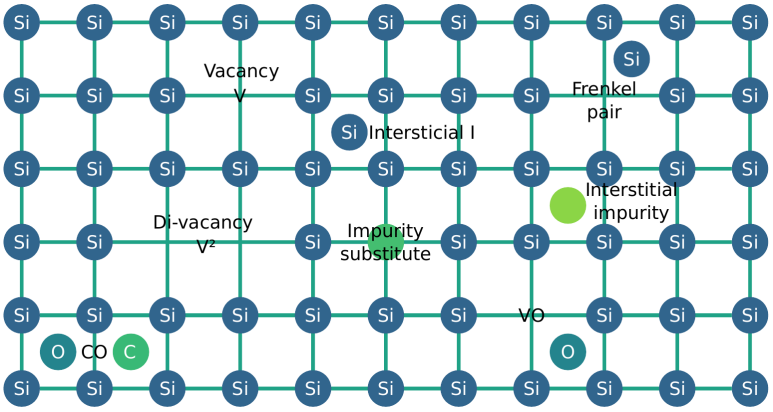

Figure 3.8: Summary of the most important crystal defects in silicon. Explanations of various defect types can be found in the text. From [Poh20].

NIEL hypothesis

The non-ionising energy loss (NIEL) is described by a so-called *damage function* $D(E)$ which depends on the particle energy E and varies for different particles [KW20]

$$\left.\frac{\mathrm{d}E}{\mathrm{d}x}\right|_{\mathrm{NIEL}}(E) = \frac{N_A}{A}\,D(E)\,. \tag{3.54}$$

The NIEL hypothesis is a first-order approximation and permits the scaling of radiation damage of different types of particles and different energies with NIEL. It assumes that radiation damage due to displacements scales linearly with NIEL. Typically, the radiation damage of particle type x is scaled to the damage of 1 MeV neutrons by introducing a so-called *hardness factor* [KW20]

$$\kappa = \frac{\int D_x(E)\phi(E)\mathrm{d}E}{D_n(1\,\mathrm{MeV})\int \phi(E)\mathrm{d}E} = \frac{\phi_{eq}}{\phi}\,, \tag{3.55}$$

with ϕ being the irradiation fluence and ϕ_{eq} the equivalent 1 MeV neutron fluence. This scaling is known as *NIEL scaling*. The hardness factor for 23 MeV protons is approximately 2.2, whereas the hardness factor for 23 GeV protons was measured to be approximately 0.6 [All+19].

As it is usually not feasible to reproduce the exact radiation environment (e.g. of the ATLAS detector at the LHC) in an irradiation campaign, a single type of particle (e.g. protons or neutrons) is used to perform irradiation of the device under test. With the NIEL hypothesis, it is possible to scale the induced radiation damage, and thus convert it into a quantity that is independent of the energy and particle type. The irradiation fluences are given in units of $\mathrm{n_{eq}/cm^2}$ (1 MeV neutron-equivalent fluence), corresponding to the damage produced by 1 MeV neutrons for the given fluence.

However, it has to be noted that there is no obvious reason for NIEL scaling and violations of

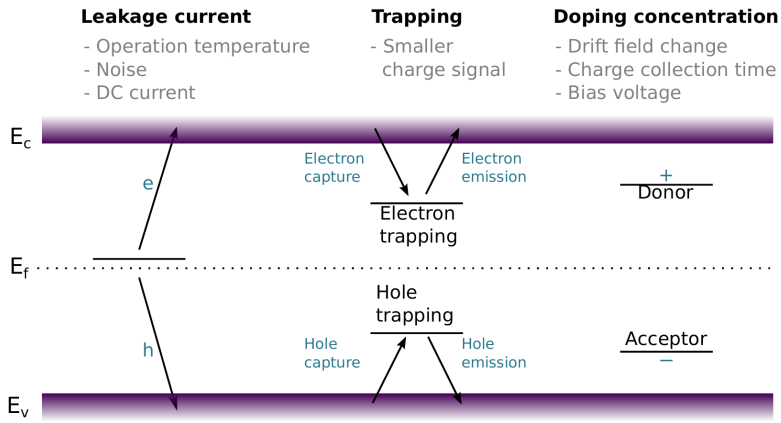

Figure 3.9: Different types of defect levels and their effect on the property of the silicon sensor. Mid-gap states cause an increase of detector leakage current (left). Trapping states which are close to the band edges create charge carrier trapping affecting the signal collection (centre). Acceptor- or donor-like states near the band edges change the doping concentration. From [Poh20].

NIEL scaling were already observed [Huh02]. Furthermore, *annealing* effects (treatment of the material with heat) are not taken into account in the NIEL hypothesis, which play an important role especially in the change of the effective doping concentration after irradiation (see below).

Shockley-Read-Hall statistics

The above discussed displacement defects can lead to new energy levels within the bandgap, so-called *defect levels* or *generation-recombination centres*. Defect levels (DL) can capture or emit free charge carriers by transitions between defect levels and the conduction band (CB) or valence band (VB). Depending on the position of the defect levels inside the bandgap they affect the properties of the semiconductor differently. Three types of defect levels changing the properties of a semiconductor sensor can be identified and are summarised in Fig. 3.9:

- **Leakage current**: So-called *mid-gap states* (located near the centre of the bandgap) act as generation-recombination centres and increase the probability of transitions between the valence and conduction band (due to "smaller distance"). This leads to an increase of leakage current in reversely biased pn-junctions (generation of electrons in the conduction band).
- **Charge carrier trapping**: So-called *trapping states* located close to the band edges trap freely moving charge carriers and release them after a given time. This leads to a reduction of the measured charge signal if the release time is larger than the signal integration time.
- **Doping concentration**: Defect levels acting as *donor* or *acceptor states* change the

effective doping concentration (space-charge). This leads to an increase of the depletion voltage, and thus requires an increase of the operation voltage (bias voltage) of irradiated detectors.

The generation-recombination processes are quantitatively described by the Shockley-Read-Hall statistics (SRH) [SR52; Hal52]. In total, four processes are considered: *electron capture*, *electron emission*, *hole capture* and *hole emission*. In the following, the rates for emission and capture are calculated and an expression for the net recombination (generation) rate is derived, based on the discussion in [KW20]. For details it is referred to [Gro67].

Assuming an equilibrium state (no "external" charge injection e.g. by ionising particles), the occupation probability of a defect level E_t is given by the Fermi statistics

$$f = f(E_t) = \frac{1}{1 + \exp\left(\frac{E_t - E_F}{k_B T}\right)} \,. \tag{3.56}$$

The rate $r_{c,e}$ for electron capture from the conduction band to a defect level (CB $\rightarrow$ DL) is proportional to the concentration n of electrons in the conduction band and the concentration of unoccupied defect levels, and thus is given by

$$r_{c,e} = c_e \cdot n \cdot n_t(1 - f) \,, \tag{3.57}$$

with n_t being the concentration of defect levels. The constant c_e is given by the product of the thermal velocity $v_{th,e}$ of electrons and the capture cross section σ_e, i.e. $c_e = v_{th,e}\sigma_e$. Analogously, the rate $r_{c,h}$ for hole capture (VB $\rightarrow$ DL) is given by

$$r_{c,h} = c_h \cdot p \cdot n_t \cdot f \,, \tag{3.58}$$

wit p being the charge carrier concentration of holes in the valence band and $c_h = v_{th,h}\sigma_h$. The electron emission rate $r_{e,e}$ (DL $\rightarrow$ CB) is proportional to the concentration of occupied defect levels, and thus

$$r_{e,e} = e_e \cdot n_t \cdot f \,, \tag{3.59}$$

with e_e being the electron emission probability. Analogously, the hole emission rate $r_{e,h}$ (DL $\rightarrow$ VB) is given by

$$r_{e,h} = e_h \cdot n_t(1 - f) \,, \tag{3.60}$$

with e_h being the hole emission probability. The smaller the distance between defect level and band edge, the larger the respective emission probability is. In a state of equilibrium the

respective emission and capture rates are the same and the emission rates are

$$e_e = c_e \cdot n_i \exp\left(\frac{E_t - E_F}{k_B T}\right) \tag{3.61}$$

$$e_h = c_h \cdot n_i \exp\left(\frac{E_F - E_t}{k_B T}\right). \tag{3.62}$$

The condition of equilibrium is no longer valid in the case of "external" charge injection (e.g. e/h-pair generation by a MIP) which produces transitions from the valence to the conduction band with rate R_{inj}. In steady state[13], the rate for transitions to the conduction band (valence band) equal the rates for transitions from the conduction band (valence band), and thus

$$\frac{\mathrm{d}n}{\mathrm{d}t} = R_{\text{inj}} - (r_{c,e} - r_{e,e}) = 0\,, \tag{3.63}$$

$$\frac{\mathrm{d}p}{\mathrm{d}t} = R_{\text{inj}} - (r_{c,h} - r_{e,h}) = 0\,. \tag{3.64}$$

It follows that

$$r_{c,e} - r_{e,e} = r_{c,h} - r_{e,h}\,, \tag{3.65}$$

and thus the probability that a defect level is occupied (by an electron) is

$$f = f(E_t) = \frac{c_e \cdot n + c_h \cdot n_i \,\mathrm{e}^{\frac{E_F - E_t}{k_B T}}}{c_e \left(n + n_i \,\mathrm{e}^{\frac{E_t - E_F}{k_B T}}\right) + c_h \left(p + n_i \,\mathrm{e}^{\frac{E_F - E_t}{k_B T}}\right)}\,. \tag{3.66}$$

Finally, the steady state net recombination (generation) rate G_t is given by

$$\begin{aligned} G_t &= r_{c,e} - r_{e,e} = r_{c,h} - r_{e,h} \\ &= \frac{c_e \cdot c_h \cdot n_t \left(np - n_i^2\right)}{c_e \left(n + n_i \,\mathrm{e}^{\frac{E_t - E_F}{k_B T}}\right) + c_h \left(p + n_i \,\mathrm{e}^{\frac{E_F - E_t}{k_B T}}\right)}\,. \end{aligned} \tag{3.67}$$

G_t is termed *generation current* if $G_t < 0$. If $G_t > 0$, it is termed *recombination current*.

In the case of minority carrier injection (e.g. by ionising particles), the recombination current ($G_t > 0$) leads to trapping (decay) of minority charge carriers. To calculate the recombination rate, consider electrons injected into a p-type substrate corresponding to the situation of e/h-pair generation in n-in-p sensors ($p \gg n$). Furthermore, only efficient recombination centres are assumed[14], i.e. defect levels are required to be located close to the middle of the bandgap for

[13] Steady state does not imply equilibrium.

[14] The probability of recombination (or generation) is maximised when the defect level is located near the middle of the bandgap, i.e. $|E_F - E_t| \approx 0$, see Eq. 3.67.

efficient recombination, and thus [Gro67]

$$p \gg n_i \, \mathrm{e}^{\frac{E_F - E_t}{k_B T}} \, . \tag{3.68}$$

Eq. 3.67 then yields the net recombination rate [Spi05]

$$G_t^{\mathrm{rec}} = \frac{\mathrm{d}N_R}{\mathrm{d}t} = \frac{c_e \cdot c_h \cdot n_t (np - n_i^2)}{c_h \cdot p} = \sigma_e \cdot v_{th,e} \cdot n_t (n - n_0) > 0 \tag{3.69}$$

which can be expressed in terms of the minority carrier lifetime τ_e

$$\frac{\mathrm{d}N_R}{\mathrm{d}t} = \frac{n - n_0}{\tau_e} \, , \qquad \text{with} \quad \tau_e = \frac{1}{\sigma_e \cdot v_{th,e} \cdot n_t} \, . \tag{3.70}$$

The decay of minority charge carriers, i.e. electrons in p-type substrate, therefore follows an exponential function with characteristic time τ_e (minority carrier lifetime).

In depleted pn-junctions, the origin of leakage current after irradiation is generation current ($G_t < 0$). To calculate the generation rate, consider a depleted pn-junction, and thus $p \ll n_i$, $n \ll n_i$ (no space-charge in depletion zone). Since there are no free charge carriers in the depletion region, no charge carriers are available for capture and only emission processes play a role (see also Eq. 3.57 and Eq. 3.58). Eq. 3.67 then yields the generation rate [Spi05]

$$G_t^{\mathrm{gen}} = -r_{e,e} = -\frac{c_e \cdot c_h \cdot n_t \cdot n_i}{c_e \cdot \mathrm{e}^{\frac{E_t - E_F}{k_B T}} + c_h \cdot \mathrm{e}^{\frac{E_F - E_t}{k_B T}}} < 0 \, . \tag{3.71}$$

From this equation it is visible that defect levels close to the middle of the bandgap (*mid-gap states*, $|E_F - E_t| \approx 0$) contribute significantly to the generation rate ("stepping stone" picture, see e.g. [Gro67]).

Based on the equations derived above, the effects of the defect levels on the properties of a semiconductor sensor (pn-junction) are discussed in the following.

Leakage current

After irradiation the generation current (Eq. 3.71) dominates the detector leakage current which is given by the sum over all defect levels in a volume $V = A \cdot d$ (with detector surface A and thickness d) [KW20]

$$I_{\mathrm{leak}} = e \cdot V \sum_{\mathrm{defects}} G_t \, . \tag{3.72}$$

Using Eq. 3.71 it can be shown that the leakage current strongly depends on the temperature T [Spi05]

$$I_{\mathrm{leak}} \sim T^2 \exp\left(-E_a / 2 k_B T\right) \, , \tag{3.73}$$

where the exponential term dominates. In silicon, the activation energy E_a is approximately 1.21 eV [Chi13]. It was observed that the leakage current after irradiation scales linearly with the irradiation fluence [Mol99]

$$I_{\text{leak}} = \alpha V \phi_{eq} \,, \tag{3.74}$$

with α being the *current related damage rate*. The damage rate α decreases with time and with temperature (*annealing*) and is parametrised by [Mol99]

$$\alpha = \alpha_0(T) + \alpha_1 \cdot \exp\left(-\frac{t}{\tau_l(T)}\right) - \beta \ln\left(\frac{t}{t_0}\right) . \tag{3.75}$$

Values for the various parameters at different temperatures can be found in [Mol99].

The drastic increase in leakage current with irradiation and temperature makes it necessary to cool the detectors during their operation (typically $-20\,^{\circ}\text{C}$). Furthermore, cooling of detectors prevents the situation that the dissipated power $P = I_{\text{leak}} V_{\text{bias}}$ heats up the sensor which in turn results in more leakage current (*thermal runaway*). To reduce leakage current after irradiation it is beneficial to reduce the thickness d of the sensor (bulk). This is one of the reasons to utilise thinner sensors (100 µm – 150 µm) for the future ATLAS pixel detector (compared to 200 µm – 250 µm of the current ATLAS pixel detector).

Higher detector leakage current also affects the readout electronics and results in larger electronic noise and (usually) in the necessity of a leakage current compensation circuit to remove a DC-offset at the input of the amplifier (see Sec. 3.3).

Charge carrier trapping

Trapping of charge carriers is caused by recombination current (Eq. 3.69). The charge carriers are trapped for some time by the defect levels and then released again. This decreases the charge carrier lifetimes and results in reduced signal amplitudes if the release time is larger than the signal collection time. The effective trapping times are (inverse of capture rates)

$$\frac{1}{\tau_{\text{eff,e}}} = \sum_{\text{defects}} c_e \cdot n_t (1 - f) \qquad \text{and} \qquad \frac{1}{\tau_{\text{eff,h}}} = \sum_{\text{defects}} c_h \cdot n_t \cdot f \,, \tag{3.76}$$

whereas the sum runs over all defect levels with a release time larger than the integration time of the readout electronics (signal collection time). In silicon, typical trapping times are in the order of a few ns, whereas release times are in the order of µs [Kra+12]. As shown above (Eq. 3.70) the charge loss (proportional to charge carrier concentration) is described by an exponential function with characteristic time $\tau_{\text{eff,e/h}}$

$$Q(t) = Q_0 \exp\left(-\frac{t}{\tau_{\text{eff,e/h}}}\right) . \tag{3.77}$$

It is observed that the effective trapping time scales linearly with the irradiation fluence and can be parametrised by

$$\frac{1}{\tau_{\text{eff,e/h}}} = \frac{1}{\tau_0} + \beta_{e/h}\phi_{eq}\,, \tag{3.78}$$

with τ_0 being the lifetime before irradiation ($> 100\,\mu\text{s}$ [KW20]) and $\beta_{e/h}$ a material independent scaling factor which shows only a slight temperature dependence [Kra+02]. A summary of trapping probabilities after irradiation is given in [Poh20]. At typical fluences of a few $10^{15}\,\text{n}_{\text{eq}}/\text{cm}^2$ effective trapping times for electrons are $0.5\,\text{ns} - 1\,\text{ns}$.

From Eq. 3.77 it is comprehensible that shorter collection times mitigate the effect of trapping. This can be achieved by either reducing the detector thickness or increasing the operational voltage so that the electrical field is higher, and therefore the drift velocity increases (although the drift velocity saturates at very high electrical fields). Another approach which reduces the susceptibility for charge carrier trapping, due to shorter drift paths, is the usage of sensors with columnar readout implants (3D sensors) [DW09; Ter+20].

Considering a $150\,\mu\text{m}$ thin detector operated at $600\,\text{V}$ yields an average electrical field of $40\,\text{kV/cm}$. This translates into a drift velocity of around $10^7\,\text{cm/s}$ [KW20] for electrons in silicon. The resulting drift time is $1.5\,\text{ns}$. According to Eq. 3.77 a significant fraction of the charge is lost, i.e. only around $20\,\%$ of the charge is collected. This calculation is based on simplified assumptions on the electrical field which might not be valid any more after irradiation to fluences in excess of $1 \times 10^{15}\,\text{n}_{\text{eq}}/\text{cm}^2$ [Mol18]. Nonetheless, it emphasises the effect of charge carrier trapping. From charge collection measurements using MIPs, charge collection efficiencies larger than $40\,\%$ were measured for fluences in excess of $1 \times 10^{15}\,\text{n}_{\text{eq}}/\text{cm}^2$ (see Sec. 6.6.4 and 6.7.6).

Effective doping concentration

The change in effective doping concentration $N_{\text{eff}} = N_D - N_A$ due to displacement damage is given by [KW20]

$$\Delta N_{\text{eff}} = \sum_D (1-f)n_t - \sum_A f n_t\,, \tag{3.79}$$

where the sum runs over all donor (D) and acceptor states (A), respectively. The behaviour of the (unsigned) effective doping concentration with irradiation is depicted in Fig. 3.10 (right axis). The depletion voltage (left axis) is proportional to the effective doping concentration (see Eq. 3.31) and changes, too. After the point of type inversion is reached, the increase in effective doping concentration after fluences of $2 \times 10^{12}\,\text{n}_{\text{eq}}/\text{cm}^2$ has a strong influence on the operation of irradiated detectors (see below).

The change in effective doping concentration $\Delta N_{\text{eff}} = N_{\text{eff},0} - N_{\text{eff}}$ with $N_{\text{eff},0}$ being the initial (effective) doping concentration can be parametrised by [Mol99]

$$\Delta N_{\text{eff}}(\phi_{eq}) = \Delta N_C(\phi_{eq}) + \Delta N_a(\phi_{eq}, T, t)\Delta N_\gamma(\phi_{eq}, T, t)\,. \tag{3.80}$$

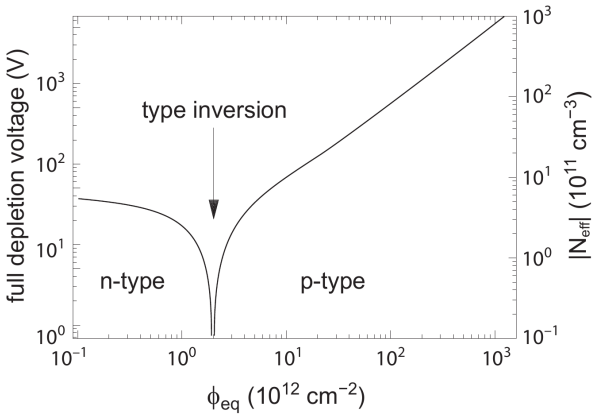

Figure 3.10: Change in (unsigned) effective doping concentration N_{eff} (right axis) due to displacement damage as a function of the neutron-equivalent fluence ϕ_{eq}. Relation to full-depletion voltage (left axis) is given by Eq. 3.31 ($V_{\text{dep}} \sim N_{\text{eff}}$). From [KW20].

A comprehensive discussion of these contributions can be found in [Mol99]. In the following, they are briefly summarised:

- **Stable damage** ΔN_C: Stable damage is independent of temperature, hence the name "stable". It can be parametrised by

$$\Delta N_C = N_{C,0}\left(1 - \mathrm{e}^{-c\phi_{eq}}\right) + g_C\phi_{eq}\,. \tag{3.81}$$

  The material-dependent parameters are extracted from fits to measured data and are summarised for various materials in [Mol99]. The first term of the above equation describes donor removal and is responsible for the decrease of N_{eff}. The second term describes the creation of acceptor states, which are occupied by electrons from the bulk, and therefore create a negative space-charge. At $\phi_{eq} \approx 2 \times 10^{12}\,\mathrm{n_{eq}/cm^2}$ donor removal and acceptor formation balance each other. For fluences beyond that, acceptor formation dominates and the space-charge changes sign and becomes more negative. This is known as *type inversion* (see Fig. 3.10), since the (n-type) semiconductor becomes p-type. Initial p-type semiconductors do not undergo type-inversion.

- **Beneficial annealing** ΔN_a: The initial decrease of N_{eff} due to an increase of donor-like defects [Mol99] when annealing irradiated devices is called *beneficial annealing* as it reduces the depletion voltage (for type-inverted materials). Beneficial annealing can be parametrised by

$$\Delta N_a(t,T) = g_a\phi_{eq}\mathrm{e}^{-t/\tau_a(T)}\,. \tag{3.82}$$

  The material-dependent parameters are extracted from fits to measured data and are

summarised for various materials in [Mol99].

- **Reverse-annealing** ΔN_γ: The effect that N_{eff} increases after annealing times longer than 80 min (at 60 °C) due to the formation of acceptor states, and thus increasing the depletion voltage is known as *reverse annealing*. It can be parametrised by

$$\Delta N_\gamma = g_\gamma \phi_{eq} \left(1 - \frac{1}{1 + t/\tau_\gamma(T)}\right) . \tag{3.83}$$

  The material-dependent parameters are extracted from fits to measured data and are summarised for various materials in [Mol99].

As mention above, the increase in effective doping concentration after irradiation leads to an increase of the depletion voltage (see Fig. 3.10). Since only the depleted region contributes to charge collection, the undepleted volume should be minimised which requires an increase of the operational voltage ($V_{\text{bias}} \approx 600\,\text{V}$) so that the sensitive volume is sufficiently depleted. After fluences of approximately $5 \times 10^{15}\,\text{n}_{\text{eq}}/\text{cm}^2$, it is usually not possible any more to fully deplete detectors with typical thicknesses of 150 µm at reasonable voltages ($< 1000\,\text{V}$, limited by breakdown voltage and power consumption). Consequently, the charge signal is reduced, an effect presented in Sec. 6.6.4 and 6.7.6.

Oxygen-enriched materials improve radiation tolerance in the sense that the change in effective doping concentration after irradiation is suppressed (for charged hadron irradiation) [Lin+01]. This is beneficial for the operational voltage of a detector after irradiation with charged hadrons, a scenario like in the inner layers of the ATLAS detector. At the same time, this is, however, an example that NIEL scaling is not always valid, since the change in effective doping concentration depends on the material and type of irradiation [Mol99], and thus breaks the assumption of NIEL scaling.

Measurements show that the assumption of a constant space-charge within the depletion region, leading to a linear electrical field, is not valid any more for highly irradiated detectors [Mol18]. Instead, a change from negative to positive space-charge within the depletion region is observed, known as the *double junction* effect [EVL02]. Consequently, the electrical field has a parabolic shape (high electrical field at both ends of the detector), see e.g. [Poh20].

Consequences of annealing

A common procedure is the annealing of irradiated detectors for 80 min at 60 °C [Lin+01; Mol99] which partially reverses radiation damage effects or enhances them. The chosen annealing procedure reduces the excess in detector leakage current by 40 % [Mol99] due to the temperature dependent damage rate. Since the trapping of charge carriers is nearly independent of temperature, the annealing procedure has no influence on the charge carrier trapping. Annealing changes the effective doping concentration (beneficial and reverse annealing). With the common

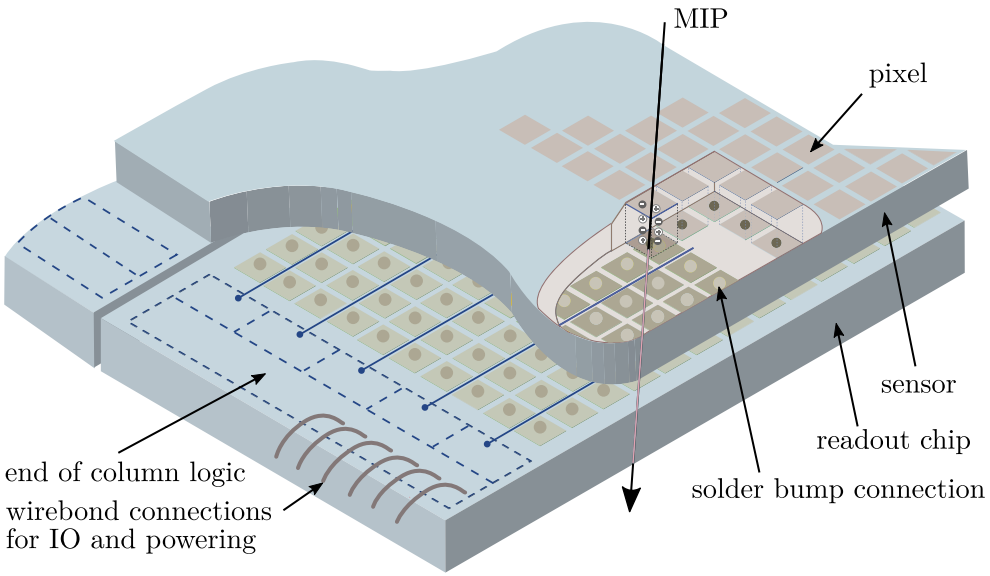

Figure 3.11: Concept of a hybrid pixel detector: A pixelated sensor is connected via fine-pitched solder bumps to the readout chip. The signal in the sensor created by MIPs is processed by the electronics of the readout chip. From [Poh20].

annealing procedure, the effect of beneficial annealing is maximal, and thus leads to a slight decrease in the effective doping concentration (beneficial for the operational voltage) [Mol99]. To suppress reverse annealing effects, which set in after annealing times longer than 80 min (at 60 °C) and increase the operational voltage, the detectors are required to be cooled during operation at the HL-LHC and warm-up times due to maintenance should be limited.

For the comparability of measurements, it is necessary to store the irradiated devices in a cooled environment (approximately −20 °C) and avoid uncontrolled interruption in the cooling chain so that sensor properties do not change unintentionally with time.

3.3 Hybrid pixel detectors

The basic concept of hybrid pixel detectors is depicted in Fig. 3.11. The pixelated sensor is separated from the readout chip which contains the signal processing electronics. Via fine-pitched solder bumps (a few µm in diameter) each pixel of the sensor is connected to a channel of the readout chip. This interconnection process is called *bump-bonding* [Ros+06]. To bump-bond thin readout chips (of down to 50 µm thickness) the flip-chip assembly [Fri+14] is used. Benefits of hybrid pixel detectors arise from the fact that the sensor and readout chip can be developed independently of each other such that advantages of both technologies can be combined. Whereas for the readout chip a CMOS process with a small feature size is used

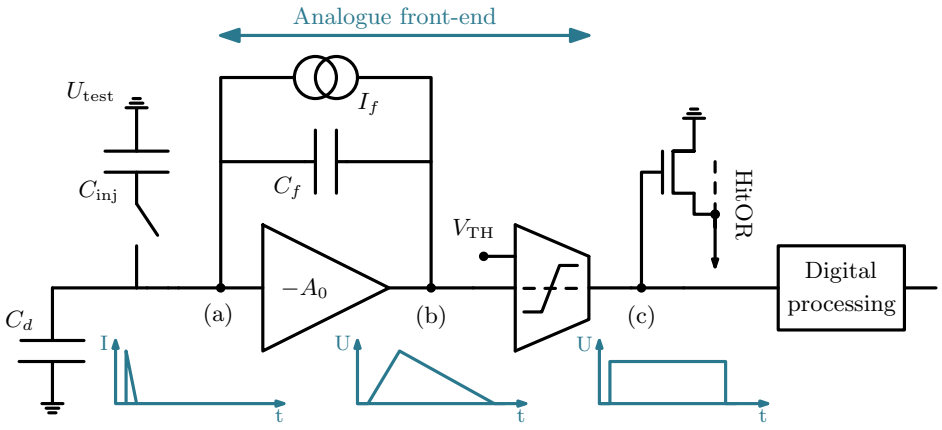

Figure 3.12: Typical readout circuit used for signal processing in hybrid pixel detectors. The logic consists of a charge-sensitive amplifier and discriminator building the analogue front-end (AFE). Signal shapes at different stages of the circuit are shown below.

to fit the complex readout logic into the area of a pixel ($50 \times 50\,\mu\text{m}^2$ for ATLAS) and reduce power consumption, a process with a larger feature size and typically no CMOS process is used for the sensor, which is simple in comparison. The utilisation of a CMOS process also for the production of a sensor for hybrid pixel detectors is discussed in Chapter 4.

Hybrid pixel detectors have demonstrated excellent radiation tolerance due to their fast charge collection ($\approx 10\,\text{ns}$) [Ros+06]. It is therefore a widely used technology for high-energy physics detectors in high rate and radiation environments [GW18]. However, the interconnection process of hybrid pixel detectors is complex and expensive, and therefore requires dedicated quality control measurements [Daa21]. In addition, the material budget is relatively large due to the stacking of the sensor ($100\,\mu\text{m} - 150\,\mu\text{m}$) and the readout chip ($100\,\mu\text{m} - 300\,\mu\text{m}$) which degrades the spatial resolution of tracking detectors.

An approach avoiding the interconnection process is to manufacture the sensor and readout electronics on the same substrate, known as monolithic active pixel sensor (MAPS) [Per07]. Depleted monolithic sensors are currently investigated to explore potential usage for detectors in high rate and radiation environments [Wan+18; Cai+19]. Even though, monolithic detectors have not yet achieved the same radiation tolerance as hybrid pixel detectors, they are a promising candidate for future particle detectors in high-energy physics.

3.3.1 Signal processing

Each channel of a readout chip has dedicated logic implemented to process the signal from the sensor. A detailed discussion of these complex circuits can be found in [Ros+06; KW20; Spi05]. In the following, the basic working principle is presented with a focus on electronic noise and

charge collection efficiency of charge-sensitive amplifiers.

A typical readout circuit used for signal processing in hybrid pixel detectors is depicted in Fig. 3.12. The detector system is based on a charge-sensitive amplifier (CSA) with feedback capacitance C_f and open-loop gain A_0. The current signal from the sensor (a), represented by the capacitance C_d, is integrated by the CSA which generates an output voltage U_{out} (with rise time τ_{CSA}) proportional to the input charge Q_{in} [Ros+06]

$$U_{\text{out}} = -\frac{Q_{\text{in}}}{C_f}\,, \tag{3.84}$$

assuming infinite gain of the CSA. Finite gain leads to a reduction of the output voltage [Ros+06]. However, the gain of the CSA is usually in the order of 10^3 and the total input capacitance is very small such that this effect is negligible in most cases (for a detailed discussion see below). A constant feedback current I_f discharges the feedback capacitor such that the output voltage linearly returns to its baseline (b). The larger the feedback current I_f, the faster the output signal returns to baseline. Typical discharge times are in the order of a few 100 ns such that dead times are small and pile-up (new charge signal arrives before output voltage returned to baseline) is avoided. A discriminator compares the output signal of the CSA to a fixed threshold V_{TH}. The discriminator output (c) switches to logical "high" as soon as the CSA signal crosses the threshold and returns to logical "low" as soon as the CSA signal falls below the threshold.

The CSA and discriminator output signals for two different input charges are visualised in Fig. 3.13. Due to the linear feedback, the length of the discriminator signal, corresponding to the *time-over-threshold* (ToT), is proportional to the input charge. Using digital processing, the discriminator output is sampled with a clock to provide a charge information (in units of ToT). The digital logic further processes the data such that it can be stored and read out. For high rate environments like at the LHC, where the arrival time of the signal is required to be detected with high precision, the timing behaviour of the discriminator is crucial. As illustrated in Fig. 3.13, the response time of the discriminator changes with varying input charge. The higher the input charge, the earlier the signal crosses the fixed discriminator threshold, which is known as *time walk*. To minimise time walk a fast discriminator in combination with a short rise time of the CSA is required [Ros+06]. The logical OR of all discriminator outputs (from each pixel) is called *HitOR* and can be used to externally measure the charge. A method using this feature is described in Sec. 6.2.2.

For testing and calibration purposes the readout electronics features an internal charge injection circuit. A test pulse with known voltage U_{test} is generated and injects a known charge into the CSA via the injection capacitor C_{inj}. This facilitates testing of the readout chip before bump-bonding it to a sensor and the calibration of the detector as presented in Sec. 6.3. Usually, charge and threshold are expressed in units of electrons ($1\,\text{e} = 1.602\,176 \times 10^{-19}\,\text{C}$ [Tie+21]).

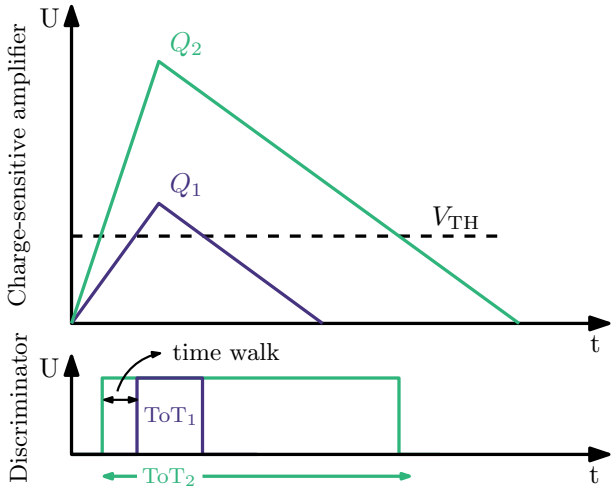

Figure 3.13: Charge-sensitive amplifier (CSA) and discriminator output signal as a function of the time for two different input charges ($Q_2 > Q_1$). Peaking time is (nearly) independent of the input charge. The discriminator compares the signal to a fixed threshold V_{TH}. The time-over-threshold (ToT) is proportional to the input charge. Smaller charge signals cross the fixed threshold later (time walk).

Electronic noise of a CSA

Every signal is superimposed by statistical fluctuations in the signal generation (*signal fluctuations*) and in the readout electronics (*baseline fluctuations*). In semiconductor detectors, the signal fluctuations are much smaller than the fluctuations of the baseline[15]. Therefore, electronic noise (statistical fluctuations in the processing electronics) strongly influences the detector performance (e.g. resolution or detection threshold). The minimisation of electronic noise is desirable and has a large impact on the design of the readout electronics. In the following, a brief overview of electronic noise is given. A comprehensive discussion of electronic noise is given in [Spi05; KW20].

Typically, noise is described as a power density $\mathrm{d}P_n/\mathrm{d}f$ specifying the power in a given frequency interval $\mathrm{d}f$. When considering electronic circuits, the power density is usually converted into a voltage or current spectral density using the assumption of a fixed resistance R [KW20]

$$\mathrm{d}P_n/\mathrm{d}f = \frac{1}{R}\,\mathrm{d}\langle v^2\rangle/\mathrm{d}f = R\,\mathrm{d}\langle i^2\rangle/\mathrm{d}f\,. \tag{3.85}$$

The noise at the output of an electronic system is calculated by integrating the product of the noise power spectrum i_{ni}^2 (current spectral density) at the input of the system and the transfer

[15] Measured spectra are composed of a baseline, the output in the absence of a signal, and the signal itself.

function[16] $H(f)$ over all frequencies f [Spi05]:

$$V_{no}^2 = \int_0^\infty i_{ni}^2 \, |H(f)|^2 \, \mathrm{d}f \, . \tag{3.86}$$

The transfer function for a CSA describes the gain as a function of the frequency. For low frequencies the gain is constant, but decreases for higher frequencies (bandwidth) leading to a finite rise time τ_{CSA}. In general, there are three different types of electronic noise [KW20]:

- thermal noise
- shot noise
- $1/f$ noise

The origin of thermal noise are velocity fluctuations of charge carriers (Brownian motion). Thermal noise is frequency-independent ("white" noise), but is proportional to temperature. Shot noise originates from statistical fluctuations in the number density when charge carriers are injected independently. Like thermal noise, also shot noise does not depend on the frequency. The origin of $1/f$ noise are also fluctuations in the number density. However, the noise spectrum is frequency-dependent when the fluctuations are not random any more, e.g. when charge carriers are trapped and released. All noise contributions with frequency-dependent spectrum according to $1/f^\alpha$ ($\alpha = 0.5...2-3$) are considered as $1/f$ noise.

Relating this to a detector system based on a CSA, as shown in Fig. 3.12, there is thermal and $1/f$ noise in the transistor channels (of the CSA). The $1/f$ noise is due to trapping and release of the charge carriers at the interface between the oxide and substrate [KW20]. In addition, there is shot noise due to leakage current from the detector. Especially after irradiation, this is the dominant contribution to electronic noise as the leakage current significantly increases due to bulk damage (see Sec- 3.2.1). Even in AC-coupled detector systems, where the DC-component of the leakage current is blocked, there is shot noise as it is a fluctuation [Spi05].

Usually electronic noise is given as equivalent noise charge (ENC) which is the charge for which the signal-to-noise ratio (S/N) equals 1 [Spi05]. In a detector system based on a CSA, the different contributions to ENC can be summarised by [KW20]

$$\mathrm{ENC}_{\mathrm{ser}} \sim C_{\mathrm{det}} \tag{3.87}$$

$$\mathrm{ENC}_{\mathrm{therm}} \sim 1/\sqrt{g_m} \, , \tag{3.88}$$

$$\mathrm{ENC}_{\mathrm{shot}} \sim \sqrt{I} \, , \tag{3.89}$$

with $\mathrm{ENC}_{\mathrm{ser}}$ being the serial component of the ENC (thermal and $1/f$ noise), C_{det} the detector capacitance, g_m the transconductance and I the leakage current of the detector. An increase in

[16] The transfer function describes the output signal of a device as a function of the input signal.

electronic noise due to a larger capacitance can therefore be compensated by a larger transconductance g_m. The transconductance is proportional to the square-root of the drain current of the device (in weak inversion) [KW20], and thus has significant impact on the power consumption of the analogue front-end (CSA). Usually, the cooling budget in a detector is limited which results in a limitation of the power consumption. Precise knowledge of the detector capacitance is therefore important to optimise the performance and power consumption of the detector system. In Sec. 6.7.2, measurements of the detector capacitance are presented.

It is important to note that also the rise time τ_{CSA} of the CSA depends linearly on the detector capacitance C_{det} [KW20]

$$\tau_{\mathrm{CSA}} \sim C_{\mathrm{det}} \,. \tag{3.90}$$

An increase in τ_{CSA}, i.e. due to higher detector capacitance, decreases the bandwidth of the CSA. Since the value of the integral in Eq. 3.86 is proportional to the bandwidth[17], the total noise decreases with decreasing bandwidth. Therefore, it is possible that elevated noise due to a higher detector capacitance (see Eq. 3.87) is balanced out by a decreased bandwidth of the detector system (due to larger τ_{CSA}).

In general, any capacitance shunting the input of the CSA (input capacitance of CSA, detector capacitance and additional parasitic capacitances) has to be considered. However, the dominant contribution to the input capacitance is the detector capacitance (several 10 fF), and thus other contributions are usually neglected.

Charge collection efficiency of a CSA

The charge collection efficiency (CCE) is a measure of the amount of reconstructed charge with the CSA (voltage drop over feedback capacitance) with respect to a given input charge Q (via the injection circuit or charge deposition in the sensor), i.e. how much of the input charge is "seen" by the CSA. For a CCE of 100 %, the input charge is fully reconstructed by the CSA. This fact is important for threshold calibration as it is assumed that the injected charge (via injection circuit) is fully "seen" by the CSA. Furthermore, the charge calibration of the detector relies on the fact that the reconstructed charge peaks correspond to the input charge, i.e. the deposited charge in the sensor (see Sec. 6.3.2).

To evaluate the CCE for a CSA the circuit depicted in Fig. 3.14 is considered. The sensor, which is represented by a capacitance C_d, is AC-coupled (via the coupling capacitance C_c) to the CSA with open-loop gain A_0 and feedback capacitance C_f. The CCE of the CSA is defined as

$$\mathrm{CCE} = T \cdot C_f = \frac{U_{\mathrm{out}}(Q)}{Q_{\mathrm{inj/det}}} \cdot C_f \,, \tag{3.91}$$

with $T = \frac{U_{\mathrm{out}}(Q)}{Q_{\mathrm{inj/det}}}$ being the charge transfer function. In the following two cases are considered:

[17] The integral is proportional to the area of the region bounded by $H(f)$.

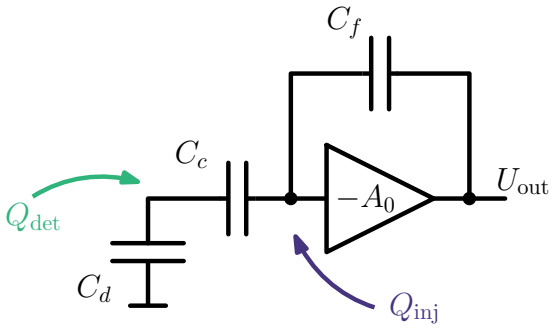

Figure 3.14: AC-coupled (coupling capacitance C_c) charge-sensitive amplifier with open-loop gain A_0 and feedback capacitance C_f. Sensor is represented as capacitance C_d. Two cases are considered: a) charge collection from injection node (Q_{inj}, blue) and b) charge collection from sensor node (Q_{det}, green).

a) Charge collection efficiency CCE_{inj} from injection circuit (Q_{inj})

b) Charge collection efficiency CCE_{det} from sensor (Q_{det})

A complete derivation of the following formulae can be found in Appendix 7. For a), the CCE (at the injection node) is given by

$$\text{CCE}_{\text{inj}} = \frac{1}{\frac{1}{A_0 C_f} \cdot \frac{C_d C_c}{C_d + C_c} + \frac{1}{A_0} + 1}\,, \tag{3.92}$$

while for b), the CCE (at the sensor node) is given by

$$\text{CCE}_{\text{det}} = \frac{1}{\frac{1}{A_0}\left(\frac{C_d}{C_f} + \frac{C_d}{C_c}\right) + \frac{C_d}{C_c} + \frac{1}{A_0} + 1}\,. \tag{3.93}$$

The CCE in case of DC-coupled detectors is obtained in the limit of $C_c \to \infty$ yielding for both cases a) and b):

$$\text{CCE}_{\text{DC}} = \frac{1}{1 + \frac{1}{A_0} \cdot \frac{C_d + C_f}{C_f}}\,. \tag{3.94}$$

It is important to note that the CCE from injection and sensor node are not identical in case of an AC-coupled detector ($\text{CCE}_{\text{inj}} \geq \text{CCE}_{\text{det}}$). Since the charge calibration depends on the ratio of both CCEs, this has an influence on the charge calibration of AC-coupled detectors (see Sec. 6.3.2). For DC-coupled detectors both CCEs are the same (no capacitive charge sharing between coupling capacitance and feedback capacitance). The CCE as a function of the coupling capacitance for two different open-loop gains A_0 is shown in Fig. 3.15a, assuming $C_f = 5\,\text{fF}$ and $C_d = 35\,\text{fF}$.[18]

[18]The value of C_d is typical for the investigated sensors. The value of C_f corresponds to the feedback capacitance

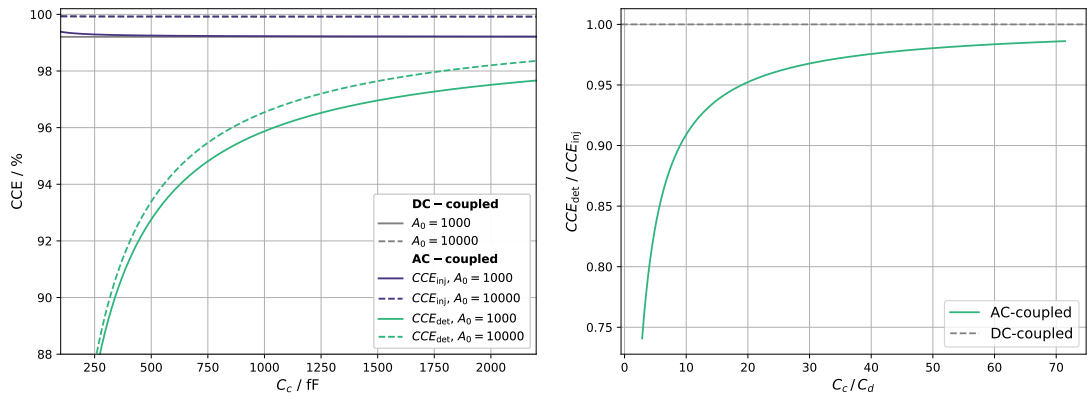

(a) **(b)**

Figure 3.15: (a) Charge collection efficiency (CCE) of a charge-sensitive amplifier for charge collection at the injection and sensor node as function of the coupling capacitance C_c (see Fig. 3.14). A detector capacitance of $C_d = 35\,\text{fF}$ and feedback capacitance of $C_f = 5\,\text{fF}$ is assumed. Two different settings of open-loop gain A_0 are shown. **(b)** Ratio of CCE for charge collection at the injection and sensor node as a function of the ratio $C_c\,/\,C_d$.

The finite open-loop gain A_0 reduces the CCE in both cases, charge collection at sensor and injection node. Larger ratios $C_c\,/\,C_d$ increase the CCE for charge deposition in the sensor, while slightly decreasing the CCE for charge collected at the injection node. For typical values of $C_c \approx 500\,\text{fF}$, the CCE of AC-coupled detectors is slightly reduced (by $5\,\% - 10\,\%$), an effect which has to be considered in the detector calibration. The CCE of DC-coupled detectors is close to $100\,\%$, and has therefore negligible influence on the detector calibration.

The ratio of CCE at the injection and sensor node is shown in Fig. 3.15b. This ratio is independent of the parameters of the CSA (A_0 and C_f). For typical values of $C_c \approx 500\,\text{fF}$ and $C_d \approx 35\,\text{fF}$ it is between 0.95 and 0.9 for AC-coupled detectors, and therefore has to be considered in the calibration of AC-coupled CSAs. It is expected that the coupling capacitance (MIM-capacitor) adds parasitic contributions which increase the effective detector capacitance (input capacitance) and further decrease the CCE by a few percent.

3.4 The ATLAS ITk pixel detector

In the course of the HL-LHC upgrade presented in Chapter 2, a new all-silicon tracking detector for the ATLAS experiment, the Inner Tracker (ITk), is installed. The ITk detector replaces the Inner Detector of the current ATLAS detector to maintain tracking and vertexing performance of the ATLAS detector in the high hit rate and radiation environment of the HL-LHC. The layout of the ITk detector in the r-z projection is shown in Fig. 3.16. It consists of a strip

of the Linear front-end of the RD53A readout chip with open-loop gain $A_0 = -76\,\text{dB} \approx 6300$ [Gar17].

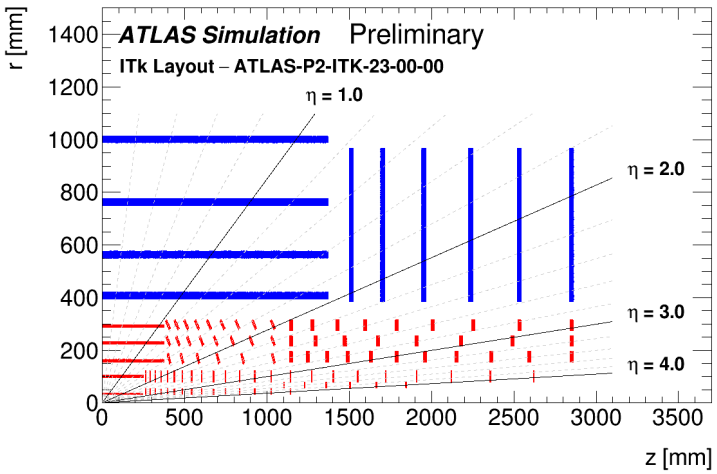

Figure 3.16: Layout of the ATLAS ITk detector. The detector consists of a strip detector (blue) and a pixel detector (red). Only one quarter of the detector and active detector elements are shown. The x-axis corresponds to the beam axis with the origin at the interaction point. The y-axis corresponds to the radius measured from the interaction point. From [ATL20].

(blue) and a pixel detector (red). In the following, the focus is put on the pixel detector of the ITk detector. Details about the strip detector can be found in [ATL17b].

The ATLAS ITk pixel detector consists of 5 barrel layers (L0 – L4), of which the innermost layer (L0) is placed at a radius of 34 mm. In combination with several end-cap disks a sufficient track reconstruction up to a pseudorapidity of $|\eta| = 4$ is ensured [Gem20]. The total area of the new pixel detector increases from $2\,\mathrm{m}^2$ to approximately $13\,\mathrm{m}^2$ [Gem20] demanding cost-effective solutions to cover this large area. Sensors utilising a CMOS process line offering high-throughput at comparatively low costs are therefore an attractive technology.

The expected fluence[19] for the innermost layer (L0) is approximately $1 \times 10^{16}\,\mathrm{n_{eq}/cm^2}$. For the outer layers the expected fluences[20] range from $5 \times 10^{15}\,\mathrm{n_{eq}/cm^2}$ (L1) to $2 \times 10^{15}\,\mathrm{n_{eq}/cm^2}$ (L2 – L4). The expected TID in the innermost layer is 1000 Mrad at the end of operation. It is foreseen to replace the inner layer after $2000\,\mathrm{fb}^{-1}$ corresponding to half of the operating time. [ATL17a]

In total, the ITk pixel detector consists of more than 9000 modules. A module consists of a readout chip bump-bonded to a passive silicon sensor (hybrid pixel detector). This "bare" module is dressed with a flexible printed circuit board providing connection to the on-detector services (low and high voltage as well as data transmission). Within the new pixel detector two types of modules are used: triplet-modules and quad-modules. Triplet-modules consist of three

[19] after an integrated luminosity of $2000\,\mathrm{fb}^{-1}$ including a safety factor of 1.5.
[20] after an integrated luminosity of $4000\,\mathrm{fb}^{-1}$ including a safety factor of 1.5.

single-chip modules, whereas a quad-module consists of four readout chips connected to a single large sensor. A CO_2-based cooling system cools the modules to approximately $-25\,°C$ to keep them operational after irradiation. [Gem20]

To meet the more demanding requirements of the ATLAS ITk pixel detector (increased hit rate and radiation level), a novel ASIC (application-specific integrated circuit), implemented in a 65 nm CMOS technology, is designed by the RD53 collaboration. The new readout chip withstands the increased radiation dose and has higher granularity (smaller pixel size) to resolve the increased track density as well as higher data rate capabilities. Details regarding the pixel detector readout chip are given in Sec. 3.4.1.

In contrast to the current pixel sensors (n-in-n sensors), the new pixel detector comprises n-in-p pixel sensors with higher granularity to decrease the average occupancy per pixel. The requirements on the performance of pixel sensors for the ATLAS ITk pixel detector are summarised in Tab. 3.1. To ensure sufficient track reconstruction efficiency a hit-detection efficiency $> 97\,\%$ after irradiation is required for sensors of the ITk pixel detector. Another critical performance parameter is the maximum allowed leakage current after irradiation, which is driven by the limited cooling power of the cooling system of the detector. Especially after irradiation, a higher operational voltage (bias voltage) is necessary, which increases the dissipated power of the sensor ($P_{\text{diss}} = I_{\text{leak}} V_{\text{bias}}$). To lower the power dissipation thinner sensors are used ($100\,\mu\text{m} - 150\,\mu\text{m}$ in contrast to $200\,\mu\text{m} - 250\,\mu\text{m}$ used in the current ATLAS pixel detector). [ATL17a]

It is foreseen to use 3D silicon sensors with $50 \times 50\,\mu\text{m}^2$ and $25 \times 100\,\mu\text{m}^2$ pixels and a substrate thickness of 150 µm for the innermost layer (L0) [Ter21]. These sensors have shown excellent radiation tolerance up to $1 \times 10^{16}\,\text{n}_{\text{eq}}/\text{cm}^2$ and low power dissipation [Ter+20]. For the outer layers (L1 – L4) planar silicon sensors with $50 \times 50\,\mu\text{m}^2$ pixels are used. L1 consists of 100 µm thin planar sensors, whereas for L2 – L4 150 µm thin planar sensors are used [Gem20]. Several planar silicon sensors using conventional processes are currently under investigation [Bey19; Nak+19; Cal+19]. Within the scope of this thesis, planar silicon sensors utilising a CMOS process line are investigated.

One of the main challenges of the ATLAS ITk pixel detector is the power distribution within the detector due to the increased amount of modules. To realise efficient powering and reduce the material budget of the detector, which significantly impacts the tracking and vertexing performance, a serial powering scheme [Via17] is used. This allows for a reduction of the number of cables and minimises the amount of inactive material. From the constant current supplied to modules within a serial powering chain, a constant operating voltage via shunt low-dropout regulators [Kar+09] is generated for the analogue and digital chip domain, while surplus current (current that is not drawn from the chip) is shunted.

	before irradiation	$\mathbf{2 \times 10^{15}}$ $\mathrm{n_{eq}/cm^2}$	$\mathbf{5 \times 10^{15}}$ $\mathrm{n_{eq}/cm^2}$
leakage current	$< 0.75\,\mu\mathrm{A}^2/\mu\mathrm{m}$ measured at $V_{\mathrm{dep}} + 50\,\mathrm{V}$	$< 25\,\mu\mathrm{A}^2/\mu\mathrm{m}$ measured at 400 V	$< 45\,\mu\mathrm{A}^2/\mu\mathrm{m}$ measured at 600 V
depletion voltage	$< 100\,\mathrm{V}$	-	-
breakdown voltage	$> V_{\mathrm{dep}} + 70\,\mathrm{V}$	$> 400\,\mathrm{V}$	$> 600\,\mathrm{V}$
hit-efficiency	$> 98.5\,\%$	$> 97\,\%$	$> 97\,\%$

Table 3.1: Requirements on the performance of planar sensors (150 µm thickness) for the ATLAS ITk pixel detector before and after irradiation. Total leakage current before irradiation measured at 20 °C and −25 °C after irradiation. Hit-efficiency measured at orthogonal incidence. Numbers according to [ATL21].

3.4.1 The RD53A prototype readout chip

The RD53A readout chip [Gar17] is a large-scale prototype chip to demonstrate suitability of the chosen 65 nm CMOS process for the HL-LHC upgrades of the ATLAS and CMS pixel detector. The development of the ASIC is a joint effort of the ATLAS and CMS collaboration. The main specifications of the RD53A readout chip [Gar15], such as a trigger rate of up to 1 MHz, a hit rate of up to $3\,\mathrm{GHz/cm^2}$, low power consumption as well as low noise and low detection threshold, are driven by the HL-LHC conditions. Furthermore, the chip is designed to withstand at least 500 Mrad of TID[21] [Gar17].

To choose the best suited design of the analogue front-end (AFE) for the two experiments the readout chip consists of different designs of the AFE. A top view of the RD53A readout chip indicating the location of the three different AFEs is shown in Fig. 3.17. The chip has a size of $20.0 \times 11.8\,\mathrm{mm^2}$ which is half of the size of the final production chip. The pixel matrix consists of 400×192 pixels with a size of $50 \times 50\,\mu\mathrm{m^2}$. Pixels are grouped in arrays of 8×8 pixels forming a pixel core. The design and verification is done for a single core which is repeated to construct the final pixel matrix. A pixel core is based on the "analogue island in a digital sea" design principle [Gar17]. For this purpose, the analogue circuit, i.e. the AFE, of 2×2 pixels is embedded as an analogue "island" into a synthesised digital "sea" as illustrated in Fig. 3.18.

Within the chip bottom (see Fig. 3.17) analogue and digital blocks for biasing, monitoring, configuration and readout of the chip are implemented [Gar17]. All bias currents generated by DACs are derived from a global reference current I_{ref} (nominal value of 4 µA). A global reference voltage V_{ref} (nominal value of 900 mV) is used as the reference for all monitoring ADCs and the generation of the injection voltage for the injection circuit. Both the reference current and voltage can be trimmed to compensate for small process variations. To cope with the increased hit rate the chip includes a high speed output transmitter [Wan+19] to send out data with a speed of 1.28 Gbit/s at four lanes. For serial powering [Via17; DS20] of the detector modules a

[21] This is sufficient, since the inner layer is replaced after $2000\,\mathrm{fb^{-1}}$, see Sec. 3.4.

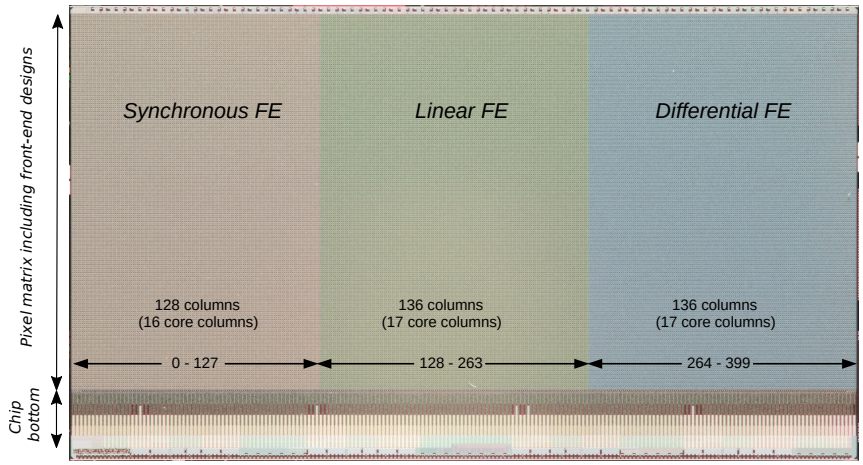

Figure 3.17: RD53A top view indicating the location of the three front-end designs (pixel matrix) and the chip bottom. At the very top and bottom of the chip are pads for wire-bonding. Modified from [Gar17].

shunt low-dropout regulator [Kar+09] was designed.

The chip can be operated in different power modes: direct, LDO or shunt LDO powering. A brief description of the powering modes can be found in [Daa21]. For the investigations in this thesis, the chip was powered directly, i.e. analogue and digital voltages (VDDA and VDDD) are fed directly to the respective power rails.

The digital logic takes care of ToT counting, hit storage and readout. ToT is counted with 40 MHz, corresponding to the bunch crossing frequency at the LHC. A time window of 25 ns equals the time between two bunch crossings (BC). Dedicated trigger logic sends out hits only when a latency timer (also 40 MHz) reaches its programmed latency (up to 12.5 µs) simultaneously to the arrival of a trigger (triggered readout) [Gar17]. For testing purposes, the chip allows for the multiplication of triggers, i.e. defining a readout window. The maximum number of consecutive triggers that can be sent to the chip is 32 corresponding to a readout window of 32 BC = 800 ns. The relative difference between the time of the first trigger (issued when the DAQ system receives a trigger) and the recorded hit is termed relative bunch-crossing ID (rel. BCID).

A comprehensive overview of the RD53A readout chip including a detailed description of the AFEs can be found in [Gar17]. A comparative study of the three different analogue front-end designs is given in [Daa21; Ada+21]. In the following, the two analogue front-end designs (Linear and Differential front-end) used for the characterisation of passive CMOS sensors are briefly described. Further, the injection circuit and HitOR feature of the RD53A readout chip are presented.

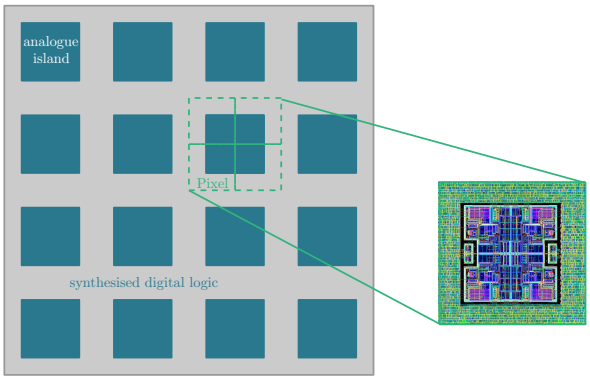

Figure 3.18: Analogue islands in digital sea design principle. A pixel array of 8×8 pixels corresponding to a core is shown. The grey area represents the synthesised digital logic which is shared by the pixels (green dashed rectangles). The blue areas represent the analogue islands containing four analogue front-end circuits. Enlarged view depicts layout of 2×2 pixels. Picture from [Gar17].

The Linear analogue front-end

The Linear front-end of the RD53A readout chip features a linear pulse amplification. The schematic of this front-end is shown in Fig. 3.19. The gain stage is based on a charge-sensitive amplifier (CSA) with Krummenacher feedback I_K [Kru91]. The CSA has two selectable gain modes: high gain (C_{F2} floating) and low gain (C_{F1} parallel to C_{F2}). The CSA is followed by a high speed and low power discriminator comparing the signal to a given (global) threshold V_{th}. The discriminator includes a transconductance stage followed by a transimpedance amplifier providing a low impedance path for fast switching. To compensate threshold dispersions between pixels (due to process variations) a per-pixel (local) 4-bit adjustable threshold trimming is available (I_{DAC}). [Gai+16; Gar17]

The Differential analogue front-end

The Differential front-end of the RD53A features a differential gain stage. The schematic of this front-end is shown in Fig. 3.20. The pre-comparator has a continuous reset I_{ff} and adjustable gain by (globally) choosing between two different feedback capacitance values C_f. The DC-coupled pre-comparator acts as a differential threshold circuit. The global threshold can be set by two voltages, Vthin1 and Vthin2, which introduce an offset between the two branches of the pre-comparator. A per-pixel (local) threshold trimming is available via the adjustable TDAC trim. The pre-comparator is followed by a classic continuous time comparator. A dedicated leakage current compensation (LCC) circuit is implemented to prevent the input from saturation for leakage currents up to 20 nA (per pixel). [Gar17]

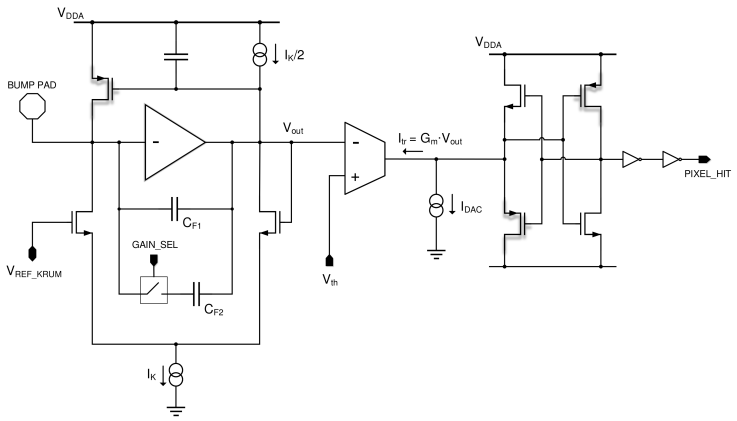

Figure 3.19: Schematic of the Linear front-end of the RD53A readout chip. From [Gar17].

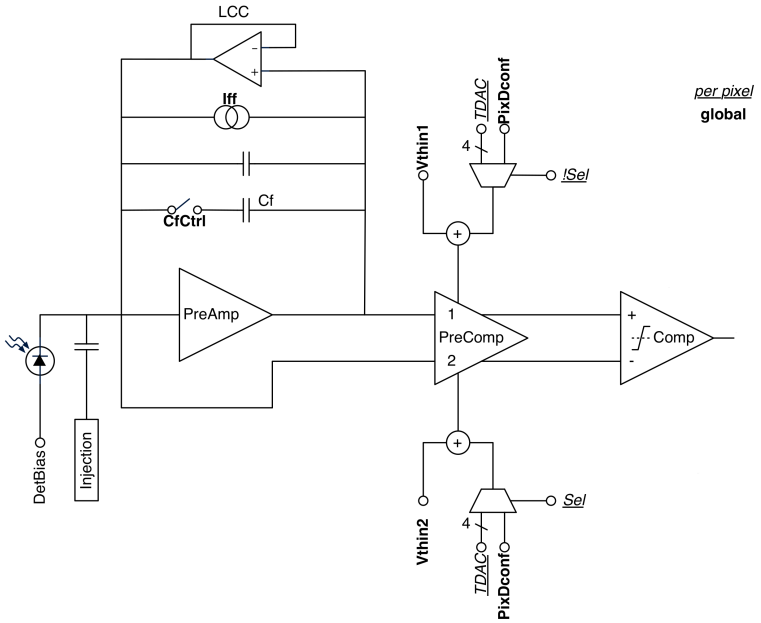

Figure 3.20: Schematic of the Differential front-end of the RD53A readout chip. From [Gar17].

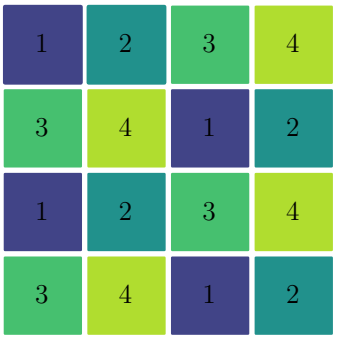

Figure 3.21: HitOR network of the RD53A readout chip for a group of 4×4 pixels. The colour scheme indicates how pixels are connected to the four independent HitOR lines ($1-4$).

Injection circuit

Each pixel of the readout chip features an injection circuit which allows the injection of a defined, programmable charge into the input of the analogue front-end. A voltage step is generated within the analogue chip bottom and distributed to the individual pixels. Within a pixel the voltage step is fed to the injection capacitor (nominal value of 8.5 fF [Gar17]) creating a charge signal at the input of the front-end. To compensate local ground variations in the chip a differential voltage step is generated from two DC-voltages `VCAL_HIGH` and `VCAL_MED` [Gar17]. The difference `VCAL_HIGH` − `VCAL_MED` of both voltages is called ΔVCAL. The maximum charge that can be injected into a single pixel is approximately 40 ke. Pixels for injection can be individually selected. This is necessary to limit the number of simultaneously injected pixels to respect timing requirements [Gar17]. Limitations of the injection circuit in terms of injection frequency and number of simultaneously injected pixels are investigated in [Daa21].

The injection circuit is used for testing the response of individual pixels or measuring their detection threshold as well as for detector calibration (see Sec. 6.3).

HitOR feature

The RD53A readout chip has a 4-net HitOR feature. The four independent HitOR networks are each fed with the discriminator outputs from every fourth pixel as illustrated in Fig. 3.21. In case two or more pixels connected to the same HitOR line are hit simultaneously, only the signal from the pixel with the highest charge is visible at the HitOR output (signal with highest charge overlaps all other signals). An unambiguous charge measurement is only possible if each HitOR line fires once (within an event), and thus restricts valid cluster shapes when utilising the HitOR feature. The arrangement of the HitOR network within the RD53A readout chip facilitates an unambiguous charge measurement of clusters up to 2×2 hit pixels. A method using the HitOR feature is presented in Sec. 6.2.2.

3.4.2 The ATLAS ITkPix readout chip

The ATLAS ITkPix readout chip [GLC19] is the pre-production chip for the HL-LHC upgrade of the ATLAS pixel detector. Like its successor, it is designed in a 65 nm CMOS process and developed by the RD53 collaboration within the RD53B design framework [GLC19]. In contrast to the RD53A readout chip, ITkPix has a single analogue front-end design: the Differential front-end (see Fig. 3.20). The analogue front-end design was slightly optimised with respect to RD53A, including a digital buffer at the comparator output ensuring fast edges. The pixel matrix has a size of $20 \times 21\,\mathrm{mm}^2$ corresponding to the size of the final production chip for the ATLAS ITk pixel detector. The pixel matrix consists of 400×384 pixels with a size of $50 \times 50\,\mu\mathrm{m}^2$. An improved version of the shunt-LDO regulators is implemented within the ITkPix readout chip. Furthermore, the new chip includes a high-precision ToT (time-over-threshold) and ToA (time-of-arrival) sampling using a 640 MHz clock, which can be used for high-precision charge measurements. [GLC19]

4 Passive CMOS sensors

Complementary metal-oxide-semiconductor (CMOS) is the most used logic family in commercial microelectronics. It is based on metal-oxide-semiconductor (MOS) junctions which are used to realise metal-oxide-semiconductor field-effect transistors (MOSFETs) [SN06]. In CMOS technology, NMOS (n-channel MOSFET) and PMOS (p-channel MOSFET) transistors are implemented in symmetrical pairs (complementary) on the same substrate. Compared to other logic families, CMOS circuits can be built without resistors and consume much less DC power, since one of the MOSFETs is always off and only during the switching of them current is drawn [SN06].

Besides the usage of CMOS technology for commercial production of integrated circuits, it is very common for the fabrication of readout electronics for high-energy physics detectors. Readout chips for hybrid pixel detectors are manufactured in CMOS technology [Mar+18; Gar+11; Poi+14] as well as a pixel of a depleted p-channel field-effect transistor (DEPFET) detector [KL87] consists of a MOSFET. Further, monolithic active pixel sensors (MAPS) [Tur+01; Per07] utilise commercial CMOS process lines and are investigated as an alternative to hybrid pixel detectors [Cai+19; Wan+18].

With this CMOS pixel development an interesting option became attractive that employs commercial CMOS process lines for the fabrication of planar sensors as the sensing part of hybrid pixel detectors. Commercial CMOS processes offer high throughput at comparatively low costs per wafer. The usage of CMOS sensors would reduce the costs by a factor of 3 – 4 compared to standard hybrid sensors. Currently, the main cost driver in production of hybrid pixel detectors is the sensor (together with the hybridisation). CMOS sensors are thus an attractive solution for large-area detectors like the future ATLAS or CMS pixel detectors (Sec. 3.4). Additional benefits arise from various features available in CMOS technology like several metal layers, MIM-capacitors and poly-silicon layers, which can help to enhance the sensor design (Sec. 4.1). These features are usually not available in conventional sensor production. In contrast to MAPS, these sensors do not contain active elements (transistors), and are therefore called *passive* CMOS sensors.

Passive CMOS sensors in a large-pixel design ($50 \times 250\,\mu m^2$ pixels) were already manufactured and investigated [Poh20]. Recent sensor submissions focus on passive CMOS sensors with a small-pixel design ($50 \times 50\,\mu m^2$ pixels). A prototype sensor is investigated in order to demonstrate the radiation tolerance of passive CMOS sensors and study different pixel designs for design optimisations [Die+20; Die+21; KK21]. Based on this, large-area sensors compatible

with the future ATLAS ITk pixel detector readout chip have been designed and investigated for the first time.

In the following, the essential steps in the fabrication of passive CMOS sensors (or any other CMOS circuits) are briefly discussed. In addition, features of CMOS processes which are especially of interest for sensors in high-energy physics are highlighted, and the processing of the backside, which is a crucial step during the production of silicon sensors, is briefly discussed. Finally, the design of the passive CMOS pixel sensors investigated in this thesis is presented.

4.1 Fabrication of passive CMOS sensors

For the fabrication of any silicon micro-chip high-purity silicon is necessary. In addition, high-resistivity substrates ($> 1\,\mathrm{k\Omega\,cm}$) are required for silicon detectors such that the depletion voltage is small and the detector can be fully depleted. There are two mono-crystalline silicon growing techniques: Float-Zone (FZ) and Czochralski (Cz). A more detailed description of both methods can be found in [Mol99]. Traditionally, silicon sensors are fabricated using FZ-silicon, since it can be produced with very high-purity and high resistivity (several $\mathrm{k\Omega\,cm}$). Further, the doping concentration is homogenous over the silicon ingot resulting in a homogeneous resistivity.

For commercial productions, mainly Cz-silicon is used. It is cheaper in fabrication but contains more impurities (mostly oxygen) compared to the FZ-technique. However, the oxygen can improve the radiation tolerance of silicon detectors [Mol99; Lin+01]. In addition, high-resistivity Cz-wafers ($> 1\,\mathrm{k\Omega\,cm}$) became available in the last years [Här+05] using the magnetic Cz-technique [Här+07]. With this technique the oxygen concentration can be controlled well and the impurity distribution is more homogeneous. This makes Cz-wafers an interesting alternative for future high-energy physics detectors in harsh radiation environments.

The implementation of the microstructures required for signal readout (charge collecting electrode) or sensor-specific features (e.g. biasing structures or guard rings) is done using photolithography. A simplified overview of the typical process steps during the fabrication of silicon sensors (here n-in-p sensor), or any CMOS device, can be seen in Fig. 4.1. A detailed description of all required steps can be found in [Lev05].

The first step is to protect the wafer with a thin layer of SiO_2 (thermal oxidation). Next, the photolithographic steps are done. First, a layer of photoresist is applied on the oxide layer. Subsequently, the photoresist layer is exposed to UV light using a mask with imprinted openings which have the shape of the desired micro-structure. The UV light exposure step is followed by a developing step which removes the exposed photoresist. Afterwards, an etching step removes the oxide which is not covered by the photoresist layer. The photolithography is finished by cleaning the wafer to remove the remaining photoresist. As a result, the wafer contains the negative of the mask as an oxide layer. In the next step, the ion implantation is done (here with phosphorus for n-doping) in order to implement shallow (a few µm) doped regions inside the

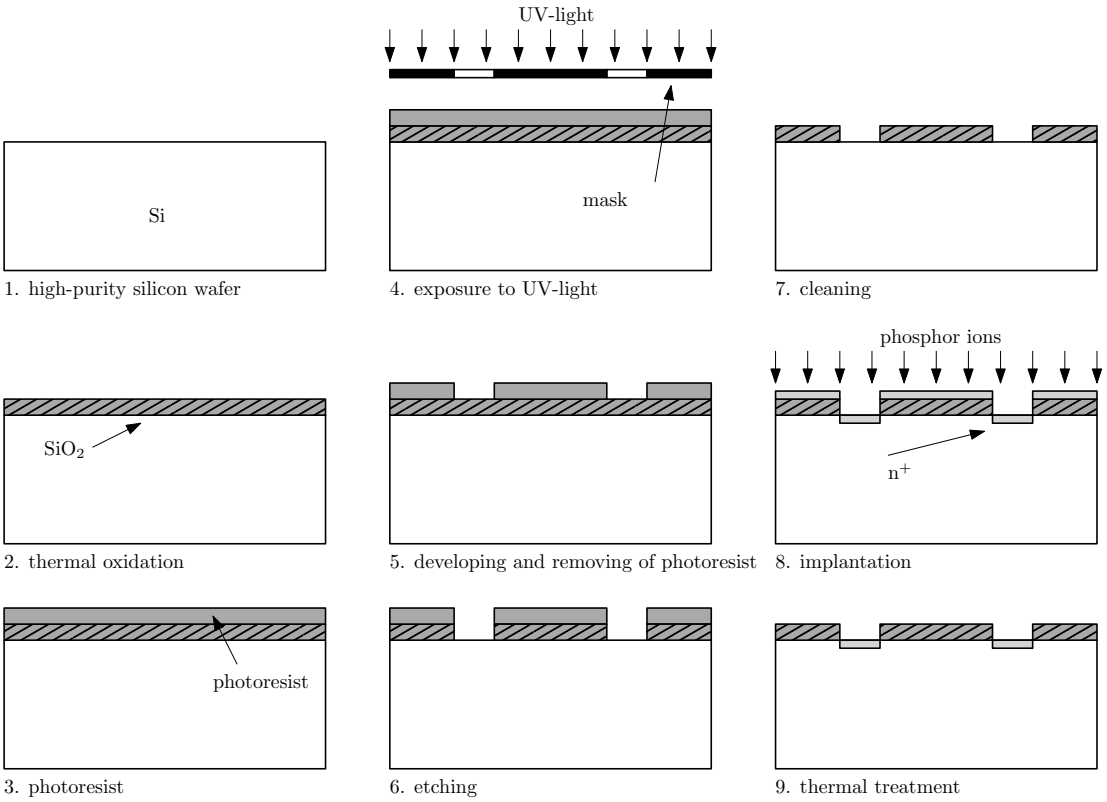

Figure 4.1: Simplified process steps of photolithography and semiconductor structuring for the fabrication of silicon sensors (here n-in-p sensor). Based on [Ros+06].

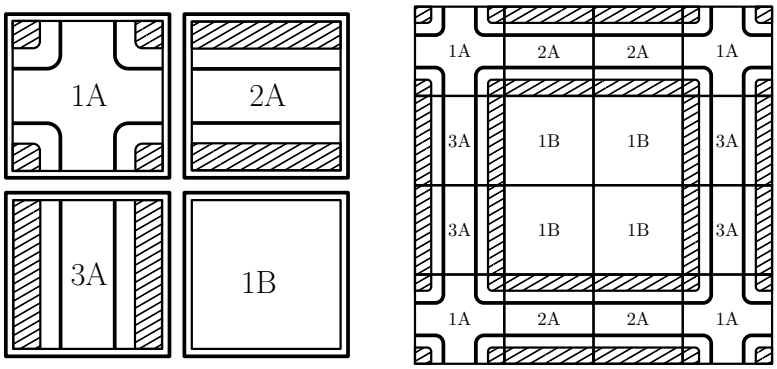

Figure 4.2: Left: Four reticles on which different blocks corresponding to the corner (1A), edge (2A and 3A) and centre regions (1B) of the sensor are implemented. Right: Stitched large-area sensor consisting of blocks 1A to 1B.

silicon bulk. Finally, the wafer undergoes a heat treatment to activate the dopants and anneal the damaged silicon caused by the ion implantation. By using additional photolithography steps, metal layers are applied to be able to contact the implantations (not shown in Fig. 4.1).

4.1.1 CMOS-features

Features like reticle stitching, poly-silicon layers and MIM-capacitors are common in CMOS technology. However, they are usually not available in conventional sensor production. In the following, these features are briefly described and it is shown how they help to enhance the sensor design.

Reticle stitching

Usually, the size of CMOS devices is limited by the reticle size which is in the order of $1\,\mathrm{cm}^2$. To fabricate sensors larger than the reticle size, so-called *reticle stitching* has to be used which is common for large-area CMOS image sensors [TGS11]. This technique requires that the sensor can be subdivided into smaller blocks (e.g. corner, edge and centre regions) that can be separately implemented on a reticle, as illustrated in Fig. 4.2. The stitched large-area sensor, shown in Fig. 4.7, is produced by illuminating the reticles one after another and stepping it accordingly. The size of the sensor is then no longer limited by the size of the reticle, but limited by the size of the wafer, which is usually much larger (e.g. 200 mm diameter). This technique is used to fabricate the large-area passive CMOS sensors described in Sec. 4.3.

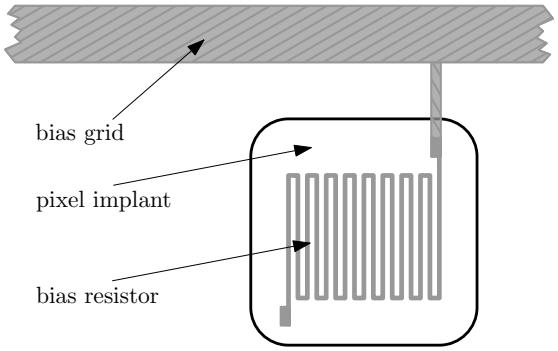

Figure 4.3: High-resistivity poly-silicon bias resistor connected to a bias grid (metal layer). Since the area of a single pixel is small, a meander-like structure is used to implement the bias resistor.

Poly-silicon as biasing structure

The complex and expensive interconnection process of hybrid pixel detectors (Sec. 3.3) requires electrical testing of the sensors (e.g. measurement of leakage current) beforehand such that malfunctioning sensors can be sorted out. To electrically test sensors it is required that all pixels can be put on a same fixed potential. This can be achieved with a bias grid (metal lines) to which all pixels are connected via a punch-through implantation [KW20] or a bias resistor. The connection has to be high-ohmic such that no current flows into the detector and the noise contribution is negligible.

As poly-silicon layers are available in CMOS processes, they can be used to realise a high-ohmic bias resistor as shown in Fig. 4.3. Since the area of a single pixel is limited, a meander-like structure is used such that resistances of several MΩ are possible. The biasing via a poly-silicon bias resistor has the advantage that there is no competing charge collecting electrode (punch-through implantation) for which an efficiency loss after irradiation is observed [Bey19]. However, both biasing structures can add parasitic capacitances degrading the performance of the readout chip (e.g. in terms of electronic noise).

MIM-capacitors for AC-coupling

In case of the usual DC-coupling of the pixels to the readout amplifier, leakage current flows into the amplifier's feedback circuit and introduces a voltage offset. Especially after irradiation, leakage currents can be large (approximately 10 nA per pixel) which would lead to a significant DC-offset at the amplifier bringing it out of its working point. To avoid this, most readout chips have extra leakage current compensation circuits [Ros+06]. AC-coupling the pixels with the readout amplifier makes an additional leakage current compensation circuit unnecessary, since the DC-component of the leakage current flowing into the amplifier is blocked. As MIM-

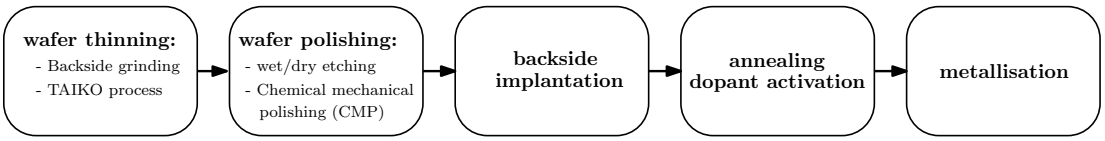

Figure 4.4: Typical steps during backside processing of silicon detectors.

capacitors are a common feature in CMOS technology they can be exploited as AC-coupling capacitors.

One aspect which has to be considered during the design of an AC-coupled sensor is the fact that the capacitor collects a fraction of the charge deposited in the sensor. This reduces the CCE of the readout chip and affects the detector calibration (Sec. 6.3.2).

4.1.2 Backside processing

The processing of the backside of silicon sensors for high-energy physics is a crucial and complex step. Since thin sensors keep the material budget of the detector low (better spatial resolution) and can be beneficial in terms of radiation hardness [Man+18] (see also Sec. 6.7), the thickness of sensors should be as low as possible. In contrast, handling and processing becomes more complex the thinner the sensors are. Typically, unthinned wafers with thicknesses of 750 µm are thinned down to 100 µm – 150 µm. Further, silicon sensors are mainly operated in overdepletion, i.e. the depletion zone extends to the backside contact. Thus, backside processing is required, which has a significant impact on the maximum operational voltage of silicon sensors, especially before irradiation. Issues due to improper backside processing during the fabrication of passive CMOS sensors were observed and are discussed in [Poh20] as well as in Sec. 6.7.1.

The typical steps of the processing of the backside for silicon detectors are shown in Fig. 4.4. First, the unprocessed wafer has to be thinned, which is usually done by grinding the wafer backside. This produces stress and leaves a layer of damaged silicon on the processed backside. Therefore, the coarse grinding step is typically followed by a chemical mechanical polishing (CMP) or etching (dry or wet), which reliefs stress and removes the damaged silicon from the processed side [Bur10]. Impacts on the production yield of passive CMOS sensors without an etching step are discussed in [Poh20]. It turned out that an etching of the backside is an essential step as it has a significant impact on the maximum operational voltage of the sensors. The thinner the wafer, the more difficult it is to handle. In order to improve the wafer handling performance, TAIKO thinning [Bur10] can be used, which leaves the outermost area of the wafer unthinned improving wafer stability and handling performance.

The remaining steps (backside implantation, annealing and metallisation) are necessary to provide a good ohmic contact (low resistance) to the backside such that the high voltage can be applied via the backside. Only if the silicon at the metal contact is highly doped (p^+

in case of n-in-p sensors) a good ohmic contact is formed [Ros+06]. Therefore, a backside implantation layer is added using ion implantation (usually Boron is used in case of p-type substrate). The thickness of this layer depends on the energy used for the ion implantation and the type of the ion. Typically, the implanted ions damage the silicon and are not electrically active. Thus, thermal treatment is necessary after this step to anneal the silicon and activate the dopants [Ros+06]. The highly doped backside implantation layer has two advantages. First, it prevents diffusion of the aluminium (from the backside metallisation, see below) into the silicon bulk, an effect known as spiking [GSS85]. Second, it restricts the expansion of the depletion zone. Both would otherwise short the silicon device as soon as the depletion zone reaches the backside. This fact makes the addition of an ion implantation layer a crucial step during backside processing, since it has to be deep enough to prevent spiking. Issues in the production of passive CMOS sensors, most likely due to a too shallow backside implantation layer, were observed and discussed in Sec. 6.7.1. This emphasises the importance of backside processing for over-depleted sensors. The last step during backside processing is the sputtering of metal onto the backside of the wafer providing contact to the sensor backside required for the application of high voltage. Typically, aluminium is used for metallisation (or an Al-Si alloy to largely suppress spiking [GSS85]).

4.2 Small-pixel prototype sensor

Passive CMOS prototype sensors are fabricated to demonstrate radiation tolerance and suitability for harsh radiation environments as for the upgrades of the LHC experiments. Further, these sensors are used to investigate charge collection properties and pixel capacitances of different pixel designs [Die+20; Die+21; KK21]. To study the performance of the sensors (Sec. 6.6), the pixel sensor is bump-bonded (by Fraunhofer IZM [IZM]) to the RD53A readout chip using fine-pitch solder bumps. In the following, the sensor design is presented.

This sensor is an n-in-p pixel sensor and is manufactured in 150 nm LFoundry CMOS technology [LFo] using a high-resistivity p-typed Czochralski wafer. The resistivity of the substrate is at least $2\,\mathrm{k\Omega\,cm}$ as stated by the foundry. Measurements show that the resistivity is $5\,\mathrm{k\Omega\,cm} - 7\,\mathrm{k\Omega\,cm}$ [Poh20]. The substrate is thinned to 100 µm using a TAIKO process including etching of the backside at Ion Beam Services (IBS) [IBS]. The thickness of the silicon that contributes to the charge collection is approximately 90 µm due to metal layers of the CMOS process. In addition, the backside was processed including a backside implantation and metallisation such that the bias voltage can be applied via the backside.

Fig. 4.5 shows the layout of the pixel matrix. It consists of 64×64 pixels with a size of $50 \times 50\,\mu\mathrm{m}^2$ compatible with the RD53A readout chip. In total, the sensor has an area of $3.8 \times 3.8\,\mathrm{mm}^2$. A schematic cross-section of a pixel can be seen in Fig. 4.6. Each pixel consists of an n-implantation (n-well) as the charge collecting electrode. The pixels are isolated from

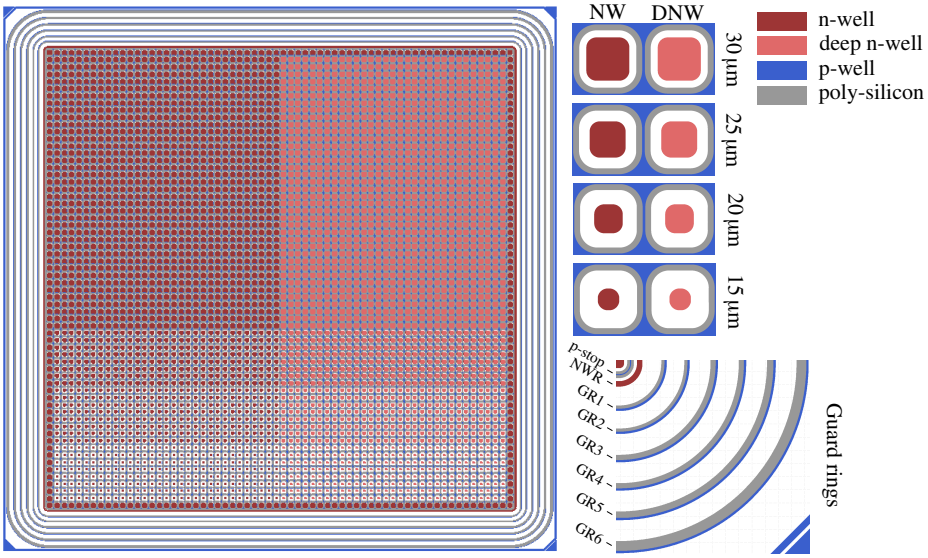

Figure 4.5: Layout of the passive CMOS prototype sensor with enlarged view of the various pixel designs (top) and guard rings (bottom). The pixel matrix consists of pixel designs with varying readout electrode sizes (top to bottom). The right half of the sensor consists of pixels with an additional deep n-well (DNW), the left half of the pixels has a standard n-well (NW) as a readout electrode. The active pixel area is surrounded by an n-implantation (n-well ring). Six guard rings isolate the pixels from the high voltage at the edge of the sensor.

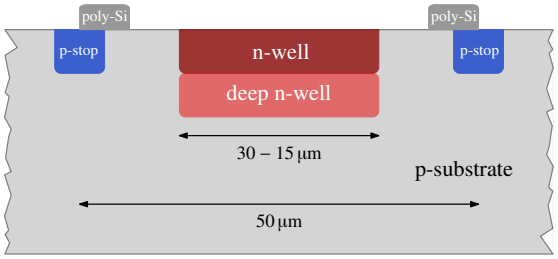

Figure 4.6: Simplified cross-section of an n-in-p pixel of the passive CMOS prototype sensor. Each pixel consists of an n-implantation (n-well), optionally with an additional deep n-implantation (deep n-well), as the charge collecting electrode embedded into a p-typed substrate. Small p-implantations (p-stop) isolate the pixels from each other. A low-resistive poly-silicon layer encloses the readout electrode. Metal layers are omitted.

each other with 4 µm-wide p-implantations, known as p-stop [Ros+06]. To investigate charge collection properties and study the pixel capacitance, the pixel matrix consists of different pixel flavours with varying size of the readout electrode (from top to bottom) ranging from 30 µm to 15 µm (later denoted as e.g. NW30). The right half of the pixel matrix has pixels with an additional deep n-implantation (deep n-well, denoted as DNW), whereas the left half of the

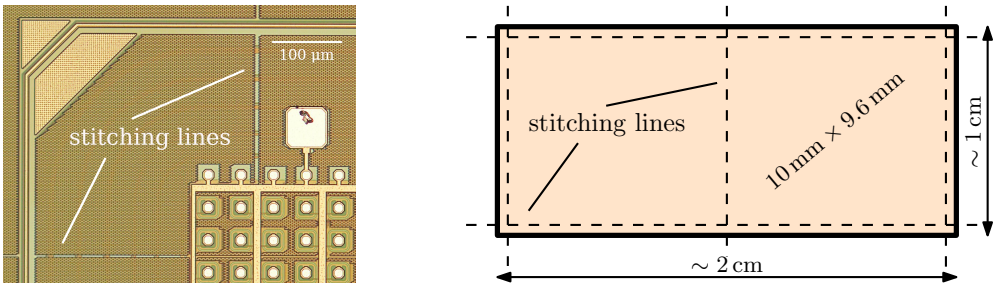

Figure 4.7: Left: Picture of stitching lines at the corner of a large-area passive CMOS sensor. Right: Schematic view of a stitched passive CMOS sensor with a size of $2 \times 1\,\mathrm{cm}^2$ (compatible with the RD53A readout chip). The locations of stitching lines are shown as dashed lines.

pixel matrix has pixels with a standard n-implantation (n-well, denoted as NW) as the charge collecting electrode. A fine-pitched low-resistivity poly-silicon layer surrounding the readout electrode is implemented with the intention to improve the breakdown voltage, especially after irradiation [Hem18]. The pixel matrix is enclosed with an n-implantation (n-well ring) confining the active pixel area. Further, six guard rings consisting of p-implantations and poly-silicon (see enlarged view in Fig. 4.5) are implemented to isolate the pixels from high voltage at the cutting edge of the sensor. The width and spacing of the guard rings increases towards the outside.

4.3 Large-area passive CMOS sensors

After several years of R&D including many submissions, large-area passive CMOS sensors for the future ATLAS and CMS experiments were designed and manufactured in a dedicated submission. The submission includes both pixel and strip sensors with various sensor designs and sizes. In the following, the design of the pixel sensors is shown. A description and characterisation of the passive CMOS strip sensors can be found in [Hön21; Rod21; Bas21].

The n-in-p sensors are fabricated in 150 nm LFoundry CMOS technology using a high-resistivity p-typed Float-Zone wafer. The design is based on the studies of the prototype sensor (pixel design) and requirements for the ATLAS and CMS experiments (wafer material and thickness). The pixel sensors are compatible with the future ATLAS ITk pixel readout chip ITkPix and its prototype RD53A. To demonstrate the production of large-area passive CMOS sensors, sensors up to sizes of approximately $4 \times 4\,\mathrm{cm}^2$ are manufactured. These sensors can be used to assemble ITkPix quad modules which are mainly used in the ATLAS or CMS detector. For characterisation (e.g. hit-detection efficiency and charge collection behaviour), sensors with sizes of approximately $2 \times 1\,\mathrm{cm}^2$ (compatible with the RD53A readout chip) are used. For the production of such large-area CMOS sensors reticle stitching (see Sec. 4.1) is used. Fig. 4.7 shows a picture of a stitching line (left) and the location of the various stitching lines for the investigated sensors.

Figure 4.8: Simplified cross-section of an n-in-p pixel of the large-area passive CMOS sensor. Each pixel consists of an n-implantation (n-well) as the charge collecting electrode embedded into the p-type substrate. Small p-implantations (p-stop) isolate the pixels from each other. A low-resistive poly-silicon layer encloses the readout electrode. Metal layers are omitted.

The sensors were thinned to 150 µm and further backside processed including etching and backside implantation done by LFoundry. A backside metallisation is added (by Fraunhofer IZM) such that the bias voltage can be applied from the backside. The pixel design follows that of the NW30-flavour from the prototype submission, as illustrated in Fig. 4.8. The n-implantation (n-well) acts as the charge collecting electrode and is isolated with 4 µm-wide p-implantations (p-stop). A fine-pitched low-resistive poly-silicon layer surrounds the readout electrode. The sensors are produced in different design variations, which are summarised in

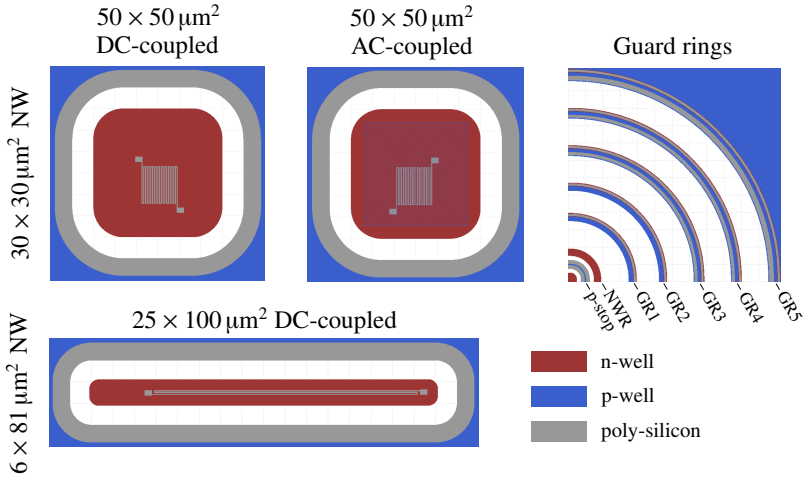

Figure 4.9: Left: Enlarged view of the various pixel designs. DC-coupled pixels are available in two different geometries ($50 \times 50\,\mu m^2$ and $25 \times 100\,\mu m^2$ pixels). AC-coupled pixels are implemented within the $50 \times 50\,\mu m^2$ geometry. All pixel designs feature a poly-silicon bias resistor connected to a bias grid. Right: Enlarged view of the guard ring structure (including n-well ring) surrounding the pixel matrix.

Fig. 4.9. Two different pixel geometries exist: $50 \times 50\,\mu m^2$ and $25 \times 100\,\mu m^2$ pixels. In case of

$50 \times 50\,\mu m^2$ pixels the readout electrode (n-well) has a size of $30 \times 30\,\mu m^2$, for the $25 \times 100\,\mu m^2$ pixels the readout electrode (n-well) has a size of $6 \times 81\,\mu m^2$. In addition, there are DC-coupled and AC-coupled sensors (using 560 fF MIM-capacitors). Common for all sensors is the feature of a bias grid and bias resistor (approximately 4.6 MΩ[1]) using high-resistivity poly-silicon enabling electrical testing of the sensors before interconnection with the readout chip. As for the prototype sensor, an n-implantation (n-well ring) surrounds the pixel matrix confining the active pixel area. Five guard rings (n- and p-implantations, see enlarged view in Fig. 4.9) with increasing width and spacing towards the outside are implemented to isolate the pixels from high voltage at the edge of the sensor.

[1] This value is extracted from measurements using dedicated test structures.

5 Beam telescope analysis

One of the main tools in testing of detectors for high-energy physics applications is a beam telescope in a minimum ionising particle beam (test beam). Typically, the beam telescope consists of several high-resolution tracking planes to obtain a precise spatial information of the traversing particles at different space points along the beam direction. Particles traversing the sensitive area of the detectors create hits which are used to reconstruct the particle tracks with high precision. The device under test (DUT) is usually installed in the centre of the beam telescope such that the reconstructed particle tracks can be extrapolated onto the DUT with a high spatial resolution. A detailed description of this complex setup can be found in Sec. 6.4. Using the reconstructed tracks, the hit-detection efficiency and the in-pixel charge collection behaviour of the DUT can be studied. Furthermore, the performance of the DUT is investigated for different parameters like the detection threshold, bias voltage, incidence angle or irradiation level in test beam studies.

From the binary raw data recorded by each detector plane to the reconstruction of particle tracks, the analysis requires dedicated software including many analysis steps. All the required steps are implemented within the *beam telescope analysis* software (BTA) [DJP]. The software is written in python and uses state-of-the-art scientific modules like NumPy [Har+20] and SciPy [Vir+20]. To reduce computation time, the package Numba [LPS15] is used for time-consuming calculations like track finding or fitting. BTA allows for detailed analysis of detector planes with high precision (a few µm) enabling in-pixel studies. Moreover, it provides a fast and easy-to-set-up analysis, which is beneficial for direct feedback on data taken during test beam measurements. BTA is already successfully used for several test beam studies of pixel detectors [Poh+17; Jan17; Ra20].

Within the scope of this thesis, the existing Kalman Filter tracking [Die17] was improved such that misalignment of the detector planes is properly considered (arbitrary orientation of detector planes). Further, a detector alignment using the Kalman Filter algorithm was implemented based on the work of [Sch14]. Details on track reconstruction and detector alignment using a Kalman Filter are given in Sec. 5.1 and 5.2. The calculation of the (in-time) hit-detection efficiency and its uncertainties are discussed in Sec. 5.3. In the following, the main analysis steps are briefly discussed.

Hit table. The raw data of each detector plane has to be converted into a *hit table* (one for each detector) containing all necessary information (*event number*, *frame*, *column*, *row*,

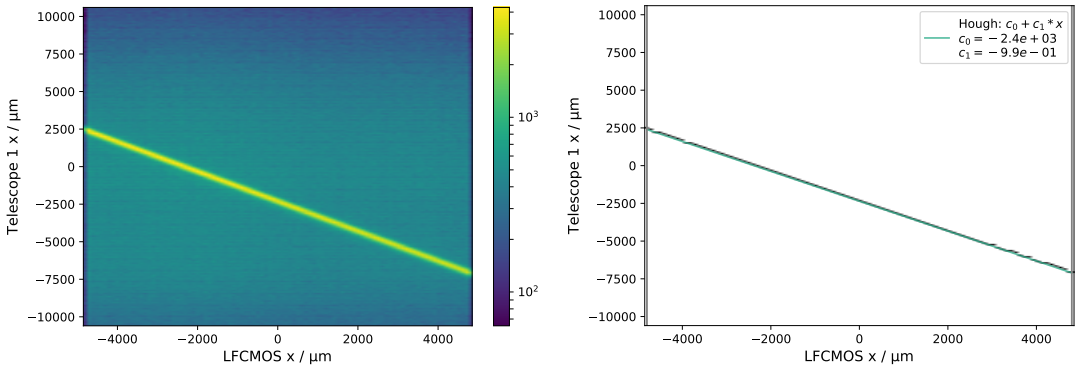

(a) Correlation of hits

(b) Pre-alignment

Figure 5.1: (a) Correlation of cluster positions in x-dimension between DUT and the first telescope plane. **(b)** Extracted correlation line (bin with highest number of entries). Using a Hough transformation, the offset is extracted yielding the alignment parameter Δx for the given plane.

charge). The *hit table* is aligned at events (*event number*). An event is defined by a trigger e.g. from a particle traversing the beam telescope. In addition, the hit arrival time relative to an event can be stored (*frame*) which is useful for timing studies.

Noisy pixel removal. Since noise hits (in the DUT) can artificially increase the measured hit-detection efficiency, it is necessary to remove noisy pixels in each detector. Noisy pixels are removed using a *median filter*.

Clustering. Locally associated hits (within an event) are grouped into clusters using the *pixel clusterizer* software [JP]. The mean cluster position x_{mean} in each dimension is calculated using the charge-weighted average (centre-of-gravity method):

$$x_{\text{mean}} = \frac{\sum_k q_k \cdot x_k}{\sum_k q_k} ,$$

with q_k being the measured charge of pixel k and x_k the measured hit position of pixel k. The cluster charge is calculated by summing up all charges from pixels belonging to the cluster. To account for masked pixels or inefficient hits, a maximum cluster distance in both dimensions can be specified between hits to decide whether they are assigned to the same cluster or not. A cluster distance of 2 is typically chosen so that one "hole" between two cluster pixels is allowed to assign them to the same cluster. Pixels masked as noisy are not considered during clustering. Clusters consisting of solely noisy pixels are masked and excluded from the analysis.

Correlation and Pre-alignment. For later track reconstruction a common coordinate

system has to be defined. Usually, the detector planes are displaced and rotated against each other. The aim of the alignment procedure is to find the translations $(\Delta x, \Delta y, \Delta z)$ and rotations (α, β, γ) for each detector plane such that measured hit positions can be transformed into the common coordinate system. The alignment procedure consists of two steps. The first step is a coarse pre-alignment that estimates the translations Δx and Δy. This is done by correlating the cluster positions (within an event) in each dimension for each detector to a given reference plane (usually the first tracking plane). If event building is properly done, a linear correlation is visible, as illustrated in Fig. 5.1a. A single wrongly reconstructed event results in no correlation. Fig. 5.1b shows the extracted correlation (bin with highest number of entries). The translations Δx and Δy are given by the offsets of the correlation lines in the respective dimension, which are extracted using a Hough transformation [DH72].

Fine-alignment. The second step of the detector alignment is the fine-alignment, which aims to improve the alignment parameters estimated from the pre-alignment and find the complete set of alignment parameters for each detector plane. The fine-alignment is an iterative procedure combining *track finding*, *track fitting* and *data selection* (see following steps). Initial values for the alignment are taken from the pre-alignment. With each iteration, the alignment parameters are updated until they do not change any more or the maximum number of iterations is reached. Within the scope of this thesis, an alignment procedure employing the Kalman Filter is implemented. Details regarding this algorithm are given in Sec. 5.2.

Track finding. Clusters from different detector planes have to be associated to track candidates, known as *track finding*. The cluster position is linearly extrapolated to the next detector plane and the best matching cluster (smallest distance) is assigned to the track candidate. Each cluster is used only once. This simple approach yields sufficient track finding efficiency, since track angles are small and the track density is low in a test beam.

Track fitting. From the track candidates found in the *track finding* step tracks are reconstructed (*track fitting*). Within BTA, two reconstruction methods based on a χ^2-minimisation are available: straight-line fit and track fitting using a Kalman Filter. In this thesis, the Kalman Filter fitting is used for track reconstruction as it accounts for the effects of multiple scattering (Sec.6.4). The algorithm is described in detail in Sec. 5.1. Detector planes used for the track fitting can be specified, as well as detector planes which are required to have a hit. In addition, a minimum number of hits per track can be defined. Usually, only the high-precision tracking planes are included in the fit and the DUT is excluded from the fit (hit information of DUT is not used) to obtain unbiased tracks for the subsequent efficiency calculation. Furthermore, quality requirements on fitted tracks

can be defined.

Data selection. During *data selection*, tracks not fulfilling the quality and hit requirements defined in the *track fitting* are discarded. Further, a χ^2 criterion for the track can be used. Applying these cuts ensures that only properly reconstructed tracks are selected for further analysis. Impacts of these criteria on the uncertainty of the hit-detection efficiency are briefly discussed in Sec. 5.3.

Residual calculation. The residuals provide important information to judge and validate the analysis of beam telescope data. The track residual in one dimension (e.g. in x-dimension)

$$\Delta r_x = x_{\text{hit}} - x_{\text{track}} \tag{5.1}$$

is defined as the difference between the track intersection x_{track} and the measured hit position x_{hit} at a given detector plane. With correct alignment and proper track reconstruction, the histogram of the track residuals should yield a Gaussian distribution centred around zero. The width of the unbiased residual distribution is given by[1]

$$\sigma_{\text{res}} = \sqrt{\sigma_{\text{int}}^2 + \sigma_{\text{point}}^2}\,, \tag{5.2}$$

where $\sigma_{\text{int}} = \frac{p}{\sqrt{12}}$, with p being the pixel size, denotes the intrinsic resolution of the detector and σ_{point} the pointing resolution at the detector plane. The residual width is therefore a measure for the track resolution.

Fig. 5.2 shows an unbiased residual distribution for the DUT (in y-dimension). The distribution is centred around zero and the 1σ-width extracted from a fit of a Gaussian function is approximately 20 µm. The width is slightly larger than the expected intrinsic resolution of 14.4 µm (with a pixel pitch p of 50 µm) which can be explained by the finite pointing resolution of a few µm (see Eq. 5.2).[2] The deviations from the Gaussian function towards the tails are due to multiple scattering, which follows a Molière distribution [Mol47]. The flat background is attributed to wrongly reconstructed tracks.

Result analysis. Using the reconstructed tracks, a detailed analysis of the DUT can be done. This includes the calculation of the hit-detection efficiency or investigation of the charge collection behaviour. It is possible to do in-pixel analyses in order to study the detector performance within a pixel. For statistical reasons, all data is mapped onto one pixel. Moreover, specific areas of interest can be selected for analysis. This is useful for analysing detectors that have different designs implemented on the same matrix.

[1] Assuming negligible influence from the hit and track reconstruction algorithm of the analysis software.
[2] The pointing resolution is slightly worsened by the additional material of the cooling infrastructure (cooling box for DUT and PCB cooling plate).

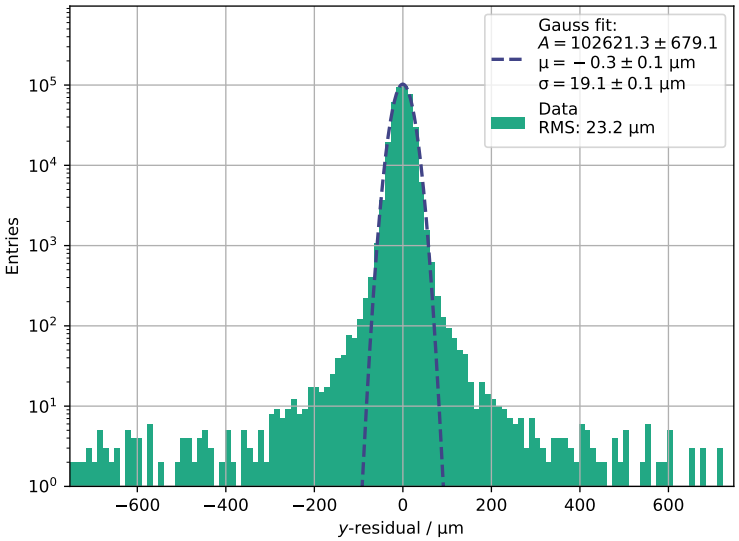

Figure 5.2: (Unbiased) residual distribution in y-direction at the DUT. Data is shown on a logarithmic scale. The distribution is fitted with a Gaussian function (dashed line) to extract the width of the distribution.

5.1 Track reconstruction with a Kalman Filter

The Kalman Filter [Kal60] is a widely used tool not only for track reconstruction in high-energy physics [Frü+93; BCR00; Sch14; Bra18; Cer+19], but also in fields outside of physics (e.g. navigation or finance). It provides an optimal estimate for (unobservable) states of a discrete linear dynamic system including noise [Frü+00]. In the case of Gaussian noise, the Kalman Filter is efficient and no other non-linear Filter yields better results (minimal variance) [Frü+93]. The Kalman Filter is an iterative procedure consisting of a *prediction step* and a *filter step*. In the filter step, the prediction from the prediction step is updated using the measurement. Thus, with each iteration more information is added. The Kalman Filter was applied to track and vertex fitting originally in [Frü87]. The discrete dynamic system is defined using a track state which describes the particle track in each point of its trajectory (e.g. at the detector planes). The track state, usually parametrised by a vector consisting of a position and direction, is linearly extrapolated from one detector plane to another including the effects of multiple scattering at each layer. The filter step updates the track state using the weighted mean of the prediction and the measurement. An explicit expression for the Kalman Filter prediction and filter formulas can be found in [Frü87]. The system and measurement equation of a linear dynamic system are

given by [Frü87]

$$x_k = F_{k|k-1} x_{k-1} + w_k \tag{5.3}$$

$$m_k = H_k x_k + \epsilon_k \,, \tag{5.4}$$

where x_k denotes the track state at detector plane k and $F_{k|k-1}$ is a matrix propagating the track state from detector plane $k-1$ to k. The process noise, here due to multiple scattering between detector plane $k-1$ and k, is described by w_k and its covariance matrix $Q_k = \mathrm{cov}\,\{\mathrm{w_k}\}$. The matrix H_k extracts the measurements m_k (usually the hit position) from the track state x_k. The measurement noise is given by ϵ_k with its covariance matrix $V_k = \mathrm{cov}\,\{\epsilon_\mathrm{k}\}$.

In contrast to "global" fit methods [Frü+00], no large matrices have to be inverted (computationally expensive) within the Kalman Filter.

Due to the progressive nature of the Kalman Filter, the precision of the estimated track state increases with the number of iterations, i.e. the best precision is obtained at the last detector plane. However, for track fitting it is desirable that the track state can be predicted as precisely as possible at the DUT (usually placed in the centre of the beam telescope). This problem is solved by using a Kalman Filter smoother (see Eq. 5.27), which combines measurements from all detector planes (except that from the DUT) at any layer, and therefore provides an optimal estimate of the track state.

If the dynamic system is non-linear, which is the case for arbitrary orientation of the detector planes (the tilts make the system equation non-linear), a linearisation (first-order Taylor expansion) is required such that the Kalman Filter equations can be applied. A linearisation around a so-called *reference state* is proposed in [Frü+93]. This linearisation is successfully used in [Sch14] to fit tracks using a Kalman Filter with arbitrary orientation of the detectors. The implementation of the Kalman Filter in BTA is based on this approach.

In the following, details of the algorithm are given including the linearisation of the system equation using a *reference state*. Further, the parametrisation of multiple scattering and the implementation of smoothing is discussed.

Local track parameters and propagation

In the absence of a magnetic field, the particle track can be parametrised as a 3D straight line. The track state p_k at detector plane k is defined as

$$p_k = \begin{pmatrix} x \\ y \\ t_x \\ t_y \end{pmatrix} \,, \tag{5.5}$$

with x and y denoting the intersections at detector plane k in the local coordinate system ($z = 0$). The direction tangents in the local coordinate system are denoted with $t_x = \mathrm{d}x/\mathrm{d}z$ and $t_x = \mathrm{d}y/\mathrm{d}z$. The uncertainty of a track state p_k is given by its 4×4 covariance matrix C_k.

The track propagator $f_{k|l}$ maps the local track state p_l of detector plane l to the track state p_k in the local coordinate system of detector plane k:

$$p_k = f_{k|l}(p_l)\,. \tag{5.6}$$

The 4×4 transport matrix $F_{k|l}$ (see Eq. 5.3) is given by the partial derivatives (Jacobian) of the track propagator with respect to the track parameters at detector plane l (linear extrapolation):

$$F_{k|l} = \frac{\partial f_{k|l}}{\partial p_l}\,. \tag{5.7}$$

The partial derivatives for an arbitrary orientation of detector planes were calculated in [Kar99].

Multiple scattering

Multiple scattering in the detector planes can be parametrised with two mutually orthogonal and uncorrelated scattering angles θ_1 and θ_2, which are assumed to be small[3] [WH93]. The 2×2 covariance matrix V_θ of the two scattering angles can be expressed as

$$V_\theta = \begin{pmatrix} \sigma^2 & 0 \\ 0 & \sigma^2 \end{pmatrix}\,, \tag{5.8}$$

where σ^2 is the variance of the projected scattering angles. The standard deviation of the approximately Gaussian distributed scattering angles is given by Eq. 3.13 and repeated here for completeness

$$\sigma = \frac{13.6}{\beta c p} z \sqrt{\frac{L}{X_0}} \left[1 + 0.038 \ln\left(\frac{L}{X_0}\right)\right]\,, \tag{5.9}$$

where βc, p and z are the velocity, the momentum (in MeV) and the electrical charge (in units of e) of the particle, L is the path length through the detector and X_0 is the radiation length of the detector material.

The scatter function $g_{\mathrm{ms}}(\theta_1, \theta_2)$ describes the scattering as a function of the two scattering angles θ_1 and θ_2, i.e. transforms the unscattered track state p_k into a scattered track state p_k^*. To calculate the covariance matrix Q_k of the process noise (see Eq. 5.3), the partial derivatives of the scatter function g_{ms} with respect to the track state p_k are required:

$$Q_k = \frac{\partial g_{\mathrm{ms}}(\theta_1, \theta_2)}{\partial p_k} = G_k V_\theta G_k^\top\,. \tag{5.10}$$

[3] Usually, thin detectors are used such that this is a valid approximation.

In the last step, the transformation of covariance matrices is used with the scatter gain matrix $G_k = \frac{\partial p_k}{\partial \theta_i}$. These partial derivatives were calculated in [WH93] with the help of a comoving coordinate system relative to the local coordinate system of the detector plane. For thin detectors, it is assumed that multiple scattering only affects the direction and displacements can be neglected. Therefore, the only non-zero entries of the 2×4 scatter gain matrix G_k are $(\theta_1, \theta_2 \to 0)$ [WH93]:

$$G_{3,3} = \left.\frac{\partial p_3}{\partial \theta_1}\right|_{\theta_1,\theta_2 \to 0} = \frac{\alpha_1\gamma_3 - \alpha_3\gamma_1}{(\gamma_3)^2} \tag{5.11}$$

$$G_{3,4} = \left.\frac{\partial p_3}{\partial \theta_2}\right|_{\theta_1,\theta_2 \to 0} = \frac{\alpha_2\gamma_3 - \alpha_3\gamma_2}{(\gamma_3)^2} \tag{5.12}$$

$$G_{4,3} = \left.\frac{\partial p_4}{\partial \theta_1}\right|_{\theta_1,\theta_2 \to 0} = \frac{\beta_1\gamma_3 - \beta_3\gamma_1}{(\gamma_3)^2} \tag{5.13}$$

$$G_{4,4} = \left.\frac{\partial p_4}{\partial \theta_2}\right|_{\theta_1,\theta_2 \to 0} = \frac{\beta_2\gamma_3 - \beta_3\gamma_2}{(\gamma_3)^2}\,, \tag{5.14}$$

with α_i, β_i, γ_i being the elements of the rotation matrix connecting the comoving coordinate system with the local coordinate system of the detector [WH93].

Measurement equation

The measurements m_k at detector plane k are given by the measurement equation

$$m_k = \begin{pmatrix} x_m \\ y_m \end{pmatrix} = H_k p_k + \epsilon_k\,, \tag{5.15}$$

where ϵ_k is the measurement noise with its covariance matrix V_k. The matrix

$$H_k = \begin{pmatrix} 1 & 0 & 0 & 0 \\ 0 & 1 & 0 & 0 \end{pmatrix} \tag{5.16}$$

extracts the measurements from the track state p_k. The covariance matrix V_k is parametrised using the intrinsic resolutions $\sigma_{\text{int},x}$ and $\sigma_{\text{int},y}$ of the detector

$$V_k = \begin{pmatrix} \sigma^2_{\text{int},x} & 0 \\ 0 & \sigma^2_{\text{int},y} \end{pmatrix}. \tag{5.17}$$

For the high-resolution tracking planes (Mimosa26 sensors, see Sec. 6.4), an intrinsic resolution of 3.5 µm is assumed, whereas for other detector planes the intrinsic resolution is estimated as $\sigma_{\text{int}} = p/\sqrt{12}$ with p being the pixel pitch.

Initial state

For the first iteration of the Kalman Filter, an estimation of the track state p_0 at the very first detector plane (initial state) is required. This track state p_0 is called track seed. A track seed is calculated by fitting all measurements (excluding that of the detector plane for which tracks are fitted) using a simple straight line fit (neglecting multiple scattering). The intersection of the fitted track with the very first detector plane is used as the track seed. Its covariance matrix C_0 is assumed to be

$$C_0 = \begin{pmatrix} \sigma_x^2 & 0 & 0 & 0 \\ 0 & \sigma_y^2 & 0 & 0 \\ 0 & 0 & \sigma_{t_x}^2 & 0 \\ 0 & 0 & 0 & \sigma_{t_y}^2 \end{pmatrix} , \tag{5.18}$$

with σ_x and σ_y being the beam size in x- and y-dimension, and σ_{t_x} and σ_{t_y} being the beam divergence in x- and y-dimension. The beam size is typically a few mm, whereas the beam divergence is a few mrad.

Linearised system equations

The linearisation of the track model (system equation) follows the discussions in [Sch14]. The track model is based on scattering at detector plane k

$$p_k^* = g_{\text{ms}}(p_k, \theta_1, \theta_2) \tag{5.19}$$

and the track propagation from detector plane k to $k+1$

$$p_{k+1} = f_{k+1|k}(p_k^*) \, . \tag{5.20}$$

It is therefore a composition of the scatter function g_{ms} and the track propagator $f_{k+1|k}$:

$$p_{k+1} = f_{k+1|k}(g_{\text{ms}}(p_k, \theta_1, \theta_2)) \, . \tag{5.21}$$

According to [Frü+93], the system can be linearised by defining a so-called *reference track*. The intersection of the *reference track* with detector plane k is denoted with $p_{k,r}$. With the assumption that the differences of the track state p_k and the reference state $p_{k,r}$ are small, they can be propagated linearly [Sch14]:

$$p_{k+1} - p_{k+1,r} = F_{k+1|k}(p_k - p_{k,r}) + F_{k+1|k} G_k w_k \, , \tag{5.22}$$

with $F_{k+1|k}$ and G_k evaluated at the reference state $p_{k,r}$. The Kalman Filter equations can then be applied (without any correction) to the differences

$$\Delta p_k = p_k - p_{k,r} \tag{5.23}$$

$$\Delta m_k = m_k - H_k p_{k,r}\,, \tag{5.24}$$

i.e. the Kalman Filter operates at the differences Δp_k, Δm_k. Finally, the linearised system equation is given by [Sch14]

$$\Delta p_{k+1} = F_{k+1|k}\Delta p_k + F_{k+1|k}G_k w_k\,. \tag{5.25}$$

Analogously to this *forward* filter (track states propagate from k to $k+1$), the system equation can be formulated for a *backward* filter (propagating from $k+1$ to k) [Sch14]

$$\Delta p_k = \left(F_{k+1|k}\right)^{-1}\Delta p_{k+1} - G_k w_k\,. \tag{5.26}$$

The *forward* filtered track state p_k^f (before scattering) at detector plane k includes all measurements of detector planes $j \leq k$, while the *backward* filtered track state p_k^b at detector plane k includes all measurements of detector planes $j \geq k$. The *forward* and *backward* filter can be combined to make use of the full hit information (smoothing).

The *reference track* is calculated by extrapolating the track seed to all detector planes and updating the reference states with a backward filter. This procedure yields *reference tracks* following the particle track close enough such that the differences between track state and reference state are small, and thus can be linearly propagated (see Eq. 5.25 and 5.26).

Smoothing

To find the optimal track estimate at detector plane k, the information from layers in front of and behind detector plane k is used. This procedure is called *smoothing*. Within the "two-filter formula" for smoothing the result of the *forward* filter (Δp_k^f, C_k^f) and *backward* filter (Δp_k^b, C_k^b) is combined using the weighted mean formalism. The smoothed track state p_k^s and its covariance matrix C_k are then given by [Frü+00]

$$\Delta p_k^s = C_k\left((C_k^f)^{-1}\Delta p_k^f + (C_k^b)^{-1}\Delta p_k^b\right)\,, \tag{5.27}$$

$$C_k = \left((C_k^f)^{-1} + (C_k^b)^{-1}\right)^{-1}\,. \tag{5.28}$$

After calculation of the smoothed result, the reference state can be added again to obtain the optimal estimate p_k of the real particle track. Its covariance matrix is given by C_k. The smoothed track state p_k contains information from all detector planes excluding the measurement at detector plane k itself (filtering at detector plane k is omitted when tracks are fitted for detector

plane k). The track estimates p_k and its covariance matrix C_k are therefore unbiased.

The χ^2 for each track is calculated by summing up the contributions from the individual detector planes

$$\chi^2 = \sum_k^{\text{hits}} r_k^\top R_k^{-1} r_k \,, \tag{5.29}$$

with $r_k = m_k - Hp_k$ being the residual and R_k the covariance matrix of the residual at detector plane k

$$R_k = HC_kH_k^\top + V_k \,. \tag{5.30}$$

5.2 Detector alignment with a Kalman Filter

The application of the Kalman Filter for the alignment of detectors was originally proposed in [FTW03]. The estimation of the shifts Δx, Δy and the rotation $\Delta\gamma$ (around the z-axis) using a Kalman-Filter-based alignment was successfully demonstrated therein. An extension of this procedure allowing for an estimation of the complete set of alignment parameters $(\Delta x, \Delta y, \Delta z, \Delta\alpha, \Delta\beta, \Delta\gamma)$ is introduced in [Sch14]. The following discussion and the implementation of a Kalman-Filter-based detector alignment within BTA is based on this work.

The basic principle of the detector alignment using a Kalman Filter is the simultaneous and iterative estimation of both track parameters (track reconstruction) and alignment parameters (detector alignment). With each processed track, the alignment parameters are updated. For the estimation of track parameters, the current best knowledge of alignment parameters is used such that the bias on the estimation of track parameters due to misaligned detectors reduces as more tracks are processed.

The misalignment of the detector planes follows the parametrisation presented in [Kar+03]. The transformation from global coordinates x_{global} to local coordinates x_{local} is described by

$$x_{\text{local}} = R(x_{\text{global}} - \vec{r}) \,, \tag{5.31}$$

with R being a rotation matrix and $\vec{r}$ the position of the detector plane in the global coordinate system. In this alignment procedure, the true rotation matrix R_i^* and position $\vec{r}_i^*$ of detector plane i are estimated by updating the initial rotation matrix R_i and position $\vec{r}_i$ of the detector plane:

$$R_i^* = \Delta R_i R_i \tag{5.32}$$

$$\vec{r}_i^* = \Delta\vec{r}_i + \vec{r}_i \,. \tag{5.33}$$

The vector $\Delta\vec{r}_i = (\Delta x, \Delta y, \Delta z)$ and the rotation matrix ΔR_i contain the differences of the shifts and rotations between true and initial alignment, respectively. In the small-angle approximation,

ΔR_i can be written as

$$\Delta R_i = \begin{pmatrix} 1 & \Delta\gamma_i & \Delta\beta_i \\ -\Delta\gamma_i & 1 & \Delta\alpha_i \\ -\Delta\beta_i & -\Delta\alpha_i & 1 \end{pmatrix} , \tag{5.34}$$

with $\Delta\alpha_i$, $\Delta\beta_i$, $\Delta\gamma_i$ being the tilts around the x-, y- and z-axis of the local coordinate system of detector plane i. For large tilts, the full rotation matrix is calculated. Finally, the misalignment can be parametrised by a six-dimensional vector $\vec{a}_i = (\Delta x_i, \Delta y_i, \Delta z_i, \Delta\alpha_i, \Delta\beta_i, \Delta\gamma_i)$ containing the alignment parameters. The goal of the alignment procedure is to find an optimal estimate for $\vec{a}_i$.

In the following, the formalism for the Kalman-Filter-based alignment of detectors is presented [FTW03]. Similar to Eq. 5.4, the measurement equation can be expressed as

$$m_{ij} = h_{ij}(p_{ij}, a_{ij}) + \epsilon_{ij} . \tag{5.35}$$

The measurement m_{ij} of detector plane i and track j depends both on the track state p_{ij} and the alignment parameters a_{ij}. The measurement noise is described by ϵ_{ij} with the covariance matrix $V_{ij} = \text{cov}\{\epsilon_{ij}\}$. After linearisation of the measurement equation (first-order Taylor expansion), the update formulas for the alignment parameters a_{ij} and their covariance matrices E_{ij} (from track j to track $j+1$) are given by [FTW03]

$$a_{ij+1} = a_{ij} + E_{ij} D_{ij}^{\top} W_{ij} \left[m_{ij} - h_{ij}(p_{ij}, a_{ij}) \right] \tag{5.36}$$

$$, \tag{5.37}$$

$$E_{ij+1} = E_{ij} - E_{ij} D_{ij}^{\top} W_{ij} D_{ij} E_{ij}^{\top} , \tag{5.38}$$

with

$$W_{ij} = \left(V_{ij} + H_{ij} C_{ij} H_{ij}^{\top} + D_{ij} E_{ij} D_{ij}^{\top} \right)^{-1} . \tag{5.39}$$

The matrices H_{ij} and D_{ij} contain the partial derivatives (Jacobian) of m_{ij} with respect to the track parameters p_{ij} and the alignment parameters a_{ij}, respectively:

$$H_{ij} = \frac{\partial m_{ij}}{\partial p_{ij}} \tag{5.40}$$

$$D_{ij} = \frac{\partial m_{ij}}{\partial a_{ij}} . \tag{5.41}$$

The matrix H_{ij} is given by Eq. 5.16, whereas the matrix D_{ij} is computed in two steps as presented in [Sch14]. The derivatives D_{ij}^{loc} with respect to the alignment parameters a_{ij}^{loc} in the

local coordinate system are calculated as in [Kar+03]:

$$D^{\text{loc}} = \begin{pmatrix} -1 & 0 & t_x & -yt_x & xt_x & -y \\ 0 & -1 & t_y & -yt_y & xt_y & x \end{pmatrix} , \tag{5.42}$$

with x, y being the position and t_x, t_y being the direction tangents in the local coordinate system. To obtain the derivatives with respect to the global alignment parameters a_{ij}, the chain rule is applied

$$D_{ij} = \frac{\partial h_{ij}}{\partial a_{ij}^{\text{loc}}} \frac{\partial a_{ij}^{\text{loc}}}{\partial a_{ij}} = D_{ij}^{\text{loc}} A_{ij} \, . \tag{5.43}$$

The 6×6 matrix A_{ij} is given by [Sch14]

$$A_{ij} = \frac{\partial a_{ij}^{\text{loc}}}{\partial a_{ij}} = \begin{pmatrix} R_i & 0_{3\times3} \\ 0_{3\times3} & \mathbb{1}_{3\times3} \end{pmatrix} , \tag{5.44}$$

with R_i being the rotation matrix of detector plane i. The advantage of using global alignment parameters becomes obvious when considering tilted detectors. In this case, the tuples $(\Delta x, \Delta z)$ and $(\Delta y, \Delta z)$ of the local alignment parameters are strongly dependent on the tilts $\Delta\alpha$ and $\Delta\beta$. Using global alignment parameters, this correlation can be avoided.

To make use of the information from all detector planes during the alignment, the smoothed track estimate p_{ij} with its covariance matrix C_{ij} is used to update the alignment parameters. With more processed tracks j, the alignment improves (converges to true alignment) as more information is gained. However, due to the fact that the estimation of the track states depends itself on the accuracy of the alignment (especially at the beginning the inaccuracy of the alignment is large), the procedure can run into a local minimum of the global χ^2-function. This was observed in [FTW03] and solved by so-called *annealing*. With annealing, the measurements are progressively weighted more (see below). Further, an update of the alignment parameters can be rejected if the relative change (full covariance matrix is known) is too large (outlier rejection). This can happen if a track is contaminated with a noise hit. In the following, details of the Kalman Filter alignment algorithm implemented within BTA are given.

Initial alignment

The alignment procedure requires initial values for the alignment parameters. The natural choice is to use the alignment parameters calculated from pre-alignment which yields initial values for the shifts Δx and Δy. The z-coordinates are given by an explicit measurement of the distances between each detector plane. The initial tilts of the detector planes are assumed to be zero, since usually the detector planes are mechanically mounted resulting in tilts of only a few mrad. For scans with intentionally tilted detectors (e.g. the DUT), non-zero starting values can be specified. Since the track finding step before the alignment procedure is done using

the pre-alignment, the vector $\vec{a}_0$ containing the change with respect to the initial alignment is set to zero. For the initial covariance matrix E_0 of the alignment parameters, the precision of the pre-alignment is used, respectively the systematic error from the z-position measurement. Typical uncertainties for the shifts are 100 µm – 300 µm, and the uncertainty on the z-position is assumed to be a few mm. The uncertainty of the tilts is assumed to be a few mrad.

The convergence of the algorithm depends strongly on the initial values and their uncertainties, so that it is recommended to adjust the initial values and their uncertainties for (intentionally) tilted detectors with tilts of a few 100 mrad.

Geometric annealing

Especially at the beginning of the alignment procedure, the alignment is not known precisely, and can therefore strongly bias the estimated track parameters, which are used to update the alignment. Thus, it can happen that the alignment does not converge or runs into a local minimum of the χ^2-function. To avoid this problem a so-called *annealing* schedule is proposed by [FTW03]. The idea is to reduce the weight of the measurements especially at the beginning of the alignment procedure. This is achieved by scaling the measurement covariance matrix $V \to \alpha V$ with an *annealing factor* $\alpha \geq 1$. The annealing factor reduces as more tracks are processed, i.e. the weight of the measurements increases with the number of processed tracks j. Various annealing schedules were tested in [FTW03], with the so-called *geometric annealing* schedule yielding best convergence behaviour:

$$\alpha(j) = \begin{cases} b^{\frac{m-j}{m-1}}, & j < m \\ 1, & j \geq m \end{cases} . \tag{5.45}$$

Annealing is turned off after processing m tracks ($\alpha(j = m) = 1$). The initial value of the annealing is b. Values of $m \approx 1000 - 5000$ and $b \approx 1000 - 10\,000$ yield good results.

Weak modes

In total, three global distortions of the telescope geometry (shearing, torsion and stretching) exist which can significantly bias the fitted track parameters. In terms of detector alignment, these distortions are so-called *weak modes*. Shearing, torsion and stretching are detailed described in [Sch14]. One approach avoiding (or at least minimising) these distortions is to fix the first and last detector plane during alignment such that a fixed axis around which the beam telescope can be aligned is provided. Another solution is to use the *collimated beam model* proposed in [Sch14]. Within BTA, two telescope planes (usually the outermost high-resolution beam telescope planes) can be defined as fixed (pre-alignment is used) to avoid weak modes. Fixing detector planes (or intentionally removing them from alignment) is easily done by setting their initial covariance matrix E_0 to zero.

Sensitivity of alignment parameters

A determination of the alignment parameters with the same precision is not feasible. Usually, the shifts Δx and Δy as well as the rotation $\Delta\gamma$ around the z-axis can be estimated with a good precision and converge fast (see Fig. 5.3). However, the typically small divergence (a few mrad) of the high-energy particle beam limits the sensitivity of the rotations $\Delta\alpha$ and $\Delta\beta$ (around the x- and y-axes). This is especially the case when these tilts are small (which is usually the case) such that the detector plane is nearly perpendicular to the beam axis. For small tilts, it is therefore recommended to exclude $\Delta\alpha$ and $\Delta\beta$ from the alignment.

5.2.1 Validation of the implementation

In this section, the implemented Kalman Filter algorithm is validated and the precision of the alignment is investigated. Using Allpix^2 [Spa+18], a set of $n = 50\,000$ tracks is simulated. An electron beam with an energy of 5 GeV and a Gaussian profile with widths of $\sigma_x = \sigma_y = 5\,\text{mm}$ is assumed. The beam divergence in both dimensions is set to 3 mrad. The simulated beam telescope consists of 6 high-resolution tracking planes (Mimosa26, see Sec. 6.4). A DUT with a geometry corresponding to that of the detectors investigated in this thesis is placed in the centre of the telescope setup. The spacing of the telescope planes corresponds to a typical setup used in test beam measurements (see Sec. 6.4). All relevant simulation parameters are summarised in Tab. 7.1 in the appendix. The validation of the alignment procedure is done as follows:

1. Create nominal telescope geometry (no misalignment): $\Delta x = \Delta y = 0$, $\Delta z = 30\,\text{mm}$, $\Delta\alpha = \Delta\beta = \Delta\gamma = 0$.

2. Misalign telescope planes (except outermost detectors to avoid telescope distortions): The positions are randomly varied within $\Delta x = \Delta y = \Delta z = \pm 2\,\text{mm}$. The tilts are randomly varied between $\Delta\alpha = \Delta\beta = \Delta\gamma = \pm 100\,\text{mrad}$.

3. Simulate $n = 50\,000$ tracks in misaligned telescope geometry.

4. Align telescope planes (except the outermost detectors, which are not misaligned). Initial values for the alignment parameters are taken from pre-alignment. Initial values for the uncertainty of the alignment parameters are taken the from pre-alignment for the shifts Δx and Δy ($\pm 100\,\mu\text{m}$), whereas the uncertainty of the other alignment parameters is set to the simulated variation (see above). In a first iteration, the robust parameters $\Delta x, \Delta y$ and $\Delta\gamma$ are aligned. In the second iteration, the z-position Δz and the tilts $\Delta\alpha$, $\Delta\beta$ are added and the alignment is re-fined. For the already aligned parameters, the initial error is reduced by a factor of 10.

Convergence of alignment parameters

The convergence of the alignment parameters is demonstrated in Fig. 5.3 for a misaligned telescope geometry. The change of the alignment parameters is shown for a detector in the centre of the beam telescope (DUT). The grey area represents the error on the alignment parameters extracted from the covariance matrix. The true values of the alignment parameters are shown by the dashed lines. It can be seen that all alignment parameters converge quickly (after 4000 processed tracks) to the true values.

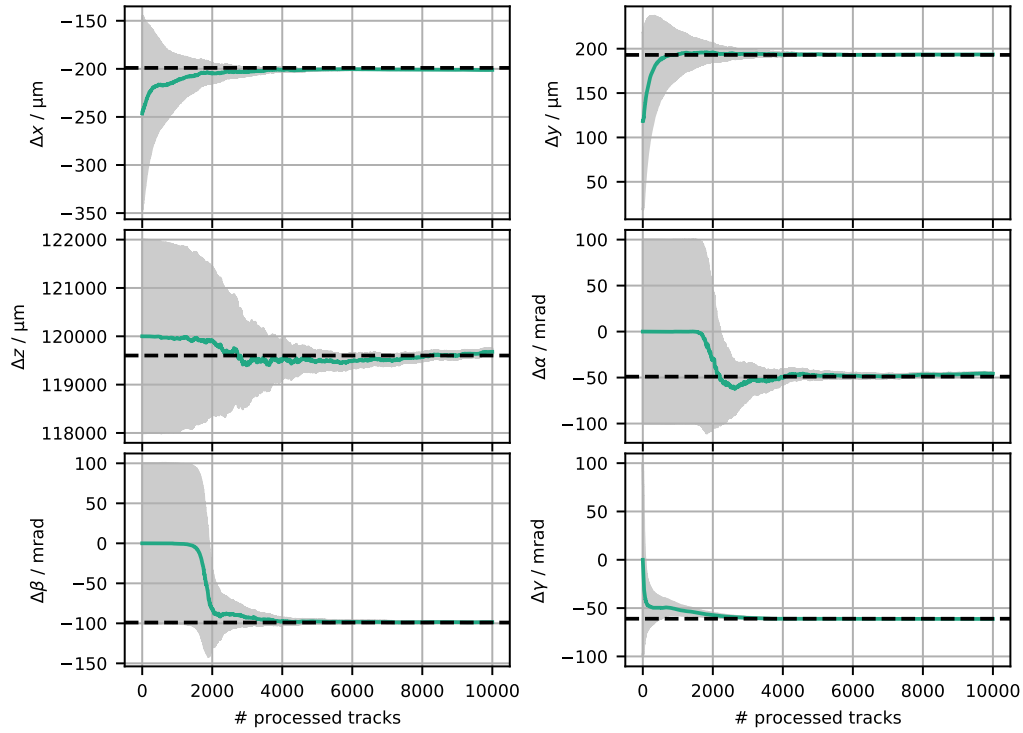

Figure 5.3: Convergence of alignment parameters for a detector in the centre of the beam telescope setup. The grey areas show the errors of the alignment parameters.

Comparison of alignment parameters to true parameters

To study the precision of the alignment algorithm, 200 randomly selected telescope geometries are simulated. The correlation between the estimated values and the true values for all six alignment parameters can be seen in Fig. 5.4. The solid line corresponds to a correlation line with a correlation coefficient of 1. The estimated values are distributed around the correlation line demonstrating that (on average) the estimated alignment parameters correspond to the true

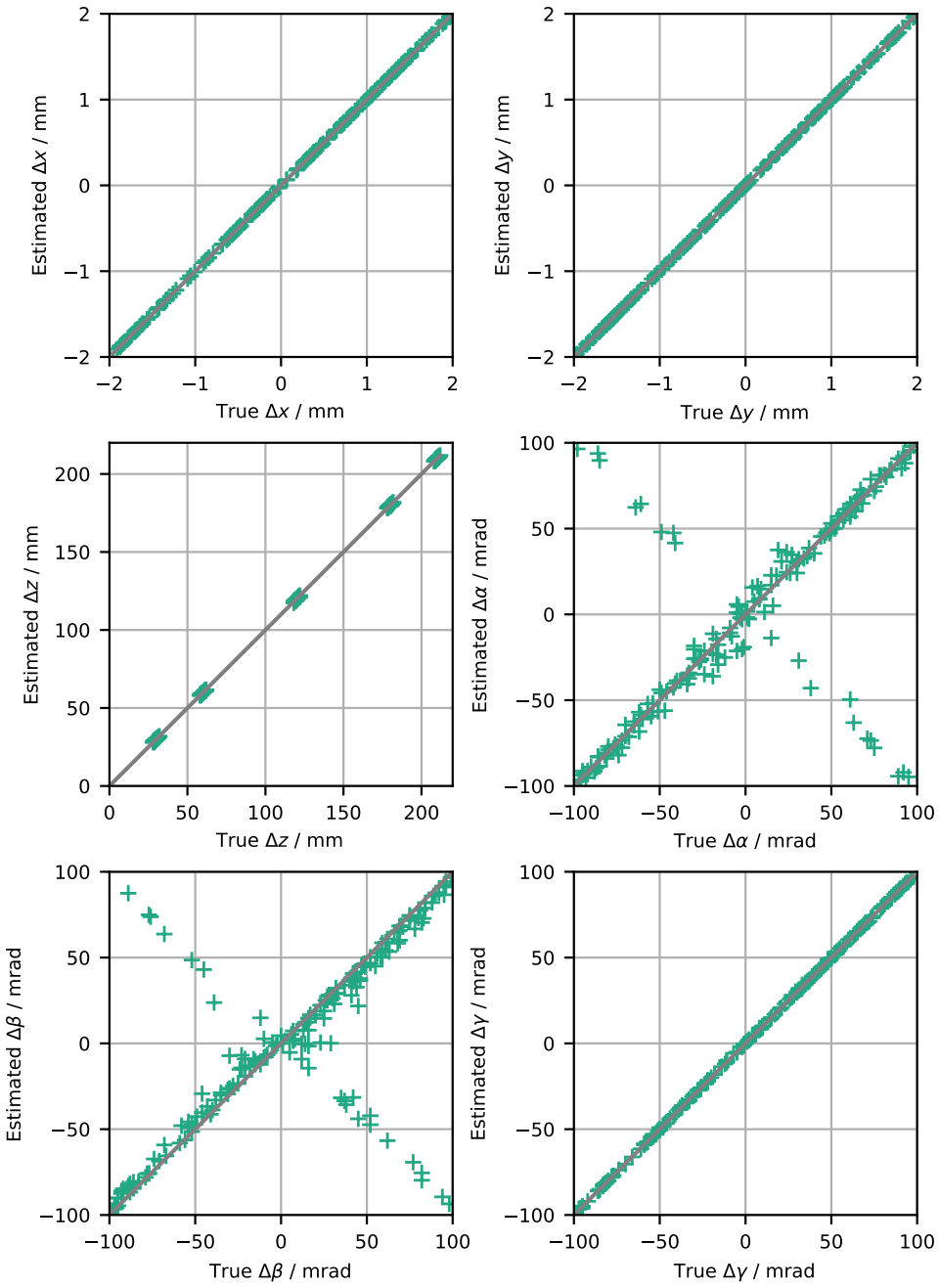

Figure 5.4: Correlation of estimated values using the Kalman Filter alignment algorithm and true values for all six alignment parameters from all telescope planes. The grey lines correspond to a correlation line with a correlation coefficient of 1. In total, 200 random telescope geometries are simulated.

values. Only the tilt $\Delta\beta$ shows a minor systematic deviation from the true values ($< 5\,\text{mrad}$). From the variation (standard deviation with respect to true value) the precision of the alignment parameters is estimated. For the robust alignment parameters Δx, Δy and $\Delta\gamma$ a precision of 1 µm and 0.5 mrad, respectively, is obtained. The precision of the z-position is approximately 0.2 mm. For the tilts $\Delta\alpha$ and $\Delta\beta$ a precision of 5 mrad is estimated.

To demonstrate successful the track reconstruction using the estimated alignment parameters and compare the achievable resolution with the expectation, the (unbiased) residual distributions at the different detector planes are depicted in Fig. 5.5 for one misaligned telescope geometry. The residual distributions are centred around zero and the widths of the distributions (see legends in Fig. 5.5) are in agreement with the expectation. For the tracking planes (Mimosa26 sensors), the residual width is slightly larger than the intrinsic resolution of the detectors (3.2 µm, see Sec. 6.4) due to the pointing resolution of a few µm (see Eq. 5.2), depending on the z-position. For the DUT (in the centre of the beam telescope setup), the residual width is larger, but is in agreement with the expectation when considering a larger intrinsic resolution (14.4 µm) due to the larger pixel pitch of 50 µm and a pointing resolution of a few µm. It can be concluded that the demonstrated alignment precision is sufficient to successfully reconstruct particle tracks with the required resolution. Further, the minor systematic offset of the alignment parameter $\Delta\beta$ has no significant influence on the track reconstruction.

5.3 (In-time) hit-detection efficiency

One of the main purposes of a test beam is the determination of the hit-detection efficiency of the DUT. The hit-detection efficiency ϵ is the probability that a detector records a charged particle that traverses the sensitive detector volume. For future applications as tracking detectors for the ATLAS and CMS experiments, a hit-detection efficiency larger than 97 % during the whole period of operation is required to ensure efficient track reconstruction [ATL17a]. The hit-detection efficiency ϵ can be calculated as

$$\epsilon = \frac{N_{\text{tracks}}^{\text{DUT}}}{N_{\text{tracks}}^{\text{total}}}\,, \tag{5.46}$$

where $N_{\text{tracks}}^{\text{DUT}}$ denotes the number of tracks with a hit in the DUT and $N_{\text{tracks}}^{\text{total}}$ is the total number of tracks. In order to exclude noise hits (spatially and temporally uncorrelated), a hit is only associated with a track if the distance between hit and track intersection is smaller than a certain association distance d_{assoc} (i.e. hit is within a circle with radius d_{assoc} around the track intersection). The impact of the association distance and noise occupancy on the hit-detection efficiency is briefly discussed below. Essential for a correct hit-detection efficiency determination is a synchronisation between the DUT and beam telescope planes, as well as a proper time stamp assignment, for example using a time reference plane (Sec.6.4). Details

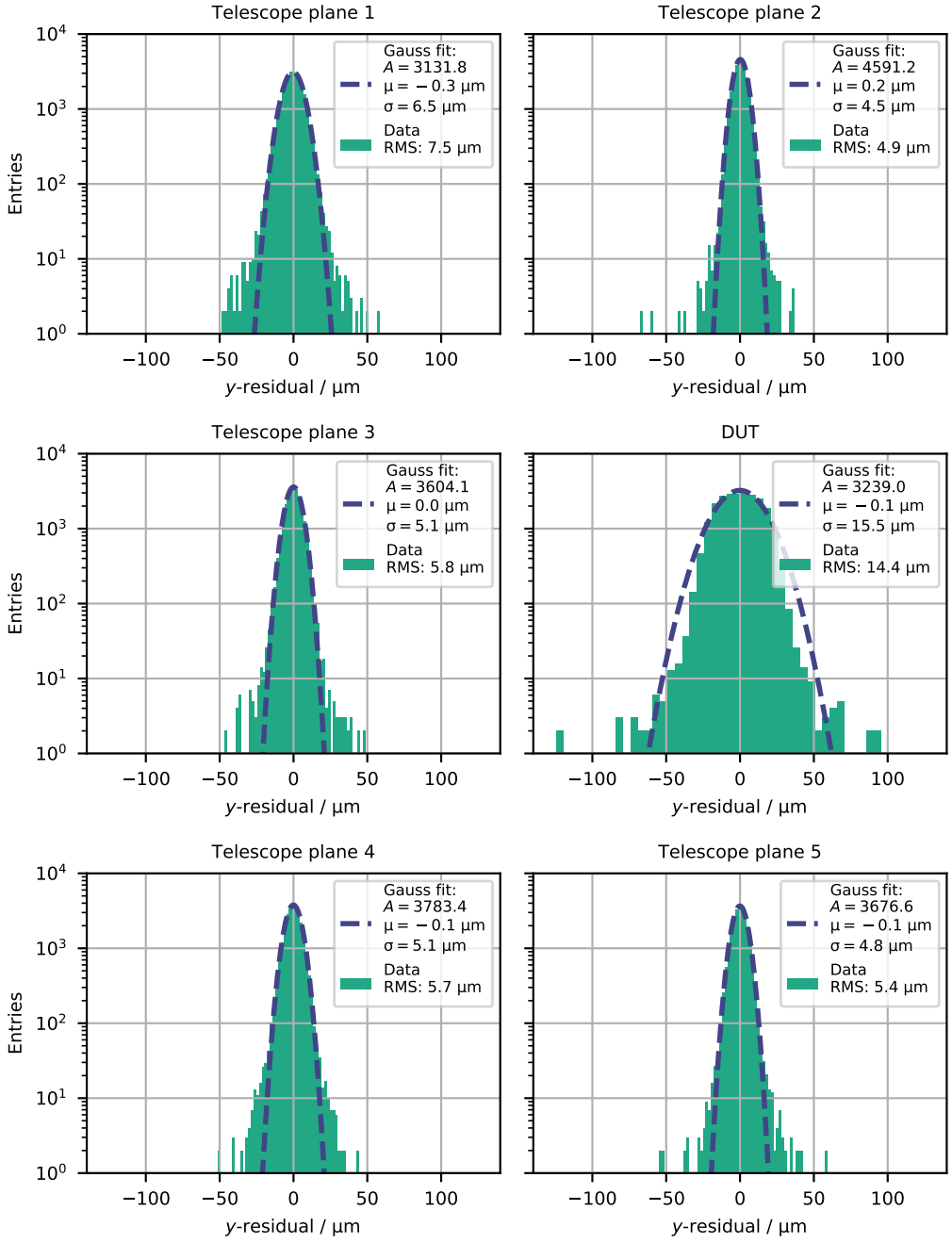

Figure 5.5: Unbiased residual distributions (in the y-dimension) for different detector planes after alignment. Residual distributions are fitted with a Gaussian function to extract the mean μ and the width σ. Residuals are shown on a logarithmic scale.

regarding the synchronisation of beam telescope data with a time reference plane can be found in [Wol16; Die17].

Recording the delay between trigger and the hit arrival time (see Sec. 6.2.2) enables the estimation of the in-time hit-detection efficiency. This includes an additional timing requirement, which ensures that only hit delays within a given time window contribute to the hit-detection efficiency. Details regarding the measurement of the in-time hit-detection efficiency are discussed in Sec. 6.7.5.

In the following, the statistical and systematic uncertainties of the hit-detection efficiency are briefly discussed. A detailed discussion of the uncertainties can be found in [Poh20].

Statistical uncertainty

Detailed discussion including the calculation of the statistical uncertainty of the hit-detection efficiency can be found in [Poh20]. Since usually the number of reconstructed tracks is in the order of 10^5 and the hit-detection efficiency is close to 100 %, the statistical uncertainty of the hit-detection efficiency is smaller than 0.05 % and therefore negligible.

Systematic uncertainty

The origins of the systematic uncertainties of the hit-detection efficiency are diverse and in detail discussed in [Poh20]. In the following, the most important reasons for an overestimation of the efficiency are briefly presented. In addition, the change in hit-detection efficiency as a function of two important analysis cuts are discussed.

One source of systematic uncertainty leading to an overestimation of the efficiency is a decrease of $N_{\text{tracks}}^{\text{total}}$ when hits in the DUT of not reconstructed tracks are assigned to tracks with no hit in the DUT, within the same event. The overestimation increases with decreasing track reconstruction probability P_{rec} and increasing association distance d_{assoc}. A hit is only assigned to a track if the distance between hit and track intersection is smaller than d_{assoc}. It is therefore important to maximise the probability that a track is reconstructed. This can be achieved by not requiring a hit in all telescope planes for reconstructing a track. The used beam telescope consists of 6 planes with an average efficiency of $\epsilon = 98\,\%$ per plane [Jan+16]. The probability for reconstructing a track consisting of at least N_{hit} from N_{tel} telescope planes with an average efficiency ϵ is given by

$$P_{\text{rec}} = \sum_{k=N_{\text{hit}}}^{N_{\text{tel}}} \binom{N_{\text{tel}}}{k} \epsilon^k \left(1-\epsilon\right)^{N_{\text{tel}}-k} ,$$

assuming a track reconstruction efficiency of the software close to 1, which is usually the case. Requiring that a track consists of 6 hits leads to 11 % not reconstructed tracks, while allowing one missing hit ($N_{\text{hit}} \geq 5$) results in less than 1 % not reconstructed tracks. Using a reasonable value for the association distance ($d_{\text{assoc}} < 0.1D$, with uniform beam size D) and optimising

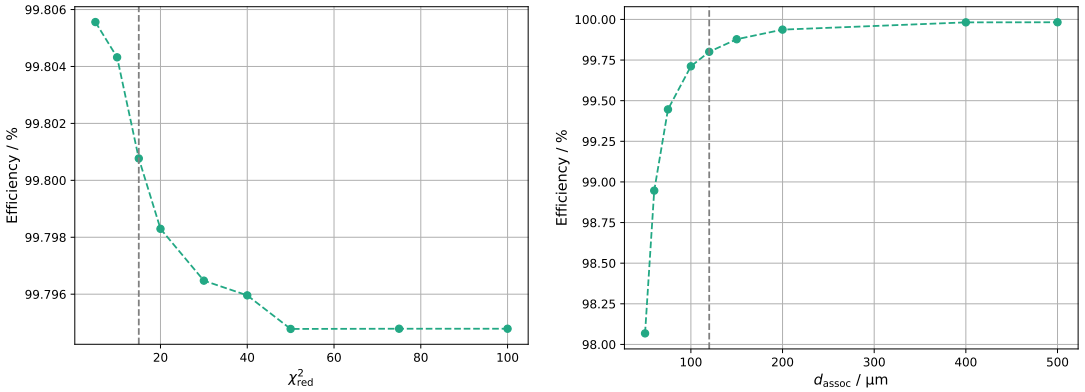

(a) Efficiency variation with χ^2_{red} cut

(b) Efficiency variation with d_{assoc}

Figure 5.6: Variation of hit-detection efficiency with analysis cuts (χ^2_{red} cut and association distance d_{assoc}). Grey dashed lines indicate chosen values used for the analysis presented in this thesis. **(a)** Calculated with $d_{\text{assoc}} \leq 120\,\mu\text{m}$ and $N_{\text{hit}} \geq 5$. **(b)** Calculated with $\chi^2_{\text{red}} \leq 15$ and $N_{\text{hit}} \geq 5$.

the track reconstruction probability ($N_{\text{hit}} \geq 5$), the systematic overestimation of the efficiency is below 0.03 % [Poh20].

Another source leading to an overestimation of the efficiency is an increase of $N^{\text{DUT}}_{\text{tracks}}$ due to fake hits assigned to reconstructed tracks. In order to minimise the probability that a fake hit (e.g. noise hits) is assigned to a reconstructed track, the DUT is tuned such that the noise occupancy per pixel is less than 10^{-6} (Sec. 6.3.1). In addition, a reasonable value for the association distance d_{assoc} is chosen (see below). The efficiency overestimation due to noise hits with a noise occupancy of less than 10^{-6} and proper association distance ($d_{\text{assoc}} < 0.1D$, with uniform beam size D) is smaller than 0.01 % and therefore negligible [Poh20].

To study the impact of analysis cuts on the efficiency the change in efficiency as a function of χ^2_{red} and association distance d_{assoc} is calculated. Besides the noise occupancy and the track reconstruction efficiency, these parameters influence the efficiency the most, and therefore have to be chosen carefully. Fig. 5.6a shows the hit-detection efficiency for different maximum χ^2_{red}. The efficiency variation for different cuts on the χ^2_{red} distribution is minor. The increase in efficiency for tighter χ^2_{red} cuts (due to better track quality) is approximately 0.02 % and therefore negligible. For the analysis presented in this thesis, a χ^2_{red} cut of 15 is chosen (grey dashed line). The change of the hit-detection efficiency as a function of the association distance d_{assoc} (at the DUT) is shown in Fig. 5.6b. The efficiency increases for larger association distances as discussed above. However, the observed change is larger, since besides a small amount of noise hits, also wrongly reconstructed tracks, which are not considered in the discussion above, are included in real data. For larger association distances more wrongly reconstructed tracks contribute to the efficiency and consequently the efficiency increases. For the analysis presented in this thesis, an

association distance of 120 µm is chosen (grey dashed line) corresponding to 6σ of the residual distribution (Fig. 5.2). This is compatible with the above discussed limit of $d_{\text{assoc}} < 0.1D$ (with beam sizes D of a few mm), ensuring an efficiency overestimation not larger than 0.03 %.

6 Characterisation of passive CMOS sensors

In this chapter, the performance of passive CMOS sensors presented in Chap. 4 is evaluated to demonstrate their suitability for harsh radiation environments like the ATLAS and CMS experiments at the future HL-LHC. A passive CMOS prototype sensor in a small-pixel design and large-area passive CMOS sensors are investigated for the first time. Important sensor properties like breakdown behaviour, electronic noise as well as charge collection behaviour and hit-detection efficiency, before and after irradiation, are discussed and compared to the performance requirements of the ATLAS ITk project listed in Tab. 3.1.

The irradiation of the detectors is briefly discussed in Sec. 6.1. The detector readout system used for the characterisation of the sensors and a high-precision charge measurement technique are introduced in Sec. 6.2. Tuning and calibration of the detectors is discussed in Sec. 6.3. In Sec. 6.4 a method for measuring the (in-time) hit-detection efficiency using a high-energy particle beam is introduced. Methods for measuring the detector capacitance of pixel sensors are briefly presented in Sec. 6.5. The characterisation of a passive CMOS prototype sensor before and after irradiation is presented in Sec. 6.6. In Sec. 6.7 the performance of large-area passive CMOS sensors before and after irradiation is investigated.

Unless specifically stated otherwise, the shown results are obtained with the Linear front-end of the RD53A readout chip as it provides the possibility to characterise the whole pixel matrix (see [Daa21]) and has a linear charge-to-ToT feedback which is better suited for charge measurements.

6.1 Detector irradiations

A summary of the irradiated detectors investigated within the scope of this thesis can be found in Tab. 6.1 including the total NIEL fluence and TID after each irradiation step as well as the irradiation facility. The irradiations were performed at the MC40 cyclotron of the University of Birmingham [All+17] with 27 MeV protons and at the (local) Proton Irradiation Site at the Bonn Isochronous Cyclotron [Wol19] using 14 MeV protons. Irradiations at the Bonn cyclotron are preferred, since the risk of uncontrolled annealing due to interruptions in the cooling chain is smaller as no shipping of the devices is necessary. The passive CMOS prototype detector

Detector	Fluence / n_{eq}/cm^2	TID / Mrad	Irradiation facility
Prototype sensor, P1	5×10^{15}	660	MC40 cyclotron, Birmingham (27 MeV protons) [All+17]
	1×10^{16}	1240	Proton Irradiation Site, Bonn (14 MeV protons) [Wol19]
Large-area sensor (DC), F1	2×10^{15}	230	Proton Irradiation Site, Bonn (14 MeV protons) [Wol19]
Large-area sensor (DC), F2	5×10^{15}	580	Proton Irradiation Site, Bonn (14 MeV protons) [Wol19]
Large-area sensor (AC), F3	2×10^{15}	230	Proton Irradiation Site, Bonn (14 MeV protons) [Wol19]
Large-area sensor (AC), F4	5×10^{15}	580	Proton Irradiation Site, Bonn (14 MeV protons) [Wol19]

Table 6.1: Summary of irradiated passive CMOS detectors. The uncertainty on the given NIEL fluences is up to 25 %. The irradiations were performed uniformly in a cold environment ($< -20\,^{\circ}C$) and the devices were unpowered during the irradiations. After each irradiations the devices were annealed for 80 min at 60 °C. Given values for detector P1 correspond to total fluence and TID after step-wise irradiation.

(denoted as P1) was step-wise irradiated to the target fluence to study the performance after different levels of irradiation. The target fluence of $1 \times 10^{16}\,n_{eq}/cm^2$ corresponds to the expected level of irradiation in the innermost layer of the ITk pixel detector (see Sec. 3.4). In total, four large-area passive CMOS detectors (denoted as F1 – F4) were irradiated to two different fluences ($2 \times 10^{15}\,n_{eq}/cm^2$ and $5 \times 10^{15}\,n_{eq}/cm^2$), corresponding to the expected range of fluences in the outer layers of the ITk pixel detector. The devices were uniformly irradiated (1 % spread over the sensor surface) with the help of a moving setup. The irradiation was performed in a cold environment (the temperature during irradiation was colder than $-20\,^{\circ}C$) to avoid uncontrolled annealing during irradiation. To suppress TID effects (Sec. 3.2) affecting the readout chip the devices were left unpowered during irradiation. The given TID values are therefore nominal values and do not correspond to the actual (unknown) TID received by the device. After each irradiation the detectors were annealed for 80 min at 60 °C, which is a common procedure [Mol99].

Since the Bonn irradiation site was still in a development phase during the time of irradiation, the uncertainty on the estimated fluences is up to 25 %, which is similar to other irradiation sites [All+19]. Details regarding the estimation of the fluence are given in [All+17] and [Wol19].

A more realistic irradiation scenario is achieved if the transistors of the readout chip are biased during irradiation, which corresponds to the situation in the final detector during operation. In this so-called *mixed irradiation scenario* the detector is damaged by TID (surface damage affecting the readout chip) and NIEL (bulk damage affecting the sensor). However, the focus

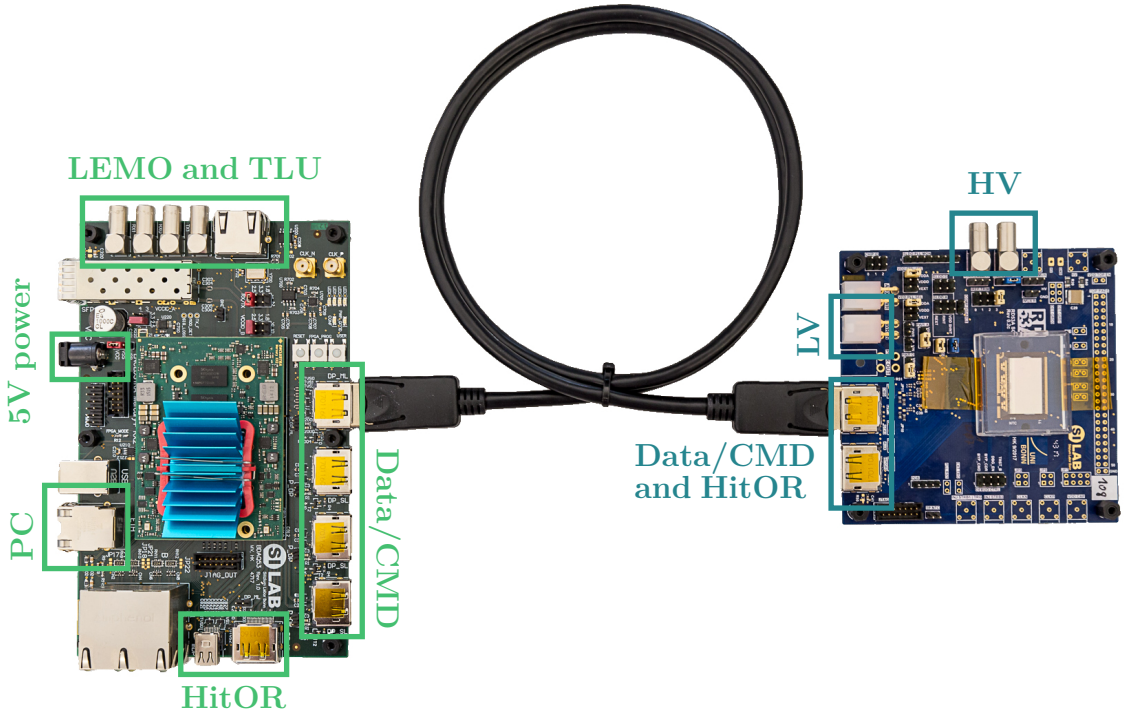

Figure 6.1: Typical setup of the *BDAQ53* test system with an RD53A Single-Chip card (SCC, right) connected to the readout board (left) via a DisplayPort cable for data and command (CMD/Data) transmission between chip and readout board. A description of the various connectors can be found in the text. Picture from [Daa+21].

of the irradiation studies presented in this thesis is the investigation of sensor properties after irradiation, and therefore TID damage was suppressed by leaving the device unpowered. Dedicated TID irradiation studies of the RD53A readout chip using X-rays can be found in [Vog19; Vog22].

6.2 Charge measurement method

6.2.1 The BDAQ53 readout system

BDAQ53 [Daa+21] is a test system for pixel detector readout chips designed by the RD53 collaboration for the ATLAS and CMS HL-LHC upgrades. It combines data acquisition and data analysis, as well as a verification environment [Vog+18] for the RD53 chips. Applications of the test system range from tests at wafer-level [Daa21] and characterisation of single-chip modules to readout and testing of several multi-chip modules [Daa21; Sch21; Fro20]. The

hardware is based on the custom-made BDAQ53 board (visible in Fig.6.1), which includes a commercially available FPGA (field-programmable gate array) and provides the hardware interface between the device under test (DUT) and the PC. The firmware is based on the modular *Basil* framework [Sil] and the software is written in Python, both available open-source [Daa+]. Detailed information about the *BDAQ53* test system can be found in [Daa+21; Daa21].

Fig. 6.1 shows a typical setup with a readout chip mounted on a PCB (Printed Circuit Board), called single-chip card (SCC), and connected to the BDAQ53 board. The SCC allows for the readout of a single chip, other carrier PCBs for the readout of several chips are supported as well [Daa21]. Communication (data and command transmission) between chip and readout board is realised via DisplayPort (DP) connectors. Several DP connectors are available for multi-chip and multi-module readout [Daa+21]. Additional DP connectors are used for readout of the HitOR signals necessary for precise charge measurements. Data between the BDAQ53 board and PC is transmitted via TCP/IP using a RJ45 connector. A second RJ45 connector realises the interface between a Trigger Logic Unit (TLU) and the BDAQ53 board necessary for triggering during test beam measurements (Sec. 6.4). LEMO connectors are used to record the hit delay for in-time efficiency measurements using the *TDC technique* (Sec. 6.2.2).

The SCC acts as a carrier for the detector providing mechanical support during measurements. The readout chip is glued to the SCC to ensure low thermal resistance between the chip and the cooling structure (thin aluminium plate) so that heat produced by the chip can be dissipated. To send and receive data, the pads of the readout chip are connected with thin wires to the SCC (wire bonding). Pins on the SCC make signals available externally for debugging and jumpers on the SCC allow for easy tuning of chip-internal voltages and currents. Various connectors on the SCC are used for low-voltage powering (LV, 1.2 V) of the detector and high-voltage biasing (HV, up to 1000 V) of the sensor.

6.2.2 TDC technique

The charge resolution obtained by using the on-chip ToT (Sec. 3.3.1) is dominated by the discretisation error $\sigma_{\mathrm{ToT}} = \frac{T_{\mathrm{clock}}}{\sqrt{6}}$ [Poh20] of the ToT measurement. With a common gain setting for the RD53A readout chip of 1 ke / ToT ($T_{\mathrm{clock}} = 25$ ns) the discretisation error is approximately 400 e. Compared to the electronic noise of the detector (see Sec. 6.7.2), this is approximately one order of magnitude higher. The purpose of the *TDC technique* (Time-to-Digital Converter) [Poh20] is to provide the possibility for charge measurements with high resolution by sampling the ToT signal externally with an increased clock speed. The discriminator output signal, whose length is proportional to the amount of detected charge, is available via the HitOR feature (Sec. 3.4.1) of the readout chip. Within the *TDC technique* the HitOR signal is sampled externally inside the FPGA with a 640 MHz clock. The discretisation error is therefore reduced by a factor of 16 with respect to the ToT method. This makes precise charge measurements

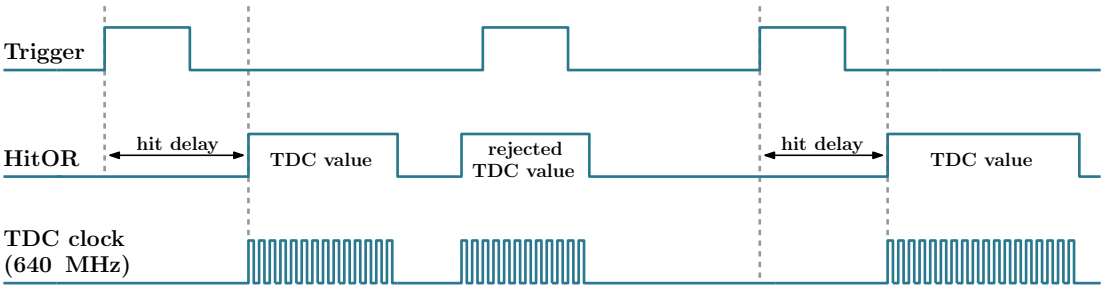

Figure 6.2: TDC-to-hit data assignment. Only TDC data followed by a trigger within a certain time window is assigned to hits. The HitOR signal is sampled using a 640 MHz clock to measure the collected charge (TDC value).

feasible, which are required for charge calibration and studying the charge collection behaviour of pixel detectors.

Since the TDC data stream is independent of the RD53A raw data stream, an assignment of TDC data to hits is necessary. First, the TDC data has to be correlated to events. In this context, an event is defined by a trigger signal (e.g. scintillator signal) sent to the readout chip. The assignment of TDC data to events is possible by recording the time difference between the TDC data and the trigger signal (hit delay). Only TDC data followed by a trigger within a certain time window (< 400 ns) is assigned to events, as illustrated in Fig. 6.2. Small variations in the hit delay are expected due to time walk. Measuring TDC charge and hit delay simultaneously facilitates a measurement of the time walk (Sec. 6.7.4). Furthermore, the information of the hit delay can be used to determine the in-time efficiency of pixel detectors using a particle beam (Sec. 6.7.5). In the second step, the TDC data has to be correlated to hits within one event. Since RD53A features four individual HitOR lines (see Fig. 3.21), an unambiguous assignment of TDC data to hits is only possible if there is only one hit per HitOR line (each HitOR line is connected to one TDC instance in the FPGA). This puts restrictions on valid cluster shapes during the analysis, since only cluster shapes including each HitOR line at most once can be used. However, most of the recorded clusters are single-pixel clusters such that this restriction does not have a significant impact on statistics.

To check that the TDC data is correctly assigned to hit data the TDC values can be correlated with the ToT values as shown in Fig. 6.3. Without any selection on the data (Fig. 6.3a) wrong TDC values are assigned to hits leading to a background on top of the expected linear correlation. Using only TDC data correlated to a trigger and valid cluster shapes the background is significantly reduced and almost every TDC value is successfully correlated ($> 99\,\%$ correlation) to a ToT value (Fig. 6.3b). The correlation saturates for TDC values larger than 250 due to the limited dynamic range of the ToT values (4 bits only). Usually about 30 % of the data is discarded for charge or in-time efficiency measurements because of the selection of valid cluster

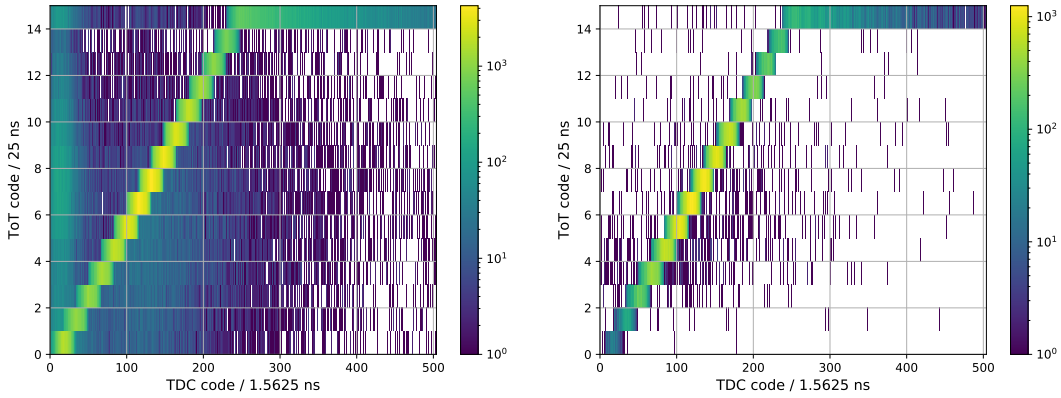

(a) Without data cuts.

(b) With data cuts.

Figure 6.3: (a) Correlation of TDC to ToT values without data cuts. **(b)** Correlation of TDC to ToT values with unambiguous assignment and TDC data correlated to a trigger only.

shapes and TDC data followed by a trigger.

6.3 Detector tuning and calibration

6.3.1 Detector tuning

For statistical reasons, measurements of charge spectra or hit-detection efficiency include data from several thousands of pixels. Since every pixel has a slightly different behaviour due to small process variations (transistor mismatch[1]), the response of each pixel to injected charge (hits) has to be adjusted by changing its threshold (TDAC setting, Sec. 3.3). This process is known as detector tuning. The threshold of each pixel can be measured in a so called *threshold scan* by injecting a fixed number of hits into each pixel with varying, known charge using the injection circuit (Sec. 3.4.1). Ideally, the response curve is a step function, however, due to electronic noise causing signal amplitude variations the step function is convolved with the Gaussian distributed noise. The result is a smeared step function, called an *s-curve*, for each pixel, as illustrated in Fig. 6.4a. This curve can be mathematically described with the following function:

$$S(x) = \frac{N_{\text{inj}}}{2}\left(1 + \text{erf}\left(\frac{x-\mu}{2\sqrt{\sigma}}\right)\right) . \tag{6.1}$$

The threshold μ of a pixel is defined as the charge with 50 % detection probability of the injected hits N_{inj}. The slope of this curve is a measure of the electronic noise σ. The electronic noise is usually given as equivalent noise charge (ENC) which is the charge for which the signal-to-noise

[1] Transistor mismatch describes the phenomenon that identically processed transistors behave differently due to process variations, e.g. tiny variations in length and width of the transistors.

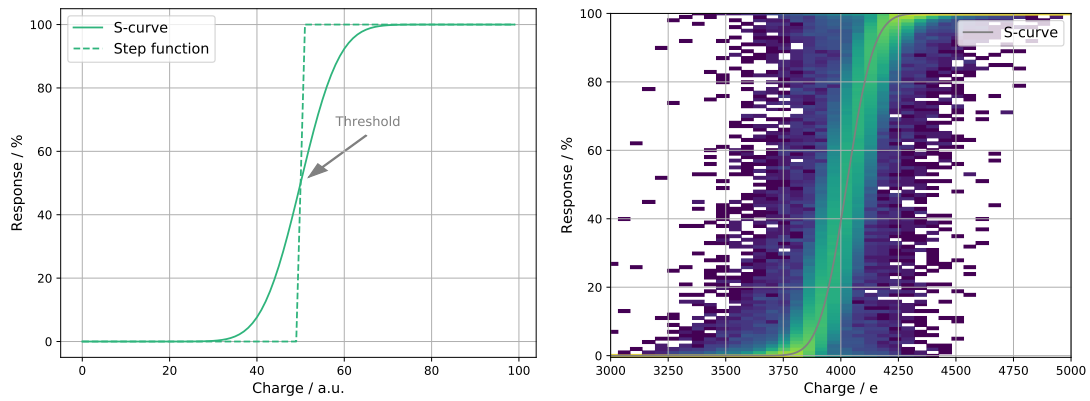

(a) **(b)**

Figure 6.4: (a) Illustration of an *s-curve*. Due to electronic noise the step function (ideal case without noise) is convolved with Gaussian distributed noise resulting in a smeared step function (*s-curve*). The threshold is defined as the charge with 50 % detection probability of the injected hits. The slope of the *s-curve* is a measure of the electronic noise. **(b)** Histogrammed *s-curves* of approximately 26 000 pixels measured in a *threshold scan*. With a fit to the data (grey line) the threshold μ and electronic noise σ are extracted, according to Eq. 6.1.

ratio (S/N) equals 1 [Spi05]. By fitting Eq. 6.1 to *s-curves* obtained from a *threshold scan* the threshold and ENC can be measured, as illustrated in Fig. 6.4b.

The global detector threshold (GDAC setting of comparator, Sec. 3.3) should be set low enough so that the whole charge spectrum is recorded to estimate its most probable value, even after irradiation. For the predecessor of the RD53A readout chip, the ATLAS FE-I4, it was observed that the charge resolution (using the *TDC technique*) decreases with lower threshold settings [Poh20]. This can be explained by the fact that the dominant contribution to charge resolution using the *TDC technique* is not electronic noise, but the finite bandwidth of the readout chip's amplifier and charge collection time, which introduces a threshold dependent jitter [Spi05]. Therefore, a lower threshold setting worsens the signal-to-noise ratio (S/N) for charge measurements. However, such a strong dependency is not observed for the RD53A chip [Gia19]. Charge resolution (width of peaks from X-ray fluorescence, Sec. 6.3.2) of the *TDC technique* as a function of the charge for a detector threshold of approximately 1000 e can be seen in Fig. 6.5. This threshold setting yields sufficient S/N of 10 – 25 for charges between 3 ke – 12 ke and is low enough to detect the full charge spectrum even after irradiation. Therefore, for every characterised detector a threshold of approximately 1000 e – 1200 e is chosen.

Fig. 6.6 compares the threshold distribution (of approximately 26 000 pixels) before and after TDAC tuning. The local threshold setting of each pixel (TDAC setting of comparator) is adjusted during tuning such that the threshold dispersion is minimised (from 344 e to 39 e). The charge corresponding to the aimed threshold is injected N_{inj} times into each pixel. Using a

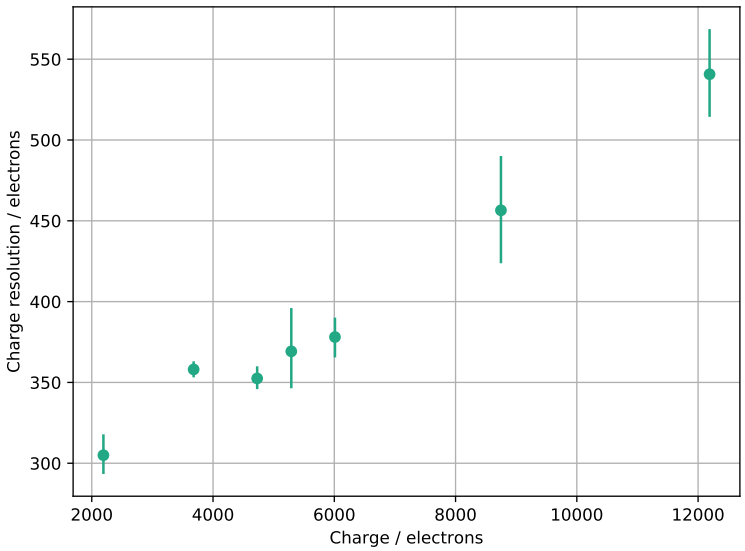

Figure 6.5: Charge resolution as a function of charge using the *TDC technique* for detector F2 (see Tab. 6.1). The charge resolution is extracted from the width of Gaussian distributions fitted to X-ray fluorescence peaks with different energies (Sec. 6.3.2). The error bars correspond to fit uncertainties. A threshold setting of approximately 1000 e is used.

binary search algorithm [Knu97], the TDAC setting of each pixel is adjusted until the occupancy of each pixels is closest to 50 % of the injected hits.

Furthermore, malfunctioning pixels (noisy or stuck) have to be detected and masked. A pixel is classified as noisy if the measured occupancy is higher than a given limit while sending a certain amount of triggers to the chip. For all detectors the occupancy limit is set to 10 while sending 10^7 triggers resulting in a noise occupancy of 10^{-6} per pixel, which is in accordance with the specifications of the readout chip [Gar15]. Especially after irradiation, the number of noisy pixels increases significantly due to the higher leakage current per pixel and front-end degradation. Since the amount of noisy pixels depends on the threshold setting, the maximal allowed fraction of deactivated pixels sets a lower limit on the detector threshold, and thus defines the lowest possible threshold for a detector. Stuck pixels are pixels for which the output of the comparator is stuck high. Since this makes a TDC measurement impossible as the HitOR is constantly high, these pixels are also required to be masked. For all characterised detectors, the maximum fraction of masked pixels is less than 1 %, at the chosen threshold setting of 1000 e – 1200 e.

Like the (local) threshold setting, chip-internal voltages and currents responsible for the injection pulse and generation of analogue biases of the front-end (see Sec. 3.4.1) vary from chip to chip due to process variations [Daa21]. To ensure operation of the chip and comparability

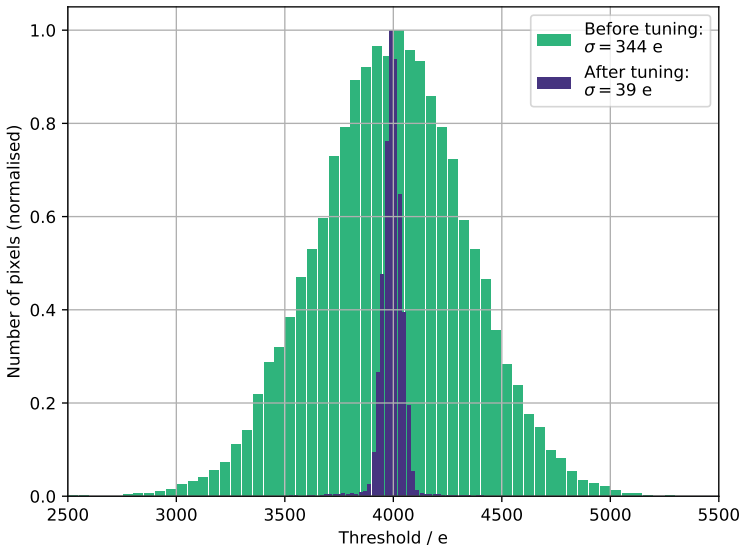

Figure 6.6: Comparison of the threshold distribution before and after TDAC tuning (data of approximately 26 000 pixels). Due to transistor mismatch the threshold dispersion before tuning is approximately 350 e. The TDAC tuning minimises the dispersion to around 40 e.

between chips, these voltages and currents are tuned to a common value. In particular, the reference voltage V_{ref} and the reference current I_{ref} (see Sec. 3.4.1) are tuned to 900 mV and 4 µA, respectively, before characterisation.

6.3.2 Detector calibration

The amplitude of the voltage step created by the injection circuit (see Sec. 3.4.1) to inject a certain amount of charge (via injection capacitor) is specified via the chip-internal unit ΔVCAL. To draw conclusions from charge measurements and compare results to expectations a conversion from the injection circuit setting ΔVCAL to the physical unit of charge is required. The process of determining this conversion is called detector calibration. Accurate calibration of the detector is important for converting the threshold to physical units of charge as a possible offset in the calibration has a significant effect on low threshold settings. The detector calibration, described by a transfer function, is divided into two parts: The calibration of the injection circuit and the charge calibration using radioactive sources. The following section describes how this transfer function is found.

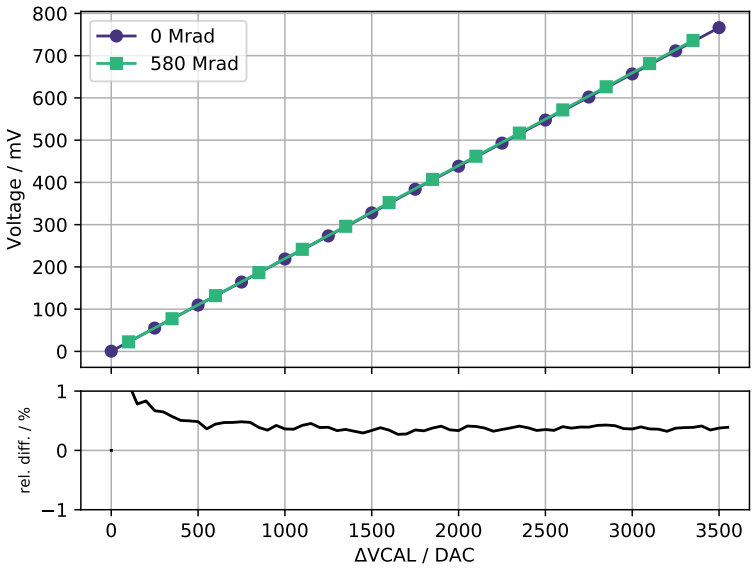

Figure 6.7: Calibration of the injection circuit before and after irradiation of detector F2. The bottom part of the plot shows the relative change after irradiation. For the sake of visibility only every 5^{th} data point is depicted.

Calibration of the injection circuit

Since TID affects the behaviour of the front-end resulting in a potential change in the charge amplification, it is important to calibrate the injection circuit after irradiation. With knowledge of the transfer function from injection circuit setting ΔVCAL to amplitude of the voltage step, it is possible to correct the recorded charge spectra after irradiation.

The injection circuit injects a known charge Q into each pixel by creating a voltage step ΔV (depending on the ΔVCAL setting) over the injection capacitor C_{inj} according to

$$Q = \Delta V \cdot C_{\text{inj}}. \tag{6.2}$$

It is not observed that the value of the injection capacitor (MOM-capacitor) changes with irradiation, and therefore C_{inj} is assumed to be constant. By measuring the amplitude of the voltage step for different ΔVCAL settings the calibration of the injection circuit is obtained, as illustrated in Fig. 6.7. The injection circuit calibration of all detectors can be found in Appendix 7.

The relationship between injection circuit setting and voltage step is linear, as expected from Eq. 6.2. In addition, the relative change (bottom of Fig. 6.7) after irradiation is smaller than 1 % and therefore negligible. Large differences were not expected, since TID damage affecting the injection circuit is suppressed as the device was left unpowered during irradiation. Furthermore,

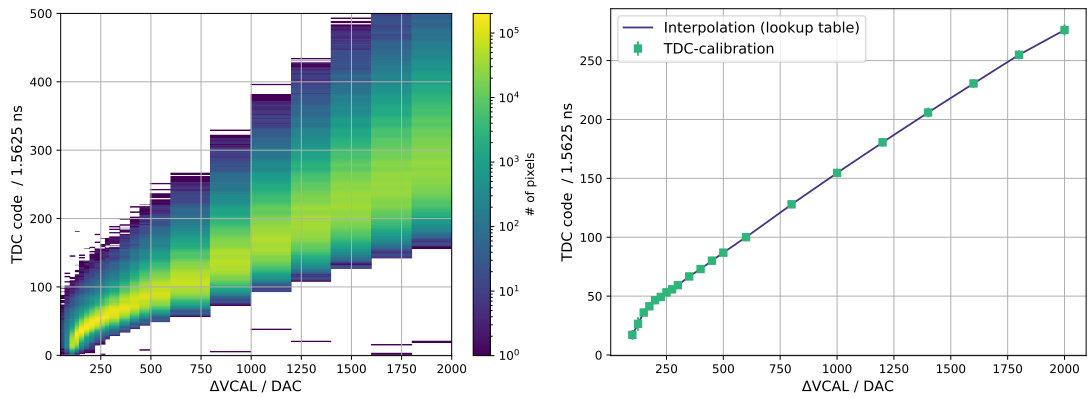

(a) **(b)**

Figure 6.8: (a) Per-pixel TDC calibration histogrammed for approximately 26 000 pixels using 100 injection per ΔVCAL setting and pixel. **(b)** TDC calibration for a single pixel. Each data point represents the mean TDC value for the corresponding ΔVCAL setting (100 injections per setting). Data points are interpolated to create a lookup table converting TDC values into ΔVCAL values. The error bars represent the standard deviations of the measured TDC value distribution.

the differential injection circuit (Sec. 3.4.1) ensures that potential changes in the injection circuit due to irradiation balance each other out.

Charge calibration

To express the detector threshold and measured charge spectra in physical units of charge (i.e. number of electrons) the transfer function from the injection circuit setting ΔVCAL to charge has to be found. Furthermore, with the help of the injection circuit calibration an irradiation independent detector calibration (voltage step to charge) is obtained.

A variable X-ray fluorescence source providing sharply defined characteristic lines (from X-ray transitions, see Sec. 3.1.1) with known energies is used for charge calibration. The X-ray fluorescence source is a ^{214}Am radioactive source with different materials as targets. The isotope ^{241}Am decays via α-decay with a 59.54 keV X-ray by-product [Bé+10] creating X-ray fluorescence photons when interacting with the target material. The following materials are available as targets and used for calibration: Copper (Cu), Rubidium (Rb), Molybdenum (Mo), Silver (Ag), Barium (Ba) and Terbium (Tb). The various target materials make a calibration over a wide range of energies possible (7 keV to 45 keV).

Before measuring the spectrum, the detector is tuned, as explained in Sec. 6.3.1. The charge spectrum is recorded using the *TDC technique* (Sec. 6.2.2) yielding TDC values from many pixels. Since, even after tuning, the behaviour of each pixel is slightly different, a per-pixel TDC calibration is performed, as shown in Fig. 6.8. Fig. 6.8a shows the measured TDC values

as a function of the ΔVCAL setting histogrammed for approximately 26 000 pixels. For each setting 100 hits are injected into every pixel and the corresponding TDC values are recorded. The TDC calibration for a single pixel is depicted in Fig. 6.8b. Each data point is the average TDC value (from 100 injections) for the corresponding ΔVCAL setting. From this, a look-up table for each pixel is created by interpolating the data points. This look-up table allows the measured charge spectra to be converted from TDC values to ΔVCAL values for each pixel. An example of such a charge spectrum (Ag as target) using single-pixel clusters can be seen

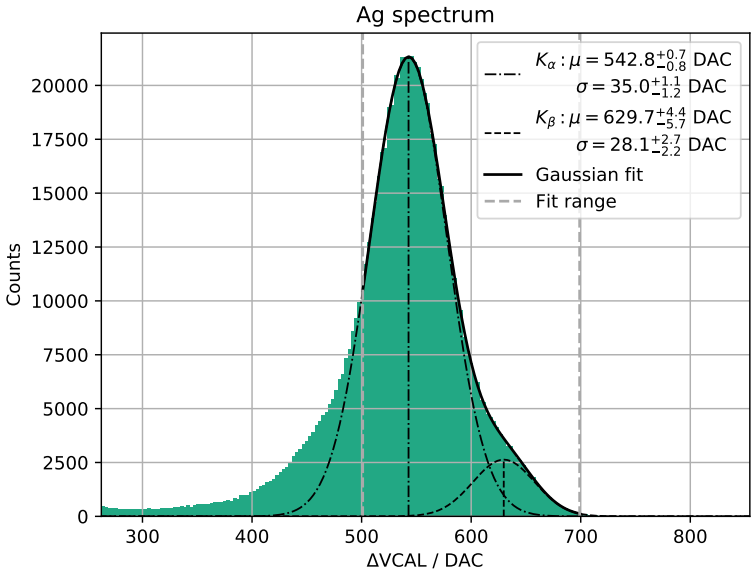

Figure 6.9: X-ray fluorescence spectrum of Ag measured with the *TDC technique* using single-pixel clusters. Two peaks corresponding to the K-series X-ray lines with energies of 21.99 keV and 22.16 keV [Des+05] are visible. Due to the finite charge resolution of the *TDC technique* the peaks are overlapping. The tail towards lower charge is due to charge sharing. Peaks are fitted with a Gaussian function to extract the mean value.

in Fig. 6.9. The reasons for considering only single-pixel clusters are: a) Most of the clusters (approximately 80 %) are single-pixel clusters and b) The charge resolution of clusters with N hits is proportional to $\sqrt{N}$ (quadratic summation), resulting in worse charge resolution for larger cluster sizes.

The X-ray fluorescence spectrum of Ag has two dominant characteristic lines corresponding to the K_α- and K_β-transitions of Ag with energies of 21.99 keV and 22.16 keV [Des+05], respectively. Due to the resolution of the *TDC technique* the characteristic lines are smeared and cannot be resolved. In addition, small effects of charge sharing between pixels are the reason for the tail towards lower charge of the measured spectrum[2]. Every peak is fitted with a Gaussian

[2]Less charge is reconstructed when clusters consist of pixels for which the collected charge is below threshold.

function to extract its mean value. The uncertainty of the measured entries N is assumed to be $\sqrt{N}$, since the fluctuations follow a Poisson distribution. As the energy of the fluorescence photons deposited in the sensor is known, the extracted mean values from the fit can be assigned to the energies of the corresponding X-ray transitions from literature (taken from [Des+05]). This is only correct under the assumption that the whole energy of the photons is deposited in the sensor and can be reconstructed with single-pixel clusters. A brief discussion of this is given later. The deposited energy is converted into a charge using $w_i = 3.65\,\text{eV}$ (see Eq. 3.19).

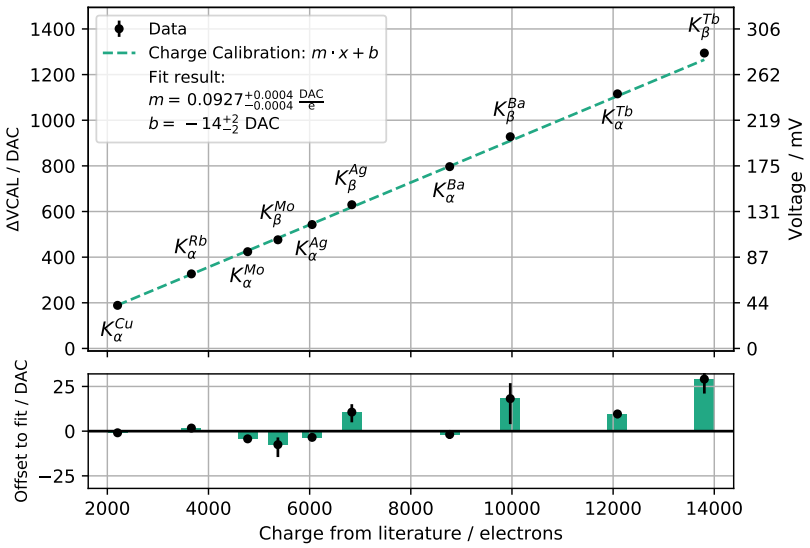

Figure 6.10: Charge calibration of detector F2. Each data point corresponds to the mean value extracted from a Gaussian fit to the measured X-ray fluorescence spectra of different target materials. The error bars correspond to the errors from the fit. Energy of X-ray transitions are taken from [Des+05] and converted into charge using 3.65 eV per e/h-pair. Injection circuit settings are converted to voltage using the transfer function obtained from the injection circuit calibration. Data is fitted with a straight line (dashed line). Below, the deviation to the fit is shown.

Data points from various fluorescence targets are summarised in Fig. 6.10. The error bar of each data point correspond to the error from the Gaussian fit including the statistical uncertainty ($\sqrt{N}$). A straight line (including an offset) is fitted to the data (dashed line) yielding the following transfer function from ΔVCAL to charge (inverse of fit):

$$Q\,[\text{e}] = (10.79 \pm 0.05)\,\frac{\text{e}}{\Delta\text{VCAL}} \cdot x\,[\Delta\text{VCAL}] + (155 \pm 21)\,\text{e}\,. \tag{6.3}$$

Using the injection circuit calibration the ΔVCAL setting is converted into the voltage (over the injection capacitor) created by the injection circuit (right y-axis in Fig. 6.10) resulting in

Device	Value
F1, DC-coupled	(7.62 ± 0.02) fF
F2, DC-coupled	(7.90 ± 0.04) fF
F3, AC-coupled	(9.29 ± 0.04) fF
F4, AC-coupled	(8.94 ± 0.04) fF
other devices [Gia19]	(7.83 ± 0.08) fF
design value [Gar17]	(8.5 ± 1.7) fF

Table 6.2: Calculated injection capacitance values for detectors F1 to F4 using γ-sources and injection circuit calibration. The uncertainties originate from the (statistical) uncertainties of the charge calibration. The results are compared to the value reported in [Gia19] using other RD53A modules. The design value is taken from [Gar17].

the following irradiation-independent transfer function:

$$Q\,[\mathrm{e}] = (49.3 \pm 0.2)\,\frac{\mathrm{e}}{\mathrm{mV}} \cdot x\,[\mathrm{mV}] + (139 \pm 21)\,\mathrm{e}\,. \tag{6.4}$$

This relation is important as a fraction of the deposited charge is trapped after irradiation preventing a calibration of the detector using γ-sources (the exact trapping constant is often not known). However, no significant differences in the calibration of the injection circuit after irradiation were found, and therefore the obtained charge calibration before irradiation can also be applied after irradiation without any correction. A calibration is done for every characterised detector before irradiation and can be found in Appendix 7.

Determination of the injection capacitance

Using Eq. 6.2, the injection capacitance C_{inj} can be determined from the slope of the charge transfer function (Eq. 6.4). By comparing the obtained value with the design value the charge calibration can be validated. The design value of the injection capacitance for the RD53A readout chip is (8.5 ± 1.7) fF [Gar17]. Since the extraction of this design value from post-layout simulation is difficult due to unknown parasitic capacitances, an uncertainty of 20 % on this value is assumed. The calculated values of the injection capacitance for all calibrated devices are summarised in Tab. 6.2. The given uncertainties originate from the (statistical) uncertainties on the charge calibration. Considering DC-coupled detectors, small variations between these are observed (approximately 5 %), which could be explained by process variations. Compared to the design value, the values extracted from calibration are slightly smaller (approximately 10 %), but agree within the uncertainty limits. The value reported using other RD53A modules (average over several modules) from [Gia19] is comparable to the values obtained here.

The value of the injection capacitance measured with AC-coupled detectors is approximately 20 % larger compared to measurements with DC-coupled detectors. The origin of this is a charge collection efficiency smaller than 100 % for AC-coupled devices (Sec. 3.3.1), and thus the mea-

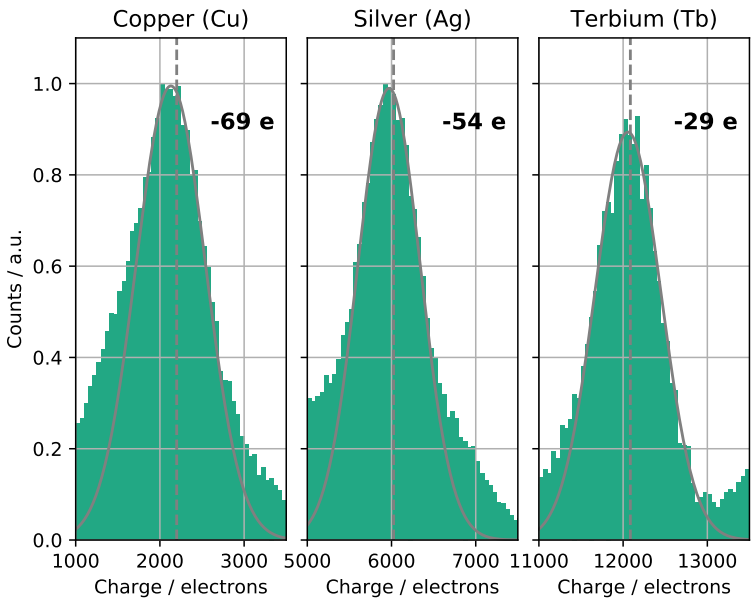

Figure 6.11: Simulated X-ray fluorescence spectra for different targets (Cu, Ag, Tb) using Allpix^2. Deposited charge is reconstructed using single-pixel clusters with a 150 µm thin detector with $50 \times 50\,\mu m^2$ pixels. Dashed lines corresponds to expected charge from literature. Values given next to distributions correspond to the differences between literature value and fitted peak position from simulation. Simulation parameters summarised in Tab. 7.2.

sured X-ray fluorescence peaks do not correspond to the assumed deposited charge (literature values of X-ray transitions) to which the peaks are associated. Consequently, the extracted conversion factor from charge calibration (Eq. 6.4) is larger for AC-coupled detectors. Since the injection capacitance corresponds to this conversion factor, the charge collection efficiency has a direct influence on the injection capacitance measurements and leads to artificially larger measured values. The injection capacitance is a feature of the readout chip and does not depend on the type of sensor. To compensate this effect, and to obtain a conversion to measured charge for AC-coupled detectors, the averaged calibration of DC-coupled sensors is used to calibrate AC-coupled detectors, assuming 10 % uncertainty to take possible variations into account.

The difference between the injection capacitance measured with AC- and DC-coupled sensors (20 %) is larger than estimated (5 % – 10 %, see Sec. 3.3.1), but still reasonable as it is expected that the coupling capacitance adds parasitic contributions to the total input capacitance which decreases the charge collection efficiency, and therefore increases the calculated value for the injection capacitance.

Limitations and systematic errors

The main assumption of the charge calibration is that the reconstructed peak position using single-pixel clusters corresponds to the charge deposited by X-ray fluorescence photons, i.e. charge sharing does not shift the reconstructed peak positions. To verify this and identify possible deviations from the expected peak positions the recorded single-pixel charge spectra are simulated using Allpix[2] [Spa+18]. The simulation includes realistic charge deposition using the GEANT4 simulation framework [Ago+03] and charge propagation using the drift-diffusion model as well as charge digitisation. Simulated X-ray fluorescence spectra for three different targets (Cu, Ag, Tb) using a ^{241}Am radioactive source can be seen in Fig. 6.11. A silicon pixel sensor with a thickness of 150 µm and $50 \times 50\,\mu m^2$ pixels is used as a detector. The detection threshold is set to 1000 e and only single-pixel clusters are considered, as it is the case for the charge calibration. All digitisation and simulation settings can be found in Tab. 7.2. Comparing the reconstructed peak position using single-pixel clusters the maximum deviation from the literature value is less than 100 e. The reason for this deviation is charge sharing resulting in lower reconstructed charge if the signal of a pixel in a cluster is smaller than the detection threshold. This effect depends on the pixel pitch and detector thickness [Poh20]. Smaller pixels would lead to more charge sharing as the charge cloud covers more pixels. In case of thicker detectors the drift distance of charge carriers is larger[3] resulting in broader charge clouds and in turn to more charge sharing (if the detector is illuminated from the backside). This deviation introduces a small systematic overestimation of the offset obtained from charge calibration using radioactive sources. However, this difference is relatively small compared to the expected amount of charge collected by MIPs (minimum ionising particles) of several thousand electrons. Furthermore, a charge collection efficiency smaller than 100 % leads to the wrong assumption that the reconstructed peaks correspond to the deposited charge by X-ray fluorescence photons. Usually the charge collection efficiency is very close to 100 % and the effect on the reconstructed peak position is negligible. However, for AC-coupled detectors this effect is in the order of a few percent (see Sec. 3.3.1), and thus contributes to the systematic uncertainty of the charge calibration if the exact value of the charge collection efficiency is unknown.

Another systematic error originates from the observed column dependence of the charge calibration. Extracted slopes and offsets from charge calibration for detector F2 as a function of the core column (average over 8 columns) are shown in Fig. 6.12. A possible reason for this behaviour could be a column-dependent value of the charge injection circuit capacitance. This effect is also observed in [Gia19]. The variation can be characterised as the standard deviation yielding approximately 50 e for the offset variation and 5 % for the slope variation.

Furthermore, a too low charge resolution would lead to merging of reconstructed spectral lines which complicates the reconstruction of individual spectral lines required for correct assignment

[3] Photons deposit their energy close to the detector surface. The drift distance is therefore given by the detector thickness for backside illumination.

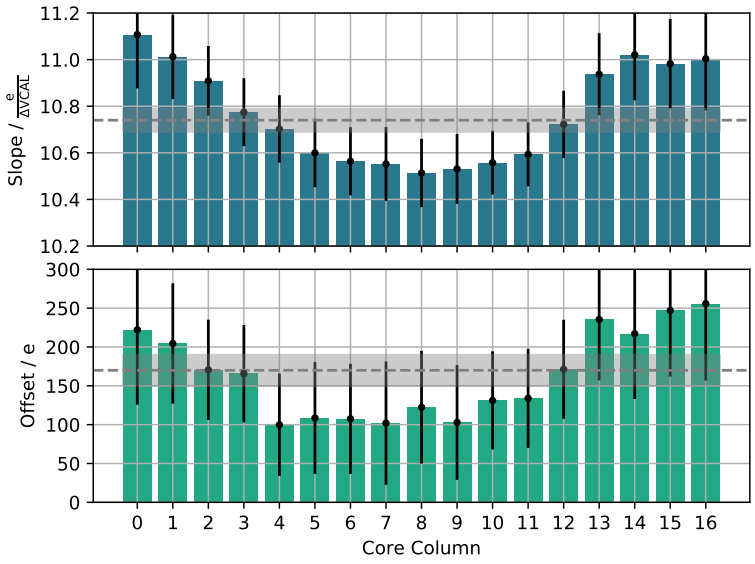

Figure 6.12: Slope (top) and offset (bottom) of fit from charge calibration as a function of the core column (average over 8 columns). The errors on the data points are taken from the fit. The grey dashed line represents the average over all columns with the 1σ uncertainty shown as grey area.

to literature values. In this case, the weighted average of the peak positions has to be calculated using the expected intensities. As mentioned above, this fact justifies the selection of single-pixel clusters which have a better charge resolution compared to clusters with several hit pixels.

The total systematic error of the charge calibration is approximately 100 e – 150 e (small charge sharing effect and column-dependent offset) plus 5 % relative uncertainty (column-dependent slope). This implies that for charge measurements with expected signals of several thousand electrons the 5 % systematic uncertainty dominates, whereas the systematic uncertainty of the calibrated detector threshold (approximately 1000 e) is approximately 100 e – 150 e.

6.4 Beam telescope setup

To measure the hit-detection efficiency and charge collection behaviour of the device under test (DUT) a beam telescope setup in a minimum ionising particle beam (referred to as test beam) is used. Dedicated test beam facilities are located at DESY[4] in Hamburg or at ELSA[5] in Bonn. The DESY II test beam facility [Die+19] offers several beam lines with electron or positron beams at particle rates of a few kHz and user-selectable beam energies ranging from

[4] **D**eutsches **E**lektronen-**SY**nchrotron
[5] **EL**ektronen-**S**tretcher-**A**nlage

1 GeV – 6 GeV. At the external beam line for detector tests at ELSA [Heu17; Heu+16] a primary electron beam with energies up to 3.2 GeV and user-adjustable particle rates (a few kHz up to 625 MHz) can be used. As test beam time is rare and expensive, particle rates as high as possible are preferred to optimise statistics. For high-energy detector tests particle rates of a few kHz are common. The limiting reasons for this are readout speed and data quality (track reconstruction efficiency). Another demand on test beam measurements is the optimisation of spatial resolution for precise particle tracking, which requires to minimise the effect of multiple scattering (see Sec. 3.1.2). Thus, the highest possible beam energy is preferred and the material budget of the setup is reduced as much as possible.

Fig. 6.13 shows a sketch of an usual test beam setup. In front of the setup a scintillator is placed in order to trigger on particles traversing the setup. The scintillator signal is connected to a Trigger Logic Unit (TLU) which distributes and synchronises the triggers between the different readout systems used in a test beam. For the measurements presented in this thesis a EUDET TLU [Cus07] is used.

The beam telescope is a EUDET-typed beam telescope [Rub12], a widely used tool for testing of high-energy physics detectors of which several copies exists. The beam telescope consists of six monolithic active pixel sensors (MAPS), called Mimosa26 [Bau+09]. Despite their binary readout (no charge information available) the sensors offer a high spatial resolution. This is achieved by small pixels with a size of $18.4 \times 18.4\,\mu m^2$. To minimise the material budget, and thus improve tracking capabilities, the sensors are thinned to 50 µm resulting in a total material budget of 7×10^{-4}. In addition, the charge carrier movement dominated by diffusion improves the spatial resolution of the Mimosa26 sensors due to enhanced charge sharing between adjacent pixels. The intrinsic resolution of the Mimosa26 sensors is estimated to be 3.2 µm [Jan+16] enabling tracking of traversing particles with excellent spatial resolution.

The Mimosa26 sensors are read out with a continuous, triggerless rolling shutter readout (115.2 µs exposure time) using the Python-based *pymosa* readout system [Die+]. This readout method allows for data acquisition at trigger rates of up to 20 kHz [Wol16; Die17]. A precise time information for telescope tracks is essential to measure the hit-detection efficiency. The relatively long readout cycle of 115.2 µs of the Mimosa26 sensors does not provide sufficient timing resolution. Therefore, an ATLAS FE-I4 pixel detector [Gar+11] with 25 ns time stamping capabilities (triggered readout using the *PyBAR* readout system [JP+]) is used as a time reference plane.

The unambiguous assignment of the time stamp from the time reference plane to the telescope tracks is realised by spatially matching the hits in the time reference plane with the Mimosa26 tracks. Therefore, the track reconstruction is more challenging as it requires additional steps like selecting only tracks with a spatially matched hit (within given distance) in the time reference plane and selecting only tracks for which the hit matching is unique. All these necessary steps are implemented inside *beam telescope analysis* (Chapter 5). Details regarding the readout concept of the Mimosa26 telescope and time stamp matching can be found in [Wol16; Die17].

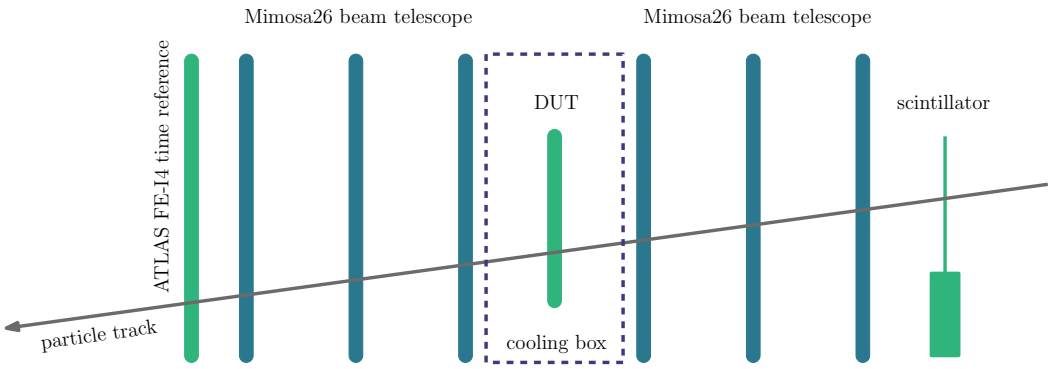

Figure 6.13: Sketch of a typical beam telescope setup consisting of six high-resolution Mimosa26 tracking detectors. A scintillator in front of the setup creates a trigger signal every time a particle traverses the beam telescope. The DUT is installed in the centre of the beam telescope. An ATLAS FE-I4 detector with high precision time stamping capabilities is used as a time reference. Irradiated DUTs are mounted inside a cooling box. Distances not to scale.

The DUT is installed in the centre of the beam telescope setup to optimise the pointing resolution at the DUT. The total material budget of the characterised detectors is 1.7×10^{-2} and dominated by the support and cooling structure of the PCB below the readout chip. Irradiated devices are mounted inside a cooling box made of styrodur to keep the leakage current at a reasonable value after irradiation. The DUTs are cooled to $-20\,^{\circ}\mathrm{C}$ using a feedback system to keep the temperature stable during measurements (variation over time less than $1\,^{\circ}\mathrm{C}$).

In contrast to a *threshold scan* where triggers are sent to the chip after each injection, during test beam measurements hits are created by traversing particles and the trigger is generated externally using the scintillator signal. Within the *BDAQ53* readout system this is a so-called *external trigger scan*. In all test beam measurements 32 consecutive triggers are sent to the readout chip for each scintillator signal corresponding to a readout window of $32 \times 25\,\mathrm{ns} = 800\,\mathrm{ns}$.

6.5 Detector capacitance measurements

In this section, the methods used for measuring the detector capacitance (Sec. 6.7.2) are briefly introduced. The detector capacitance is a crucial property of a sensor as it has influence on the performance of a detector in terms of electronic noise, charge collection efficiency and bandwidth, as explained in Sec. 3.3.

Detector capacitance measurement using an LCR meter

The most commonly used tool to measure the capacitance of silicon sensors is to use an LCR meter [Wit13; Kli13; Gor+01]. An LCR meter is a device that measures the complex impedance

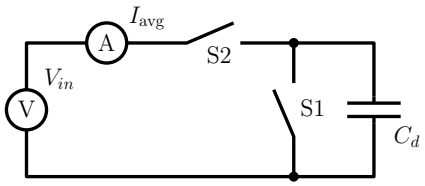

Figure 6.14: Basic principle of the Charge Based Capacitance Measurement (CBCM) method. Two switches, S1 and S2, are periodically switched to charge the capacitance C_d to the voltage V_{in} and discharge it. Measuring the average switching current I_{avg} allows the determination of the capacitance C_d.

of devices. Applying an AC-signal with fixed frequency the LCR meter determines the complex impedance from the signal phase and amplitude change over the device. Since, especially after irradiation, high bias voltages are necessary to deplete sensors, an additional high voltage source meter is used. The high voltage is decoupled from the LCR meter via a so-called "bias box" to protect the inputs of the LCR meter. A bias box that can be operated at up to 1000 V and has a precision of 0.5 pF was designed [Him21]. This is not sufficient for measuring the capacitance of a single pixel (a few tens fF). However, it is sufficient to measure the bulk capacitance (capacitance between all pixels and back plane) so that the full depletion voltage can be extracted. For details regarding the setup and measurement procedure see [Him21].

Detector capacitance measurement using the PixCap65 chip

To provide the possibility of capacitance measurements with sub-fF precision the PixCap65 chip was designed [KK21]. The chip consists of a 40×40 pixel matrix with $50 \times 50\,\mu\text{m}^2$ pixels. The capacitance measurement within the PixCap65 chip is based on the Charge Based Capacitance Measurement (CBCM) [McG+97]. The basic principle is depicted in Fig. 6.14. This circuit consists of two switches S1 and S2 which can be periodically switched with a frequency f to charge (S1 open, S2 closed) the capacitor C_d (represents capacitance of device under test) to the voltage V_{in} or discharge (S1 closed, S2 open) it. By measuring the average switching current I_{avg} (charge and discharge currents have different paths) the capacitance C_d can be determined using the following equation [KK21]:

$$C_d = \frac{Q}{V_{in}} = \frac{\int_0^T I(t)\mathrm{d}\,t}{V_{in}} = \frac{\frac{1}{T}\int_0^T I(t)\mathrm{d}\,t}{f \cdot V_{in}} = \frac{I_{\text{avg}}}{f \cdot V_{in}}\,. \tag{6.5}$$

Since the leakage current from the sensor adds up to the measured switching current, the switching current is measured for frequencies between 1 MHz and 4 MHz. With a linear fit, the capacitance can be calculated using the slope (see Fig. 7.9). The precision using the PixCap65 is estimated to be 0.3 fF, which is limited by the inherent process variations of the CMOS technology [KK21]. This is three orders of magnitudes smaller than the precision achieved with

the LCR meter setup, and therefore well suited to measure the capacitance of a single pixel as well as inter-pixel capacitances. The pixel capacitance values in the following chapters refer to the total pixel capacitance (sum of contributions from coupling to back plane, p-stop and neighbouring pixels) which is measured by toggling one pixel at a time while all other pixels are set to ground.

The measured values always include a parasitic contribution from the switching circuit, routing and bump bonds. Important for the evaluation is the total input capacitance of the analogue front-end which is given by the pure pixel capacitance and the (parasitic) contributions due to routing and bump bonds[6]. The parasitic contributions were determined in [KK21] using several samples. The contribution from the switching circuit was estimated to be approximately 5 fF, and the contribution due to routing and bump bonds is about 10 fF. Subtracting the known contribution of the switching circuit from the measured value yields the total input capacitance (due to the pixel sensor). Details regarding the PixCap65 chip and the setup can be found in [KK21]. Dedicated small pixel arrays (64×64 pixels) are bump-bonded to the PixCap65 chip to measure the pixel capacitance.

6.6 Characterisation of a passive CMOS prototype sensor

In the following section the characterisation of a passive CMOS prototype sensor before and after irradiation is presented. Various pixel designs (different readout electrode size), discussed in Sec. 4.2, are compared to each other and a motivation for the pixel design chosen for the large-area passive CMOS sensors is given. Special emphasis is put on the performance after irradiation to demonstrate the radiation tolerance of passive CMOS pixel sensors. The performance is compared to the performance requirements of the ATLAS ITk project listed in Tab. 3.1.

Although only one sample is investigated, the obtained results are still representative for a full batch of passive CMOS sensors, since process variations are negligible (150 nm CMOS process) with respect to the size of the microstructures (a few µm). In addition, no significant differences in breakdown behaviour were found with passive CMOS sensors from a previous submission, and the results obtained with one sample were representative for the entire batch [Poh20].

6.6.1 IV-curves

To check the functionality of a sensor and determine its maximum operational voltage the leakage current as a function of the applied (reverse) bias voltage is measured (IV-curve).

IV-curves before and after irradiation for 100 µm thin passive CMOS sensors after bump-bonding are depicted in Fig. 6.15. Before irradiation (solid blue line), the maximum operational voltage, measured at room temperature, is approximately 220 V due to a breakdown most likely

[6] The contribution of the capacitance of the CSA to the total input capacitance is neglected, since the capacitance of the sensor is much larger than the capacitance of the CSA.

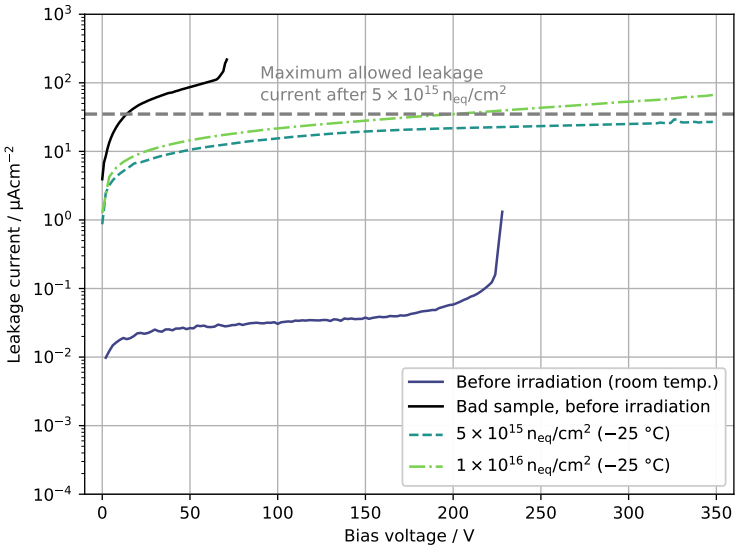

Figure 6.15: IV-curves of 100 µm thin passive CMOS pixel sensors after bump-bonding at different levels of irradiation. The leakage current is normalised to the total area of the sensor. The IV-curve before irradiation (blue solid line) was taken at room temperature. After irradiation (green dashed lines), the IV-curves were taken at an environmental temperature of −25 °C and a relative humidity of < 20 %. The grey dashed line shows the maximum allowed leakage current (35 µA/cm^2) after a fluence of 5×10^{15} n$_{eq}$/cm^2 according to the ATLAS ITk specifications listed in Tab. 3.1.

in the pixel matrix. This is well above the requirement listed in Tab. 3.1 ($> V_{dep} + 70$ V) assuming a reasonable full depletion voltage of $V_{dep} \approx 30$ V (see Sec. 6.6.4). Some sensors show an ohmic behaviour and high leakage current even before irradiation, as well as an early current increase at about 70 V. This behaviour has already been reported in [Poh20] and is due to the fact that the sensor edge (at high voltage level) can touch adjacent unused bump bonds as the sensor is smaller than the readout chip. In accordance with this, significantly higher electronic noise is measured for pixels located at the sensor edge compared to pixels located in the inner part of the pixel matrix (see Fig. 7.10 in the Appendix), indicating high current flow into these pixels. This issue can be mitigated by electrical insulation of the sensor edge and unused bump bonds of the readout chip. After irradiation (dashed lines), there is no breakdown visible any more up to the maximum tested bias voltage of 350 V, measured at an environmental temperature of −25 °C. Even after a fluence of 1×10^{16} n$_{eq}$/cm^2 the sensors are still functional. The maximum measured leakage current[7] of 23 µA/cm^2 after a fluence of 5×10^{15} n$_{eq}$/cm^2 is below the maximum allowed leakage current of 35 µA/cm^2 at the same fluence as required by

[7] Although the leakage current is measured below the required voltage of 400 V, it is expected that the leakage current is below the limit event at a bias voltage of 400 V.

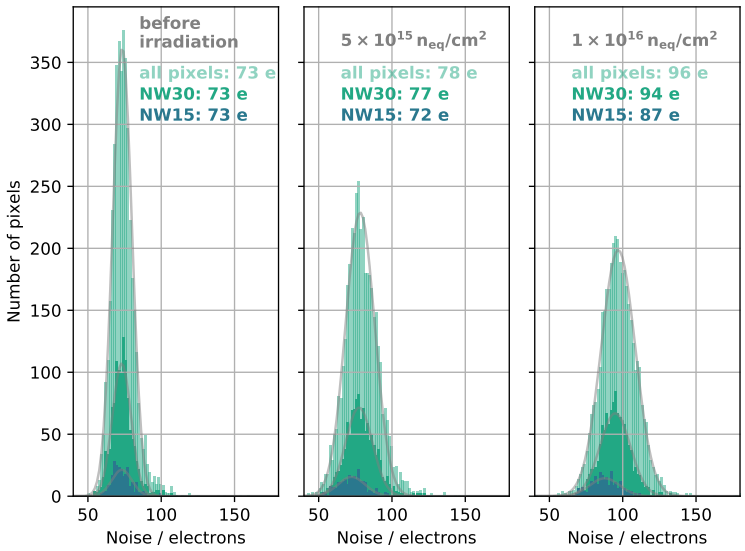

Figure 6.16: Electronic noise before and after irradiation extracted from a *threshold scan*. Distributions are fitted with a Gaussian function to extract the mean noise (values shown in legend). Noise distributions depicted for different pixel designs of the sensor (all pixels, NW30-pixels, NW15-pixels). Measurements are done at room temperature before irradiation and at an environmental temperature of $-17\,^{\circ}\mathrm{C}$ after irradiation. Electronic noise is measured using the Linear front-end of the RD53A readout chip.

ATLAS ITk (see Tab. 3.1).

The power dissipation of the sensor after a fluence of $1 \times 10^{16}\,\mathrm{n_{eq}/cm^2}$ necessary for a hit-detection efficiency larger than 97 % (Sec. 6.6.3) is approximately $7\,\mathrm{mW/cm^2}$ ($35\,\mu\mathrm{A/cm^2}$ at 200 V). This is comparable to 3D sensors, which are known to have a low power dissipation [Ter+20].

6.6.2 Electronic noise

An important parameter in evaluating the performance of sensors is the electronic noise. A measure of the electronic noise is the ENC which can be extracted from a *threshold scan* (Sec. 6.3). The ENC for a detector system based on a CSA depends linearly on the detector capacitance (ENC $\sim C_{\mathrm{det}}$), as discussed in Sec. 3.3. For this reason, the detector capacitance is kept as small as possible to minimise the electronic noise. ENC distributions (histogrammed per pixel) measured in a *threshold scan* for a passive CMOS sensor can be seen in Fig. 6.16. The ENC is shown for different levels of irradiation (left to right) and for different pixel designs of the sensor (colour-coded).

Before irradiation, an ENC of 73 e is measured, which is comparable to other planar sensors

read out with the same amplifier chip (see Fig. 7.11 in the Appendix). No difference between pixel designs is observed, although the pixel capacitance is slightly different for the various pixel geometries´. For the NW15 design a pixel capacitance of $(22.4 \pm 0.3)\,\mathrm{fF}$ is measured, whereas for the NW30 design a pixel capacitance of $(33.5 \pm 0.3)\,\mathrm{fF}$ is measured[8] [KK21]. A possible explanation for this is that the increase in noise due to a larger detector capacitance ($\mathrm{ENC_{ser}} \sim C_{\mathrm{det}}$) is counteracted by a smaller bandwidth due to the larger detector capacitance ($\tau_{\mathrm{CSA}} \sim C_{\mathrm{det}}$), according to Eq. 3.86. The resulting net effect is zero and no change in electronic noise is observed. However, this depends strongly on the exact transfer function of the detector system, which is different for different analogue front-end designs.

After a fluence of $1 \times 10^{16}\,\mathrm{n_{eq}/cm^2}$, the ENC increases to approximately 100 e. Most likely this is due to the increase in leakage current (90 µA corresponding to 22 nA per pixel, measured at an environmental temperature of $-17\,^{\circ}\mathrm{C}$) resulting in an increase of shot noise (see Eq. 3.89). Further, the performance of the analogue front-end degrades with irradiation (i.e. transconductance g_m decreases), which is likely responsible for a not specifiable additional noise contribution (see Eq. 3.88). In addition, it cannot be excluded that the detector capacitance changes with irradiation. Dedicated measurements with irradiated sensors are planned in future.

After irradiation, the electronic noise of pixels with larger readout electrode size is slightly higher. In particular, the ENC of the NW30-pixels is approximately 8 % higher than the one of the NW15-pixels, after the highest measured fluence of $1 \times 10^{16}\,\mathrm{n_{eq}/cm^2}$.

6.6.3 Hit-detection efficiency

To ensure an efficient track reconstruction in the later experiment, an (in-time) hit-detection efficiency > 97 % during the whole period of operation is required for the ATLAS ITk pixel detector modules. To verify that this requirement is fulfilled for passive CMOS sensors and demonstrate radiation tolerance, the efficiency as a function of the bias voltage for different levels of irradiation was measured. Details regarding the beam telescope setup used for this measurement are explained in Sec. 6.4. The necessary steps for track reconstruction and efficiency calculation are summarised in Chap. 5. The detector was tuned to a threshold of approximately 1000 e with a noise occupancy (per pixel) less than 10^{-6} for all presented measurements. The number of masked pixels (stuck or noisy) was below 1 %. The efficiency was measured using a minimal ionising particle beam (5 GeV electrons) at orthogonal incidence.

Fig. 6.17 shows the hit-detection efficiency as a function of the bias voltage for the NW- and DNW-flavours before and after irradiation. For simplicity, only the pixel flavours with 30 µm and 25 µm n-well width are shown. Before irradiation, there is no significant difference between the shown pixel geometries and the hit-detection efficiency is above 99.5 % at 5 V only. After irradiation, a "turn-on" behaviour of the efficiency is visible, i.e. the efficiency increases (until it reaches a saturation) with increasing bias voltage. This is expected as the sensitive volume of

[8] Including 10 fF of parasitic capacitance due to routing and bump bonds.

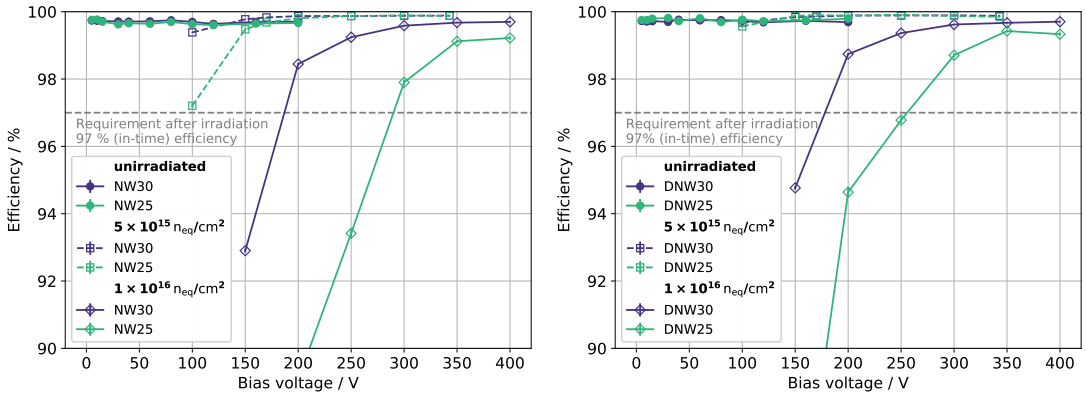

(a) Hit-detection efficiency of NW-flavours **(b)** Hit-detection efficiency of DNW-flavours

Figure 6.17: Hit-detection efficiency as a function of bias voltage for different pixel flavours and different irradiation levels. The grey dashed line represents the requirement of an (in-time) efficiency larger than 97 % according to Tab. 3.1. For the sake of clarity, not all pixel designs are shown. The shown error bars are purely statistical. Left: NW-flavours. Right: DNW-flavours.

the detector is not fully depleted any more after irradiation (for the tested voltages). Therefore, the depletion zone keeps increasing with increasing bias voltage resulting in a larger charge signal, and thus higher efficiency. At a fluence of $5 \times 10^{15}\,\mathrm{n_{eq}/cm^2}$ and the highest tested bias voltage (350 V), the efficiency for the NW30-design is $(99.88 \pm 0.01)\,\%$. This is well above the 97 %-limit (grey dashed line) as required for sensors for the ATLAS ITk detector (see Tab. 3.1). Even after a fluence of $1 \times 10^{16}\,\mathrm{n_{eq}/cm^2}$ the sensor is highly efficient and meets the efficiency requirement for voltages above 200 V. At 400 V a hit-detection efficiency of $(99.78 \pm 0.01)\,\%$ for the NW30-design is measured.

The DNW-flavours (pixels with additional deep n-well) show a slightly higher efficiency (2 % – 3 %) after irradiation, especially for pixels with smaller readout electrode and at lower bias voltages. However, no significant differences between DNW-flavours and NW-flavours are observed for pixels with the largest readout electrode. Pixels with larger readout electrodes are more efficient after irradiation. The efficiency measured for the various NW-pixel geometries after irradiation is summarised in Fig. 6.18. It is clearly visible that for a fixed bias voltage, the efficiency increases with increasing size of the readout electrode for both fluences. The efficiency of the NW30-design is approximately 3 % higher with respect to the NW15-design, after a fluence of $5 \times 10^{15}\,\mathrm{n_{eq}/cm^2}$. This difference increases to approximately 6 % at a fluence of $1 \times 10^{16}\,\mathrm{n_{eq}/cm^2}$. To study the efficiency loss in more detail the efficiency within an area of a pixel is calculated. This so-called *in-pixel efficiency map* is obtained by mapping all data into the area of a single pixel, as illustrated in Fig. 6.19. The average efficiency for different areas within a pixel (centre, edge and corner) is calculated. It is visible that pixels with smaller readout electrodes (right, NW15-design) are inefficient, especially at the pixel corners. This can

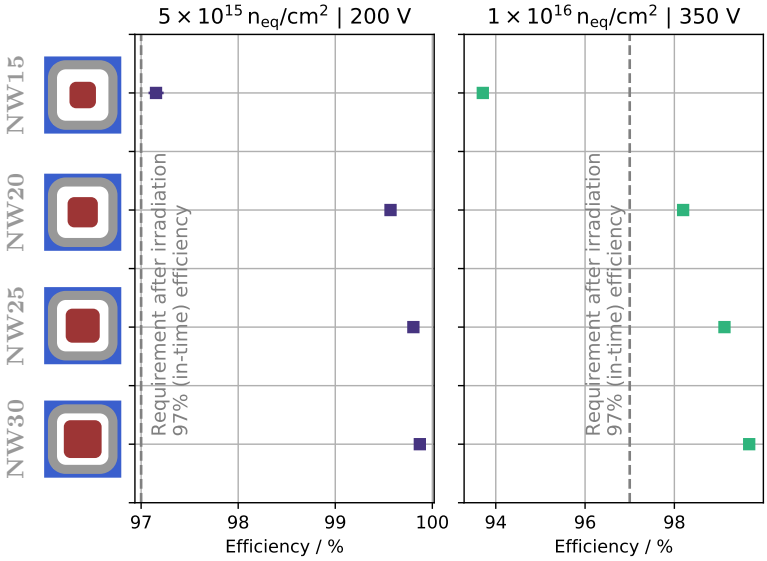

Figure 6.18: Hit-detection efficiency for different pixel designs (NW30, NW25, NW20 and NW15) after irradiation. Left: Efficiency at a fluence of $5 \times 10^{15}\,\mathrm{n_{eq}/cm^2}$ at 200 V. Right: Efficiency at a fluence of $1 \times 10^{16}\,\mathrm{n_{eq}/cm^2}$ at 350 V.

be explained by enhanced charge sharing at the pixel corners and by a lower electrical field at the pixel corners for pixels with smaller readout electrodes leading to a smaller charge signal (see Sec. 6.6.4), and thus lower efficiency. Detailed studies of the charge collection behaviour are shown in the following section.

In summary, it can be concluded that the advantage of designs with smaller n-wells in terms of noise do not outweigh the worse performance in terms of hit-detection efficiency, after irradiation. Further, the deep n-well design does not show significantly better performance in terms of hit-detection efficiency after irradiation (for designs with a large n-well, i.e. NW30-flavour). Consequently, the most-suited pixel design for large-area passive CMOS sensors is the NW30-design.

6.6.4 Charge collection

As explained in Sec. 6.2.2, the *TDC technique* enables a precise measurement of the charge signal of pixel detectors. Therefore, this method is employed to investigate the charge collection behaviour of passive CMOS pixel sensors before and after irradiation. The charge spectra are recorded using a minimum ionising particle beam (5 GeV electrons) at orthogonal incidence. Although the RD53A readout chip features four independent HitOR lines (Sec. 3.4.1) allowing charge measurements with clusters consisting of up to 2×2 pixels, only single-pixel clusters are

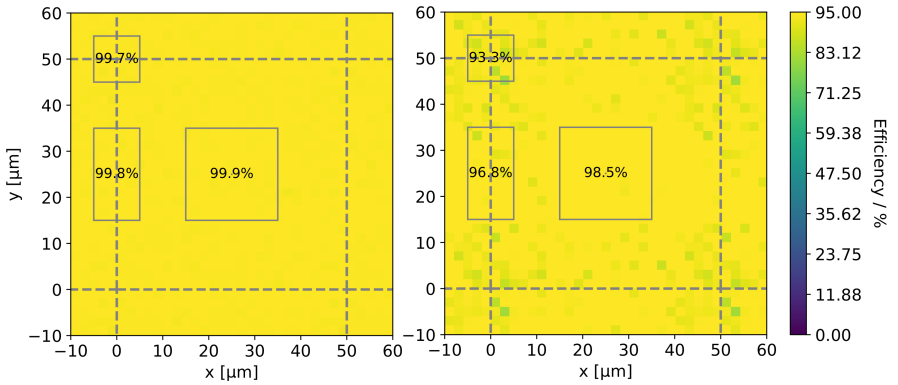

Figure 6.19: In-pixel efficiency map after a fluence of $1 \times 10^{16}\,\mathrm{n_{eq}/cm^2}$ for two different pixel flavours (left: NW30 and right: NW15) at a bias voltage of 400 V. The average efficiency is calculated for different areas within a pixel ($50 \times 50\,\mu\mathrm{m}^2$): centre, edge and corner. The grey dashed lines represent the pixel borders.

considered for the following analysis. The reasons for this are explained in Sec. 6.3.2.

Charge spectra recorded with the NW30-design at different levels of irradiation can be seen in Fig. 6.20. The charge spectra follow a Langau function (Landau function convolved with a Gaussian function). The Landau function describes the energy fluctuations and the Gaussian function includes the electronic noise and the uncertainty originating from the *TDC technique*, as well as charge smearing due to charge sharing. A convolution of a Landau function with a Gaussian function always shifts the measured charge towards higher values due to the asymmetric shape of the Landau function [Poh20]. Therefore, the recorded charge spectra are usually deconvolved to extract the true charge. However, given the charge resolution with the RD53A readout chip the artificial shift towards larger collected charge is negligible, and therefore the additional deconvolution step is omitted here.

The most probable value (MPV) of the Langau distribution is used as an estimator for the amount of collected charge, as motivated in Sec. 3.1.1. To extract the MPV, the charge spectra are fitted with a Langau (black line in Fig. 6.20) using the MINUIT algorithm [JR75] implemented by the Python package *Iminuit* [Dem+20]. The Landau function with the MPV as an input is defined within the Python package *pylandau* [Poh], details can be found in [Poh20]. The number of entries N of the charge spectra follow a Poisson distribution, and therefore the uncertainty is estimated with $\sqrt{N}$, which is used as an input to the fit. The quoted error bars on the MPVs originated from the uncertainty of the fit.

As shown in Fig. 6.20, the charge signal (MPV) decreases with increasing irradiation levels. The reasons for that are (see Sec. 3.2.1):

(a) the sensitive detector volume cannot be fully depleted any more after irradiation in the range of the tested bias voltages due to an increase in the effective doping concentration

N_{eff}

(b) charge carrier trapping due to bulk damage after irradiation

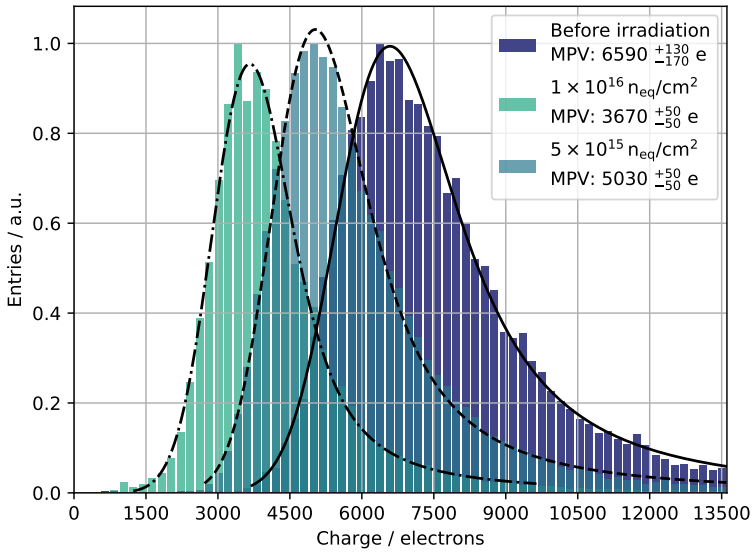

Figure 6.20: Measured charge distributions (single-pixel cluster) for different irradiation levels using the NW30 flavour. Distributions are fitted with a Langau to extract the most probable value (MPV). Before irradiation an MPV of (6590 ± 170) e is measured at 80 V. At a fluence of 5×10^{15} n$_{eq}$/cm^2 an MPV of (5030 ± 50) e is measured at 350 V and at a fluence of 1×10^{16} n$_{eq}$/cm^2 an MPV of (3670 ± 50) e is measured at 400 V.

While before irradiation a charge signal of (6590 ± 130) e is measured with the NW30-design, the charge signal reduces to (3670 ± 50) e at 400 V, after a fluence of 1×10^{16} n$_{eq}$/cm^2.

The charge collection behaviour, before and after irradiation, as a function of the applied bias voltage for the NW30- and DNW30-design is depicted in Fig. 6.21. Each data point corresponds to the MPV extracted from a fit to the recorded charge spectra. The error bars originate from the uncertainty of the fit. The measured charge signal increases with increasing bias voltage as the depleted region (only contribution to collected charge) grows with increasing bias voltage. Before irradiation, the charge signal saturates at approximately 30 V – 40 V resulting in a charge signal of about 6600 e (grey dashed line). This indicates that the sensitive detector volume is fully depleted at approximately 30 V, before irradiation. This value is a little larger than the calculated full depletion voltage of about 20 V using Eq. 3.31 under the assumption of a bulk resistivity of 5 kΩ cm – 7 kΩ cm [Poh20]. The reason for this is most likely a slightly lower resistivity of the substrate than expected.

Assuming that 73 e/h-pairs are created per µm (extracted from a GEANT4 simulation) the measured charge signal of approximately 6600 e after reaching full depletion corresponds to a

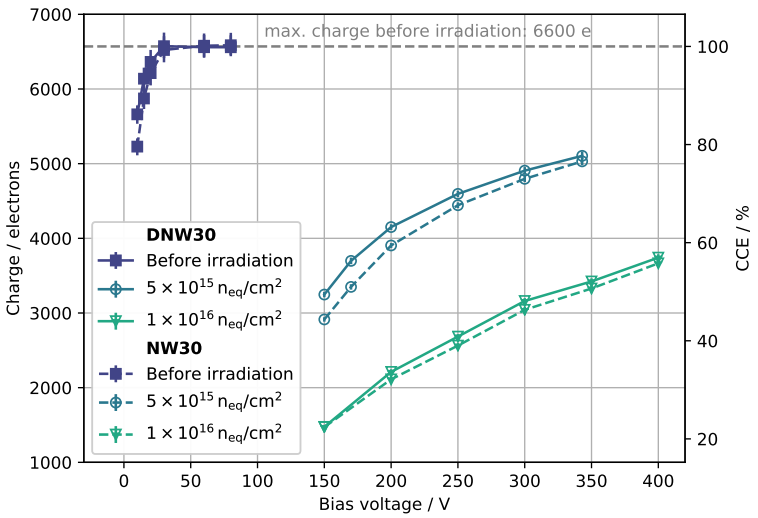

Figure 6.21: Charge collection behaviour for NW30-pixels (dashed lines) and DNW30-pixels (solid lines) as a function of the bias voltage before and after irradiation. The data points represent the most probable value extracted from a fit to the measured charge spectra. The error bars correspond to the uncertainty of the fit. The y-axis on the right-hand side shows the charge collection efficiency (CCE).

thickness of the sensitive detector volume of 90 µm. This is a reasonable value and agrees with the fact that the total detector thickness of 100 µm includes a few µm of metal layers decreasing the thickness contributing to charge collection. After irradiation, the charge signal decreases for the reasons mentioned above. The observation that the charge signal still increases with increasing bias voltage supports the argument that the detector volume cannot be fully depleted after irradiation (up to the tested voltages), and therefore the depletion zone still expands with increasing bias voltage, resulting in an increasing charge signal.

The charge collection efficiency (CCE), defined here as the ratio of the charge signal before irradiation (grey dashed line) and the charge signal after irradiation, is shown on the right y-axis in Fig. 6.21. After a fluence of 5×10^{15} $\mathrm{n_{eq}/cm^2}$ a CCE of approximately 80 % is measured for the highest tested bias voltage. The CCE reduces to about 55 % after a fluence of 1×10^{16} $\mathrm{n_{eq}/cm^2}$. Pixels with additional deep n-implantation (solid lines) collect slightly more charge than pixels with only the standard n-implantation (dashed lines). However, as shown in Sec. 6.6.3, this has no significant influence on the efficiency as the charge signal is well above the threshold.

At least within the range of tested bias voltages, there is no sign of charge multiplication visible, which is a known effect for highly irradiated detectors [Cas10a]. Charge multiplication can be beneficial for highly irradiated sensors to recover the amount of collected charge from before irradiation, or even beyond this.

Fig. 6.22 shows the measured charge signals for different pixel designs after irradiation. It is

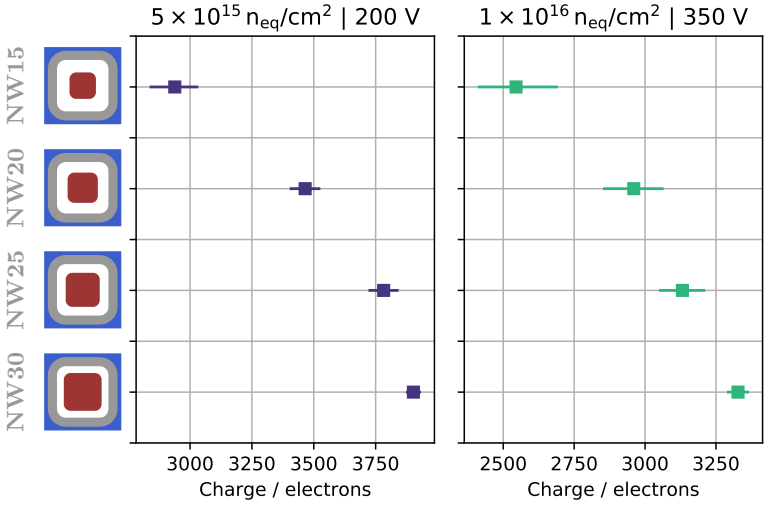

Figure 6.22: Measured charge signal (MPV) for different pixel designs (NW30, NW25, NW20 and NW15) after irradiation. Left: Collected charge at a fluence of $5 \times 10^{15}\,\mathrm{n_{eq}/cm^2}$ and a bias voltage of 200 V. Right: Collected charge at a fluence of $1 \times 10^{16}\,\mathrm{n_{eq}/cm^2}$ and a bias voltage of 350 V.

visible that pixels with smaller readout electrode (n-well) collect less charge after irradiation. In particular, the NW15-design collects approximately 25 % less charge than the NW30-design, after irradiation. The charge, especially for pixel designs with small readout electrode, is mainly lost in the pixel corners, as illustrated in Fig. 6.23 (*in-pixel charge map*). There are two reasons for this. Firstly, enhanced charge sharing at the pixel corners, resulting in a lower charge per pixel for single-pixel hits. Secondly, a lower electrical field[9], especially at the pixel corners for pixels with smaller readout electrode leads to more charge trapping (slower charge collection), and thus to a smaller charge signal. The charge loss at the pixel corners explains the efficiency loss (at the pixel corners) shown in Fig. 6.19.

6.7 Characterisation of large-area passive CMOS sensors

In the following section large-area passive CMOS sensors are examined to investigate their suitability for harsh radiation environments like the ATLAS and CMS experiments. A detailed discussion of the sensor layout is given in Sec. 4.3. The performance of these sensors is investigated for two reference fluences corresponding to the expected fluences in the outer ($2 \times 10^{15}\,\mathrm{n_{eq}/cm^2}$) and inner layers ($5 \times 10^{15}\,\mathrm{n_{eq}/cm^2}$) of the ATLAS detector and is compared to the performance requirements of the ATLAS ITk project listed in Tab. 3.1. Besides the

[9] A simulation of the electrical field with a simplified pixel geometry (no p-stop) can be seen in App. 7.

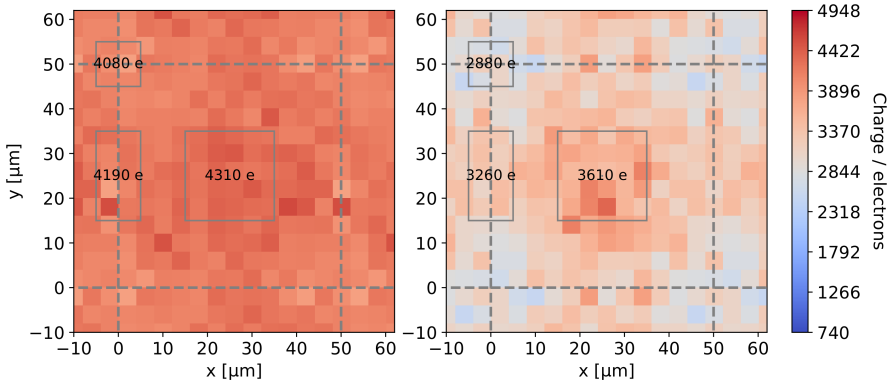

Figure 6.23: In-pixel charge map (mean value) after a fluence of $1 \times 10^{16}\,\mathrm{n_{eq}/cm^2}$ for two different pixel flavours (left: NW30 and right: NW15) at a bias voltage of 400 V. The average charge is calculated for different areas within a pixel ($50 \times 50\,\mu\mathrm{m}^2$): centre, edge and corner. The grey dashed lines represent the pixel borders.

estimation of the production yield which is important for later production and the investigation of the stitching process, advantages of different sensor designs are explored. Special emphasis is put on the measurement of the in-time hit-detection efficiency, a crucial parameter for detectors in high-rate environments.

6.7.1 IV-curves

Measuring the leakage current as a function of the (reverse) bias voltage (IV-curve) allows for the identification of production issues at wafer level, before the expensive bump-bonding process. Issues in the processing of the backside during the production of passive CMOS sensors were found. IV-curves of sensors that received different backside processing are illustrated in Fig. 6.24. Using the "original" backside processing procedure, the sensors show a significant excess of leakage current at approximately 30 V corresponding to the full depletion voltage, i.e. when the depletion zone touches the backside of the sensor. Sensors without any backside metallisation do not show this behaviour. It is therefore suspected that due to a too shallow backside implantation, aluminium from the backside metal is diffusing into the depleted silicon (see Sec. 4.1.2) and causes a short circuit between the frontside (pixels) and the backside, after full depletion is reached. To increase the depth of the backside implantation and prevent spiking, the dose of the backside implantation is increased. With the "fixed" backside processing, the sensors can be easily operated in overdepletion until at least 200 V. This emphasizes the importance of a proper backside processing when operating sensors in overdepletion. All further measurements were done with sensors with "fixed" backside processing.

One of the key parameters in electrical testing of sensors is the production yield specifying the percentage of working sensors. Especially for applications where large areas have to be

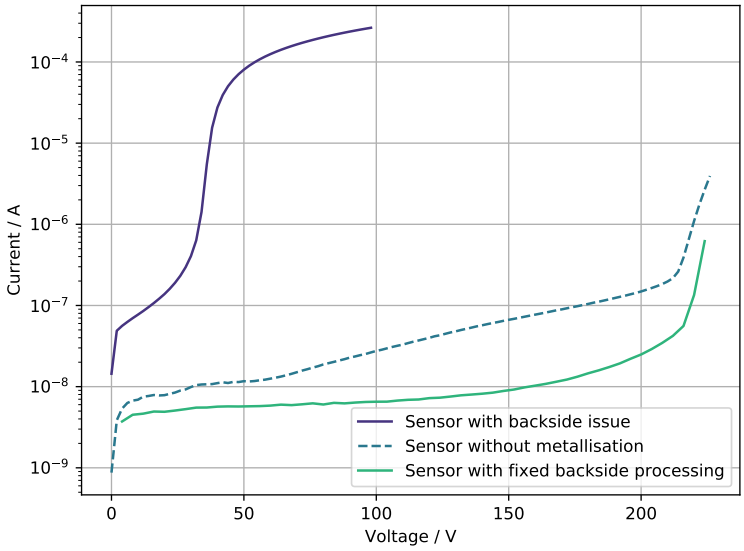

Figure 6.24: IV-curve measurements of bare passive CMOS sensors with different backside processing steps.

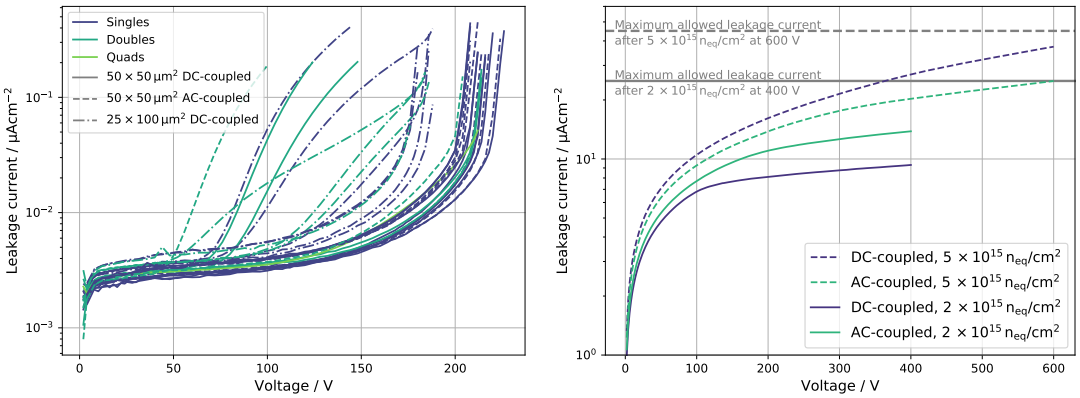

(a) **(b)**

Figure 6.25: **(a)** IV-curves measurements from two wafers of 150 µm thin passive CMOS sensors probed with needles, before dicing. The leakage current is normalised to the sensor area. The n-well ring surrounding the pixel matrix is floating. Different sensor sizes (Quads, Doubles, Singles) are colour-coded. Different sensor types are depicted in different line styles. The yield is estimated to 82 %. **(b)** IV-curve measurements of irradiated passive CMOS sensors bump-bonded to the RD53A readout chip. Leakage current is normalised to sensor area. Measurements were done at an environmental temperature of −25 °C. The readout chip was not powered during measurements and the bias grid was grounded. The grey lines represent the maximum allowed leakage current after the given fluence, according to the ATLAS ITk requirements listed in Tab. 3.1.

covered the yield has to be sufficiently high to reduce production costs. Further, it is important to check possible process variations which could cause different breakdown behaviours. IV-curves of sensors from two wafers before dicing[10] (one wafer was fully probed, from the other wafer sensors were randomly chosen) resulting in 33 IV-curves in total is used to estimate the yield of passive CMOS sensors. The corresponding IV-curves are depicted in Fig. 6.25a. The leakage current is normalised to the sensor area to compare different sensor sizes. Sensors of different sizes are colour-coded, whereas the line style differentiates the type of the sensor (DC-, AC-coupled, pixel size). It is visible that only a few sensors are not functional resulting in a yield of 82 % when applying the requirement on the breakdown voltage ($\gtrapprox 100\,\mathrm{V}$) according to ATLAS ITk specifications (see Tab. 3.1). This proves that reticle stitching is working. In addition, IV-curves of malfunctioning sensors cannot be attributed to any specific type. The leakage current per area before breakdown is approximately the same for all sensors indicating that it scales linearly with the area of the sensor, as expected. Small variations in leakage current arise from different environmental temperatures during testing of the wafers. The measured breakdown voltage of $210\,\mathrm{V} - 220\,\mathrm{V}$ does not vary much across the full wafer (for a more detailed investigation of the breakdown behaviour, see below). Therefore, it can be concluded that process variations are negligible which is in agreement with measurements of passive CMOS sensors from former submissions [Poh20]. Further, the breakdown voltage is well above the ATLAS ITk requirement ($> V_{\mathrm{dep}} + 70\,\mathrm{V}$) listed in Tab. 3.1 assuming a reasonable full depletion voltage of $V_{\mathrm{dep}} \approx 35\,\mathrm{V}$ (see Sec. 6.7.2).

Comparing IV-curves between sensors with $50 \times 50\,\mu\mathrm{m}^2$ pixels (solid lines) and $25 \times 100\,\mu\mathrm{m}^2$ (dash-dotted lines), it is visible that sensors consisting of the rectangular pixel geometry exhibit an earlier breakdown (approximately 30 V less). The reason for this behaviour is still under investigation, but it is suspected that it is caused by the smaller radius of curvature of the rectangular pixel geometry (see Fig. 4.9). This leads to higher electrical fields at the corners between the (floating) p-stop and the pixel implant (n-well), and thus to an earlier breakdown compared to the square pixel geometry (larger radius of curvature).

Fig. 6.25b shows IV-curves of irradiated passive CMOS sensors bump-bonded to the RD53A readout chip. Due to bulk damage, the leakage current after irradiation is several orders of magnitude higher compared to unirradiated devices. No breakdown is visible up to the maximum measured bias voltage of 400 V (for $2 \times 10^{15}\,\mathrm{n_{eq}/cm^2}$) or 600 V (for $5 \times 10^{15}\,\mathrm{n_{eq}/cm^2}$). The sensors can therefore be operated at least up to this operational voltage, in agreement with the specifications listed in Tab. 3.1. The observed differences in leakage current at the same nominal fluence are not attributed to differences in the sensor designs (DC- vs. AC-coupled), since the main contribution to leakage current after irradiation is bulk damage, which is independent of the exact sensor design, but could be explained with the uncertainty on the nominal fluence of up to 25 %. Most likely one sensor was irradiated to a higher fluence compared to the other

[10] Dicing describes the process of cutting the wafer into its single structures (e.g. sensors) implemented on the wafer.

sensors. The leakage current for all devices is lower than the maximum allowed leakage current for the respective fluence (grey lines) as required for ATLAS ITk (see Tab. 3.1). The leakage currents at 400 V and 600 V translate into a power dissipation of 15 mW – 22 mW for a fluence of $5 \times 10^{15}\,\mathrm{n_{eq}/cm^2}$ and 6 mW – 4 mW for a fluence of $2 \times 10^{15}\,\mathrm{n_{eq}/cm^2}$, respectively. However, the required bias voltage necessary to meet the 97 % efficiency requirement is significantly lower (see Sec. 6.7.5), which lowers the power dissipated by the sensor.

6.7.2 Detector capacitance and electronic noise

The detector capacitance C_{det} is a crucial property of a sensor as it has influence on important properties of a detector system like the electronic noise and the bandwidth, as discussed in Sec. 3.3. The goal is to minimise the capacitance of a detector to minimise the electronic noise (scales linearly with C_{det}). Further, precise knowledge of the detector capacitance is necessary for an optimisation of the power consumption, since an increase in noise due to a larger detector capacitance can be compensated with a larger transconductance (proportional to power consumption), as shown in Sec. 3.3.

From measurements of the bulk capacitance (capacitance of all pixels to back plane) as a function of the bias voltage (CV-curve) the depletion voltage can be extracted. Assuming that the pixel sensor can be represented by a parallel plate capacitor (first-order approximation), $1/C_{\mathrm{det}}^2$ is proportional to the bias voltage V_{bias} before full depletion is reached, according to Eq. 3.33. After full depletion the capacitance saturates, and thus from the resulting "kink" of the CV-curve the full depletion voltage can be estimated.

Detector capacitance

The capacitance of passive CMOS pixel sensors is measured using both an LCR meter and the PixCap65 chip. A brief description of these setups is given in Sec. 6.5. Due to the limited precision of the LCR meter setup (0.5 pF), only the bulk capacitance is measured. The bias grid of the sensor connects all pixels simultaneously to ground, while the high voltage is applied at the backside contact. Using the PixCap65 chip the measurement precision is at sub-fF level (0.3 fF), and thus allows for a measurement of the capacitance of a single pixel, which is useful for a detailed study of the sensor.

The CV-curves for $50 \times 50\,\mu\mathrm{m}^2$ and $25 \times 100\,\mu\mathrm{m}^2$ pixel sensors measured with both setups are shown in Fig. 6.26. As expected for a parallel plate capacitor, $1/C_{\mathrm{det}}^2$ increases nearly linearly with increasing bias voltage before full depletion and is (almost) constant after full depletion. Small deviations from this behaviour can be explained by additional contributions to the capacitance from the p-stop and guard rings, which are not described by the parallel plate capacitor model. From Fig. 6.26a a full depletion voltage of 30 - 35 V for 150 µm thin passive CMOS sensors can be extracted (point at which capacitance saturates). This is a reasonable value assuming a bulk resistivity of 8 kΩ cm – 9 kΩ cm, as estimated from independent measurements

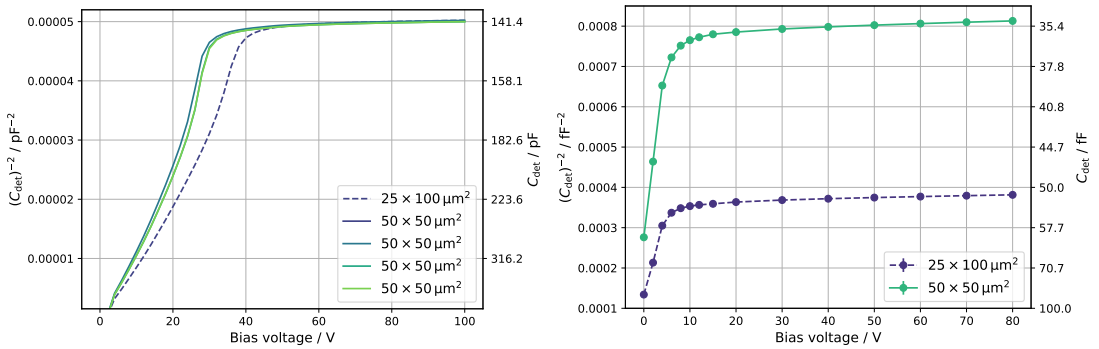

(a) CV-curves using an LCR meter

(b) CV-curves using the PixCap65 chip

Figure 6.26: (a) Bulk capacitance ($1/C^2$) of unirradiated passive CMOS sensors (150 µm thin) as a function of the bias voltage using the LCR meter setup (Sec. 6.5). A frequency of 10 kHz is used. Measurement uncertainty is 0.5 pF. Data from [Him21]. **(b)** Total pixel capacitance ($1/C^2$) of unirradiated passive CMOS sensors (150 µm thin) as a function of the bias voltage using the PixCap65 chip (including parasitic capacitances). Each data point is an average over 400 pixels. Measurement uncertainty is 0.3 fF.

presented in Sec. 6.7.6 and in agreement with the ATLAS ITk requirement ($V_{\text{dep}} < 100\,\text{V}$) listed in Tab. 3.1. Small variations in the CV-curves (and therefore in the full depletion voltage) are attributed to small inhomogeneities in the bulk resistivity across the wafer and process variations. An explanation for the slightly larger full depletion voltage of the $25 \times 100\,\mu\text{m}^2$ pixel sensor (blue dashed line) is most likely a stronger lateral expansion of the depletion zone (before full depletion) due to the rectangular geometry of the pixels. However, as expected for sensors with the same thickness, both pixel geometries yield the same bulk capacitance of approximately 140 fF after full depletion.

The measurement of the total pixel capacitance using the PixCap65 chip is shown in Fig. 6.26b. The shown values include a parasitic capacitance due to routing and bump bonds of 10 fF, and thus correspond to the total detector capacitance "seen" by the analogue front-end. For $50 \times 50\,\mu\text{m}^2$ pixels, a total pixel capacitance of (35.1 ± 0.3) fF after full depletion (at 80 V) is estimated. The total pixel capacitance of $25 \times 100\,\mu\text{m}^2$ pixels is measured to be (51.2 ± 0.3) fF (at 80 V), which is approximately 40 % larger than for the $50 \times 50\,\mu\text{m}^2$ geometry. This is reasonable as the surface of the pixel implant (n-well) and p-stop, which is the dominant contribution to the pixel capacitance for these sensors [KK21], is larger for rectangular pixels with respect to the square pixels (see Fig. 4.9), and thus is responsible for a larger capacitance ($C \sim A$). In addition, the distance between the p-stop and the pixel implantation is slightly smaller (7.5 µm) for the rectangular geometry compared to the square geometry (8 µm) and therefore leading to an additional increase in capacitance ($C \sim 1/d$). Since the contribution to the back plane capacitance (pixel implant to back plane) of a single pixel is negligible compared to the capacitance between the pixel implant and p-stop (detector thickness is much larger than the distance

between the p-stop and pixel implant), the capacitance saturates already at much lower bias voltages (when the depletion zone reaches the p-stop), compared to Fig. 6.26a. This voltage does not correspond to the "regular" full depletion voltage (voltage at which whole detector volume is depleted).

For the prototype passive CMOS sensor[11], which has no bias grid, a pixel capacitance of (33.5 ± 0.3) fF is measured. It can therefore be concluded that the contribution of the bias grid to the pixel capacitance is negligible, since the measured pixel capacitance of (35.1 ± 0.3) fF for the same pixel design but with a bias grid is not much larger.

Electronic noise

The electronic noise of large-area passive CMOS sensors, before and after irradiation, is summarised in Fig. 6.27. The ENC is extracted from a *threshold scan* using the Linear front-end of the RD53A readout chip. Different pixel geometries as well as DC- and AC-coupled detectors are compared. An uncertainty of 5 % is assumed for calibrated detectors, whereas for uncalibrated detectors an uncertainty of 10 % is assumed to account for the observed variations of the charge calibration between different detectors (see Sec. 6.3.2).

Before irradiation, the electronic noise is estimated to be approximately 85 e. This value is roughly 10 % higher than the value measured with the prototype passive CMOS sensor, and thus slightly larger than for conventional sensors for hybrid pixel detectors (see Fig. 7.11 in the Appendix). The reason for this is unknown and requires future investigation. The electronic noise of detectors with $50 \times 50\,\mu m^2$ pixels and $25 \times 100\,\mu m^2$ pixels is the same within the measurement uncertainty, although the pixel capacitance is higher for the rectangular pixel geometry (see Fig. 6.26). Similar to the discussion in Sec. 6.6.2, this can be explained by two effects which balance out each other: The increased detector capacitance increases the serial component of the electronic noise ($ENC_{ser} \sim C_{det}$), however simultaneously decreases the bandwidth ($\tau_{CSA} \sim C_{det}$) and hence the electronic noise (see Eq. 3.86). The net effect is therefore zero and no change in electronic noise is measured for different pixel geometries. It is important to note that this depends strongly on the used analogue front-end as different designs have different transfer functions.

No significant difference in terms of noise is visible comparing DC- and AC-coupled sensors, before irradiation. Unlike in former passive CMOS sensors [Poh20], the additional parasitic contributions to the pixel capacitance due to the implementation of the AC-coupling MIM-capacitor are negligible in terms of an increase in electronic noise.

After irradiation, the electronic noise of DC-coupled passive CMOS sensors is measured to be approximately 100 e (at $2 \times 10^{15}\,n_{eq}/cm^2$ with 1 nA leakage current per pixel) and 110 e (at $5 \times 10^{15}\,n_{eq}/cm^2$ with 3 nA leakage current per pixel), respectively. The electronic noise of AC-coupled sensors remains at the level from before irradiation (80 e). Although the AC-

[11] Using the NW30 pixel design (Sec. 4.2).

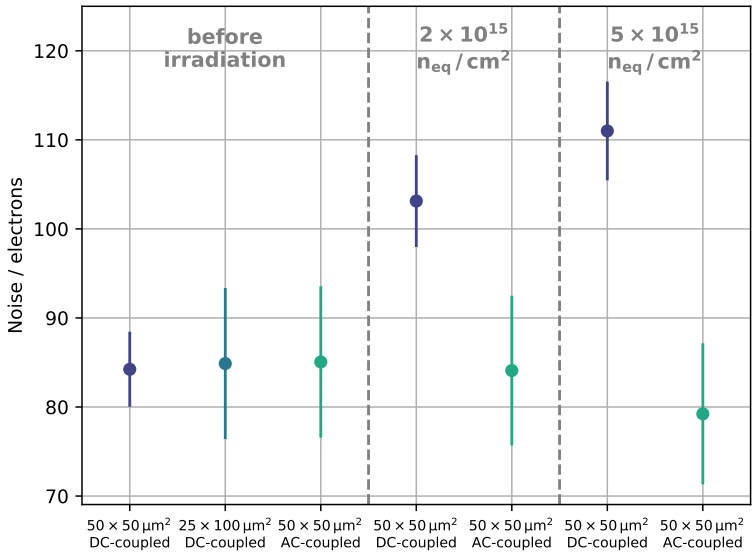

Figure 6.27: Electronic noise of large-area passive CMOS sensors before and after irradiation. The noise is measured in a *threshold scan* using the Linear front-end of the RD53A readout chip. Different pixel geometries and DC- and AC-coupled sensors are compared. Measurements with unirradiated detectors were performed at room temperature, while measurements after irradiation were performed at −20 °C. The leakage current after irradiation varies between 1 nA and 3 nA per pixel. For calibrated detectors an uncertainty of 5 % is assumed, whereas for uncalibrated detectors an uncertainty of 10 % is assumed. All detectors are tuned to a threshold of 1200 e.

coupling capacitance blocks the DC-component of the leakage current, the leakage current still contributes to shot noise (scales with leakage current) as it originates from fluctuations. Since no significant increase in electronic noise is observed for AC-coupled sensors, it is assumed that the contribution of shot noise to the total noise is negligible. This is reasonable as leakage currents of up to 3 nA per pixel are still relatively small. Most likely the reason for the up to 20 % larger electronic noise of DC-coupled sensors, is that the leakage current flowing into the amplifier's input creates a small DC-offset at the input of the amplifier, which slightly shifts the operational point from its optimum, depending on the amount of leakage current, and thus increases electronic noise.

6.7.3 Cross-talk

Cross-talk is the effect that charges from the hit pixel partially couple into neighbouring pixels. If the coupled charge exceeds the threshold of the pixel this effect can lead to artificial hits. Large (unwanted) cross-talk should be avoided, since it can deteriorate the reconstruction of the cluster position and thus decreases spatial resolution. Further, this effect can lead to higher

data rates if many pixels suffer from cross-talk. Cross-talk occurs most often in the sensor, via the coupling between neighbouring pixels.

Cross-talk is measured by injecting charge into a pixel while reading out the neighbouring pixel(s). Since cross-talk is usually a small effect (a few %) and the amount of injected charge using the injection circuit is limited, charge is injected simultaneously into several neighbouring pixels. Injection patterns used for this study are shown in Fig. 6.28a. The pixels into which the charge is injected are coloured in blue and the pixel that is read out is coloured in green. Measuring the threshold using these injection patterns (cross-talk threshold) the cross-talk can be calculated according to the following equation:

$$\text{cross-talk}\,[\%] = \frac{\mu_{\text{reg}}}{\mu_{\text{x}} \cdot n_{\text{inj}}} \times 100\,, \tag{6.6}$$

with μ_{reg} being the regular threshold, μ_{x} the cross-talk threshold and n_{inj} the number of injected pixels. The minimum measurable cross-talk is given by the maximum charge that can be injected using the injection circuit ($4096\,\Delta\text{VCAL} \approx 43\,000\,\text{e}$) and the threshold setting (approximately $1000\,\text{e}$).

Cross-talk of approximately 10 % has been observed with $25 \times 100\,\mu\text{m}^2$ pixel sensors bump-bonded to the RD53A readout chip [Jof+19]. The reason for this is an inevitable pairwise overlap of the metal layer and the pixel implant to map the rectangular pixel geometry to the $50 \times 50\,\mu\text{m}^2$ bump-bond pattern of the RD53A readout chip, as illustrated in Fig. 6.28b. The advantage of utilising a commercial CMOS process line for the production of pixel sensors is that many fine-pitched metal layers are offered. Thus, an overlap of metal layers and the pixel

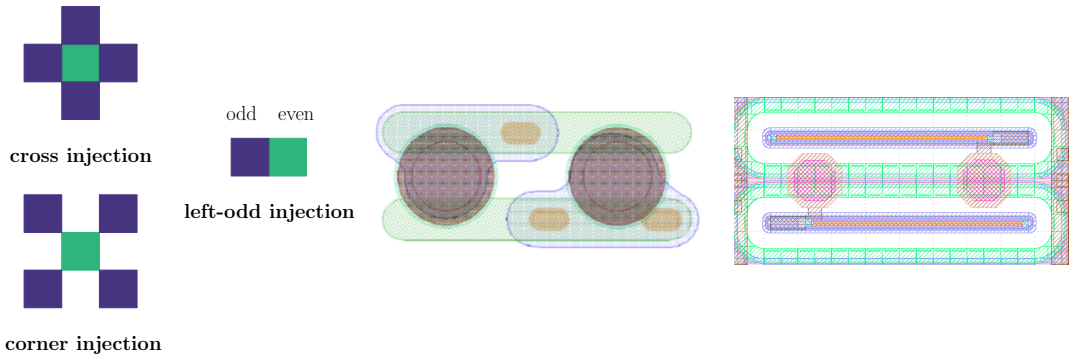

(a) Injection patterns **(b)** Conventional sensor **(c)** CMOS sensor

Figure 6.28: (a) Various injection patterns used for cross-talk studies. Injected pixels are coloured in blue, the pixel that is read out is coloured in green. The terms "even" and "odd" refer to pixels with even and odd column indices, respectively. **(b)** $25 \times 100\,\mu\text{m}^2$ pixel design of conventional sensors. The metal pads (blue) overlap with the pixel implants causing pairwise cross-talk in horizontal direction. From [Jof+19]. **(c)** $25 \times 100\,\mu\text{m}^2$ pixel design of passive CMOS sensors. The metal pads (octagonal shape) do not overlap with the pixel implants (blue).

implantation can be avoided in the case of passive CMOS sensors, as illustrated in Fig. 6.28c. This leads to much lower cross-talk compared to conventional sensor designs.

Cross-talk for sensors with square pixel geometry is measured using the corner-injection and cross-injection pattern (measurable cross-talk of $\geq 0.6\,\%$). Cross-talk for sensors with rectangular pixel geometry is measured using the left-odd injection pattern (measurable cross-talk of $\geq 2.5\,\%$). Using passive CMOS sensors the cross-talk for both pixel geometries, $50 \times 50\,\mu m^2$ and $25 \times 100\,\mu m^2$, is below the minimum measurable cross-talk. It is therefore assumed that for passive CMOS sensors the impact on data rate and position reconstruction due to cross-talk is negligible.

6.7.4 Time walk

As already discussed in Sec. 3.3.1, time walk describes the effect that the smaller the charge signal, the later the signal crosses the fixed comparator threshold, assuming constant peaking time. Therefore, the hit delay (time between charge deposition and hit detection) increases with decreasing charge. For applications in high rate environments like at the LHC it is important to minimise the time walk, since a precise estimation of the arrival time is necessary. Time walk measurements using the injection circuit are a fast way to characterise the timing behaviour of a pixel detector readout chip as no particle beam is required.

The hit delay is recorded as a function of the injected charge by measuring the time difference between a signal relative to the injection pulse and the hit arrival time (HitOR leading edge) using the *TDC technique*. Such a time walk curve with data from approximately 26 000 pixels using a passive CMOS pixel sensor bump-bonded to the RD53A readout chip is illustrated in Fig. 6.29. The time walk is measured using the Linear front-end with a threshold setting of approximately 1000 e. Since time walk is a relative quantity (important is the hit delay with respect to highest charge), the hit delay measured for the highest injected charge is subtracted from each measurement. Hit delay variations due to propagation delays of the injection pulse across the pixel matrix [Gar17] are not corrected. The average hit delay is shown as the green line and the variations (standard deviation) are illustrated by the grey area. During detector operation at the LHC, hits with hit delays larger than 25 ns are associated to the wrong bunch crossing ID unless a complex logic circuit is implemented (not the case for RD53A or ITkPix readout chips). On the second y-axis the percentage of hits with delay below a given value are shown. From Fig. 6.29 it can be concluded that 99.4 % of the pixel hits have a time walk below 25 ns.

Although this allows for an investigation of the timing behaviour of a pixel detector, the measured time walk curve has to be convolved with the expected charge spectrum to obtain a more realistic estimation of the percentage of in-time pixel hits (in-time efficiency). One approach that allows a direct measurement of the in-time efficiency is to record the hit delay using a minimum ionising particle beam simultaneously to the measurement of the hit-detection

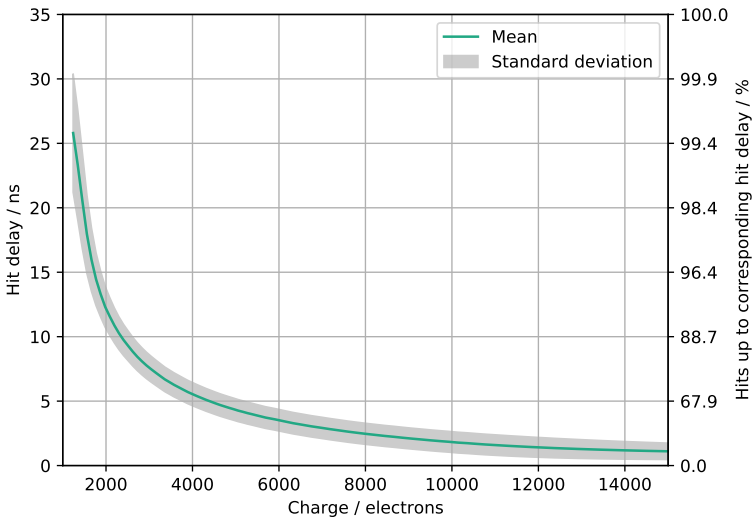

Figure 6.29: Time walk curve (hit delay as a function of injected charge) measured with a passive CMOS pixel sensor using the RD53A Linear front-end with data from approximately 26 000 pixels. The green line represents the average hit delay and the grey area shows the standard deviation.

efficiency with a beam telescope setup, as presented in the following section.

6.7.5 Hit-detection efficiency

The main focus of this section is to demonstrate that large-area passive CMOS sensors are radiation tolerant in terms of hit-detection efficiency and fulfil the requirement of an (in-time) hit-detection efficiency larger than 97 % after irradiation, as required for the use in the ATLAS ITk detector (see Tab. 3.1). Further, the influence of the stitching process on the hit-detection efficiency is investigated. The efficiency was measured using a minimum ionising particle beam (5 GeV electrons) at orthogonal incidence. The beam telescope setup used for this measurement is described in Sec. 6.4. Details regarding the track reconstruction and efficiency calculation can be found in Sec. 5. All detectors were tuned to a threshold of 1000 e – 1200 e with a noise occupancy (per pixel) less than 10^{-6}. The percentage of masked pixels (stuck or noisy) was below 1 %.

Fig. 6.30 shows the efficiency of a stitched passive CMOS sensor as a function of the x-position (column direction). Each data point corresponds to the average over all activated rows within a column. The grey dashed line indicates the position of the (central) reticle stitching line (see Fig. 4.7). Since not the whole sensor was illuminated, the efficiency drops to zero at the borders. The efficiency measured with pixels close to the stitching line is statistically consistent with the efficiency measured with pixels far away from the stitching line. Therefore, it can be concluded

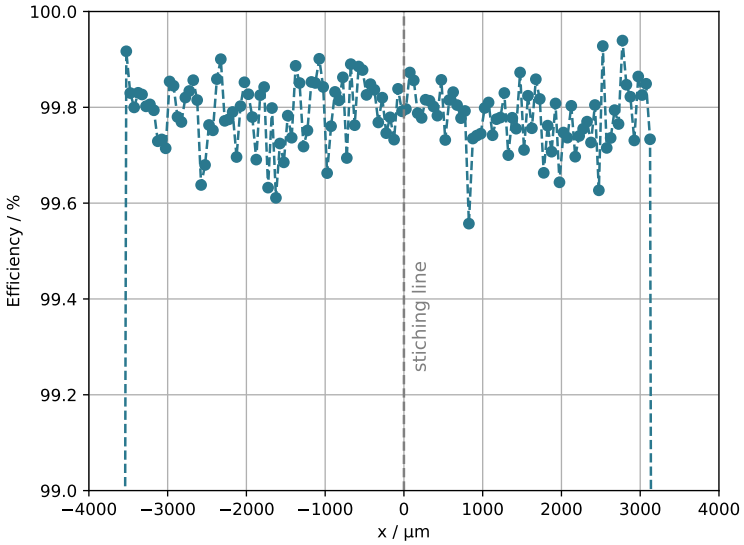

Figure 6.30: Efficiency of a stitched passive CMOS sensor as a function of the x-position (column direction). Each data point is calculated as the average over all activated rows within a column. The grey dashed line indicates the position of the (central) reticle stitching line (see also Fig. 4.7).

that reticle stitching works and has no influence on the efficiency.

The hit-detection efficiency, before and after irradiation, for DC- and AC-coupled sensors as a function of the bias voltage is shown in Fig. 6.31. The minimum efficiency after irradiation of 97 % required by ATLAS ITk is indicated by the grey dashed line. Before irradiation (Fig. 6.31a), the sensors are fully efficient at 10 V only. The maximum achievable efficiency for DC- and AC-coupled sensors is the same, which is consistent with the expectation. The hit-detection efficiency measured at 80 V is (99.80 ± 0.01) %. At bias voltages < 10 V (before full depletion), the efficiency measured with AC-coupled sensors is a few percent smaller with respect to DC-coupled sensors. This can be explained by small differences in threshold, which have an influence on the efficiency especially at low bias voltages, since the charge signal is close to the detection threshold (approximately 1200 e). Another explanation for this could be a smaller charge signal for AC-coupled detectors, which is investigated in Sec 6.7.6.

After irradiation (Fig. 6.31b), a considerably higher bias voltage is necessary for fully efficient detectors. As already explained in Sec. 3.2.1 there are two reasons for this: a) charge carrier trapping sets in after irradiation and b) the detector cannot be fully depleted any more. Both reasons lead to a significant lower charge signal after irradiation resulting in lower efficiency for a given bias voltage compared to before irradiation. After a fluence of $2 \times 10^{15}\,\mathrm{n_{eq}/cm^2}$, the maximum measured efficiency is (99.77 ± 0.01) % at a bias voltage of 400 V. This is well

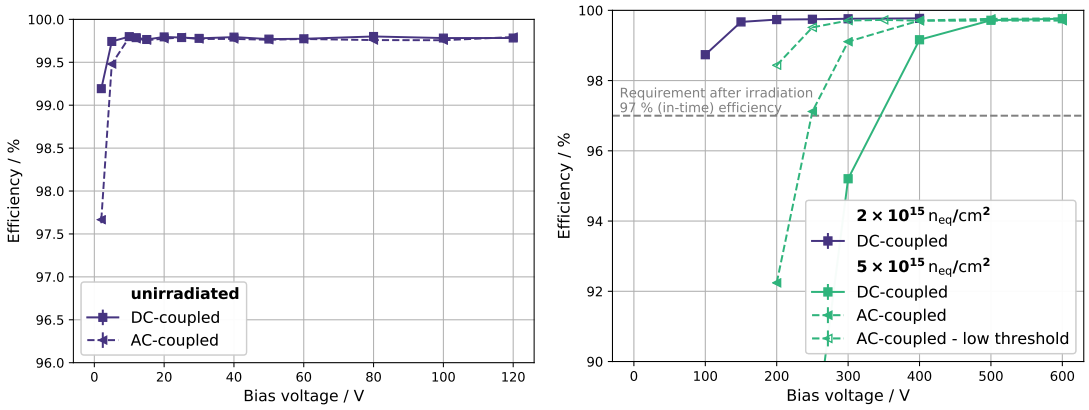

(a) Before irradiation **(b)** After irradiation

Figure 6.31: (a) Hit-detection efficiency before irradiation as a function of the bias voltage. Efficiency is shown for a DC-coupled and AC-coupled sensor. **(b)** Hit-detection efficiency after irradiation as a function of the bias voltage. The grey dashed line indicates the minimum required efficiency after irradiation. Efficiency is shown for DC- and AC-coupled sensors as well as for a low threshold setting (approximately 850 e) using the Differential front-end.

above the required efficiency after irradiation of 97 % for ATLAS ITk. Even after a fluence of $5 \times 10^{15}\,\mathrm{n_{eq}/cm^2}$ the efficiency is well above the requirement. At the highest measured bias voltage of 600 V an efficiency of $(99.76 \pm 0.01)\,\%$ is achievable with passive CMOS sensors.

Comparing DC- and AC-coupled sensors, it is visible that below voltages of 500 V the efficiency of the AC-coupled sensor is a few percent higher than for the DC-coupled sensor. The reasons for this are a slightly different threshold of the two different detectors and, as indicated from leakage current measurements, a slightly lower irradiation level (see Sec. 6.7.1). More important to note is that with sufficiently high bias voltages the hit-detection efficiency of DC- and AC-coupled sensors is the same. However, AC-coupled sensors have the advantage that leakage current does not flow into the amplifier of the front-end, and therefore performance degradation of the front-end due to large leakage current from the sensor is negligible. Especially for the Differential front-end of the RD53A readout chip, which can be tuned to low thresholds (below 1000 e) before irradiation, this is advantageous as the low threshold can be maintained even after irradiation[12]. To demonstrate possible performance improvements in terms of efficiency, the efficiency with a low threshold setting of approximately 850 e using the Differential front-end (open triangles) is compared to the efficiency measured with the standard threshold setting of 1000 e – 1200 e using the Linear front-end (filled triangles) with the same sensor. Due to the lower threshold setting, a lower bias voltage is required to reach the efficiency plateau with the advantage that the power dissipated by the sensor is lower (at least 20 %). Lower power dissipation is beneficial in terms of a reduction of the required cooling power.

[12]Due to limited tuning performance of the Linear front-end, this effect is not observed for this front-end.

In-time hit-detection efficiency

At the LHC the proton bunches collide every 25 ns (bunch crossing). Instead of reading out several bunch crossings (here: 32×25 ns) as it is the case for example in test beam measurements, the readout window is synchronised with the bunch crossing frequency and only a single bunch crossing is read out (25 ns readout window) during data taking with the detector at the LHC. To disentangle single bunch collisions, which define one event, and make sure that hits are assigned to the correct bunch crossing, all hits detected from a bunch collision have to be registered within 25 ns. All hits with a hit delay (time between trigger and hit detection) larger than 25 ns are assigned to the wrong bunch crossing. The maximum variation of the hit delay, given by time walk (see Sec. 6.7.4), is therefore restricted to 25 ns. The quantity that combines this crucial timing requirement with the hit-detection efficiency is known as *in-time* hit-detection efficiency. The in-time efficiency after irradiation is especially interesting, since the charge signal is significantly smaller resulting in larger hit delay variations due to time walk.

The challenging and complex determination of the in-time efficiency is realised by recording the delay between the trigger signal (scintillator signal) and the hit arrival time (HitOR leading edge) simultaneously to data taking using a beam telescope. The hit delay is measured using the *TDC technique*, as explained in Sec. 6.2.2. Uncertainties due to the quantization error of the *TDC technique* and jitter of the considered signals are negligible as they are smaller than 1 ns. Due to the relatively low yield of the *TDC technique*, a proper hit delay cannot be measured for all detected hits. The calculation of the in-time efficiency $\epsilon_{\mathrm{in-time}}$ is therefore separated into the calculation of the hit efficiency ϵ_{hit} and the probability $P_{\Delta t}$ that a hit is detected within a given time window Δt. The in-time hit-detection efficiency $\epsilon_{\mathrm{in-time}}$ is estimated with the following equation:

$$\epsilon_{\mathrm{in-time}} = \epsilon_{\mathrm{hit}} \times P_{\Delta t} \, . \tag{6.7}$$

To avoid an overestimation of the in-time efficiency and include jitter from additional system components, a time window of $\Delta t = 20$ ns (smaller than the 25 ns bunch spacing at the LHC) is chosen. The assignment of the hit delay to single-pixel clusters is trivial. For all other cluster sizes (only valid cluster shapes are considered, see Sec. 6.2.2), the hit delay of the seed pixel (pixel with highest charge in a cluster) is assigned to the hit delay of a cluster.

Fig. 6.32 shows the timing distribution of clusters belonging to reconstructed telescope tracks measured with an irradiated passive CMOS detector (5×10^{15} $\mathrm{n_{eq}/cm^2}$ at 600 V bias voltage). On the left hand side of the figure the coarse timing distribution using the relative BCID can be seen (25 ns sampling). On the right hand side of the figure the high-resolution timing distribution using the *TDC technique* is depicted (1.5625 ns sampling). Due to the finite amount of bits available for the sampling of the hit delay, the timing distribution using the *TDC technique* covers only 16 bunch crossings (400 ns). The in-time probability is given by the fraction of clusters with a hit delay within a given timing window (here 20 ns). To extract the optimal timing window (position of timing window with respect to timing distribution) the left border

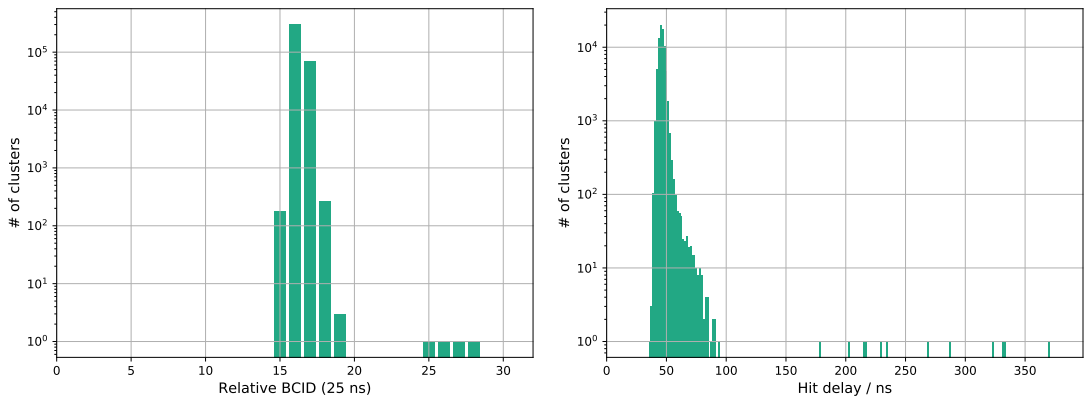

(a) Relative BCID distribution

(b) Hit delay distribution

Figure 6.32: Timing distribution of an irradiated ($5 \times 10^{15}\,\mathrm{n_{eq}/cm^2}$) passive CMOS detector using the Linear front-end of the RD53A readout chip obtained with data recorded using minimum ionising particles (5 GeV electron beam). **(a)** On-chip coarse timing measurement using the relative BCID (40 MHz sampling). **(b)** High-resolution timing measurement using the *TDC technique* (640 MHz sampling).

of the timing window is varied. This yields a so-called in-time probability plateau as illustrated in Fig. 6.33 with the maximum in-time probability defined by the plateau. The extracted

	$\mathbf{2 \times 10^{15}}\,\mathrm{n_{eq}/cm^2}$		$\mathbf{5 \times 10^{15}}\,\mathrm{n_{eq}/cm^2}$	
	100 V	400 V	400 V	600 V
regular efficiency	98.74 %	99.77 %	99.16 %	99.76 %
in-time probability	97.14 %	99.82 %	97.29 %	99.65 %
in-time efficiency	95.91 %	99.59 %	96.47 %	99.41 %

Table 6.3: Summary of estimated in-time probabilities and efficiencies of irradiated passive CMOS detectors using the Linear front-end of the RD53A readout chip. The in-time efficiency is calculated using Eq. 6.7.

maximum in-time probability is 99.65 %, resulting in an in-time efficiency of 99.41 % according to Eq. 6.7. In-time efficiencies at different bias voltages and the two reference fluences using DC-coupled passive CMOS detectors are summarised in Tab. 6.3. The estimated in-time efficiency is only slightly lower than the "regular" efficiency and well above the requirement of 97 % for sufficiently high bias voltages. The reason for the decrease in in-time probability for lower bias voltages is a smaller charge signal (see Sec. 6.7.6). As presented in Sec. 6.7.4, hits with smaller charge are detected later (larger hit delay), and thus the fraction of hits outside the required time window (20 ns) is larger. Consequently, the in-time efficiency decreases.

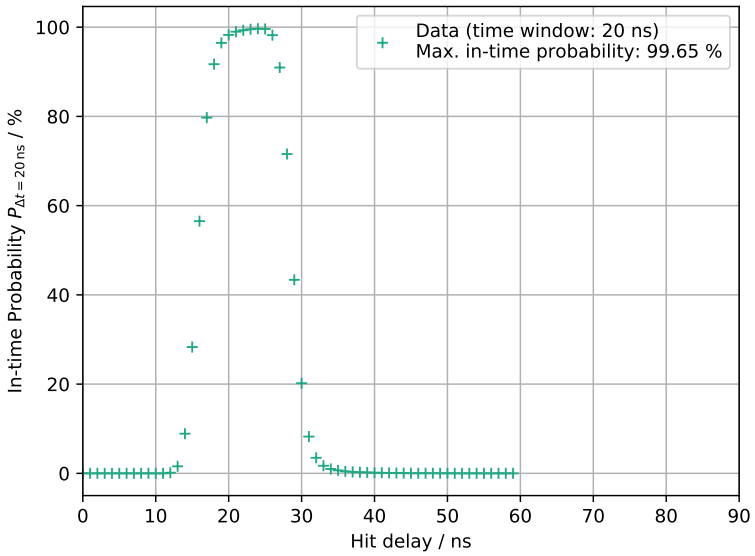

Figure 6.33: In-time probability of an irradiated ($5 \times 10^{15}\,\mathrm{n_{eq}/cm^2}$) passive CMOS detector using the Linear front-end of the RD53A readout chip obtained with data recorded using minimum ionising particles (5 GeV electron beam). The plateau is obtained by scanning data with a time window of 20 ns. See text for explanation.

6.7.6 Charge collection

In this section the charge collection behaviour of passive CMOS sensors before and after irradiation is studied using minimum ionising particles (5 GeV electron beam). In particular, the charge collection of AC- and DC-coupled sensors is compared. Furthermore, the bulk resistivity is extracted from the measured charge signal. As an estimator for the charge signal the most probable value, extracted from a fit to the charge spectra, is used.

Fig. 6.34 shows the charge signal of 150 µm thin passive CMOS sensors before irradiation as a function of the bias voltage for DC- and AC-coupled sensors. With increasing bias voltage the depleted detector volume increases, and therefore the charge signal increases (only the depleted volume contributes to the charge signal). After full depletion, at approximately 35 V – 40 V, the charge signal saturates at approximately 12 000 e for the DC-coupled detector. Due to capacitative charge sharing (see Sec. 3.3) in case of the AC-coupled sensor, the charge recorded by the amplifier is smaller than the charge deposited in the sensor. As estimated in Sec. 3.3.1, AC-coupled detectors record approximately 5 % – 10 % less charge than DC-coupled detectors. The measured difference of approximately 20 % between AC- and DC-coupled devices is larger than expected, which suggests a smaller charge collection efficiency of AC-coupled devices as estimated in Sec. 3.3.1. Additional parasitic contributions due to the AC-coupling capacitor (MIM-capacitor), which increase the total input capacitance, are expected, and therefore likely

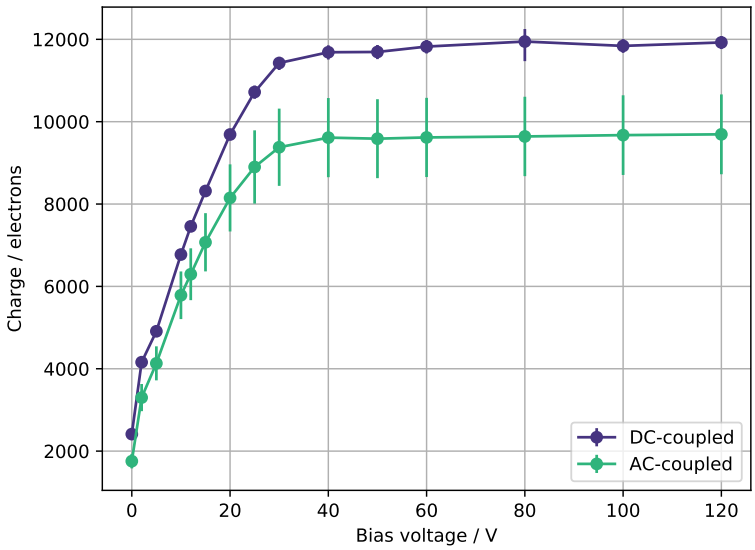

Figure 6.34: Charge signal created by MIPs before irradiation as a function of the bias voltage for DC-coupled and AC-coupled 150 µm thin passive CMOS detectors. Each data point corresponds to the most probable value extracted from a fit to the charge spectrum. The error bars correspond to the fit errors. For the AC-coupled detector an uncertainty of 10 % due to unknown charge calibration is assumed.

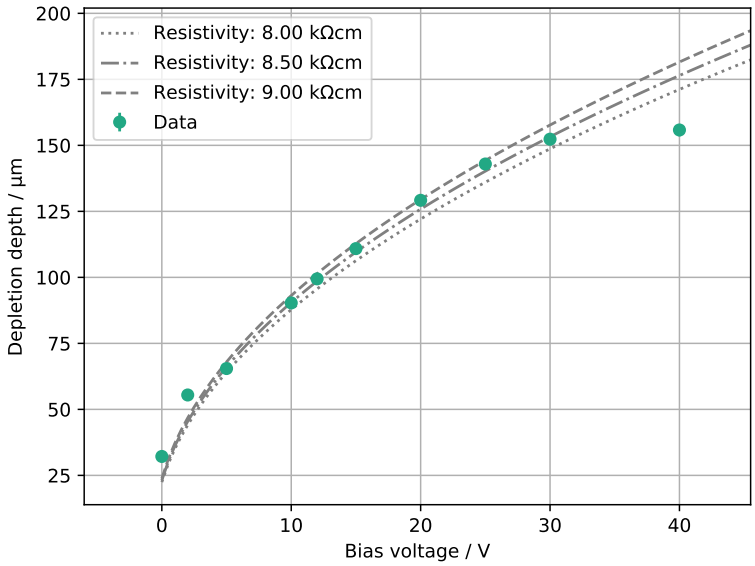

Figure 6.35: Depletion depth as a function of bias voltage for a DC-coupled 150 µm thin passive CMOS sensor. The measured charge signal is converted into a depletion depth assuming that on average 75 e/h-pairs per µm are created. The grey lines represent the expected curves for different bulk resistivities according to Eq. 6.8.

responsible for a smaller charge collection efficiency. Further, the value of the coupling capacitor can slightly deviate from its nominal value. Nevertheless, the fact that the AC-coupled detector records slightly less charge, explains why the measured efficiency at low bias voltages (see Fig. 6.31a) for the AC-coupled detector is slightly lower than the efficiency for the DC-coupled detector.

With the knowledge of the average number of created e/h-pairs per µm, the amount of collected charge can be converted into a depletion depth. From a GEANT4 simulation a value of 75 e/h-pairs per µm is extracted for minimum ionising particles in a 150 µm thin sensor. Fig. 6.35 shows the depletion depth calculated from the charge signal measured with the DC-coupled detector as a function of the bias voltage. The depletion depth d as a function of the bias voltage V_{bias} is given by Eq. 3.30 and is repeated here for completeness:

$$d\,[\mu\text{m}] \approx 0.3\sqrt{\rho\,[\Omega\,\text{cm}] \cdot V_{\text{bias}}\,[\text{V}]}\,, \tag{6.8}$$

with ρ being the bulk resistivity. The grey dashed lines in Fig. 6.35 show the expected curves for different bulk resistivities according to Eq. 6.8. It can be concluded that the resistivity of the bulk material is between $8\,\text{k}\Omega\,\text{cm} - 9\,\text{k}\Omega\,\text{cm}$ (float-zone wafer). This is slightly larger than the bulk resistivity of Czochralski wafers ($5\,\text{k}\Omega\,\text{cm} - 7\,\text{k}\Omega\,\text{cm}$ [Poh20]) used in former passive CMOS

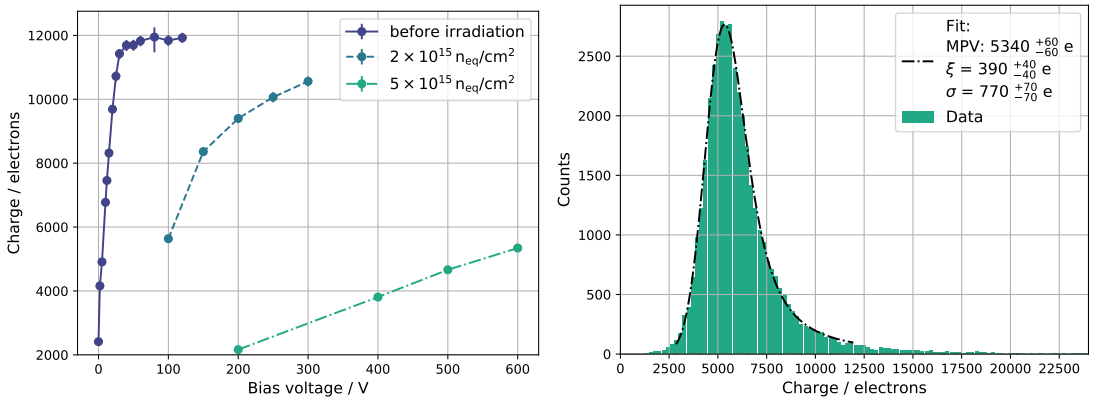

(a) Charge signal versus bias voltage

(b) Charge spectrum after irradiation

Figure 6.36: (a) Charge signal before and after irradiation as a function of bias voltage for DC-coupled 150 µm thin passive CMOS detectors. Each data point corresponds to the most probable value extracted from a fit to the measured charge spectra. The error bars correspond to the fit error. **(b)** Charge spectrum recorded using minimum ionising particles after a fluence of $5 \times 10^{15}\,\mathrm{n_{eq}/cm^2}$ at a bias voltage of 600 V. The spectrum is fitted with a Langau (black line) to extract the most probable value (MPV).

submissions, and thus beneficial for a reduction of the full depletion voltage. The maximum charge signal is a few percent larger than expected from a detector with a nominal thickness of 150 µm. However, the backside grinding is not perfectly homogeneous such that small deviations in the thickness of a few µm are expected, especially in case of large-area sensors here.

The charge collection behaviour of DC-coupled sensors before and after irradiation is depicted in Fig.6.36a. The charge signal is significantly smaller after irradiation due to charge carrier trapping and the fact that the sensor cannot be fully depleted any more, within the tested bias voltages. Even at the highest measured bias voltages the charge signal still increases and no saturation is visible at the two reference fluences indicating that the depletion zone is still expanding. The measured charge signal after a fluence of $5 \times 10^{15}\,\mathrm{n_{eq}/cm^2}$ (Fig. 6.36b) is approximately 5300 e at a bias voltage of 600 V. This results in a charge collection efficiency (charge signal after irradiation with respect to charge signal before irradiation) of 44 %. As shown in the previous section, this is sufficient to reach a hit-detection efficiency above 99 %.

6.7.7 High-η studies

In the innermost barrel layer of the ATLAS ITk detector (see Fig. 3.16), particles hit the detectors with the smallest track angle of $\theta \approx 8°$ (in the ATLAS coordinate system, θ is the polar angle). Typically, instead of the track angle a quantity called pseudorapidity[13] is used at

[13]The pseudorapidity η is preferred over the polar angle θ, since particle production is constant as a function of η and differences in pseudorapidity are Lorentz invariant under boosts along the longitudinal axis.

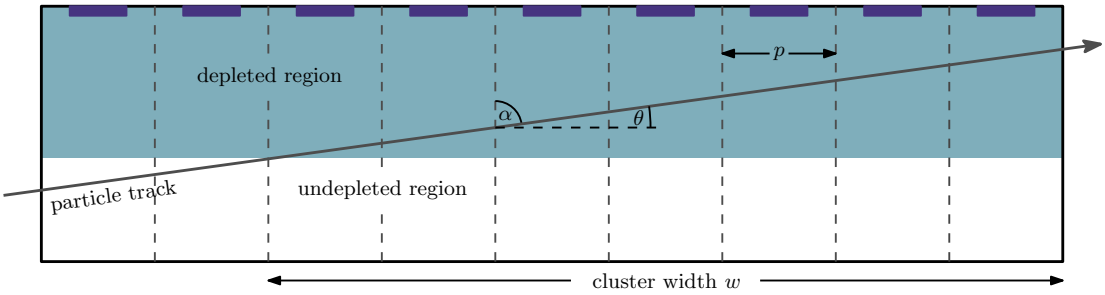

Figure 6.37: Visualisation of an inclined particle track in an (irradiated) pixel detector. The particle hits the pixel detector with an incidence angle α. The track angle $\theta = 90° - \alpha$ corresponds to the polar angle measured in the ATLAS coordinate system and is related to the pseudorapidity. The cluster width w is defined by the depletion depth (green area). The pixel pitch is denoted with p.

hadron colliders [ATL17a]:

$$\eta = -\ln\left(\tan\theta/2\right) . \tag{6.9}$$

A track angle of $\theta = 8°$ corresponds to a pseudorapidity of $\eta \approx 2.66$. Highly inclined tracks lead to the formation of elongated clusters, since charge is shared between many pixels. This results in a significantly smaller charge per pixel (compared to perpendicular incidence), and thus could lead to split clusters[14] which are difficult to reconstruct. To investigate this, dedicated measurements were conducted with an irradiated passive CMOS sensor at different track angles ($\theta = 8°, 20°, 40°$) using a minimum ionising particle beam. In addition, these measurements allow for a determination of the depletion depth after irradiation. The measurements were performed with a 150 µm thin passive CMOS sensor ($50 \times 50\,\mu m^2$ pixels) irradiated to a fluence of $5 \times 10^{15}\,n_{eq}/cm^2$ and operated at a bias voltage of 600 V. The precision on the quoted angles is estimated to be $\pm 1°$ (mechanical precision).

Fig. 6.37 shows an inclined particle track with incidence angle α (track angle $\theta = 90° - \alpha$) passing through a pixel detector (dashed lines indicate the pixel borders). Due to the small track angle, the deposited charge is shared between many pixels. This leads to the formation of elongated clusters with an average cluster width w. In general, irradiated detectors cannot be operated as fully depleted sensors any more so that the average cluster width w is determined by the depletion depth (green region) as charge carriers in the undepleted region (white region) do not contribute to the charge signal. From geometrical calculations, the average cluster width w is given by

$$w\,[\text{pixel}] = \frac{d}{p \cdot \tan\theta} + 1\,, \tag{6.10}$$

with d being the depth of the depletion zone, p the pixel pitch and θ the track angle. From

[14] Clusters are split if the charge in one pixel (or more) is below the detection threshold.

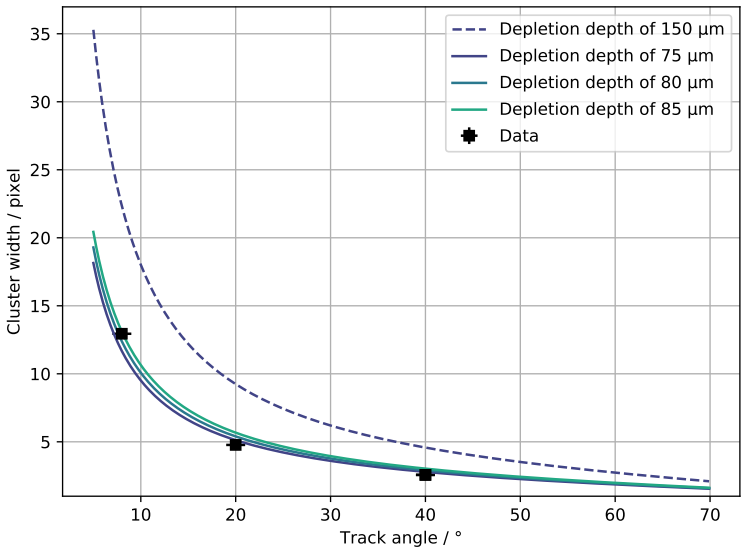

Figure 6.38: Average cluster width as a function of the track angle using an irradiated passive CMOS sensor ($50 \times 50\,\mu m^2$ pixels and 150 µm thin). The relation between cluster width and track angle is calculated for different depletion depths (dashed and solid lines) according to Eq. 6.10. An uncertainty of $\pm 1°$ is assumed on the track angle. The statistical error on the cluster width is smaller than the marker size.

a measurement of the cluster width w at different track angles θ, the depletion depth can be estimated. For the subsequent analysis it is sufficient to analyse only data from the DUT (irradiated passive CMOS sensor), and thus no track reconstruction using a beam telescope is required. The hits in the DUT are clustered with a maximum cluster distance of 2 (see Chap. 5).

Fig. 6.38 shows the average cluster width measured at different track angles using a passive CMOS sensor ($50 \times 50\,\mu m^2$ pixels, 150 µm thin) irradiated to a fluence of $5 \times 10^{15}\,n_{eq}/cm^2$. Furthermore, the relation between the cluster width w and the track angle θ for different depletion depths according to Eq. 6.10 is depicted (dashed and solid lines). The measured data is consistent with a depletion depth of approximately 80 µm, which clearly demonstrates that the detector volume ($d = 150\,\mu m$) cannot be fully depleted any more after irradiation. To check that this value is reasonable, the depletion depth is estimated from the expected effective doping concentration after irradiation using Eq. 3.30. With a depletion voltage of 35 V before irradiation (see Sec. 6.7.2), which corresponds to an effective doping concentration of $N_{eff,0} \approx 2 \times 10^{12}\,cm^{-3}$ (see Eq. 3.31), the effective doping concentration after irradiation is estimated with data from [Bal+07][15] to $N_{eff,irrad} \approx 1.2 \times 10^{14}\,cm^{-3}$. Using Eq. 3.30, this results in a depletion depth of approximately 80 µm at an operational voltage of 600 V after irradiation.

[15] For p-type Float-Zone silicon (without oxygen impurities), a value of $\beta = 0.023\,cm^{-1}$ is quoted in [Bal+07]($N_{eff,irrad} = N_{eff,0} + \beta \cdot \phi_{eq}$).

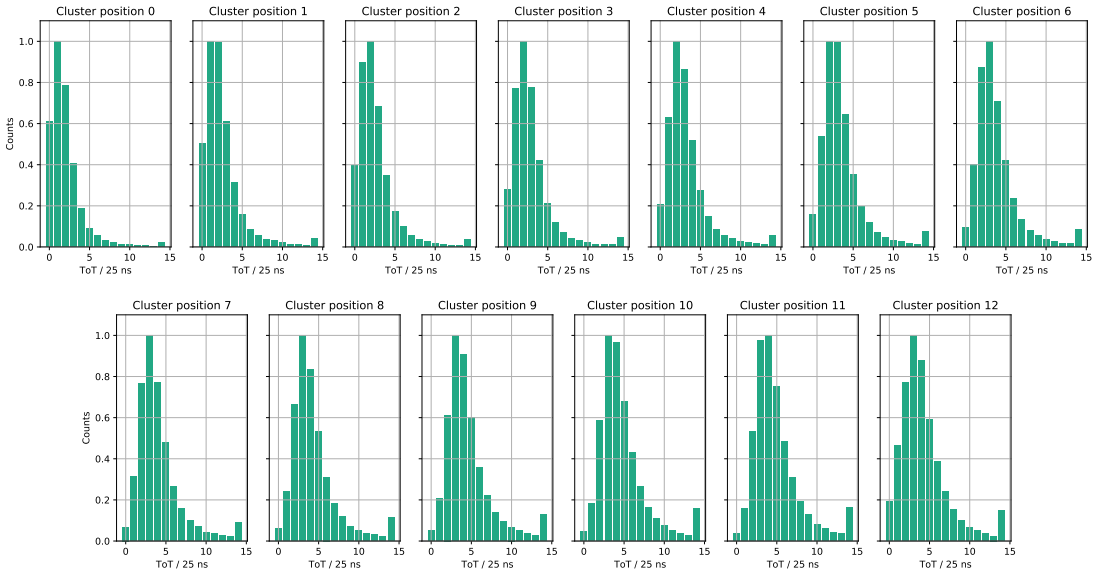

Figure 6.39: Charge signal (in units of ToT) for different cluster positions measured with an irradiated passive CMOS sensor at a track angle of $\theta = 8°$. Only clusters with a width of $w = 13$ are selected. Cluster position 0 corresponds to the pixel closest to the entry point of the particle track (longest drift distance), whereas position 12 corresponds to the pixel farthest from the entry point (shortest drift distance).

This value is only a rough estimation and has a rather large uncertainty, since the exact oxygen concentration is not known, the constants are material-dependent and annealing is neglected (see Sec. 3.2). In addition, Eq. 6.10 neglects the threshold of the readout electronics which slightly decreases the measured cluster width [Bey19]. However, the calculated and measured values do not contradict each other so that the measured depletion depth of approximately 80 µm (at 600 V) after a fluence of $5 \times 10^{15}\,\mathrm{n_{eq}/cm^2}$ seems reasonable.

For highly inclined tracks, the average charge signal per pixel is not determined by the amount of material traversed by the particle (like in the case of perpendicular tracks), but is approximately given by the pixel pitch (here 50 µm). Moreover, the drift distance of charge carriers to the electrode (blue rectangles in Fig. 6.37) decreases the farther the pixel is from the entry point of the particle track (see Fig. 6.37). For irradiated sensors it is therefore expected that the charge signal decreases the closer the pixel is to the entry point, since longer drift distances lead to more charge carrier trapping. This behaviour is demonstrated in Fig. 6.39 for the "worst-case scenario" of a track angle of $\theta = 8°$. For the analysis, only clusters with a width of $w = 13$ (corresponding to the most probable cluster width) are selected. The charge signal is shown in units of ToT (time-over-threshold) for different positions inside the cluster. A precise charge information using the *TDC technique* is not available due to the selection

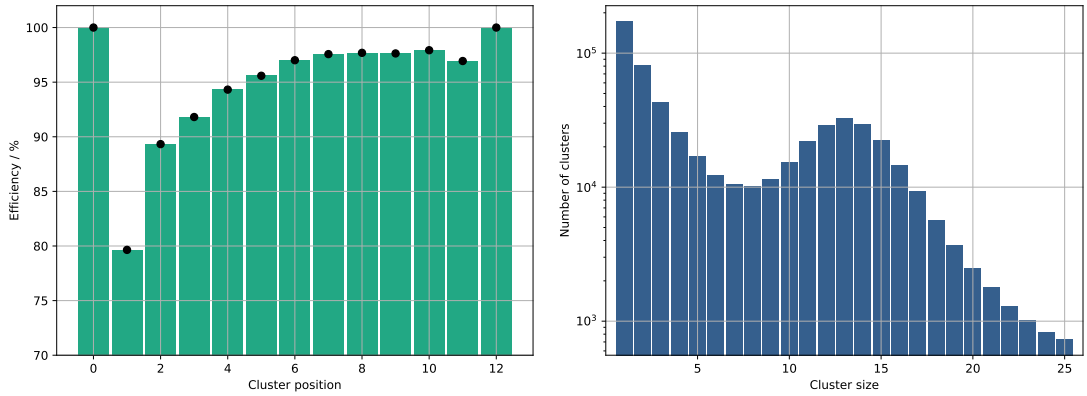

(a) Efficiency **(b)** Cluster size distribution

Figure 6.40: (a) Hit-detection efficiency as a function of the cluster position measured with an irradiated passive CMOS sensor at a track angle of $\theta = 8°$. Only clusters with a width of $w = 13$ are selected. Cluster position 0 corresponds to the pixel closest to the entry point of the particle track, whereas position 12 corresponds to the pixel farthest from the entry point (see Fig. 6.37). **(b)** Cluster size distribution measured at a track angle of $\theta = 8°$ using an irradiated passive CMOS sensor.

of elongated clusters (see Sec. 6.2.2). Cluster position 0 corresponds to the pixel closest to the entry point of the particle track (longest drift distance), whereas position 12 corresponds to the pixel farthest from the entry point (shortest drift distance). As explained above, the charge signal decreases the closer the pixel is to the particle entry point, which is due to charge carrier trapping. The maximum charge signal is approximately 3 – 4 ToT which corresponds to approximately 2000 e – 2500 e and is significantly smaller than the charge signal at perpendicular incidence (approximately 5000 e).

The hit-detection efficiency as a function of the cluster position measured with an irradiated passive CMOS sensor at $\theta = 8°$ is shown in Fig. 6.40a. Only clusters with a width of $w = 13$ are selected for the analysis. The hit-detection efficiency is here defined by the ratio of hits for a given cluster position and the total number of clusters. By definition, the efficiency of the outermost pixels is fixed to 100 %, since theses pixels define the selected cluster width, and thus are always hit. The efficiency correlates with the charge signal, i.e. a smaller charge signal leads to a lower efficiency, since the average charge per pixel is close to the detection threshold ($\approx$ 1200 e), and therefore explains the drop in efficiency towards cluster position 0 (longer drift distance). For cluster positions between 5 and 11 the hit-detection efficiency saturates at approximately 96 %. Compared to the efficiency measured at perpendicular incidence (> 99 %) this is considerably smaller and can be explained with the considerably smaller charge signal. During operation in the ATLAS detector, the probability to not detect a cluster at a given incidence angle is important. With the estimated efficiencies, this probability is estimated to

be 1×10^{-15} at $\theta = 8°$ and is thus negligible. However, the rapidly dropping efficiency towards cluster position 0 (closer to entry point of track) indicates that a measurable fraction of clusters is split. This behaviour is visible in the cluster size distribution shown in Fig. 6.40b (at $\theta = 8°$). A clear peak around the expected cluster width of 13 is visible, however most of the clusters have a cluster size of $1-3$. This can be explained by the fact that the efficiency drops towards cluster position 0 (see Fig. 6.40a), and thus the probability that a cluster is split (more than two pixels not hit between the clusters) is largest at the "beginning" of the cluster (towards the entry point of the track). Consequently, a short and a long cluster are reconstructed as visible from the cluster size distribution shown in Fig. 6.40b.

6.8 Conclusions

In the previous sections it was shown that thin passive CMOS sensors are radiation tolerant and still functional even after a fluence of $1 \times 10^{16}\,\mathrm{n_{eq}/cm^2}$. In particular, the hit-detection efficiency of a 100 µm thin prototype passive CMOS sensor after a fluence of $1 \times 10^{16}\,\mathrm{n_{eq}/cm^2}$ was estimated to be well above 99 % for an operational voltage of 400 V (with the NW30-design). Pixels with smaller readout electrode (n-well) show less noise (up to 8 %), but have the disadvantage that the hit efficiency is lower after irradiation, since the charge signal is lower.

The suitability of passive CMOS pixel sensors for detectors in high particle rate and radiation environments (like the upgrade of the ATLAS and CMS detector) was demonstrated with a dedicated submission of large-area passive CMOS sensors. With the advantage of high production throughput at comparatively low costs of CMOS processing lines, passive CMOS sensors are a cost-effective solution for large-area detectors. Issues during backside processing could be mitigated by increasing the dose of the backside implantation. The production yield of the large-area passive CMOS sensors was estimated to be approximately 70 %. In terms of noise, passive CMOS sensors perform equally well compared to conventional planar sensors for hybrid pixel detectors. Although the increase in noise of approximately 10 % observed with large-area sensors (with respect to the prototype sensor) is not yet understood. The in-time hit-detection efficiency was estimated to be well above the requirement of 97 % at the two reference fluences of $2 \times 10^{15}\,\mathrm{n_{eq}/cm^2}$ and $5 \times 10^{15}\,\mathrm{n_{eq}/cm^2}$ (> 99 % in-time efficiency). In summary, this makes passive CMOS sensors an attractive alternative to conventional sensors for large-area detectors in high particle rate and radiation environments.

A comparison of the charge collection behaviour of the two passive CMOS sensors (100 µm Czochralski and 150 µm Float-Zone) after a fluence of $5 \times 10^{15}\,\mathrm{n_{eq}/cm^2}$ is shown in Fig. 6.41a. It is visible that the 100 µm Czochralski sensor (blue curve) collects significantly more charge after irradiation compared to the 150 µm Float-Zone sensor (green curve). This can be explained by the higher electrical field of the thinner sensor, which leads to faster charge collection, and therefore less trapped charge [Man+18]. Another reason for the better charge collection is

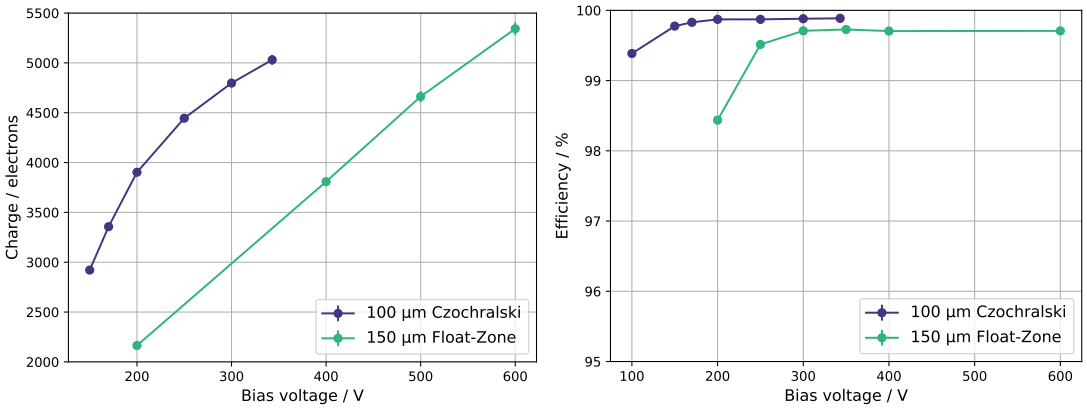

(a) **(b)**

Figure 6.41: Charge signal (**a**) and hit-detection efficiency (**b**) as a function of the bias voltage after a fluence of $5 \times 10^{15}\,\mathrm{n_{eq}/cm^2}$ for 100 µm Czochralski and 150 µm Float-Zone passive CMOS sensor. For both detectors a similar threshold setting was chosen.

the fact that oxygen impurities in Czochralski silicon improve radiation tolerance, as reported in [Mol99; Lin+01]. Consequently, better charge collection leads to higher hit efficiency at a fixed bias voltage, as shown in Fig. 6.41b. This results in less power dissipated by the sensor, since a lower operational voltage can be chosen to reach a given efficiency limit.

7 Summary

With the high-luminosity upgrade of the LHC, the instantaneous luminosity increases by a factor of five with respect to its design luminosity of $\mathcal{L} = 10^{34}\,\mathrm{cm}^{-2}\,\mathrm{s}^{-1}$. The goal is to collect $3000\,\mathrm{fb}^{-1}$ within the planned operating period of 12 years. starting in 2027 This imposes challenging requirements on future tracking detectors at the HL-LHC in terms of hit rate capabilities and radiation tolerance. To maintain the tracking and vertexing performance of the ATLAS detector under the new operating conditions, a high-granularity all-silicon tracking detector (ATLAS ITk) consisting of silicon strip and pixel sensors replaces the current Inner Detector. The new pixel detector covers an area of approximately $13\,\mathrm{m}^2$ demanding cost-effective solutions. The innermost layer of the ITk pixel detector is exposed to extreme fluences of up to $1.3 \times 10^{16}\,\mathrm{n_{eq}/cm^2}$ and TID of up to 1000 Mrad. It is therefore necessary to develop fast and radiation tolerant readout electronics as well as radiation hard sensors with fast charge collection.

In this thesis, passive CMOS pixel sensors (in 150 nm LFoundry technology) were investigated with respect to their use in harsh radiation environments, like the ATLAS experiment at the HL-LHC. Utilising a CMOS process line for the production of sensors for hybrid pixel detectors offers the advantage of high production throughput at comparatively low costs. Other benefits arise from the availability of poly-silicon layers, MIM-capacitors and several metal layers which can help to enhance the sensor design.

Besides the determination of important sensor properties like breakdown behaviour and electronic noise, the charge collection behaviour of CMOS pixel sensors was studied and high-precision timing measurements (in-time efficiency) were performed using minimum ionising particles. A track reconstruction algorithm based on a Kalman Filter was implemented, which allows for a precise track reconstruction of minimum ionising particles, and thus an in-pixel investigation of the charge collection behaviour and hit-detection efficiency of pixel detectors. The application of the Kalman Filter algorithm for the alignment of pixel detectors was demonstrated and verified using simulations.

Using a 100 µm thin prototype sensor consisting of various pixel designs (different readout electrode sizes), the radiation tolerance of passive CMOS sensors up to a fluence of $1 \times 10^{16}\,\mathrm{n_{eq}/cm^2}$ was demonstrated and the performance of different pixel designs was compared. In particular, the hit-detection efficiency after a fluence of $1 \times 10^{16}\,\mathrm{n_{eq}/cm^2}$ was estimated to be well above 99 % (at 400 V), with a charge collection efficiency of 55 %. The electronic noise of passive CMOS sensors is comparable to conventional sensors for hybrid pixel detectors (75 e before ir-

radiation). The electronic noise of pixel designs with smaller readout electrode is up to 8 % less after irradiation, but with the disadvantage of a lower efficiency (up to 6 %) after irradiation to a fluence of $1 \times 10^{16}\,\mathrm{n_{eq}/cm^2}$, due to worse charge collection. It is therefore concluded that the pixel design with the "standard" readout electrode (size of 30 µm, NW30) is the most suitable design for sensors in harsh radiation environments.

Based on this pixel design (NW30 design), 150 µm thin large-area passive CMOS sensors compatible with the future readout chip for the ITk detector were manufactured for the first time. To produce these large-area sensors (up to $4 \times 4\,\mathrm{\mu m^2}$) reticle stitching was utilised. The performance of the sensors was investigated before and after irradiation, and compared to the requirements of sensors for the ATLAS ITk pixel detector. It was verified that the stitching process has no influence on the performance of the sensor and the production yield of passive CMOS pixel sensors was estimated to be approximately 82 %. It was observed that the electronic noise is slightly higher (10 %) compared to the prototype sensor, although the pixel capacitance was estimated to be the same as for the prototype sensor (35 fF). Further, the in-time hit-detection efficiency was measured to be above 99 % after a fluence of $5 \times 10^{15}\,\mathrm{n_{eq}/cm^2}$ (at 600 V) which is well above the 97 % requirement of ATLAS ITk. The leakage current at this operational voltage is below the limit according to the ATLAS ITk specifications.

In summary, it was demonstrated that passive CMOS pixel sensors are radiation tolerant and represent a cost-effective solution for large-area detectors in high particle rate and radiation environments. Potential applications for passive CMOS sensors include the ATLAS and CMS detectors at the HL-LHC, or other tracking detectors at the HL-LHC or in high radiation environments which require cost-effective solutions to cover large areas of silicon pixel detectors. The pixel sensors are fully characterised and in a production-ready state for future applications.

Appendices

Charge collection efficiency of an AC-coupled CSA

Consider the circuit illustrated in Fig. 3.14. The charge collection efficiency (CCE) of the AC-coupled CSA is defined as

$$\mathrm{CCE} = T \cdot C_f = \frac{U_{\mathrm{out}}(Q)}{Q} \cdot C_f \,, \tag{7.1}$$

with T being the charge transfer function and C_f the feedback capacitance. Depending on the position of charge deposition (at sensor node or injection node) the transfer function is different.

Charge injection at injection node

The transfer function when charge is injected at the injection node (see Fig. 3.14) is given by

$$T = A_0 \cdot \frac{U_{in}}{Q_{\mathrm{inj}}} \,, \tag{7.2}$$

with $A_0 = \frac{U_{\mathrm{out}}}{U_{in}}$ being the open-loop gain. The voltage U_{in} at the CSA input is given by the injected charge Q_{inj} and the effective capacitance C_{eff} of the injection node

$$U_{in} = \frac{Q_{\mathrm{inj}}}{C_{\mathrm{eff}}} = \frac{Q_{\mathrm{inj}}}{\frac{C_c C_d}{C_c + C_d} + C_{in}} = \frac{Q_{\mathrm{inj}}}{\frac{C_c C_d}{C_c + C_d} + (A_0 + 1)\, C_f} \,, \tag{7.3}$$

with $C_{in} = (A_0 + 1)\, C_f$ being the CSA input capacitance [KW20]. The transfer function can then be expressed by

$$T = \frac{1}{\frac{1}{A_0}\frac{C_c C_d}{C_c + C_d} + \left(\frac{1}{A_0} + 1\right) C_f} \,. \tag{7.4}$$

Multiplying this with C_f yields the CCE (see Eq. 7.1)

$$\mathrm{CCE}_{\mathrm{inj}} = \frac{1}{\frac{1}{A_0 C_f}\frac{C_c C_d}{C_c + C_d} + \frac{1}{A_0} + 1} \,. \tag{7.5}$$

Charge injection at sensor node

The transfer function when charge is injected at the injection node (see Fig. 3.14) is given by

$$T = g \cdot \frac{U_{det}}{Q_{\mathrm{det}}}\,, \tag{7.6}$$

with the closed-loop gain

$$g = \frac{1}{\frac{1}{A_0}\left(\frac{C_c+C_f}{C_c}\right) + \frac{C_f}{C_c}}\,. \tag{7.7}$$

The voltage U_{det} at the sensor node is given by the effective capacitance C_{eff} at the sensor node and the charge Q_{det} deposited in the sensor

$$U_{\mathrm{det}} = \frac{Q_{\mathrm{det}}}{C_{\mathrm{eff}}} = \frac{Q_{\mathrm{det}}}{C_d + \frac{C_{in}C_c}{C_{in}+C_c}}\,. \tag{7.8}$$

The transfer function can then be expressed by

$$T = \frac{1}{\frac{1}{A_0}\left(C_d + \frac{C_dC_f}{C_c}\right) + \frac{C_dC_f}{C_c} + \left(\frac{1}{A_0}+1\right)C_f}\,. \tag{7.9}$$

Multiplying this with C_f yields the CCE (see Eq. 7.1)

$$\mathrm{CCE}_{\mathrm{det}} = \frac{1}{\frac{1}{A_0}\left(\frac{C_d}{C_f} + \frac{C_d}{C_c}\right) + \frac{C_d}{C_c} + \frac{1}{A_0} + 1}\,. \tag{7.10}$$

Kalman Filter alignment verification

Parameter	Value
Beam type	5 GeV electrons
Beam size (x, y)	(5 mm, 5 mm)
Beam divergence (x, y)	(3 mrad, 3 mrad)
Number of tracks	50 000
Tracking planes	6 × Mimosa26 sensors (see Sec. 6.4)
DUT	50 µm × 50 µm × 150 µm pixel sensor
Telescope geometry	See Fig. 7.1
Variation of $\Delta x, \Delta y, \Delta z$	±2 mm
Variation of $\Delta\alpha, \Delta\beta, \Delta\gamma$	±100 mrad

Table 7.1: Summary of simulation parameters for the Kalman Filter alignment using Allpix^2.

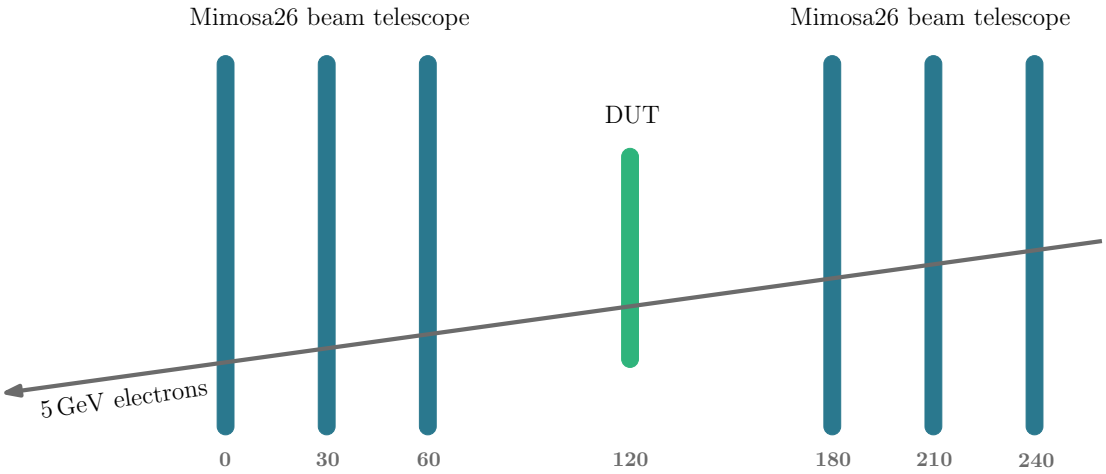

Figure 7.1: Telescope geometry used for the simulation of tracks using Allpix^2 to validate the Kalman Filter alignment (see Tab. 7.1). Numbers indicate z-position (in mm).

Charge calibration

Detector calibration

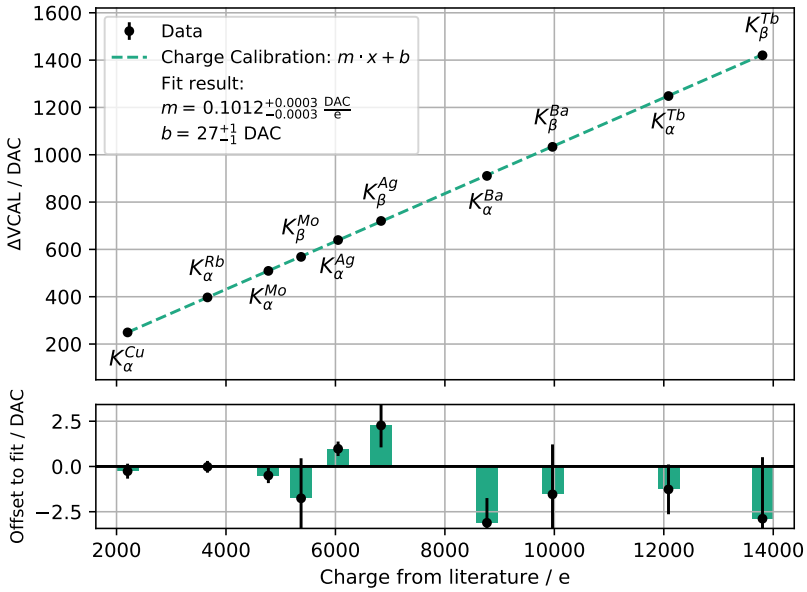

Figure 7.2: Charge calibration of detector P1 using x-ray fluorescence.

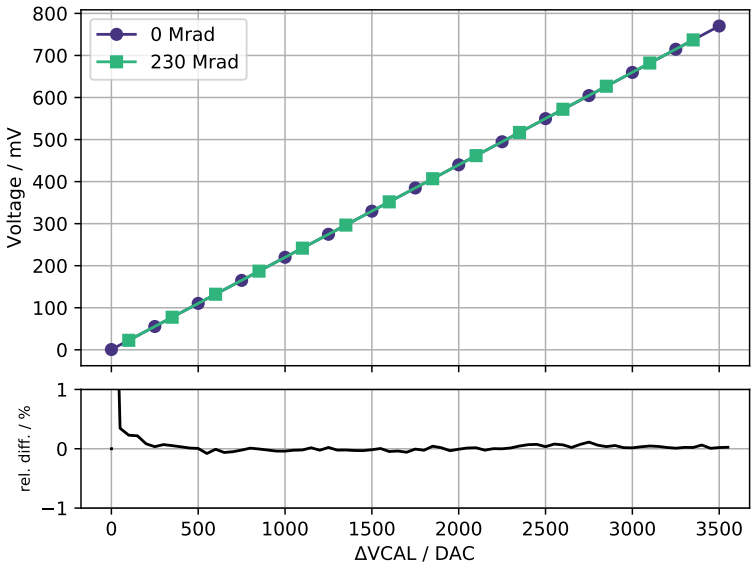

Figure 7.3: Calibration of the injection circuit of detector F1 before and after irradiation.

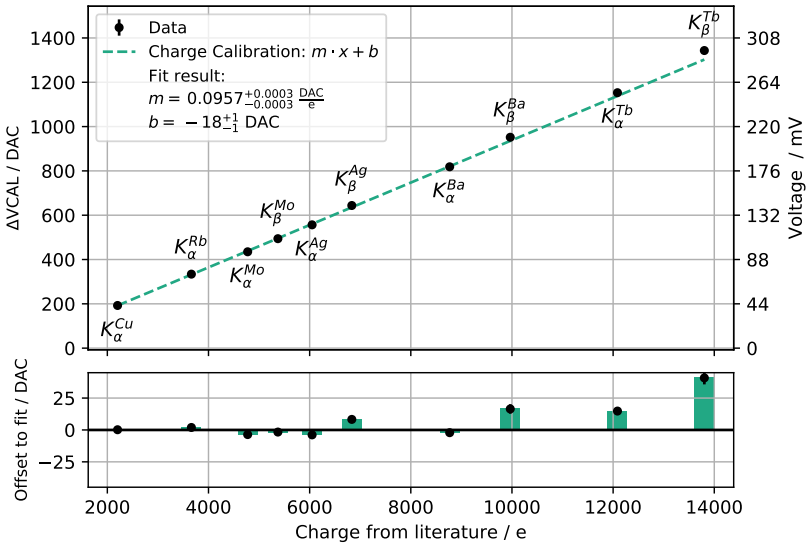

Figure 7.4: Charge calibration of detector F1 using x-ray fluorescence.

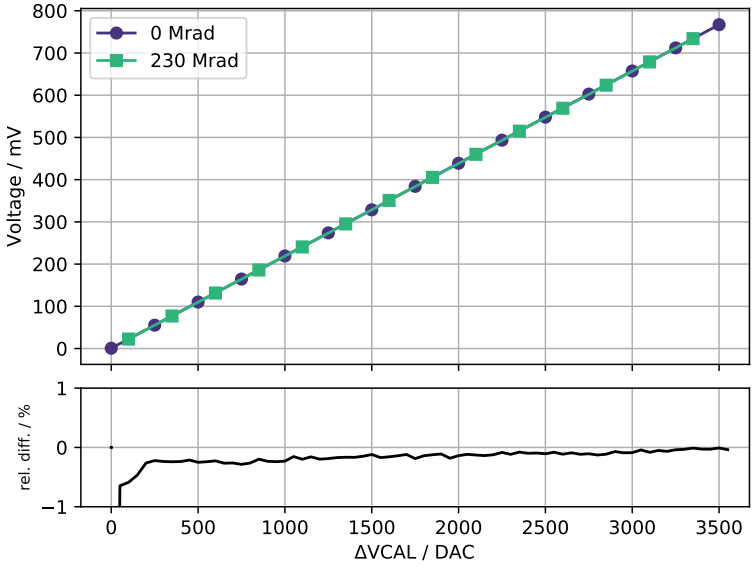

Figure 7.5: Calibration of the injection circuit of detector F3 before and after irradiation.

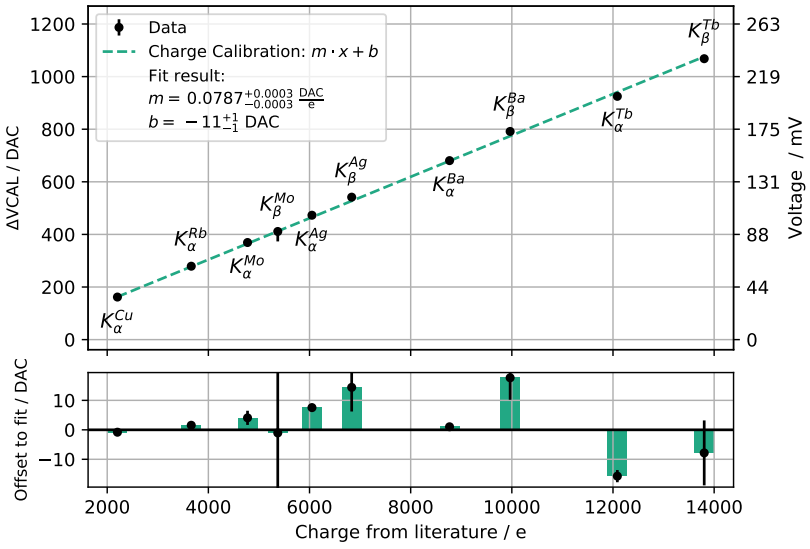

Figure 7.6: Charge calibration of detector F3 using x-ray fluorescence.

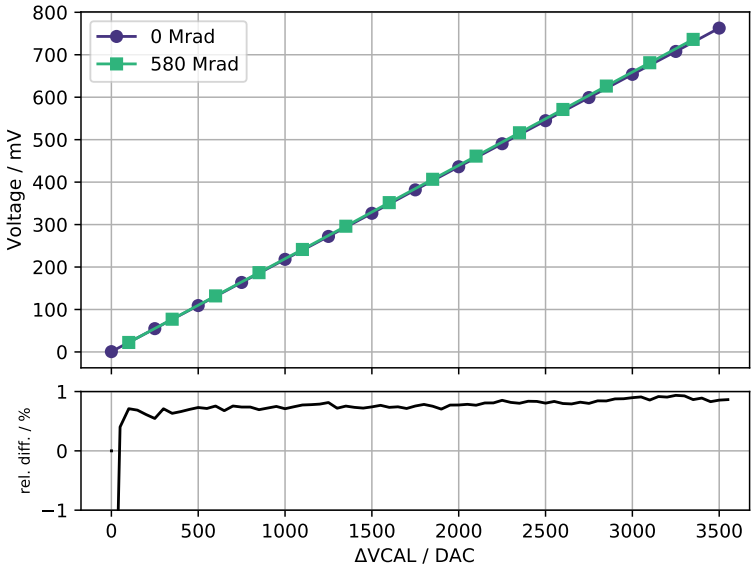

Figure 7.7: Calibration of the injection circuit of detector F4 before and after irradiation.

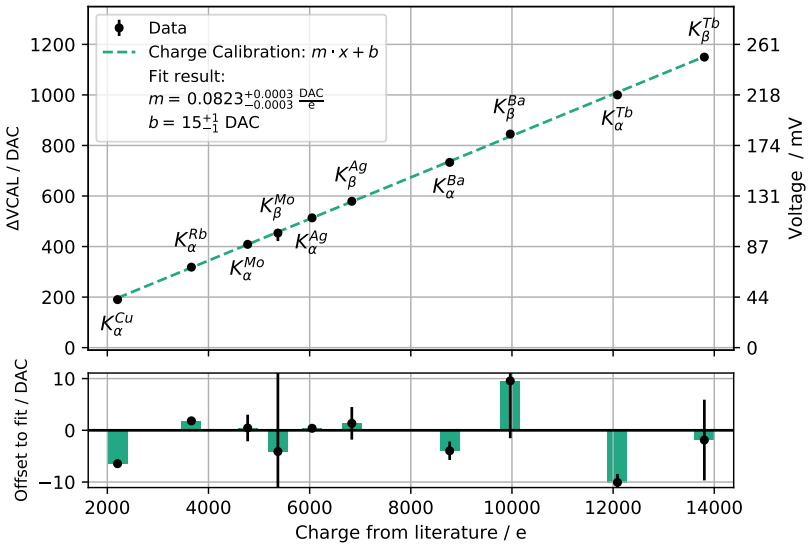

Figure 7.8: Charge calibration of detector F4 using x-ray fluorescence.

Allpix^2 simulation parameters

Parameter	Value
Source type	^{241}Am
Target materials	Cu, Ag, Tb
Pixel size	$50 \times 50\,\mu m^2$
Sensor thickness	150 µm
Bias voltage	80 V
Depletion voltage	30 V
Substrate type	p-type
Temperature	300 K
e/h-pair creation energy	3.65 eV
Electronic noise	70 e
Threshold	1000 e
Threshold dispersion	50 e
Digitiser resolution	12 bit
Digitiser slope	50 e
Digitiser smearing	300 e

Table 7.2: Summary of settings for x-ray fluorescence charge spectra simulation using Allpix^2.

Detector capacitance measurement

Capacitance measurement with PixCap65 chip

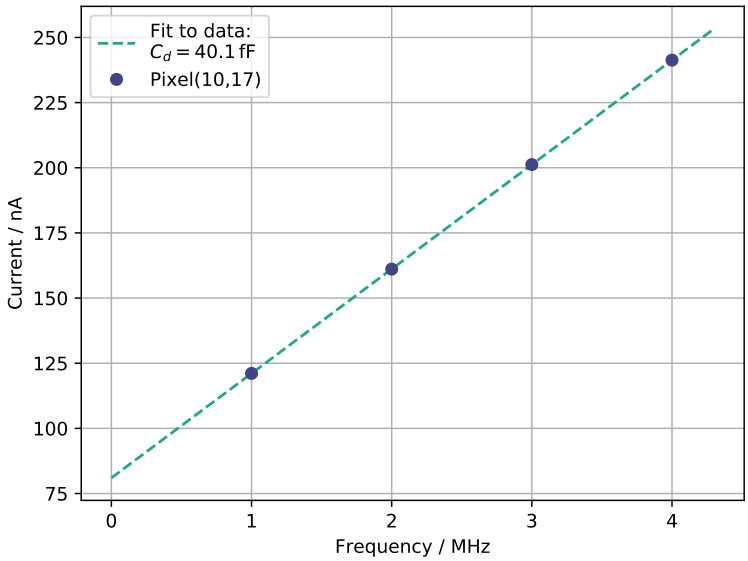

Figure 7.9: Switching current as a function of switching frequency measured with the PixCap65 chip. By a fit to the data (dashed line) the detector capacitance is estimated according to Eq. 6.5.

Electronic noise of prototype passive CMOS sensor

Electronic noise (2D map) of a prototype passive CMOS sensor is shown in Fig. 7.10. The region of the (active) pixel matrix (64×64 pixels) which is connected to the sensor is visible (higher noise). The physical size of the sensor extends by five pixels due to guard rings. For a few pixels located near the cutting edge (edge of sensor) a higher noise is measured, indicating a high current flow into these pixels due to an unintentional connection of these pixels to the cutting edge (connected to high voltage).

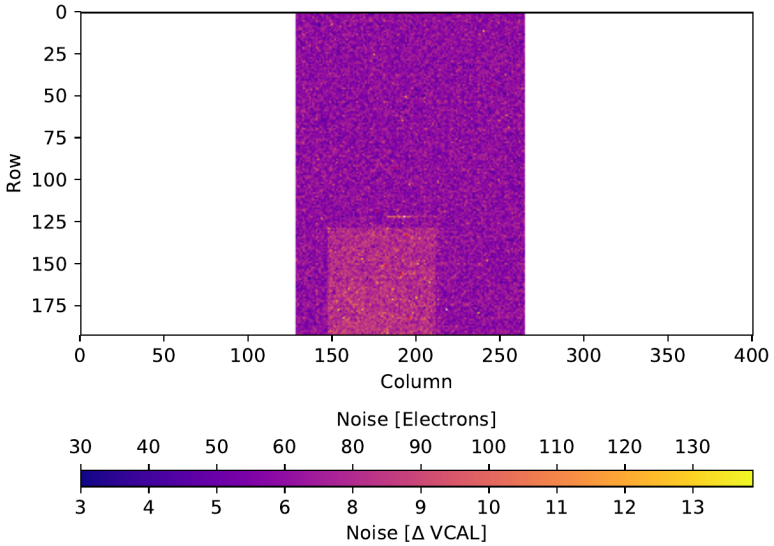

Figure 7.10: Electronic noise of a prototype passive CMOS sensor measured in a *threshold scan* with the Linear front-end of the RD53A.

Electronic noise comparison

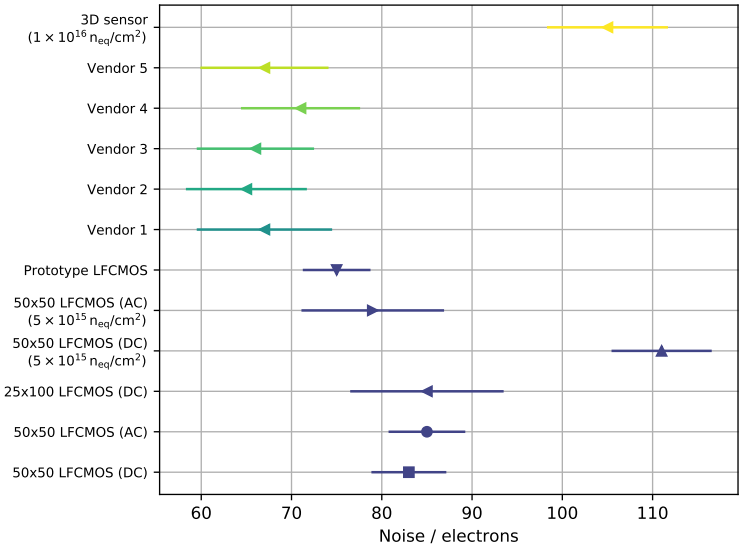

Figure 7.11: Comparison of electronic noise of passive CMOS sensors investigated within this study and pixel sensors from other vendors (data from hybridisation market survey [Daa21]). Electronic noise measured in a *threshold scan* using the Linear front-end of the RD53A readout chip.

Simulation of electrical fields in a pixel detector

Simulation of the electrical field (and potential) in a pixel detector using Scarce [Poh20] is shown in Fig. 7.12. A fully depleted pixel detector with 50 µm × 50 µm with a thickness of 100 µm is considered ($V_{\text{bias}} = 80$ V). Two different readout electrode sizes are shown (30 µm and 15 µm) corresponding to the NW30 and NW15 pixel design of the passive CMOS prototype sensor (see Sec. 4.2). Electrical field and potential along the z-axis (depth) through the pixel centre (top row) and between two pixels (bottom row) are shown. Left figures depict the electrical field and potential, and right figures depict the weighting field and weighting potential. Electrical fields through the centre of a pixel are similar for the two electrode sizes. However, electrical field between two pixels is slightly for larger electrode sizes.

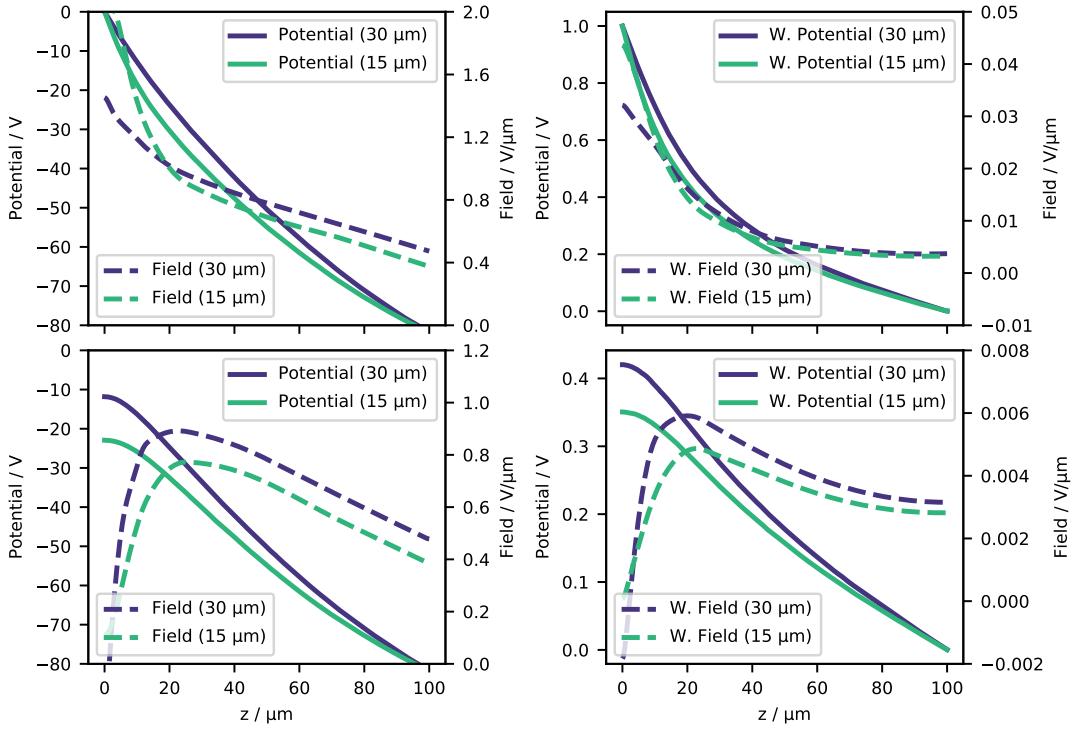

Figure 7.12: Simulated electrical field and potential in a fully depleted pixel detector (50 µm × 50 µm × 100 µm) with different readout electrode size (15 µm and 30 µm) as a function of the depth z. Electrical field and potential along the z-axis (depth) through the pixel centre (top row) and between two pixels (bottom row) are shown. Left figures depict the electrical field and potential. Right figures depict the weighting field and weighting potential. Simulation done with Scarce.

Abbreviations

List of abbreviations. Only the page number with the first occurrence of the respective abbreviation is displayed.

ADC Analogue-to-digital converter. 52
AFE Analogue front-end. 43
ASIC Application-specific integrated circuit. 51

BC Bunch crossing. 53
BCID Bunch crossing ID. 53
BTA Beam telescope analysis. 71

CBCM Charge based capacitance measurement. 112
CCE Charge collection efficiency. 47
CMOS Complementary metal-oxide-semiconductor. 1
CSA Charge-sensitive amplifier. 44
Cz Czochralski. 60

DAC Digital-to-analogue converter. 52
DAQ Data acquisition. 53
DUT Device under test. 71

ENC Equivalent noise charge. 46

FPGA Field-programmable gate array. 96
FZ Float-Zone. 60

GDAC Global threshold DAC. 99

HL-LHC High-Luminosity Large Hadron Collider. 1
HV High voltage. 96

ID Inner Detector. 6
ITk Inner Tracker. 1

Langau Landau-Gauss convolution. 15
LAr Liquid-Argon. 6

LCC Leakage current compensation. 54
LDO Low-dropout regulator. 53
LHC Large Hadron Collider. 1
LV Low voltage. 96

MAPS Monolithic active pixel sensors. 43
MIM Metal-insulator-metal. 1
MIP Minimum ionising particle. 12
MOM Metal-oxide-metal. 102
MOS Metal-oxide-semiconductor. 59
MOSFET Metal-oxide-semiconductor field-effect transistor. 59
MPV Most probable value. 119

NIEL Non-ionising energy loss. 31

PC Personal computer. 96
PCB Printed ciruit board. 74
PS Proton Synchrotron. 3

S/N Signal-to-noise ratio. 99
SCC Single-chip card. 95
SCT Semiconductor Tracker. 8
SM Standard Model of particle physics. 1
SPS Super Proton Synchrotron. 3

TCP/IP Transmission control protocol/internet protocol. 96
TDAC Threshold DAC (per pixel). 54
TDC Time-to-digital converter. 96
TID Total ionising dose. 31
TLU Trigger logic unit. 96
ToT Time-over-threshold. 44
TRT Transition radiation tracker. 8

Bibliography

[Dru00] P. Drude. "Zur Elektronentheorie der Metalle". In: *Annalen der Physik* 306.3 (1900), pp. 566–613. eprint: https://onlinelibrary.wiley.com/doi/pdf/10.1002/andp.19003060312. DOI: https://doi.org/10.1002/andp.19003060312.

[Wil27] C. T. R. Wilson. *On the Cloud Method of Making Visible Ions and the Tracks of Ionizing Particles*. Nobel Lecture. 1927. URL: https://www.nobelprize.org/prizes/physics/1927/wilson/lecture/.

[And32] C. D. Anderson. "The Apparent Existence of Easily Deflectable Positives". In: *Science* 76.1967 (1932), pp. 238–239. DOI: 10.1126/science.76.1967.238.

[Sho38] W. Shockley. "Currents to Conductors Induced by a Moving Point Charge". In: *Journal of Applied Physics* 9.10 (1938), pp. 635–636. eprint: https://doi.org/10.1063/1.1710367. DOI: 10.1063/1.1710367.

[Ram39] S. Ramo. "Currents Induced by Electron Motion". In: *Proceedings of the IRE* 27.9 (1939), pp. 584–585. DOI: 10.1109/JRPROC.1939.228757.

[Lan44] L. Landau. "On the energy loss of fast particles by ionization". In: *J. Phys. (USSR)* 8 (1944), pp. 201–205.

[Mol47] G. Molière. "Theorie der Streuung schneller geladener Teilchen I. Einzelstreuung am abgeschirmten Coulomb-Feld". In: *Zeitschrift Naturforschung Teil A* 2.3 (Mar. 1947), pp. 133–145. DOI: 10.1515/zna-1947-0302.

[Hal52] R. N. Hall. "Electron-Hole Recombination in Germanium". In: *Phys. Rev.* 87 (2 July 1952), pp. 387–387. DOI: 10.1103/PhysRev.87.387.

[SR52] W. Shockley and W. T. Read. "Statistics of the Recombinations of Holes and Electrons". In: *Phys. Rev.* 87 (5 Sept. 1952), pp. 835–842. DOI: 10.1103/PhysRev.87.835.

[Vav57] P. V. Vavilov. "Ionization losses of high-energy heavy particles". In: *Sov. Phys. JETP* 5 (1957), pp. 749–751.

[Gla60] D. A. Glaser. *Elementary Particles and Bubble Chambers*. Nobel Lecture. 1960. URL: https://www.nobelprize.org/prizes/physics/1960/glaser/lecture/.

[Kal60] Rudolph Emil Kalman. "A New Approach to Linear Filtering and Prediction Problems". In: *Transactions of the ASME–Journal of Basic Engineering* 82.Series D (1960), pp. 35–45.

[Bar+64] V. E. Barnes et al. "Observation of a Hyperon with Strangeness Minus Three". In: *Phys. Rev. Lett.* 12 (8 Feb. 1964), pp. 204–206. DOI: 10.1103/PhysRevLett.12.204.

[EB64] F. Englert and R. Brout. "Broken Symmetry and the Mass of Gauge Vector Mesons". In: *Phys. Rev. Lett.* 13 (9 Aug. 1964), pp. 321–323. DOI: 10.1103/PhysRevLett.13.321.

[CT67] D. M. Caughey and R. E. Thomas. "Carrier mobilities in silicon empirically related to doping and field". In: *Proceedings of the IEEE* 55.12 (1967), pp. 2192–2193. DOI: 10.1109/PROC.1967.6123.

[Gro67] A. S. Grove. *Physics and Technology of Semiconductor Devices*. Wiley International edition. Wiley, 1967.

[DH72] Richard O. Duda and Peter E. Hart. "Use of the Hough Transformation to Detect Lines and Curves in Pictures". In: *Commun. ACM* 15.1 (Jan. 1972), pp. 11–15. DOI: 10.1145/361237.361242.

[JR75] F. James and M. Roos. "Minuit: A System for Function Minimization and Analysis of the Parameter Errors and Correlations". In: *Comput. Phys. Commun.* 10 (1975), pp. 343–367. DOI: 10.1016/0010-4655(75)90039-9.

[Jac+77] C. Jacoboni et al. "A review of some charge transport properties of silicon". In: *Solid-State Electronics* 20.2 (1977), pp. 77–89. DOI: https://doi.org/10.1016/0038-1101(77)90054-5.

[Van+80] V. A. J. Van Lint et al. *Mechanisms of Radiation Effects in Electronic Materials*. A Wiley-Interscience publication Bd. 1. Wiley, 1980.

[SB82] Stephen M. Seltzer and Martin J. Berger. "Evaluation of the collision stopping power of elements and compounds for electrons and positrons". In: *The International Journal of Applied Radiation and Isotopes* 33.11 (1982), pp. 1189–1218. DOI: https://doi.org/10.1016/0020-708X(82)90244-7.

[SBS84] R. M. Sternheimer, M. J. Berger, and S. M. Seltzer. "Density effect for the ionization loss of charged particles in various substances". In: *Atomic Data and Nuclear Data Tables* 30.2 (1984), pp. 261–271. DOI: https://doi.org/10.1016/0092-640X(84)90002-0.

[GSS85] T. J. Garosshen, T. A. Stephenson, and T. P. Slavin. "Aluminum Metallization Technology for Semiconductor Devices". In: *JOM* 37.5 (1985), pp. 55–59. DOI: https://doi.org/10.1007/BF03257742.

[Frü87] R. Frühwirth. "Application of Kalman filtering to track and vertex fitting". In: *Nuclear Instruments and Methods in Physics Research Section A: Accelerators, Spectrometers, Detectors and Associated Equipment* 262.2 (1987), pp. 444–450. DOI: https://doi.org/10.1016/0168-9002(87)90887-4.

[KL87] J. Kemmer and G. Lutz. "New detector concepts". In: *Nuclear Instruments and Methods in Physics Research Section A: Accelerators, Spectrometers, Detectors and Associated Equipment* 253.3 (1987), pp. 365–377. DOI: https://doi.org/10.1016/0168-9002(87)90518-3.

[Bic88] Hans Bichsel. "Straggling in thin silicon detectors". In: *Rev. Mod. Phys.* 60 (3 July 1988), pp. 663–699. DOI: 10.1103/RevModPhys.60.663.

[Kru91] F. Krummenacher. "Pixel detectors with local intelligence: an IC designer point of view". In: *Nuclear Instruments and Methods in Physics Research Section A: Accelerators, Spectrometers, Detectors and Associated Equipment* 305.3 (1991), pp. 527–532. DOI: https://doi.org/10.1016/0168-9002(91)90152-G.

[LD91] Gerald R. Lynch and Orin I. Dahl. "Approximations to multiple Coulomb scattering". In: *Nuclear Instruments and Methods in Physics Research Section B: Beam Interactions with Materials and Atoms* 58.1 (1991), pp. 6–10. DOI: https://doi.org/10.1016/0168-583X(91)95671-Y.

[Frü+93] R. Frühwirth et al. "The DELPHI forward track fit Track fitting with outlier rejection". In: *Nuclear Instruments and Methods in Physics Research Section A: Accelerators, Spectrometers, Detectors and Associated Equipment* 334.2 (1993), pp. 528–536. DOI: https://doi.org/10.1016/0168-9002(93)90817-2.

[WH93] E. J. Wolin and L. L. Ho. "Covariance matrices for track fitting with the Kalman filter". In: *Nuclear Instruments and Methods in Physics Research Section A: Accelerators, Spectrometers, Detectors and Associated Equipment* 329.3 (1993), pp. 493–500. DOI: https://doi.org/10.1016/0168-9002(93)91285-U.

[AFW96] V. Alex, S. Finkbeiner, and J. Weber. "Temperature dependence of the indirect energy gap in crystalline silicon". In: *Journal of Applied Physics* 79.9 (1996), pp. 6943–6946. eprint: https://doi.org/10.1063/1.362447. DOI: 10.1063/1.362447.

[Knu97] D. E. Knuth. *The Art of Computer Programming*. Addison-Wesley series in computer science and information processing. Addison-Wesley, 1997.

[McG+97] B. W. McGaughy et al. "A simple method for on-chip, sub-femto Farad interconnect capacitance measurement". In: *Electron Device Letters, IEEE* 18 (Feb. 1997), pp. 21–23. DOI: 10.1109/55.553064.

[Jac98] J. D. Jackson. *Classical Electrodynamics*. Wiley, 1998.

[Air+99] A. Airapetian et al. “ATLAS: Detector and physics performance technical design report. Volume 1”. In: (May 1999).

[Kar99] Veikko Karimäki. “Straight Line Fit for Pixel and Strip Detectors with Arbitrary Plane Orientations”. In: *CMS-NOTE-1999-041* (July 1999).

[Mol99] Michael Moll. “Radiation damage in silicon particle detectors: Microscopic defects and macroscopic properties”. PhD thesis. Hamburg U., 1999.

[BCR00] David Norvil Brown, Eric Charles, and Douglas A. Roberts. “The BaBar Track Fitting Algorithm”. In: *Proc. Computing in High Energy Physics Conference, Padova*. 2000.

[Frü+00] R. Frühwirth et al. *Data Analysis Techniques for High-Energy Physics*. Cambridge Monographs on Particle Physics, Nuclear Physics and Cosmology. Cambridge University Press, 2000.

[Sch+00] F. Scholze et al. “Determination of the electron–hole pair creation energy for semiconductors from the spectral responsivity of photodiodes”. In: *Nuclear Instruments and Methods in Physics Research Section A: Accelerators, Spectrometers, Detectors and Associated Equipment* 439.2 (2000), pp. 208–215. DOI: https://doi.org/10.1016/S0168-9002(99)00937-7.

[Gor+01] Grant Gorfine et al. “Capacitance of silicon pixels”. In: *Nuclear Instruments and Methods in Physics Research Section A: Accelerators, Spectrometers, Detectors and Associated Equipment* 460.2 (2001), pp. 336–351. DOI: https://doi.org/10.1016/S0168-9002(00)01081-0.

[Lin+01] G. Lindström et al. “Radiation hard silicon detectors—developments by the RD48 (ROSE) collaboration”. In: *Nuclear Instruments and Methods in Physics Research Section A: Accelerators, Spectrometers, Detectors and Associated Equipment* 466.2 (2001). 4th Int. Symp. on Development and Application of Semiconductor Tracking Detectors, pp. 308–326. DOI: https://doi.org/10.1016/S0168-9002(01)00560-5.

[Tur+01] R. Turchetta et al. “A monolithic active pixel sensor for charged particle tracking and imaging using standard VLSI CMOS technology”. In: *Nuclear Instruments and Methods in Physics Research Section A: Accelerators, Spectrometers, Detectors and Associated Equipment* 458.3 (2001), pp. 677–689. DOI: https://doi.org/10.1016/S0168-9002(00)00893-7.

[EVL02] V. Eremin, E. Verbitskaya, and Z. Li. “The origin of double peak electric field distribution in heavily irradiated silicon detectors”. In: *Nuclear Instruments and Methods in Physics Research Section A: Accelerators, Spectrometers, Detectors and Associated Equipment* 476.3 (2002). Proc. of the 3rd Int. Conf. on Radiation Effects

on Semiconductor Materials, Detectors and Devices, pp. 556–564. DOI: https://doi.org/10.1016/S0168-9002(01)01642-4.

[Huh02] M. Huhtinen. "Simulation of non-ionising energy loss and defect formation in silicon". In: *Nuclear Instruments and Methods in Physics Research Section A: Accelerators, Spectrometers, Detectors and Associated Equipment* 491.1 (2002), pp. 194–215. DOI: https://doi.org/10.1016/S0168-9002(02)01227-5.

[Kra+02] G. Kramberger et al. "Effective trapping time of electrons and holes in different silicon materials irradiated with neutrons, protons and pions". In: *Nuclear Instruments and Methods in Physics Research Section A: Accelerators, Spectrometers, Detectors and Associated Equipment* 481.1 (2002), pp. 297–305. DOI: https://doi.org/10.1016/S0168-9002(01)01263-3.

[Ago+03] S. Agostinelli et al. "Geant4—a simulation toolkit". In: *Nuclear Instruments and Methods in Physics Research Section A: Accelerators, Spectrometers, Detectors and Associated Equipment* 506.3 (2003), pp. 250–303. DOI: https://doi.org/10.1016/S0168-9002(03)01368-8.

[FTW03] R. Frühwirth, T. Todorov, and M. Winkler. "Estimation of detector alignment parameters using the Kalman filter with annealing". In: *Journal of Physics G: Nuclear and Particle Physics* 29.3 (Feb. 2003), pp. 561–574. DOI: 10.1088/0954-3899/29/3/309.

[Kar+03] V. Karimaki et al. *Sensor Alignment by Tracks*. 2003. arXiv: physics/0306034 [physics.data-an].

[Ber+05] M. J. Berger et al. *ESTAR, PSTAR, and ASTAR: Computer Programs for Calculating Stopping-Power and Range Tables for Electrons, Protons, and Helium Ions (version 1.2.3)*. en. 2005. URL: http://physics.nist.gov/Star.

[Des+05] R. Deslattes et al. *X-ray Transition Energies Database*. 2005. DOI: https://dx.doi.org/10.18434/T4859Z.

[Här+05] J. Härkönen et al. "Particle detectors made of high-resistivity Czochralski silicon". In: *Nuclear Instruments and Methods in Physics Research Section A: Accelerators, Spectrometers, Detectors and Associated Equipment* 541.1 (2005). Development and Application of Semiconductor Tracking Detectors, pp. 202–207. DOI: https://doi.org/10.1016/j.nima.2005.01.057.

[Lev05] H. J. Levinson. *Principles of Lithography*. Online access with subscription: SPIE Digital Library. Society of Photo Optical, 2005.

[Spi05] H. Spieler. *Semiconductor Detector Systems*. Oxford science publications. OUP Oxford, 2005.

[Ros+06] L. Rossi et al. *Pixel Detectors: From Fundamentals to Applications*. Particle Acceleration and Detection. Springer, 2006.

[SN06] S. M. Sze and K. K. Ng. *Physics of Semiconductor Devices*. Wiley, 2006.

[Bal+07] P. Balbuena et al. *RD50 Status Report 2006: Radiation hard semiconductor devices for very high Luminosity colliders*. Tech. rep. Geneva: CERN, Jan. 2007. URL: http://cds.cern.ch/record/1009713.

[Cus07] D. Cussans. *Description of the JRA1 Trigger Logic Unit (TLU), v0.2c*. https://www.eudet.org/e26/e28/e42441/e57298/EUDET-MEMO-2009-04.pdf. 2007.

[Gon+07] L. Gonella et al. "Total Ionizing Dose effects in 130-nm commercial CMOS technologies for HEP experiments". In: *Nuclear Instruments and Methods in Physics Research Section A: Accelerators, Spectrometers, Detectors and Associated Equipment* 582.3 (2007). VERTEX 2006, pp. 750–754. DOI: https://doi.org/10.1016/j.nima.2007.07.068.

[Här+07] J. Härkönen et al. "Magnetic Czochralski silicon as detector material". In: *Nuclear Instruments and Methods in Physics Research Section A: Accelerators, Spectrometers, Detectors and Associated Equipment* 579.2 (2007). Proceedings of the 6th "Hiroshima" Symposium on the Development and Application of Semiconductor Detectors, pp. 648–652. DOI: https://doi.org/10.1016/j.nima.2007.05.264.

[Per07] Ivan Perić. "A novel monolithic pixelated particle detector implemented in high-voltage CMOS technology". In: *Nuclear Instruments and Methods in Physics Research Section A: Accelerators, Spectrometers, Detectors and Associated Equipment* 582.3 (2007). VERTEX 2006, pp. 876–885. DOI: https://doi.org/10.1016/j.nima.2007.07.115.

[Aad+08] G. Aad et al. "The ATLAS Experiment at the CERN Large Hadron Collider". In: *JINST* 3 (2008), S08003. DOI: 10.1088/1748-0221/3/08/S08003.

[Aam+08] K. Aamodt et al. "The ALICE experiment at the CERN LHC". In: *JINST* 3 (2008), S08002. DOI: 10.1088/1748-0221/3/08/S08002.

[Alv+08] A. Augusto Alves Jr. et al. "The LHCb Detector at the LHC". In: *JINST* 3 (2008), S08005. DOI: 10.1088/1748-0221/3/08/S08005.

[Cha+08] S. Chatrchyan et al. "The CMS Experiment at the CERN LHC". In: *JINST* 3 (2008), S08004. DOI: 10.1088/1748-0221/3/08/S08004.

[EB08] Lyndon Evans and Philip Bryant. "LHC Machine". In: *Journal of Instrumentation* 3.08 (Aug. 2008), S08001–S08001. DOI: 10.1088/1748-0221/3/08/s08001.

[Peq08a] Joao Pequenao. "Computer generated image of the ATLAS inner detector". Mar. 2008. URL: https://cds.cern.ch/record/1095926.

[Peq08b] Joao Pequenao. "Computer generated image of the whole ATLAS detector". Mar. 2008. URL: https://cds.cern.ch/record/1095924.

[Bau+09] Jerome Baudot et al. "First test results Of MIMOSA-26, a fast CMOS sensor with integrated zero suppression and digitized output". In: Dec. 2009, pp. 1169–1173. DOI: 10.1109/NSSMIC.2009.5402399.

[DW09] C. DaVia and S. J. Watts. "The geometrical dependence of radiation hardness in planar and 3D silicon detectors". In: *Nuclear Instruments and Methods in Physics Research Section A: Accelerators, Spectrometers, Detectors and Associated Equipment* 603.3 (2009), pp. 319–324. DOI: https://doi.org/10.1016/j.nima.2009.02.030.

[Göt+09] P. Göttlicher et al. "The adaptive gain integrating pixel detector (AGIPD): A detector for the European XFEL. development and status". In: *2009 IEEE Nuclear Science Symposium Conference Record (NSS/MIC)*. 2009, pp. 1817–1820. DOI: 10.1109/NSSMIC.2009.5402196.

[Kar+09] Michael Karagounis et al. "An integrated Shunt-LDO regulator for serial powered systems". In: *2009 Proceedings of ESSCIRC*. 2009, pp. 276–279. DOI: 10.1109/ESSCIRC.2009.5325974.

[Bé+10] M.-M. Bé et al. *Table of Radionuclides*. Vol. 5. Monographie BIPM-5. Pavillon de Breteuil, F-92310 Sèvres, France: Bureau International des Poids et Mesures, 2010. URL: http://www.bipm.org/utils/common/pdf/monographieRI/Monographie_BIPM-5_Tables_Vol5.pdf.

[Ber+10] M. J. Berger et al. *XCOM: Photon Cross Section Database (version 1.5)*. 2010. URL: http://physics.nist.gov/xcom.

[Bur10] J. Burghartz. *Ultra-thin Chip Technology and Applications*. SpringerLink : Bücher. Springer New York, 2010.

[Cap+10] M. Capeans et al. *ATLAS Insertable B-Layer Technical Design Report*. Tech. rep. Sept. 2010. URL: https://cds.cern.ch/record/1291633.

[Cas10a] Gianluigi Casse. "Charge multiplication in highly irradiated planar silicon sensors". In: *PoS* VERTEX2010 (2010), p. 020. DOI: 10.22323/1.113.0020.

[Cas10b] Gianluigi Casse. "Radiation hardness of p-type silicon detectors". In: *Nuclear Instruments and Methods in Physics Research Section A: Accelerators, Spectrometers, Detectors and Associated Equipment* 612.3 (2010). Proceedings of the 7th International Conference on Radiation Effects on Semiconductor materials, Detectors and Devices, pp. 464–469. DOI: https://doi.org/10.1016/j.nima.2009.08.050.

[Gar+11] M. Garcia-Sciveres et al. "The FE-I4 Pixel Readout Integrated Circuit". In: *Nuclear Instruments and Methods in Physics Research Section A: Accelerators, Spectrometers, Detectors and Associated Equipment* 636 (Apr. 2011). DOI: 10.1016/j.nima.2010.04.101.

[Ros11] L. Rossi. "LHC Upgrade Plans: Options and Strategy". In: (Dec. 2011), TUYA02. 6 p. URL: https://cds.cern.ch/record/1407911.

[TGS11] R. Turchetta, N. Guerrini, and I. Sedgwick. "Large area CMOS image sensors". In: *Journal of Instrumentation* 6.01 (Jan. 2011), pp. C01099–C01099. DOI: 10.1088/1748-0221/6/01/c01099.

[Aad+12] G. Aad et al. "Observation of a new particle in the search for the Standard Model Higgs boson with the ATLAS detector at the LHC". In: *Physics Letters B* 716.1 (2012), pp. 1–29. DOI: https://doi.org/10.1016/j.physletb.2012.08.020.

[Cha+12] S. Chatrchyan et al. "Observation of a new boson at a mass of 125 GeV with the CMS experiment at the LHC". In: *Physics Letters B* 716.1 (2012), pp. 30–61. DOI: https://doi.org/10.1016/j.physletb.2012.08.021.

[Kra+12] G. Kramberger et al. "Determination of detrapping times in semiconductor detectors". In: *Journal of Instrumentation* 7.04 (Apr. 2012), P04006–P04006. DOI: 10.1088/1748-0221/7/04/p04006.

[Rub12] I. Rubinskiy. "An EUDET/AIDA Pixel Beam Telescope for Detector Development". In: *Physics Procedia* 37 (2012). Proceedings of the 2nd International Conference on Technology and Instrumentation in Particle Physics (TIPP 2011), pp. 923–931. DOI: https://doi.org/10.1016/j.phpro.2012.02.434.

[Chi13] A. Chilingarov. "Temperature dependence of the current generated in Si bulk". In: *Journal of Instrumentation* 8.10 (Oct. 2013), P10003–P10003. DOI: 10.1088/1748-0221/8/10/p10003.

[Hin13] F. Hinterberger. *Physik der Teilchenbeschleuniger und Ionenoptik*. Springer Berlin Heidelberg, 2013.

[Jaz13] A. H. Jazwinski. *Stochastic Processes and Filtering Theory*. Dover Books on Electrical Engineering. Dover Publications, 2013.

[Kli13] R. Klingenberg. "Quality control on planar n-in-n pixel sensors — Recent progress of ATLAS planar pixel sensors". In: *Nuclear Instruments and Methods in Physics Research Section A: Accelerators, Spectrometers, Detectors and Associated Equipment* 699 (2013). Proceedings of the 8th International "Hiroshima" Symposium on the Development and Application of Semiconductor Tracking Detectors, pp. 56–60. DOI: https://doi.org/10.1016/j.nima.2012.04.076.

[Man13] Igor Mandić. "Silicon sensors for HL-LHC tracking detectors". In: *Nuclear Instruments and Methods in Physics Research Section A: Accelerators, Spectrometers, Detectors and Associated Equipment* 732 (2013). Vienna Conference on Instrumentation 2013, pp. 126–129. DOI: https://doi.org/10.1016/j.nima.2013.06.030.

[Wit13] Tobias Wittig. "Slim edge studies, design and quality control of planar ATLAS IBL pixel sensors". PhD thesis. Technische Universität Dortmund, Apr. 2013. URL: http://hdl.handle.net/2003/30362.

[Fri+14] T. Fritzsch et al. "Flip chip assembly of thinned chips for hybrid pixel detector applications". In: *Journal of Instrumentation* 9.05 (May 2014), pp. C05039–C05039. DOI: 10.1088/1748-0221/9/05/c05039.

[Poi+14] T. Poikela et al. "Timepix3: a 65K channel hybrid pixel readout chip with simultaneous ToA/ToT and sparse readout". In: 9.05 (May 2014), pp. C05013–C05013. DOI: 10.1088/1748-0221/9/05/c05013.

[RA14] W. Riegler and G. Aglieri Rinella. "Point charge potential and weighting field of a pixel or pad in a plane condenser". In: *Nuclear Instruments and Methods in Physics Research Section A: Accelerators, Spectrometers, Detectors and Associated Equipment* 767 (2014), pp. 267–270. DOI: https://doi.org/10.1016/j.nima.2014.08.044.

[Sch14] Benjamin Schwenker. "Development and validation of a model for the response of the Belle II vertex detector". PhD thesis. Georg-August-Universität Göttingen, Oct. 2014. URL: http://hdl.handle.net/11858/00-1735-0000-0023-992D-9.

[Ser14] CERN Service graphique. "Overall view of the LHC. Vue d'ensemble du LHC". In: (June 2014). General Photo. URL: https://cds.cern.ch/record/1708849.

[Gar15] Mauricio Garcia-Sciveres. *RD53A Integrated Circuit Specifications*. Tech. rep. Geneva: CERN, Dec. 2015. URL: https://cds.cern.ch/record/2113263.

[LPS15] Siu Kwan Lam, Antoine Pitrou, and Stanley Seibert. "Numba: A LLVM-Based Python JIT Compiler". In: *Proceedings of the Second Workshop on the LLVM Compiler Infrastructure in HPC*. LLVM '15. Austin, Texas: Association for Computing Machinery, 2015. DOI: 10.1145/2833157.2833162.

[Gai+16] L. Gaioni et al. "65 nm CMOS analog front-end for pixel detectors at the HL-LHC". In: *Journal of Instrumentation* 11.02 (Feb. 2016), pp. C02049–C02049. DOI: 10.1088/1748-0221/11/02/c02049.

[Heu+16] N. Heurich et al. "The New External Beamline for Detector Tests at ELSA". In: *Proc. of International Particle Accelerator Conference (IPAC'16), Busan, Korea, May 8-13, 2016* (Busan, Korea). International Particle Accelerator Conference 7. doi:10.18429/JACoW-IPAC2016-THPOY002. Geneva, Switzerland: JACoW, June 2016, pp. 4088–4090. DOI: doi:10.18429/JACoW-IPAC2016-THPOY002.

[Jan+16] Hendrik Jansen et al. "Performance of the EUDET-type beam telescopes". In: *EPJ Techniques and Instrumentation* 3 (Mar. 2016). DOI: 10.1140/epjti/s40485-016-0033-2.

[Wol16] Pascal Wolf. "Testing and extending a Python-based readout system for a high-resolution pixel detector telescope". BA thesis. Rheinische Friedrich-Wilhelms-Universität Bonn, Sept. 2016.

[Aab+17] M. Aaboud et al. "Performance of the ATLAS Transition Radiation Tracker in Run 1 of the LHC: tracker properties". In: *Journal of Instrumentation* 12.05 (May 2017), P05002–P05002. DOI: 10.1088/1748-0221/12/05/p05002.

[All+17] P. Allport et al. "Recent results and experience with the Birmingham MC40 irradiation facility". In: *Journal of Instrumentation* 12.03 (Mar. 2017), pp. C03075–C03075. DOI: 10.1088/1748-0221/12/03/c03075.

[ATL17a] ATLAS. *Technical Design Report for the ATLAS Inner Tracker Pixel Detector*. Tech. rep. CERN-LHCC-2017-021. ATLAS-TDR-030. Geneva: CERN, Sept. 2017. URL: https://cds.cern.ch/record/2285585.

[ATL17b] ATLAS. *Technical Design Report for the ATLAS Inner Tracker Strip Detector*. Tech. rep. Geneva: CERN, Apr. 2017. URL: https://cds.cern.ch/record/2257755.

[ATL17c] ATLAS. *Technical Design Report for the Phase-II Upgrade of the ATLAS Muon Spectrometer*. Tech. rep. Geneva: CERN, Sept. 2017. URL: https://cds.cern.ch/record/2285580.

[ATL17d] ATLAS. *Technical Design Report for the Phase-II Upgrade of the ATLAS TDAQ System*. Tech. rep. Geneva: CERN, Sept. 2017. URL: https://cds.cern.ch/record/2285584.

[Die17] Yannick Dieter. "Setup and Characterization of the Test Beam Area for Pixel Detector Tests at ELSA". MA thesis. Rheinische Friedrich-Wilhelms-Universität Bonn, Sept. 2017. URL: https://www.hep1.physik.uni-bonn.de/results/data/internal/Dieter_Master.pdf.

[Gar17] Maurice Garcia-Sciveres. *The RD53A Integrated Circuit*. Tech. rep. Geneva: CERN, Oct. 2017. URL: https://cds.cern.ch/record/2287593.

[Heu17] Nikolas Heurich. "Die externe Strahlführung für Detektortests X3ED an der Elektronen-Stretcher-Anlage ELSA". PhD thesis. Rheinische Friedrich-Wilhelms-Universität Bonn, Dec. 2017. URL: https://hdl.handle.net/20.500.11811/7310.

[Jan17] J. Janssen. "Test beam results of ATLAS DBM pCVD diamond detectors using a novel threshold tuning method". In: 12.03 (Mar. 2017), pp. C03072–C03072. DOI: 10.1088/1748-0221/12/03/c03072.

[Poh+17] D.-L. Pohl et al. “Radiation hard pixel sensors using high-resistive wafers in a 150 nm CMOS processing line”. In: 12.06 (June 2017), P06020–P06020. DOI: 10.1088/1748-0221/12/06/p06020.

[Via17] Viacheslav Filimonov. “Development of a serial powering scheme and a versatile characterization system for the ATLAS pixel detector upgrade”. PhD thesis. Rheinische Friedrich-Wilhelms-Universität Bonn, Aug. 2017. URL: https://hdl.handle.net/20.500.11811/7265.

[BCL18] Rafael Ballabriga, Michael Campbell, and Xavier Llopart. “Asic developments for radiation imaging applications: The medipix and timepix family”. In: *Nuclear Instruments and Methods in Physics Research Section A: Accelerators, Spectrometers, Detectors and Associated Equipment* 878 (2018). Radiation Imaging Techniques and Applications, pp. 10–23. DOI: https://doi.org/10.1016/j.nima.2017.07.029.

[Bra18] Nils Braun. “Combinatorial Kalman Filter and High Level Trigger Reconstruction for the Belle II Experiment”. PhD thesis. Karlsruhe: Karlsruhe Institute of Technology (KIT), 2018. URL: https://doi.org/10.5445/IR/1000089317.

[CER18] CERN. *Technical Proposal: A High-Granularity Timing Detector for the ATLAS Phase-II Upgrade*. Tech. rep. Geneva: CERN, June 2018. URL: http://cds.cern.ch/record/2623663.

[GW18] Maurice Garcia-Sciveres and Norbert Wermes. “A review of advances in pixel detectors for experiments with high rate and radiation”. In: *Reports on Progress in Physics* 81 (Feb. 2018). DOI: 10.1088/1361-6633/aab064.

[Hem18] Tomasz Hemperek. “Exploration of advanced CMOS technologies for new pixel detector concepts in High Energy Physics”. PhD thesis. Rheinische Friedrich-Wilhelms-Universität Bonn, Apr. 2018. URL: https://hdl.handle.net/20.500.11811/7541.

[Man+18] Igor Mandić et al. “Charge-collection properties of irradiated depleted CMOS pixel test structures”. In: *Nuclear Instruments & Methods in Physics Research Section A-accelerators Spectrometers Detectors and Associated Equipment* 903 (2018), pp. 126–133.

[Mar+18] S. Marconi et al. “Design implementation and test results of the RD53A, a 65 nm large scale chip for next generation pixel detectors at the HL-LHC”. In: *2018 IEEE Nuclear Science Symposium and Medical Imaging Conference Proceedings (NSS/MIC)*. 2018, pp. 1–4. DOI: 10.1109/NSSMIC.2018.8824486.

[Mol18] Michael Moll. “Displacement Damage in Silicon Detectors for High Energy Physics”. In: *IEEE Transactions on Nuclear Science* 65.8 (2018), pp. 1561–1582. DOI: 10.1109/TNS.2018.2819506.

[Owe18] Rhys Edward Owen. "The ATLAS Trigger System". In: (Feb. 2018). URL: https://cds.cern.ch/record/2302730.

[Spa+18] S. Spannagel et al. "Allpix2: A modular simulation framework for silicon detectors". In: *Nuclear Instruments and Methods in Physics Research Section A: Accelerators, Spectrometers, Detectors and Associated Equipment* 901 (2018), pp. 164–172. DOI: https://doi.org/10.1016/j.nima.2018.06.020.

[Vog+18] Marco Vogt et al. "Characterization and Verification Environment for the RD53A Pixel Readout Chip in 65 nm CMOS". In: *Proceedings of Topical Workshop on Electronics for Particle Physics — PoS(TWEPP-17)* (Mar. 2018). DOI: 10.22323/1.313.0084.

[Wan+18] T. Wang et al. "Depleted fully monolithic CMOS pixel detectors using a column based readout architecture for the ATLAS Inner Tracker upgrade". In: *Journal of Instrumentation* 13.03 (Mar. 2018), pp. C03039–C03039. DOI: 10.1088/1748-0221/13/03/c03039.

[All+19] P. Allport et al. "Experimental determination of proton hardness factors at several irradiation facilities". In: *Journal of Instrumentation* 14.12 (Dec. 2019), P12004–P12004. DOI: 10.1088/1748-0221/14/12/p12004.

[Bey19] Julien-Christopher Beyer. "Optimisation of pixel modules for the ATLAS inner tracker at the high-luminosity LHC". PhD thesis. Ludwig-Maximilians-Universität München, Mar. 2019. URL: http://nbn-resolving.de/urn:nbn:de:bvb:19-239390.

[Cai+19] I. Caicedo et al. "The Monopix chips: depleted monolithic active pixel sensors with a column-drain read-out architecture for the ATLAS Inner Tracker upgrade". In: *Journal of Instrumentation* 14.06 (June 2019), pp. C06006–C06006. DOI: 10.1088/1748-0221/14/06/c06006.

[Cal+19] G. Calderini et al. "Performance of the FBK/INFN/LPNHE thin active edge pixel detectors for the upgrade of the ATLAS Inner Tracker". In: *Journal of Instrumentation* 14.07 (July 2019), pp. C07001–C07001. DOI: 10.1088/1748-0221/14/07/c07001.

[Cer+19] Cerati, Giuseppe et al. "Parallelized and Vectorized Tracking Using Kalman Filters with CMS Detector Geometry and Events". In: *EPJ Web Conf.* 214 (2019), p. 02002. DOI: 10.1051/epjconf/201921402002.

[Die+19] R. Diener et al. "The DESY II test beam facility". In: *Nuclear Instruments and Methods in Physics Research Section A: Accelerators, Spectrometers, Detectors and Associated Equipment* 922 (2019), pp. 265–286. DOI: https://doi.org/10.1016/j.nima.2018.11.133.

[GLC19] Maurice Garcia-Sciveres, Flavio Loddo, and Jorgen Christiansen. *RD53B Manual*. Tech. rep. Geneva: CERN, Mar. 2019. URL: https://cds.cern.ch/record/2665301.

[Gia19] Georgios Giakoustidis. "Characterisation of Hybrid Pixel Detector Modules Based on the 65nm Readout Chip RD53A". MA thesis. Rheinische Friedrich-Wilhelms-Universität Bonn, Oct. 2019.

[Jof+19] Arash Jofrehei et al. "Investigation of crosstalk effects in RD53A modules with 100 and 150 μm thick n-in-p planar sensors". In: *PoS* EPS-HEP2019 (2019), 151. 5 p. DOI: 10.22323/1.364.0151.

[Nak+19] Koji Nakamura et al. "Development of a radiation tolerant fine pitch planar pixel detector by HPK/KEK". In: *Nuclear Instruments and Methods in Physics Research Section A: Accelerators, Spectrometers, Detectors and Associated Equipment* 924 (2019). 11th International Hiroshima Symposium on Development and Application of Semiconductor Tracking Detectors, pp. 64–68. DOI: https://doi.org/10.1016/j.nima.2018.09.015.

[Vog19] M. Vogt. "Radiation-induced effects on data integrity and link stability of the RD53A pixel readout chip". In: *Journal of Instrumentation* 14.05 (May 2019), pp. C05018–C05018. DOI: 10.1088/1748-0221/14/05/c05018.

[Wan+19] Tianyang Wang et al. "A high speed transmitter circuit for the ATLAS/CMS HL-LHC pixel readout chip". In: *PoS* TWEPP2018 (2019), p. 098. DOI: 10.22323/1.343.0098.

[Wer19] N. Wermes. "Pixel detectors ... where do we stand?" In: *Nuclear Instruments and Methods in Physics Research Section A: Accelerators, Spectrometers, Detectors and Associated Equipment* 924 (2019). 11th International Hiroshima Symposium on Development and Application of Semiconductor Tracking Detectors, pp. 44–50. DOI: https://doi.org/10.1016/j.nima.2018.07.003.

[Wol19] Pascal Wolf. "Development of a Proton Irradiation Site at the Bonn Isochronous Cyclotron". MA thesis. Rheinische Friedrich-Wilhelms-Universität Bonn, June 2019.

[Abe+20] O. Aberle et al. *High-Luminosity Large Hadron Collider (HL-LHC): Technical design report*. CERN Yellow Reports: Monographs. Geneva: CERN, 2020. DOI: 10.23731/CYRM-2020-0010.

[ATL20] ATLAS. *ITk Pixel Layout Update*. Technical Report ITK-2020-002. CERN, Geneva. Apr. 2020. URL: https://atlas.web.cern.ch/Atlas/%20GROUPS/PHYSICS/PLOTS/ITK-2020-002/.

[CER20] CERN. *HL-LHC Upgrade Schedule*. 2020. URL: https://project-hl-lhc-industry.web.cern.ch/content/project-schedule.

[Dem+20] Hans Dembinski et al. “scikit-hep/iminuit”. In: (Dec. 2020). DOI: 10.5281/zenodo.3949207.

[Die+20] Y. Dieter et al. “Characterization of small-pixel passive CMOS sensors in 150 nm LFoundry technology using the RD53A readout chip”. In: *Nuclear Instruments and Methods in Physics Research Section A: Accelerators, Spectrometers, Detectors and Associated Equipment* 972 (May 2020), p. 164130. DOI: 10.1016/j.nima.2020.164130.

[DS20] Aleksandra Dimitrievska and Andreas Stiller. “RD53A: A large-scale prototype chip for the phase II upgrade in the serially powered HL-LHC pixel detectors”. In: *Nuclear Instruments and Methods in Physics Research Section A: Accelerators, Spectrometers, Detectors and Associated Equipment* 958 (2020). Proceedings of the Vienna Conference on Instrumentation 2019, p. 162091. DOI: https://doi.org/10.1016/j.nima.2019.04.045.

[Fro20] Markus Frohne. “Developments for a multi-module test system for ATLAS ITk pixel detector modules”. MA thesis. Rheinische Friedrich-Wilhelms-Universität Bonn, Mar. 2020.

[Gem20] Claudia Gemme. “The ATLAS Tracker Detector for HL-LHC”. In: *Proceedings of the 29th International Workshop on Vertex Detectors (VERTEX2020)*. 2020. eprint: https://journals.jps.jp/doi/pdf/10.7566/JPSCP.34.010007. DOI: 10.7566/JPSCP.34.010007.

[Har+20] Charles R. Harris et al. “Array programming with NumPy”. In: *Nature* 585.7825 (Sept. 2020), pp. 357–362. DOI: 10.1038/s41586-020-2649-2.

[KW20] H. Kolanoski and N. Wermes. *Particle Detectors: Fundamentals and Applications*. Oxford University Press, 2020.

[Poh20] David-Leon Pohl. “3D-Silicon and Passive CMOS Sensors for Pixel Detectors in High Radiation Environments”. PhD thesis. Rheinische Friedrich-Wilhelms-Universität Bonn, Oct. 2020. URL: http://hdl.handle.net/20.500.11811/8743.

[Ra20] M. Reichmann and et al. “New test beam results of 3D and pad detectors constructed with poly-crystalline CVD diamond”. In: *Nuclear Instruments and Methods in Physics Research Section A: Accelerators, Spectrometers, Detectors and Associated Equipment* 958 (2020). Proceedings of the Vienna Conference on Instrumentation 2019, p. 162675. DOI: https://doi.org/10.1016/j.nima.2019.162675.

[Ter+20] Stefano Terzo et al. “A new generation of radiation hard 3D pixel sensors for the ATLAS upgrade”. In: *Nuclear Instruments and Methods in Physics Research Section A: Accelerators, Spectrometers, Detectors and Associated Equipment* 982 (2020), p. 164587. DOI: https://doi.org/10.1016/j.nima.2020.164587.

[Vir+20] Pauli Virtanen et al. "SciPy 1.0: Fundamental Algorithms for Scientific Computing in Python". In: *Nature Methods* 17 (2020), pp. 261–272. DOI: 10.1038/s41592-019-0686-2.

[Zyl+20] P. A. Zyla et al. "Review of Particle Physics". In: *PTEP* 2020.8 (2020), p. 083C01. DOI: 10.1093/ptep/ptaa104.

[Ada+21] W. Adam et al. "Comparative evaluation of analogue front-end designs for the CMS Inner Tracker at the High Luminosity LHC". In: *Journal of Instrumentation* 16 (Dec. 2021), P12014. DOI: 10.1088/1748-0221/16/12/P12014.

[ATL21] ATLAS ITk Pixel. *Technical Specification Supply of Planar Pixel Sensors for the ATLAS Inner Tracker upgrade project*. ITk Pixel Sensor meeting. Mar. 2021. URL: https://indico.cern.ch/event/1015557/contributions/4262170/attachments/2203094/3727611/IT-4339_Technical_Specification_Technical_Auditing_V3.pdf.

[Bas21] Marta Baselga. *Performance of Stitched Passive CMOS Strip Sensors*. The 38th RD50 Workshop. June 2021. URL: https://indico.cern.ch/event/1029124/contributions/4411297/.

[Daa+21] M. Daas et al. "BDAQ53, a versatile pixel detector readout and test system for the ATLAS and CMS HL-LHC upgrades". In: *Nuclear Instruments and Methods in Physics Research Section A: Accelerators, Spectrometers, Detectors and Associated Equipment* 986 (2021), p. 164721. DOI: https://doi.org/10.1016/j.nima.2020.164721.

[Daa21] Michael Daas. "Characterization and Quality Control of RD53A Readout Chips and Modules for the ATLAS ITk Pixel Detector". PhD thesis. Rheinische Friedrich-Wilhelms-Universität Bonn, Dec. 2021. URL: https://hdl.handle.net/20.500.11811/9487.

[Die+21] Y. Dieter et al. "Radiation tolerant, thin, passive CMOS sensors read out with the RD53A chip". In: *Nuclear Instruments and Methods in Physics Research Section A: Accelerators, Spectrometers, Detectors and Associated Equipment* 1015 (2021), p. 165771. DOI: https://doi.org/10.1016/j.nima.2021.165771.

[Him21] Adrian Valentin Himmelreich. "Development of a Capacitance Measurement Setup for Silicon Pixel Sensors". BA thesis. Rheinische Friedrich-Wilhelms-Universität Bonn, Aug. 2021.

[Hön21] Jan Cedric Hönig. "Investigation of nitrogen enriched silicon sensors and characterization of passive CMOS strip sensors". PhD thesis. Albert-Ludwigs-Universität Freiburg, Oct. 2021. DOI: 10.6094/UNIFR/222371.

[KK21] H. Krüger and E. Kimmerle. “Precision measurement of pixel sensor capacitance”. In: *Journal of Instrumentation* 16.01 (Jan. 2021), P01029–P01029. DOI: 10.1088/1748-0221/16/01/p01029.

[Rod21] Arturo Rodriguez Rodriguez. *Laboratory Measurements of Stiched Passive CMOS Strip Sensors*. 16th "Trento" Workshop on Advanced Silicon Radiation Detectors. Feb. 2021. URL: https://indico.cern.ch/event/983068/contributions/4223225/.

[Sch21] Lars Schall. “Tests and Characterization of RD53A Modules for the High-Luminosity Upgrade of the ATLAS Detector at the LHC”. MA thesis. Rheinische Friedrich-Wilhelms-Universität Bonn, July 2021.

[Ter21] Stefano Terzo. “ATLAS ITk pixel detector overview”. In: *PoS* ICHEP2020 (2021), p. 878. DOI: 10.22323/1.390.0878.

[Tie+21] Eite Tiesinga et al. “CODATA recommended values of the fundamental physical constants: 2018”. In: *Rev. Mod. Phys.* 93 (2 June 2021), p. 025010. DOI: 10.1103/RevModPhys.93.025010.

[Vog22] Marco Vogt. “Development of the Readout System BDAQ53 and Verification and Characterization of the RD53 Hybrid Pixel Readout Chips”. Unpublished. PhD thesis. Rheinische Friedrich-Wilhelms-Universität Bonn, 2022.

[Daa+] Michael Daas et al. *A DAQ and test system for the RD53 readout chips*. https://gitlab.cern.ch/silab/bdaq53. Accessed: 2021-09-30.

[DJP] Yannick Dieter, Jens Janssen, and David-Leon Pohl. *Beam Telescope Analysis (BTA) is a testbeam analysis software written in Python (and C++)*. https://github.com/SiLab-Bonn/beam_telescope_analysis. Accessed: 2021-11-20.

[Die+] Yannick Dieter et al. *A readout software for Mimosa26 CMOS pixel sensors in Python together with the FPGA-based MMC3 (Multi Module Card) readout hardware*. https://github.com/SiLab-Bonn/pymosa. Accessed: 2021-09-30.

[IBS] IBS. *Ion Beam Services (IBS)*. https://www.ion-beam-services.com/. Accessed: 2021-09-30.

[IZM] IZM. *Fraunhofer-Institut für Zuverlässigkeit und Mikrointegration IZM*. https://www.izm.fraunhofer.de/. Accessed: 2021-09-10.

[JP] Jens Janssen and David-Leon Pohl. *A clusterizer to cluster hits of a pixel detector with Python*. https://github.com/SiLab-Bonn/pixel_clusterizer. Accessed: 2021-11-20.

[JP+] Jens Janssen, David-Leon Pohl, et al. *Software package pyBAR, versatile readout and test system for the ATLAS FE-I4(A/B) pixel readout chip*. https://github.com/SiLab-Bonn/pyBAR. Accessed: 2021-09-30.

[LFo] LFoundry. *LFoundry*. `http://www.lfoundry.com/en/technology`. Accessed: 2021-10-09.

[Poh] David-Leon Pohl. *Software package pyLandau*. `https://github.com/SiLab-Bonn/pylandau`. Accessed: 2021-09-30.

[Sil] Silab. *Software package basil, a modular data acquisition system and system testing framework in Python*. `https://github.com/SiLab-Bonn/basil`. Accessed: 2021-09-30.